Università degli Studi di Ferrara

DOCTORAL COURSE IN PHYSICS

CYCLE XXXVI

COORDINATOR Prof. Eleonora LUPPI

Development of new technologies and methods for next-generation gamma-ray telescopes

Scientific/Disciplinary Sector (SDS) FIS/05

Candidate

Dr. Lisa Ferro

Supervisor

Prof. Piero ROSATI

Co-advisor

Prof. Cristiano GUIDORZI

YEARS 2021/2024

Contents

List of Figures

List of Tables

Abstract

The need for new technologies for High Energy Astrophysics

High Energy Astrophysics (HEA) studies are fundamental to understanding extreme stellar and cosmological scale phenomena. The field of HEA was born in 1962, with Rossi and Giacconi's rocket experiment leading to the discovery of the first extraterrestrial X-ray sources. Over the last seventy years, vast improvements have been made in technologies, techniques, and instruments to study the X and gamma-ray sky. To mention a few examples, high-energy observations have led to the discovery of the most powerful transient sources, such as Gamma-Ray Bursts (GRBs), to the study of Active Galactic Nuclei (AGN) powered by the accretion onto super-massive black holes, with emission mechanisms far more efficient than nuclear fusion, in addition to stellar-size black holes and neutron stars.

However, outstanding questions are still open, in particular in the hard X–ray/soft gamma–ray regime: for example, the origin of the e^+/e^- annihilation line coming from the galactic centre, the nature of the engine that powers GRBs' explosions, the geometry and explosion mechanisms of supernova emission, the role of magnetic fields in magnetars, or in other transient HE sources. The currently available instrumentation in this band lacks sufficient localisation capabilities, spatial and energetic resolution, sensitivity, and the ability to perform polarimetric measurements. Such limitations have thus hindered further advancements in the HEA field.

In this context, this thesis aims to explore and advance the technologies and methods that will allow us to overcome such limits and prepare us for an optimal exploitation of upcoming HE missions. We will focus specifically on the recent experimental progress we have made in advancing the technological readiness of Laue lenses for astrophysics applications. Laue lenses are innovative hard X/soft gamma-ray optics based on Bragg's diffraction law, allowing HE focusing instruments to operate beyond the current limit of $\sim$70 keV, based on multi-layer grazing incident mirrors (as in the NuSTAR mission), up to $\sim$700 keV. The implementation of soft gamma-ray focusing optics is expected to result in a significant increase in sensitivity, up to three orders of magnitude higher than direct view instruments. This development is expected to revolutionise soft gamma astrophysics in a similar way to how the grazing incident optics technology in the sixties opened up unexplored territories in soft X-ray astronomy.

We will describe the design of a new space mission concept based on this type of optics: the Advanced Surveyor for Transient Events and Nuclear Astrophysics (ASTENA), proposed to ESA for the call "Voyage 2050". ASTENA will include two instruments: the Wide Field Monitor (WFM), a wide field detector with both imaging and spectrometric capabilities, and the Narrow Field Telescope (NFT), a soft gamma-ray telescope based on a Laue lens made of hundreds of bent crystals of silicon and germanium. We concentrated our efforts on optimising the design of those two instruments and characterising their properties to meet a number of scientific requirements. In this work, we specifically focused on estimating the polarimetric capabilities of both NFT and WFM to understand how those instruments can play a new competitive role in high-energy polarimetry. This field has recently been revitalised with the Imaging X-ray Polarimetry Explorer (IXPE) launch in 2021. With ASTENA, we expect to reach unprecedented

continuum and line emission sensitivities, enabling highly sensitive polarisation measurements of soft gamma-ray sources.

Finally, technological advancements should always be accompanied by new methodological advancements. We focused on a long-standing challenge in the GRB field: finding a robust and reliable way to simulate light curves (LCs) of GRB events. GRBs are among the most fascinating sources observed in the high-energy sky, and mock GRB LCs can be used to exploit future HE missions optimally and characterise current GRB observations. However, simulating their light curves remains challenging since physical models based on the internal shock paradigm fail to reproduce the diversity of the observed LCs' morphologies. On the other hand, by constructing LC templates from other instruments/missions, one faces the challenge of properly decoupling the real signal from the noise. This work investigates a new approach to simulate GRB LCs based on stochastic models combined with modern machine learning techniques.

This thesis work aims to develop innovative technologies to advance our instrumentation for high-energy astrophysics from different, interconnected points of view. These technologies will overcome the limitations of grazing incident optics, which become ineffective at energies exceeding the hard X-ray band. At the same time, we start exploring new artificial intelligence-based techniques, which inevitably will play a key role in the analysis of upcoming HE missions, particularly in the ever-expanding field of GRBs.

Thesis organization

In the first chapter, we will briefly discuss the state of the art of the observations and the main open questions in HE astrophysics, specifically in the hard X–ray/soft gamma–ray band. We will review the main figures of merit for the characterisation of X/gamma–ray instruments, and we will also give a non-exhaustive overview of some of the most important active or expected space missions in this energy band. We will close the first chapter by describing the technology of Laue lenses and how we plan to implement these optics in the ASTENA concept mission.

The second chapter will describe our recent progress in advancing the technological readiness of Laue lenses. In particular, we will describe the results of the TRILL (Technological Readiness Increase for Laue Lenses) project, which allowed us to develop a technique to bond bent crystal tiles of silicon and germanium on a glass-like substrate through the use of a UV-curable adhesive paste. We will discuss the level of positional accuracy of the tiles we could reach and the results achieved on the point response function (PSF) of the diffracted beam on the focal plane. Even though we are still far from the ambitious requirement of 30″, this is currently one of the best result obtained in the energy range 70–150 keV. We will also discuss how to overcome these limitations with different approaches.

The third chapter will be devoted to a characterisation study of the ASTENA mission itself from the point of view of its polarimetric capabilities, also addressing the innovative science cases that such capabilities will allow one to tackle. In particular, we will describe a Monte Carlo-based model of the instruments onboard ASTENA to assess their capabilities as Compton scattering polarimeters and use this model to investigate some realistic scientific cases.

Finally, in the last chapter, we will describe the development of a new methodology to simulate the light curve of gamma-ray bursts based on a stochastic pulse avalanche model, whose parameters are optimised by implementing a machine-learning algorithm. With this new technique, we aim to simulate realistic, ex-novo GRB light curves in a way that is currently impossible with any existing methods in the literature. Such mock LCs will be an effective tool to make realistic, minimally biased forecasts of observations with upcoming and future GRB missions.

Chapter 1

Introduction: open questions and technological prospects in high energy astrophysics

1.1 Open question in hard X-/soft gamma-ray astronomy

The hard X and soft gamma-ray energy band (70 keV – 10 MeV) is crucial to investigate the physical nature of the most extreme phenomena in the universe (supernovae explosions, gamma-ray bursts, and so on), to study extreme gravity regimes (Active Galactic Nuclei galaxies' emission, X-ray emission from degenerate stars in binary systems, and more), and even to test fundamental physics, such as the Lorentz invariance and the constancy of the speed of light. However, the technological limitations of our current instruments limit the statistical quality measurements in this energy band and deter us from exploiting the hard X/soft gamma-ray sky to its full extent.

In this section, I will describe some of the most interesting open questions in the field and why we need a new generation of instruments to obtain meaningful answers. An extensive review of the main open questions in the field of soft gamma-ray astrophysics can be found in ASTENA's white papers [Frontera et al., 2021, Guidorzi et al., 2021].

1.1.1 Type Ia and core-collapse supernovae physics

Supernovae (SNe) explosions represent the final act of the life of different types of massive stars. Here we consider two main classes: (i) Ia SNe, due to the thermonuclear runaway blast of white dwarfs near the Chandrasekhar limit or by merging of white dwarfs; (ii) core-collapse (cc) SNe, which marks the end of the lifetime of massive stars: the collapse of core triggers an outgoing shock which disrupts the entire star. The mechanisms underlying Ia and cc-SNe explosions are not fully constrained. For both classes, many questions still hold, ranging from the type of explosion mechanism to the presence of asymmetries and clumpiness and the nuclear yields beyond iron.

Ia SNe, especially, plays a key role in cosmology since they are one of the most well-calibrated standard candles thanks to the Phillips empirical relation [Phillips, 1993], which relates the peak luminosity of the SN emission to its total duration. Cosmological distance measurements would greatly benefit from a robust, theoretical formulation of the Phillips relation, which requires a better understanding of Ia SNe explosion mechanisms.

The light curve of Ia SNe is powered by the decay $^{56}\mathrm{Ni} \rightarrow {}^{56}\mathrm{Co}$, with a half-life of 6.1 days, and by the $^{56}\mathrm{Co} \rightarrow {}^{56}\mathrm{Fe}$ decay, with half-life of 77.7 days [Churazov et al., 2014, Diehl, 2015].

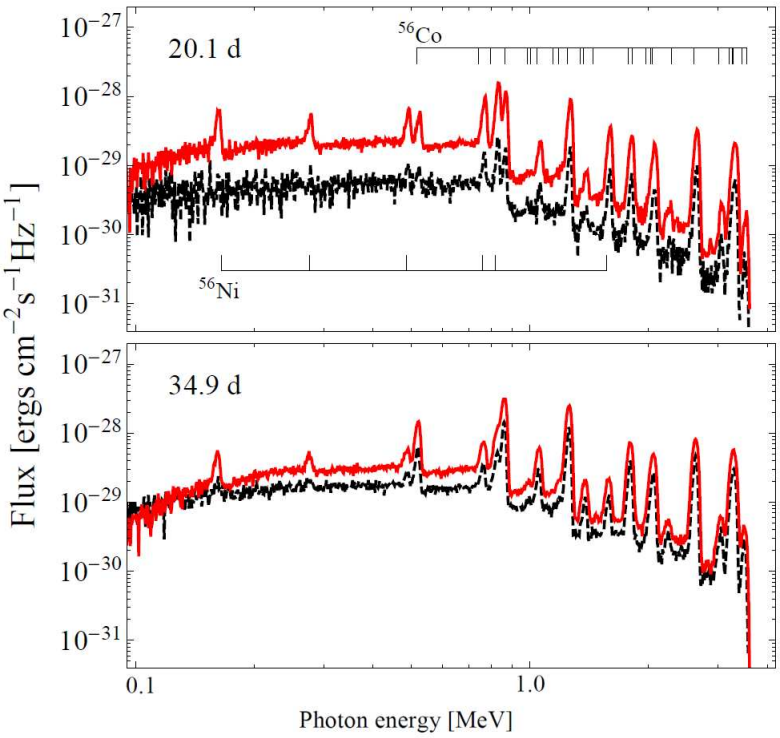

.

Figure 1.1: Expected gamma-ray spectrum of an Ia-SN after 20.1 and 34.9 days from the explosion for two different detonation mechanisms: delayed detonation (red) and violent merger (dashed, black). Adapted from Summa et al. [2013]

The most prominent decay lines are the 158 keV and 812 keV lines from the ^{56}Ni decay and the 847 keV and 1.24 MeV lines from the ^{56}Co decay. The intensity and spatial distribution inside the remnant of the corresponding radioactive nuclei are crucial to determine the amount of nickel and cobalt synthesised during the explosion and the presence of explosion asymmetries. Different explosion models predict different amounts of synthesised nickel and emission line intensities (Fig. 1.1).

For core-collapse SNe, instead, the main diagnostic lines come from the ^{44}Ti through the decay chain $^{44}\text{Ti} \rightarrow {}^{44}\text{Sc} \rightarrow {}^{44}\text{Ca}$ (half-life: 58.9 ± 0.3 yrs, Ahmad et al. 2006). The main lines emitted through this decay are at 4.1, 67.9, 78.4, 511, and 1.157 keV. Due to the chain's long decay time, they turn visible when the ejecta becomes optically thin, so they are a crucial probe of the innermost regions of the SN and the explosion mechanism.

For Ia and cc-SNe, current instruments cannot accurately measure those line emissions to discriminate among the different explosion models. For example, with INTEGRAL, Diehl et al. [2014] measured a line intensity for the 158 keV emission line from SN2014J of $(1.1 \pm 0.4) \times 10^{-4}$ photons cm^{-2} s^{-1}, which corresponds to a detection level of 2.5σ in 150 ks. An increase in instrument sensitivity is thus necessary to lower the minimum amount of detectable synthesised nickel, to obtain measurements from fainter and farther supernovae, and to constrain asymmetries and clumpiness.

1.1.2 Prompt and afterglow emission of GRBs

Besides supernovae, gamma-ray bursts (GRBs) are among the most studied high-energy transients. GRBs show a short-lived gamma-ray prompt emission (~ms – 10 min duration), followed by a long-lived, multi-wavelength afterglow emission, which typically lasts several weeks up

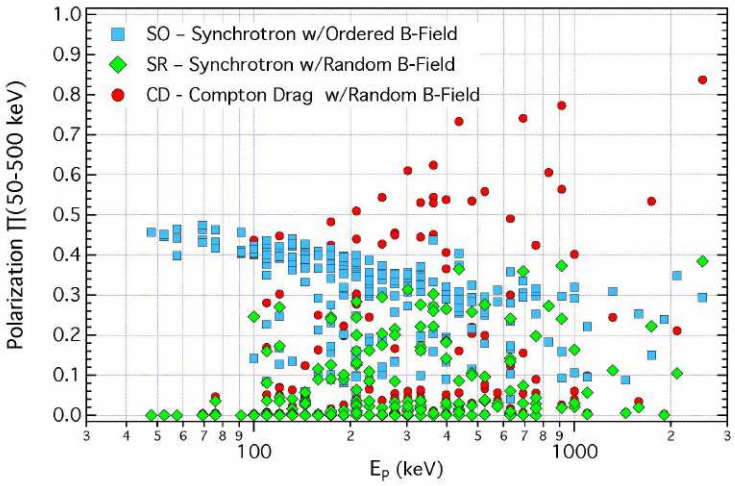

Figure 1.2: Polarisation level vs intrinsic peak energy E_p as predicted by three emission models, as presented in McConnell [2017]

to months after the prompt. GRBs are grouped into two categories depending on their prompt duration: short GRBs, with durations <2 s, and long GRBs, with duration from a couple of seconds up to a tenth of a minute. Most recently, due to the discovery of at least two types of GRBs' progenitors, GRBs started to be classified as either Type I (or, equivalently, binary mergers) if their progenitor is a binary compact object merger or Type II (or equivalently, collapsar) if they are due to the collapse of some special kind of massive stars [Zhang, 2006]. In either case, GRB prompt and afterglow emission show some key features: the light curves of the prompt emission show an extreme degree of variability. In contrast, the emission spectrum is strongly non-thermal and has a typical shape known "Band function" [Band et al., 1993]. Radiation is thought to be emitted along two collimated jets, whose opening angle is not well constrained yet [Salafia and Ghirlanda, 2022], but is estimated in the range of a few degrees typically. The afterglow emission, instead, is mainly synchrotron generated by the interstellar medium electrons, which are shock-accelerated by the GRB relativistic ejecta as they sweep the medium up. The afterglow spans several decades of energies, from radio up to TeV emission. [Kumar and Zhang, 2015].

GRBs have widely been studied since the '70s when the Vela satellites discovered them by accident [Klebesadel et al., 1973]. They have been observed in the following years by many high energy missions, including the Compton Gamma-Ray Observatory [Kniffen, 1989], Swift [Gehrels et al., 2004], AGILE [Tavani, M. et al., 2009], Fermi [Atwood et al., 2009, Meegan et al., 2009], INTEGRAL [Winkler et al., 2002, 2003] and more. With the BeppoSAX satellite [Frontera, 2019], which discovered GRB afterglows, their long-suspected cosmological distance was finally established. However, many key questions regarding the prompt emission mechanism, the role of magnetic fields, the high-energy spectra, the mechanism that powers the afterglow emission, and the kind of progenitors of those events remain unanswered.

From the point of view of the prompt emission, the mechanism responsible for its generation is still not well constrained, as current models can hardly account for the whole variety of temporal and spectral properties within a self-consistent picture. More so, the effect of the magnetic field and its configuration is yet to be understood [Granot et al., 2015]. Measurements of the prompt gamma-ray polarisation hold a unique potential in this respect [Lazzati, 2010].

Recently, the ground-breaking measurements performed by the IXPE [Soffitta et al., 2021] team, which were able to constrain the polarisation level of both prompt and afterglow emission [Negro et al., 2023] of the brightest GRB yet observed, 221009A[1], significantly boosted the

[1]The direction of this GRB was low on the Galactic plane: several complex dust scattering halos was observed

interest in high-energy polarisation measurements. Before IXPE, polarisation measurements were obtained by the POLAR mission [Produit et al., 2018], which measured the time-resolved prompt polarisation of 14 GRBs, finding results compatible with a low polarisation level [Kole et al., 2020], and by AstroSat [Chattopadhyay et al., 2019], which found a high polarisation level on the prompt emission of 5 GRBs, at variance with POLAR results. Instruments with a high effective area and polarimetric capabilities are now required to increase the sample of time-average and time-resolved gamma-ray polarimetric measurements of prompt emission.

Afterglow emission studies would also greatly benefit from new spectroscopic and polarimetric measurements. Discovered by BeppoSAX in the X-ray band [Costa et al., 1997], afterglows were then extensively observed and studied in different energy bands with various instruments. With the advent of Swift [Gehrels et al., 2004], the number of early-time, soft X-ray (<10 keV) afterglows ramped up (e.g. Margutti et al. 2013), while the Large Area Telescope (LAT) on board Fermi detected a few hundreds of afterglows in the energy range 100 MeV - 100 GeV [Ajello et al., 2019]. However, GRB afterglows are still poorly constrained in hard X and soft gamma rays. Hard X-ray afterglows were detected by BeppoSAX/PDS [Maiorano et al., 2005], NuSTAR [Kouveliotou et al., 2013], and INTEGRAL [Martin-Carrillo et al., 2014] up to 60 keV.

With new instruments operating in the hard X-ray/soft gamma-ray energy range, we can start to cover the gap between X-rays and very high-energy measurements.

1.1.3 Electromagnetic counterparts of gravitational wave events

The joint detection of GW170817 by the LIGO-Virgo collaboration and of the short GRB 170817A ushered in the era of multi-messenger astronomy [Abbott et al., 2017]. The data obtained from the coincident GW and GRB detection, along with the multi-wavelength observation campaign for the GRB170817A afterglow and its associated kilonova in the host galaxy NGC 4993 at 40 Mpc, brought a new understanding of the GRB jet structure, the kinematics of the explosion, and of the amount of heavy elements produced. Localising the GRB as the counterpart of a GW transient is also crucial to assess the latter's genuine nature and reduce the localisation error of the event. This will help identify the event's host galaxy and consequently determine its distance. In addition, data from GW and GRB events can be combined to obtain independent estimations of the Hubble constant [Guidorzi et al., 2017] and investigate fundamental physics, such as the Lorentz invariance violation foreseen in some theories [Amelino-Camelia et al., 1998]. In the 2030s, the next generation of GW detectors, such as KAGRA [Abe et al., 2022], the Einstein Telescope [Hild et al., 2008], the Cosmic Explorer [Reitze et al., 2019], the Laser Interferometer Space Antenna (LISA) [Danzmann and the LISA study team, 1996], and more will start operations, thus significantly increasing the number of detection of GW events detected per year. To make the most of the GW triggers, a new generation of full sky monitors that can deliver fast and accurate detections of the associated GRBs is a must for benefiting from the clues that only a multi-messenger picture can finally provide.

1.1.4 The positron annihilation line from the Galactic Centre

The diffused 511 keV e+/e- annihilation line emission in the Galactic Centre (GC) was first detected in the '70s [Johnson et al., 1972, Leventhal et al., 1978, 1980] through balloon flights. In the '80s, the emission was then detected consistently by the Solar Maximum Mission (SMM) and the OSSE experiment aboard CGRO, which both found a flux level of $\sim 10^{-3}$ photons cm^{-2} s^{-1} [Purcell et al., 1993, Share et al., 1990], then a first mapping of the emission was obtained with CGRO, WIND and SMM data [Purcell et al., 1997], which showed that the emission was

[Tiengo et al., 2023], which enabled inference on the GRB prompt emission polarisation properties.

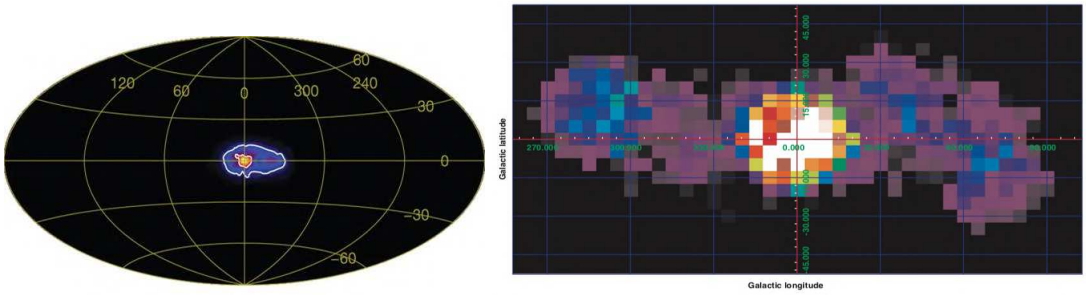

Figure 1.3: Sky map of the 511 keV positron annihilation line found with INTEGRAL/SPI by Weidenspointner et al. [2008] (left) and by Bouchet et al. [2009] (right).

dominated by a central bulge, with an enhancement at positive latitudes. INTEGRAL/SPI has been detecting the emission from the GC for more than ten years. The most up-to-date maps show that the emission presents a central, highly symmetric bulge and strongly asymmetric disc emission, with an enhancement at positive latitudes (Weidenspointner et al. 2008; Fig. 1.3). At the time of writing, the asymmetry is not confirmed yet since this claim contrasts with other results [Bouchet et al., 2009].

The total estimated flux for the whole Milky Way is $(2.7 \pm 0.3) \times 10^3$ photons cm^{-2} s^{-1}, which translates to an annihilation rate of $(3.7 \pm 1.2) \times 10^{43}$ e^+ s^{-1} (assuming a positronium fraction of 1.0) [Siegert et al., 2016]. A flux of this level requires a stable source of positrons, and the debate on its nature is open.

Low-mass X-ray binaries (LMXBs) surrounding the GC are the most promising candidates among discrete sources. LMXBs may be responsible for the emission due to pair annihilation happening in their jets and by photon-photon interaction in the accretion discs of the binaries [Celotti and Blandford, 2001]. The soft X-ray telescope Chandra detected thousands of sources within 17×17 arcmin of Sgr A*, which, combined with the effects of Sgr A* itself, may add to the emission and support the discrete source hypothesis [Alexis et al., 2014, Hailey et al., 2018, Prantzos et al., 2011]. Other possible discrete sources for the emission are dense clusters of stars, such as flaring M- to G- type stars, or globular clusters, which can account for the 511 keV emission [Bisnovatyi-Kogan and Pozanenko, 2017], or the decay from radioactive ejecta in supernovae. The hypothesis that the emission is not an unresolved emission by many point sources but a truly diffuse emission has also been advanced, with some studies suggesting that it could be due to the decay of dark matter particles in Standard Model particles [Bœhm, 2009, Boehm et al., 2004, Finkbeiner and Weiner, 2007]. An updated, in-depth review of the positron emission from the galactic centre can be found in Siegert [2023].

At the time of writing, INTEGRAL/SPI can reach an angular resolution of 2.7 deg [Vedrenne et al., 2003], which is neither enough to understand if the 511 keV emission in the GC is diffuse or not, nor to discriminate among the different kind of possible point-like sources. A new generation of soft gamma-ray instruments is needed to unveil this mystery.

1.1.5 Emission from Active Galactic Nuclei

Active Galactic Nuclei (AGN) galaxies are a class of galaxies whose central regions emit strong, non-stellar radiation spanning different decades of energies, from radio to gamma rays. This strong electromagnetic emission results from the accretion of matter on the super-massive black holes inhabiting the centre of those galaxies [Lynden-Bell, 1969]. High energy data can be used to probe the accretion disc's inner region.

In the case of radio-quiet AGNs, the consensus is that the hard X-ray emission is due to the

Inverse Compton of lower energy (UV/soft X-rays) photons in the accretion disc. Most of this emission is above 100 keV, where the sensitivity of our instrumentation is currently very limited. Measurements were performed with BeppoSAX [Perola et al., 2002], INTEGRAL [Molina et al., 2006], and, in softer bands, by different X-ray telescopes, such as Swift [Parisi, P. et al., 2009], NuSTAR [Harrison et al., 2016], Chandra [Liu et al., 2017], and more. Those data suggest that the cut-off energy for AGNs high energy spectra can be found around 100 keV, with a lower limit below 300 keV [Bassan, 2013].

In the case of radio-loud AGNs, so-called Blazars, we can see that their spectra show two main humps: the first from millimetre microwaves to soft X-rays, while the second from hard X-rays up to high-energy gamma-rays. The two humps are explained as synchrotron emission and Inverse Compton of the same emission, so we expect to see a "dip" in the spectra in the energy range between the two regions, i.e. between 100 keV and 1 MeV.

This means that exploring the hard X-ray band is necessary to characterise the properties of those systems properly.

1.1.6 Low luminosity GRBs and other classes of transients

Besides GRBs and SNe, there is a great variety of different classes of transients, some of which are very recent discoveries.

Low luminosity GRBs (ll-GRBs) are one of those classes. Ll-GRBs are characterised by a peak luminosity of $10^{47} - 10^{48}$ erg/s, in contrast with typical luminosities of $10^{50} - 10^{51}$ erg/s. Most of them have been associated with Ic SNe, with some exceptions [Fynbo et al., 2006], which indicates that the study of this GRB class could help us understand the link between gamma-ray bursts and regular supernovae. Due to the low luminosity, all the observed ll-GRBs are at low redshift. However, studies infer that their volumetric rates can be larger than the ones of regular long GRBs [Liang et al., 2007, Virgili et al., 2009].

Another interesting class of astrophysical objects are the Fast Blue Optical Transients (FBOT), whose spectra show a prominent emission in the blue, and their peak luminosity can be as high as Ibc SNe luminosity ($> 10^{43}$ erg/s). Their light curves show a very fast evolution, incompatible with the nickel decay chain thought to power regular SNe [Pursiainen et al., 2018]. Their progenitors and possible emission at different energy bands are still vastly unknown, and newer and more accurate data in hard X and gamma-rays are necessary to understand their nature and the possible link with other transients. Fast Radio Bursts (FRBs) are also another very interesting class of transients. They are bursts of radio waves with a typical duration of a few ms, which are isotropically distributed in the sky. At the time of writing, almost one thousand FRB sources have been detected, whereas, as of March 2024, the redshift was measured for 51 of them [Bhandari et al., 2020, 2022, Chatterjee et al., 2017, CHIME/FRB Collaboration et al., 2021a, Nicastro et al., 2021, Petroff et al., 2022, Ravi et al., 2019].

At the time of writing, only for the FRB-like event FRB 200428, detected by the Canadian Hydrogen Intensity Mapping Experiment (CHIME; CHIME/FRB Collaboration et al. 2021b), it was possible to localise a hard X-ray counterpart coming from the Galactic magnetar SGR J1935+2154 [Li et al., 2021, Mereghetti et al., 2020, Ridnaia et al., 2021, Tavani et al., 2020].

Lastly, there are a number of unknown high-energy transients encompassing a broad range of physical properties, which were discovered in recent years and whose nature is unknown. They do not seem to have homogeneous properties: their luminosity varies in the range $10^{40} - 10^{46}$ erg/s, while their durations vary from some seconds to hours. A new broadband, wide field survey can help us detect and promptly localise more of them to help understand their nature and origin.

1.2 Performances of High Energy Telescopes

Due to the interaction between X/gamma-ray radiation and the Earth's atmosphere, astronomical high-energy photons can be observed only from space. This imposes heavy constraints on the weight and geometry of high-energy telescopes, demanding significant time and resources for their construction and operation. More so, our ability to concentrate high-energy radiation is very limited. At the time of writing, the only instrument able to focus X-rays up to 70 keV is NuSTAR, thanks to its multilayer mirrors [Harrison and NuSTAR Team, 2013]. Above this limit, high energy missions resort on direct-view instruments, with limited source localisation capabilities obtained using collimators and coded masks. This limits X-/soft gamma-ray telescopes' imaging, spectroscopic and polarimetric performances. In this section, we will describe the main figures of merit used to describe telescopes' performances, and we will highlight why focusing is a crucial feature to achieve new technological advancements.

1.2.1 Telescope sensitivity to continuum

The sensitivity $S_{min}(E)$ of a telescope, in the case of continuous emission, is defined as the minimum source flux such that the signal can be detected above a fixed Signal to Noise (S2N) threshold in an observation time T_{obs}.

The total number N of photons collected by a detector pointing at a source can be written as:

$$N = N_S + N_B \tag{1.1}$$

where N_S is the number of photons coming from the source and N_B are the photons from the background. For a direct view telescope, those can be written as:

$$N_S = \eta(E) S(E) A_D T_{obs} \Delta E \tag{1.2}$$

$$N_B = B(E) A_D T_{obs} \Delta E \tag{1.3}$$

Where $\eta(E)$ is the detector's sensitivity as a function of the photons' energy E, S(E) is the source's flux, measured in photons s^{-1} cm^{-2} keV^{-1}, B(E) is the background's counts, measured in counts s^{-1} cm^{-2} keV^{-1}, A_D is the detector's collection area, and ΔE is the energy band of the observation.

We can write N_S as:

$$N_S = N - N_B = (N_S + N_B) - N_B \tag{1.4}$$

Assuming Poisson statistics and that the fluxes from the source and background are uncorrelated, the standard deviation on the source photon count can be written as:

$$\sigma_{N_S} = \sqrt{\sigma_N^2 + \sigma_{N_B}^2} = \sqrt{\sigma_{N_S}^2 + 2\sigma_{N_B}^2} = \sqrt{N_S + 2N_B} \tag{1.5}$$

In a background-dominated regime, which is a reasonable assumption while evaluating the minimum detectable significative flux, the standard deviation is reduced to $\sigma_{N_S} \sim \sqrt{2N_B}$. Then, the S2N ratio n can be written as:

$$n = \frac{N_S}{\sigma_{N_S}} = \frac{\eta(E) S(E) A_D T_{obs} \Delta E}{\sqrt{2B(E) A_D T_{obs} \Delta E}} \tag{1.6}$$

At this point, we can invert the relation and define the minimum source flux, $S_{min}(E)$, which allows us to measure a signal with a S2N equal to n.

$$S_{min}(E) = \frac{n}{\eta(E)} \sqrt{\frac{2B(E)}{A_d T_{obs} \Delta E}} \tag{1.7}$$

It is worth noticing that, for a direct view telescope, the sensitivity scales as the inverse square root of the detector's area and observation time, which means that, to increase the sensitivity of the instrument by a factor of 10, either the detection area or the observation time must be increased by a factor 100. This is not always easily doable in the contest of a space mission, in which we must take into account constraints both on the observation time and on the total volume and mass of the instruments. However, the situation changes in the case of instruments based on focusing optics. In this case, N_S and N_B are given by:

$$N_S = \eta(E)S(E)f(E)A_{eff}(E)T_{obs}\Delta E \tag{1.8}$$

$$N_B = B(E)A_{f(E)}T_{obs}\Delta E \tag{1.9}$$

Where f(E) is the fraction of PSF in which the data are collected, A_{eff} is the effective area of the optics, and $A_{f(E)}$ is the area below the PSF fraction in which the background is collected. In this case, the sensitivity then becomes:

$$S(E) = \frac{n}{\eta(E)f(E)A_{eff}(E)}\sqrt{\frac{2B(E)A_{f(E)}}{T_{obs}\Delta E}} \tag{1.10}$$

Now, the sensitivity scales with the inverse of the effective area of the telescope's optics, and only the background collected inside the collection area accounts for the background of the measurement. In this way, the sensitivity of a focusing telescope can be from 1 to 3 orders of magnitude greater w.r.t. the sensitivity of a direct-view telescope working in the same energy band, with the same observation time.

1.2.2 Telescope sensitivity to line emission

Emission lines are very important observational targets, and they usually appear superimposed on a continuum emission spectrum. Sensitivity to emission lines for an instrument can be determined by comparing the total flux from the lines with the flux of the continuum and background emission. In most cases, we can describe the spectrum G(E) of an emission line as a Gaussian distribution with total line intensity $\mathrm{I_L}$, peak energy $\mathrm{E_L}$ and standard deviation σ_E:

$$G(E) = \frac{I_L}{\sqrt{2\pi}\sigma_E}\exp\Big[-\frac{1}{2}\Big(\frac{E-E_L}{\sigma_E}\Big)^2\Big] \tag{1.11}$$

The FWHM of the line can be expressed as $\Delta\mathrm{E} = 2.35\sigma_\mathrm{E}$. For a Gaussian-shaped line, we can see that the following relation holds:

$$\int_{E_L-\Delta E/2}^{E_L+\Delta E/2} G(E)\mathrm{d}E = 0.76I_L \tag{1.12}$$

This is often used in real cases to evaluate the total intensity of the emission line from the area below the FWHM. At this point, for a direct viewing telescope, we can write the signal counts $\mathrm{N_S}$ as:

$$N_S = 0.76I_L\eta(E)A_DT_{obs} \tag{1.13}$$

and noise N as:

$$N = \sqrt{I_C(E_L)\eta(E)A_DT_{obs}\Delta E + 2B(E_L)A_DT_{obs}\Delta E} \tag{1.14}$$

where $\mathrm{I_C(E_L)}$ is the flux of the continuum emission under the line. At this point, the S2N ratio becomes:

$$S2N = \frac{0.76I_L\eta(E)A_DT_{obs}}{\sqrt{I_C(E_L)\eta(E)A_DT_{obs}\Delta E + 2B(E_L)A_DT_{obs}\Delta E}} \tag{1.15}$$

We assume again that the intensity of the line is negligible with respect to the background so that we can obtain the line sensitivity as:

$$S_L(E) = 1.31 \frac{n}{\eta(E)} \sqrt{\frac{(I_C(E_L)\eta(E) + 2B(E_L))\Delta E}{A_D T_{obs}}} \tag{1.16}$$

Again, the sensitivity scales with the root of the detection area and the observation time. Furthermore, we can see that the continuum flux contributes to worsening the sensitivity and makes line detection harder.

For a focusing telescope, we can modify the expression of signal and noise as follows:

$$N_S = 0.76 I_L \eta(E) f(E) A_{eff} T_{obs} \tag{1.17}$$

$$N = I_C(E_L)\Delta E \eta(E) f(E) A_{eff} T_{obs} + 2B(E_L) A_{f(E)} \Delta E T_{obs} \tag{1.18}$$

such that the sensitivity becomes:

$$S_L(E) = 1.31 \frac{n}{\eta(E)} \frac{1}{A_{eff}} \sqrt{\frac{\Big(\eta(E) C(E_L) A_{eff} + 2B(E_L) A_{f(E)}\Big)\Delta E}{f(E) T_{obs}}} \tag{1.19}$$

Again, we can see that the sensitivity scales with the inverse of the effective area. At the same time, less background is collected, thus greatly increasing the spectroscopic sensitivity w.r.t. a direct-view instrument.

1.2.3 Minimum detectable polarisation

X/gamma-ray polarisation is a critical yet very hard-to-measure feature of high-energy radiation. Polarisation measurements are based on the fact that the cross-section of the main interactions of X-rays with matter, i.e., photoelectric absorption, Compton/Rayleigh scattering, diffraction, and pair production, depends on polarisation. In all these cases, polarisation measurements are performed by dividing the detection plane in angular bins, and then exploiting the fact that the signal collected can be described by a function of the type [Chattopadhyay, 2021]:

$$S = S_0(1 + a_0 \cos[2(\phi - \phi_0)]) \tag{1.20}$$

This is called modulation curve and, in the most general case, ϕ is the azimuthal angle with respect to a reference axis, S_0 is the mean number of events per bin, a_0 is proportional to the degree of polarisation and ϕ_0 is proportional to the polarisation angle. Estimating the minimum level of polarisation detectable by an instrument is crucial to qualify a polarimeter. Taking into account the presence of Poisson noise, the probability of measuring a polarisation level a and a polarisation angle ϕ, even though the real polar level and angle of the signal are a_0 and ϕ_0, can be written as [Weisskopf et al., 2010]:

$$P(a, \phi) = \frac{Na}{4\pi} \exp\left[- \frac{N}{4}\Big(a^2 + a_0^2 - 2aa_0 \cos(\phi - \phi_0)\Big)\right] \tag{1.21}$$

where $N = nS_0$, and n is the number of angular bins used to reconstruct the modulation curve. Notice that, even in the case of unpolarised radiation ($a_0 = 0$), the probability of measuring an amplitude a is still finite. It is possible to integrate analytically and invert this equation to determine the value of the amplitude that has a 1% probability of being detected due to random fluctuations while observing an unpolarised source. This amplitude $a_{1\%}$ can be obtained from:

$$\frac{N}{2} \int_{a_{1\%}}^{+\infty} a \exp\left[- \frac{Na^2}{4}\right] \mathrm{d}a = 0.01 \tag{1.22}$$

from which we obtain:

$$a_{1\%} = \frac{4.29}{\sqrt{N}} \tag{1.23}$$

Now we must take into account that there may be a contribution from the background to the detected signal. We define R_S and R_B as the signal and background count rates, and a_S as the polarisation amplitude of the source, such that:

$$a_{1\%} = a_S \frac{R_S}{R_S + R_B} \tag{1.24}$$

This means that we can invert and obtain the following:

$$a_S = a_{1\%} \frac{R_S + R_B}{R_S} \tag{1.25}$$

Finally, we define the modulation factor M, which is the amplitude of modulation for a 100% polarised beam in the absence of background, and we can define the Minimum Detectable polarisation as:

$$MDP = \frac{a_S}{M} = \frac{4.29}{QR_S} \sqrt{\frac{R_S + R_B}{T_{obs}}} \tag{1.26}$$

where we have rewritten N as $N = (R_S + R_B)T_{obs}$, in which T_{obs} is the observation time of the measurement. In the case of a direct-view instrument, we can rewrite the MPD as follows:

$$MDP = \frac{a_S}{M} = \frac{4.29}{MS} \sqrt{\frac{S + B}{A_D T_{obs}}} \tag{1.27}$$

where, as before, S and B are the source and background fluxes, and A_D is the detector area. For a focusing telescopes, instead, the MDP becomes:

$$MDP = \frac{a_S}{M} = \frac{4.29}{MS\, f(E) A_{eff}} \sqrt{\frac{S\, f(E) A_{eff} + B A_{f(E)}}{T_{obs}}} \tag{1.28}$$

The MDP is an indication of the minimum level of polarisation that an instrument can detect with good statistical significance and is the main figure of merit in the characterisation of a polarimeter. Due to the need to reconstruct the shape of the modulation curve with enough accuracy, polarimetry is one of the most "photon-hungry" types of measurements; thus, concentrating the radiation and collecting as little background as possible is crucial to measure polarisation.

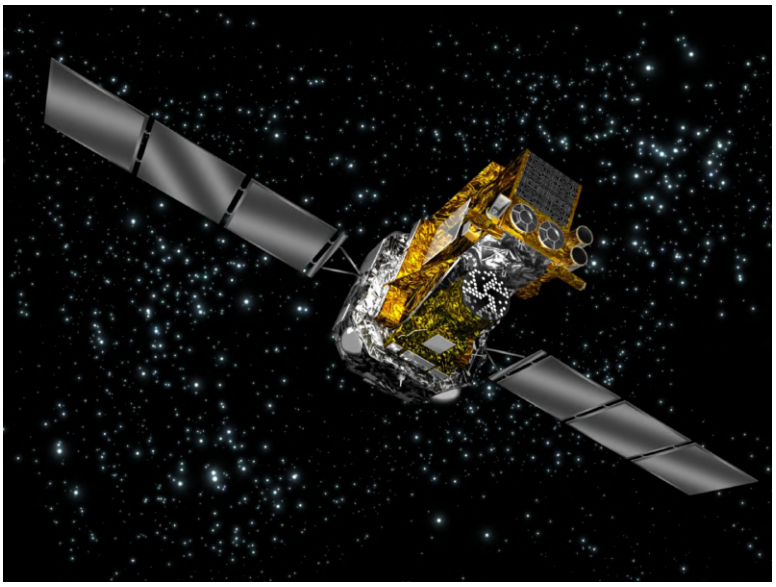

Figure 1.4: Artistic rendition of the INTEGRAL spacecraft in-flight. Credits: ESA/D. Ducros

1.3 Missions for High Energy Astrophysics

It is clear that, with so much left unexplored in the field of high-energy astrophysics, and with so many more possibilities opened in the era of multi-messenger observations, it is now crucial to improve our instrumentation above the current limitations. Moreover, many active hard X and gamma-ray missions, such as INTEGRAL, Fermi, Swift, and more, have been active for at least a decade. The need for a new generation of high-energy missions becomes stronger day by day.

In this section, we will provide a non-exhaustive list of the main high-energy missions active now, the ones scheduled to fly in the next decades, and the most innovative proposed space missions.

1.3.1 The INTEGRAL space mission

The INTErnational Gamma-Ray Astrophysics Laboratory (INTEGRAL) (Fig. 1.4) was launched on October 17, 2002, as part of the ESA program Horizon 2020, and is still active [Winkler et al., 2002, 2003]. INTEGRAL's payload is composed of the imager IBIS (Imager on-Board the INTEGRAL Satellite), the spectrometer SPI (SPectrometer of INTEGRAL), the Joint European X-ray Monitor (JEM-X), and the Optical Monitoring Camera (OMC).

IBIS [Goldwurm et al., 2001] works in the energy band 20 keV - 10 MeV and is an imager constituted by a tungsten coded mask, with a Modified Uniformly Redundant Arrays (MURA) pattern, combined with a lower energy detector (Integral Soft Gamma-Ray Imager, ISGRI, 20 keV - 1 MeV) and a higher energy detector layer (Pixelized Imaging CsI Telescope, PICsIT, 175 keV - 20 MeV). ISGRI is a CdTe pixelised detector [Limousin et al., 1999], while PICsIT is composed of CsI(Tl) scintillators readout by photodiodes [Labanti et al., 2003]. IBIS has a total FoV of 29.1×29.4 deg^2 and a point-source localisation accuracy of 12 arcmin.

The spectrometer SPI [Vedrenne et al., 2003] is an array of 19 High Purity Germanium (HPGe) detectors surrounded by a BGO anticoincidence shield, coupled with a tungsten coded mask with a hexagonal pseudorandom pattern. SPI works in the energy range 18 keV - 8 MeV, has a spectral resolution of 2.2 keV at 1.33 MeV, and an angular resolution of 2.5 deg.

The JEM-X instrument [Lund et al., 2000] is a set of two coded aperture microstrip gas chamber detectors, working in the energy band 3 keV - 35 keV as lower energy counterparts of

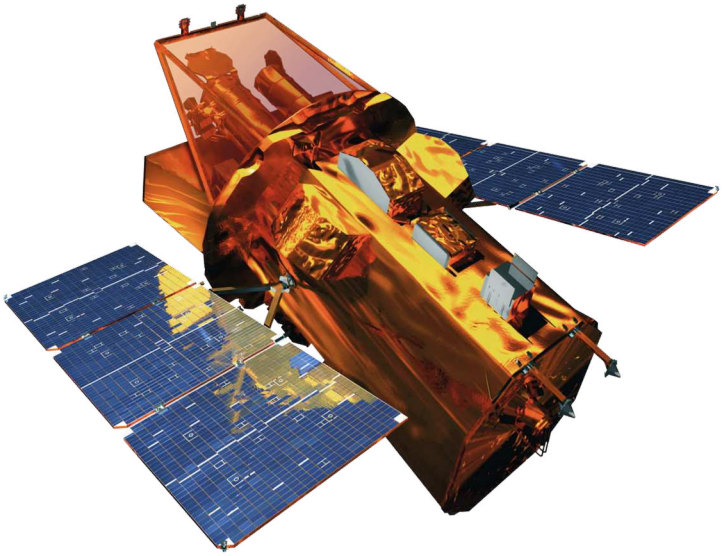

Figure 1.5: The Swift satellite. Credits: NASA E/PO, Sonoma State University/Aurore Simonnet

IBIS and SPI. JEM-X has a fully illuminated FoV of 4.8 deg, with an angular resolution of 3 arcmin, a point source localisation accuracy of 1 arcmin, an energy resolution of 1.3 keV at 10 keV, and a temporal resolution of 122 μs.

Finally, the OMC [Mas-Hesse et al., 2007] is an optical telescope (500–600 nm) with a passively cooled CCD, an aperture of 5 cm diameter and a focal length of 153.7 mm. It has a FoV of 4.979×4.979 deg^2, a time resolution >3 s, a point source localisation accuracy of about 2 arcsec, and an angular resolution of 23 arcsec.

INTEGRAL was the first space mission to observe sources in gamma rays, X-rays, and visible light simultaneously, and it has been a crucial surveyor of the most extreme events in the high-energy sky.

1.3.2 The Swift Observatory

The Neil Gehrels Swift Observatory [Gehrels et al., 2004] was launched on November 20, 2004 and has been observing the X and gamma-ray sky for almost 20 years (Fig. 1.5). As the name suggests, Swift has been designed to perform ultra-fast follow-ups of GRBs and is able to repoint to a target in less than 90 seconds. This is obtained trough an advanced steering technology developed for military applications.

Swift's payload consists of three instruments: the Burst Alert Telescope (BAT), the X-Ray Telescope (XRT), and the UV/Optical Telescope (UVOT). BAT is a coded mask imaging instrument with a CdZnTe pixelated detector array [Barthelmy et al., 2005]. The instrument can perform imaging measurements in the 15-150 keV and act as a full-sky spectrometer up to 500 keV. The FoV of view of BAT is 1.4 steradians and has a point source localisation accuracy of 17 arcmin. The XRT, instead, is constituted of a Wolter-I optics coupled with a CCD detector [Burrows et al., 2005], working in the energy range 0.2-10 keV and with a PSF of 18 arcsec HPD. Finally, the UVOT [Roming et al., 2004] works in the 170-600 nm band and can be used to localise optical GRB afterglows with an accuracy <0.5 arcsec.

Following the successful strategy set up by the Italian-Dutch satellite BeppoSAX [Frontera, 1998], BAT acts as a wide field X/gamma-ray monitor, which triggers the XRT to immediately follow up the high energy signal and obtain a fine localisation of the source through its afterglow emission. The addition of an optical telescope allows Swift to immediately perform

Figure 1.6: The Fermi spacecraft in-flight model. Credits: NASA

fast and accurate afterglow measurements, thus enabling host-galaxy identification and redshift measurement.

1.3.3 Fermi

The Fermi Gamma-ray Space Telescope (formerly GLAST, Gamma-ray Large Area Space Telescope; Fig. 1.6), was launched on June 11, 2008, and is currently the gamma-ray telescope sensitive to the highest energy band in orbit. Fermi's payload consists of two instruments: the Large Area Telescope (LAT; Atwood et al. 2009) and the Gamma-ray Burst Monitor (GBM; Meegan et al. 2009).

The GBM is made up of 12 Sodium Iodide (NaI) scintillation detectors, sensible to the energy band 8 keV - 1 MeV, and two Bismuth Germanate (BGO) scintillators, active in the energy band 150 keV - 40 MeV. GBM can obtain a rough source localisation <15 deg for brighter sources by exploiting the different count rates on the twelve NaI scintillators, thus allowing Fermi to repoint toward the gamma-ray source.

The Large Area Telescope is a successor of the EGRET instrument on board the Compton Gamma-Ray Observatory (CGRO). It is a pair-conversion telescope comprising a tracker, a calorimeter and an anti-coincidence detector. LAT is an array of 4×4 acquisition towers, each comprising a silicon strip detector tracker and a calorimeter made by eight layers of twelve Cesium Iodide (CsI) scintillators readout by photomultipliers. It has an energy band of 20 MeV - 300 GeV, with an energy resolution <10% in all the band, a FoV >2 steradians, and a source localisation accuracy <0.5 arcmin.

Thanks to its sensitivity in the wide energy band spanning five decades, Fermi has been crucial for studying the high-energy sky and allowed us to obtain a deeper insight into GRB prompt emission physics, blazar emission, and more.

1.3.4 NuSTAR: the highest energy focusing telescope

The first and most used technique to focus soft X-rays is grazing incidence optics [Christensen and Ramsey, 2022]. The most typical configuration consists of mirrors, or nested mirrors, of heavy elements (gold, platinum, etc.) in the so-called Wolter I configuration, in which the mirrors are made by a confocal parabolic and hyperbolic segment [Wolter, 1952]. This technique exploits the properties of X-ray refraction to focus the radiation, and many successful instruments, such

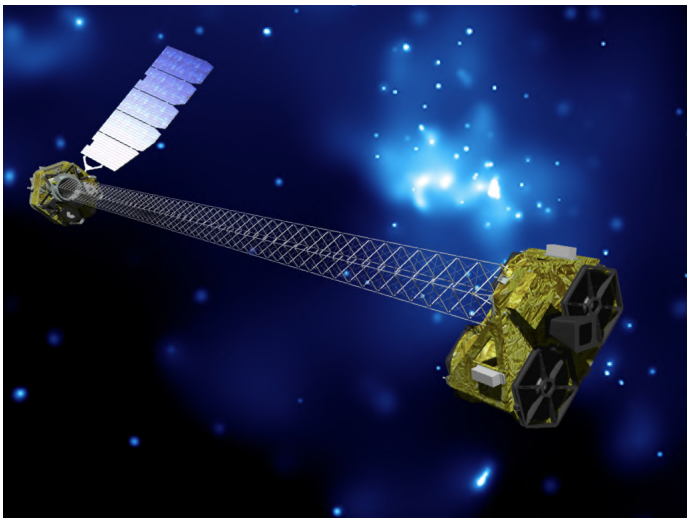

Figure 1.7: Artistic view of NuSTAR's in-flight configuration. Credits: NASA

as the Einstein Observatory [Giacconi et al., 1979], Chandra X-ray Observatory [Weisskopf et al., 2002], XMM-Newton [Jansen, F. et al., 2001], and more, has been based on grazing incidence optics. However, this technique can be applied only for energies up to 30 keV, after which the effective area grazing incidence optics becomes too low to be useful.

The Nuclear Spectroscopic Telescope ARray (NuSTAR) (Fig. 1.7) was designed to overcome these limits by exploiting innovative multilayer optics. NuSTAR was launched on June 13, 2012, and has been the first astronomical telescope able to focus in the energy band 3 keV - 79 keV [Harrison and NuSTAR Team, 2013].

NuSTAR's optics consist of alternate layers of high-Z materials (tungsten and platinum), with low-Z materials (silicon, carbon, and silicon carbide). This mimics the structure of a crystal lattice and creates constructive interference, enhancing the reflectivity to hard X-rays compared to what is possible with standard grazing incidence optics.

NuSTAR is equipped with two optics modules containing 133 of such nested multilayer grazing incidence shells, in Wolter-I geometry [Harrison et al., 2005]. The focal length of the optics is 10.14 m, which required a deployable mast to be reached [Harp et al., 2010]. Each optics is equipped with a pixelated CdZnTe pixelated detector, surrounded by a CsI anti-coincidence shield.

NuSTAR can reach an angular resolution of 58 arcsec (HPD), with an energy resolution of 0.9 keV at 60 keV, and a temporal resolution of 0.1 msec. NuSTAR conducted important surveys of the main X-ray sources, including black holes, AGNs, supernova explosions, and many more.

1.3.5 HXMT

The Insight-Hard X–ray Modulation Telescope (HXMT) is the first Chinese X-ray astronomy satellite (Fig. 1.8). HXMT was launched on June 15, 2017. Its scientific payload consists of three main instruments: the High Energy X-ray telescope (HE, 20-250 keV energy band, 5100 cm^2 detector area), the Medium Energy X-ray telescope (ME, 5-30 keV energy band, 952 cm^2 detector area), and the Low Energy X-ray telescope (LE, 1-15 keV energy band, 384 cm^2 detector area) [Zhang et al., 2020].

The HE telescope [Liu et al., 2020] consists of 18 cylindrical High Energy Detectors (HEDs), each composed of a phoswich module and its collimator. Each detector unit is a NaI(Tl)/CsI(Na) phoswich scintillation detector with a diameter of 19.6 cm. The thickness of the NaI main detector is 3.5 mm, while the thickness of the CsI shielding is 40 mm. A 5-inch PMT is used to

Figure 1.8: Artistic rendering of HXMT. Reprinted from Zhang et al. [2020]

collect the fluorescence of both NaI and CsI crystals. The FoV of the HE telescope is 5.7 × 5.7 degrees^2 and its energy resolution is about 15% at 60 keV.

The ME telescope [Cao et al., 2020] is a pixelated Si-PIN detector (1728 pixels) coupled with mechanical collimators. The ME telescope has an energy resolution of 3 keV at 17.8 keV and a time resolution of 255 μs. Finally, the LE telescope [Chen et al., 2020] features a swept charge device (SCD) sensor coupled with mechanical collimators. The LE telescope reaches an energy resolution of 140 eV at 5.9 keV and has a time resolution of 0.98 ms.

Insight-HXMT aims to conduct an all-sky survey to detect obscured supermassive black holes, build a comprehensive AGN catalogue, observe X-ray binaries, and detect GRBs.The first HXMT gamma-ray bursts catalogue was published in 2022 Song et al. [2022], containing 322 GRBs detected by the satellite in the first four years of activity.

1.3.6 The SVOM mission

The Space-based multi-band astronomical Variable Objects Monitor (SVOM) mission [SVOM Collaboration et al., 2023, Yu et al., 2020] is a French-Chinese satellite scheduled for launch in the present year 2024 (Fig. 1.9). The payload of SVOM consists of four instruments: the ECLAIRs telescope, the Microchannel X-ray Telescope (MXT), the Gamma Ray burst Monitor (GRM), and the Visible Telescope (VT).

The ECLAIRs [Schanne et al., 2018] consists of a coded mask paired with a CdTe focal plane detector, with a FoV of 2 steradians, passband of 4 keV - 250 keV, and an expected point-source localisation <10 arcmin. The ECLAIRs will give gamma-ray burst triggers for the other instruments onboard SVOM. The MXT [Meuris et al., 2023] is a soft X-ray telescope composed of a 40 mm micro-channel plates optics and an X-ray-sensitive pnCCD camera. The MXT will work in the 0.2 - 10 keV energy range and will provide both images and spectra with a resolution of 75 eV at 1.5 keV. The FoV of the instrument is 1.1 × 1.1 degrees^2, and it will detect sources with an accuracy <1 arcmin. The GRM [Wen et al., 2021] is a set of three gamma-ray detectors based on sodium iodide (NaI) scintillators, working in the energy range 15 keV - 5 MeV and covering a FoV of 2.6 steradians. Each scintillator has a collection area of 200 cm^2 and is attached to a photomultiplier tube. The main scope of the GRM will be to measure the spectrum and the variation of the gamma-ray emission during a gamma-ray burst. It will also provide a rough source localisation through triangulation with an accuracy of 15 × 15 degrees^2. Finally, the VT is designed to measure the visible afterglow of the gamma-ray bursts triggered by ECLAIRs. It will be able to measure the position of the afterglows with an accuracy of a few arcseconds and allow us to localise GRBs up to a redshift of 6.5.

Figure 1.9: The qualification model of SVOM during the integration in Shanghai. Credits: the SVOM collaboration website (https://www.svom.eu/en/the-svom-mission/)

Designed to follow in Swift's footsteps and build on Swift's legacy, SVOM is complemented by two dedicated ground-based segments: the Ground-based Wide Angle Camera (GWAC) in China and the Ground Follow-up Telescopes. The instruments on SVOM will trigger the ground segment, thus granting a quick follow-up of the transients detected by the satellite.

1.3.7 The HERMES Pathfinder

HERMES (High Energy Rapid Modular Ensemble of Satellites) is a pathfinder for a mission based on a constellation of nano-satellites in low Earth orbit (Fig. 1.10). The HERMES constellation will consist of six 3U Cubesats, each containing a miniaturised detector to probe the X-ray temporal emission of bright high-energy transients [Fiore et al., 2022]. A seventh detector is hosted on the SpIRIT 6U nanosat [Auchettl et al., 2022]. The first three HERMES modules and the one onboard SpIRIT are already in orbit and active, while the last three modules will be deployed in the second half of 2024.

The idea behind HERMES is overcoming the concept of monolithic instruments, which has been a staple in high-energy astrophysics, to explore the possibility of increasing the detection area of direct-view instruments through deploying a fleet of small detector satellites and exploiting triangulation algorithms to localise sources. This would allow one to limit the size and weight of space detectors and, at the same time, reduce the cost of high-energy missions through the application of "low-cost" nanosats and launchers.

The detectors aboard the HERMES satellites are made up of cerium-doped gadolinium-aluminium-gallium garnet (GAGG:Ce) scintillator crystals coupled with two Silicon Drift Detectors (SDDs) each [Evangelista et al., 2020]. Lower energy X-rays (<30 keV) are detected by the SDDs, while gamma-rays are absorbed in the scintillators, producing light that the SDDs

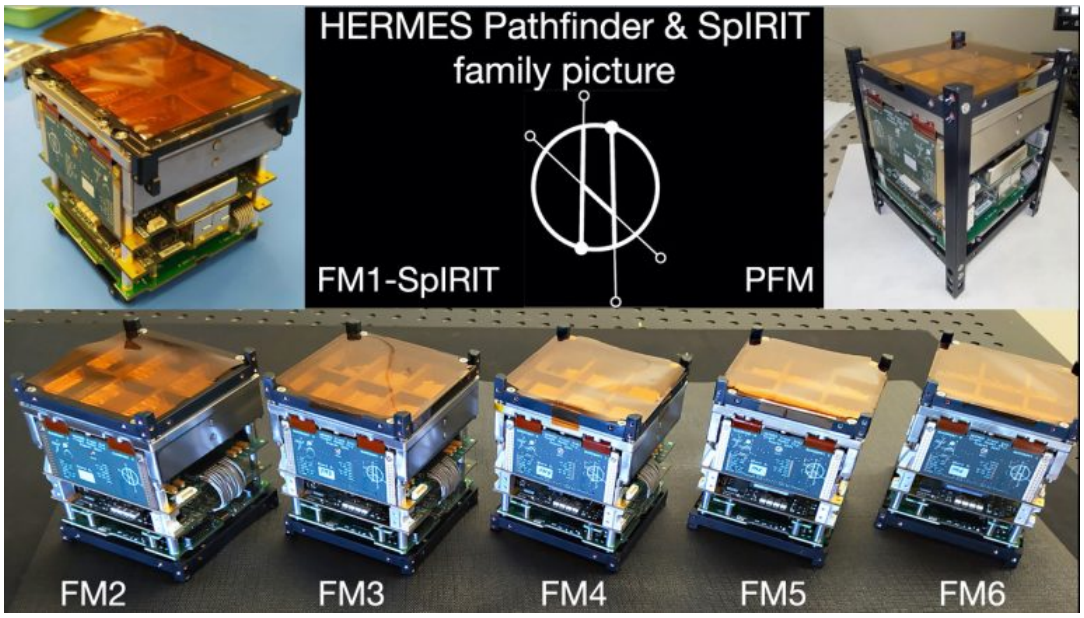

Figure 1.10: The HERMES Pathfinder modules, before integration. Credits: Marco Citossi, the HERMES Collaboration website. (https://www.hermes-sp.eu/?p=10554)

then detect. The different time constant of those two interactions allows us to distinguish between X and gamma rays. This technology allows HERMES's detectors to cover the 2 keV - 2 MeV energy band.

The main objective of the HERMES pathfinder is to demonstrate the feasibility of employing nanosat for high energy astrophysics. It will be among the firsts of a new generation of constellation-based instruments [Burderi et al., 2021, Cinelli et al., 2021].

1.3.8 Transient High Energy Sky and Early Universe Surveyor (THESEUS)

The THESEUS mission concept (Fig. 1.11) was proposed in response to the ESA M7 call for missions within the Cosmic Vision Programme and selected by ESA in 2023 to enter phase A study. THESEUS' primary scientific goal is to explore the early universe by studying the population of early universe GRBs (first billion years of the universe) while performing a deep monitoring of the X-ray transient universe [Amati et al., 2021]. THESEUS is designed to be highly synergic with the forthcoming new generations of gravitational wave interferometers (Einstein Telescope, LISA), X and gamma-ray satellites (Athena, SVOM), astroparticle experiments (IceCube-Gen 2, Km3Net), Cherenkov telescopes (CTA), and more.

The payload of THESEUS will include three instruments: an X/Gamma-ray Imaging Spectrometer (XGIS) [Amati et al., 2022], a Soft X-ray Imager (SXI), and an InfraRed Telescope (IRT). The XGIS (Fig. 1.12, top) is made up by two coded-mask X/Gamma-ray cameras. Each XGIS camera consists of a tungsten coded mask and collimator system, mounted on a position sensitive detector. The detector consists of Cesium Iodide scintillator bars, with 5 mm sides, readout on top and bottom by square Silicon Drift Detectors (SDDs), forming a "siswich" (silicon sandwich) system [Marisaldi et al., 2004]. The XGIS will work as a coded-mask spectra-imager for 2 keV up to 150 keV, and as a full-sky spectrometer above 150 keV, up to 10 MeV. The siswich architecture enables us to distinguish between low-energy X-rays up to 30 keV, which the top SDD detects alone, and higher-energy gamma rays. The gamma rays are absorbed in the scintillator, producing scintillation light that triggers both the top and bottom SDDs. The

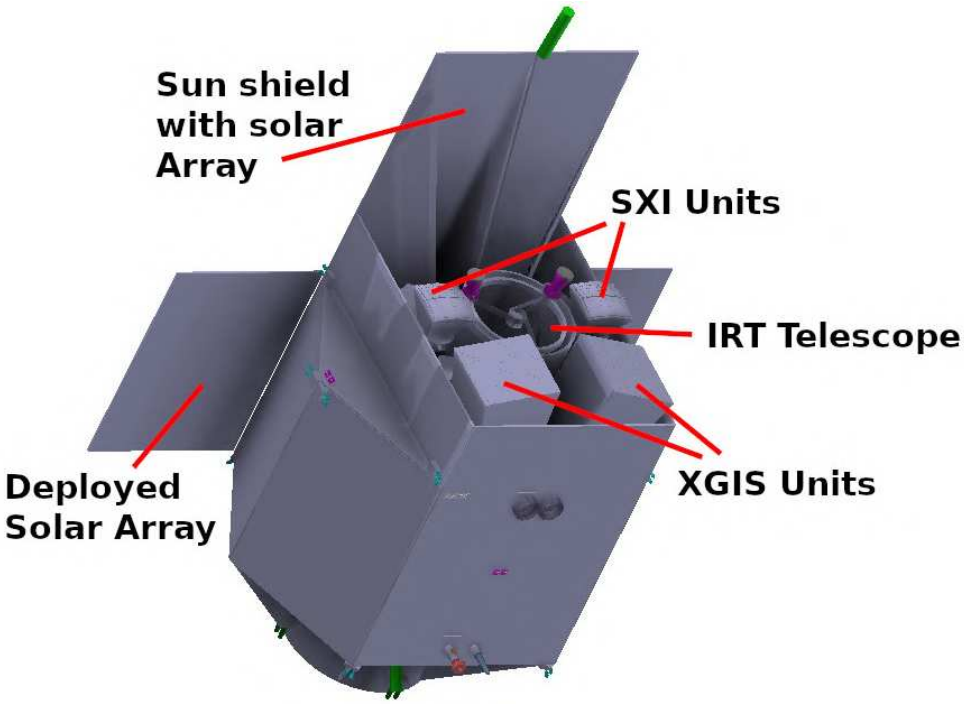

Figure 1.11: Sketch of the THESEUS satellite in-flight configuration. Credits: the THESEUS consortium website (https://www.isdc.unige.ch/theseus/)

different time constants of the two types of interactions are used for the discrimination. The two XGIS cameras are misaligned by ±20 deg from the satellite's body, thus providing a total imaging FoV of 117×77 degrees^2, while the total non-imaging FoV is about 2π steradians. The point-source localisation capabilities of the XGIS will be ≤ 15 arcminutes inside the imaging FoV, while outside it is possible to obtain a rough localisation accuracy of a few tens of degrees by exploiting Compton imaging and the detection plane architecture [Cavazzini, 2021].

The SXI (Fig. 1.12, centre), instead, will be a set of two lobster-eye telescope units focusing on CMOS X-ray detectors, working in the 0.3–5 keV energy range and covering a FoV of 0.5 sr [O'Brien et al., 2021]. Finally, the IRT (Fig. 1.12, bottom) is a 0.7-m class IR telescope with a FoV of 15 x 15 arcmin^2 and working in the band 0.7-1.8 μm [Götz et al., 2021]. IRT will have imaging capabilities in the I, Z, Y, J and H bands, and spectroscopic capabilities (resolving power, R = 400, through 2' $\times$ 2' grism).

Thanks to its combination of a wide field localisation camera, a soft X-ray telescope, and an IRT telescope for immediate IR-VIS counterpart localisation, THESEUS will double the sample size of detected GRBs with known redshift, allowing us to investigate the early Universe in a unique way. Furthermore, THESEUS will be crucial for the fast localisation of electromagnetic counterparts of gravitational wave events, thus playing a crucial role in multi-messenger and time-domain astrophysics.

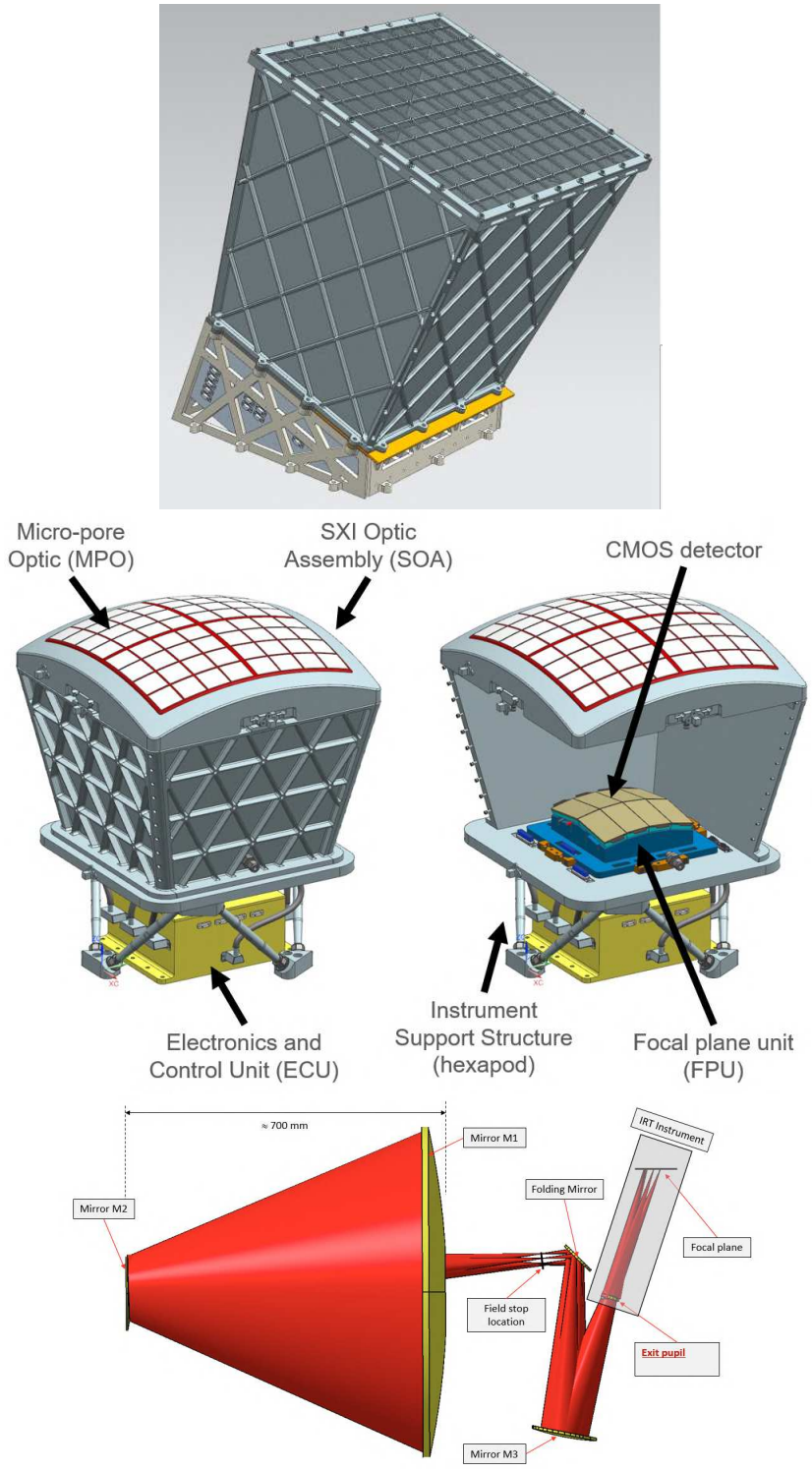

Figure 1.12: *Top:* One of the two cameras of the XGIS instrument on board THESEUS. Reprinted from Amati et al. [2021] *Center:* The SXI instrument model. Reprinted from Amati et al. [2021]. *Bottom:* Schematics of the IRT. Reprinted from Götz et al. [2021]

1.4 Laue lenses and the ASTENA mission concept

With multilayer grazing incidence optics, it is possible to focus hard X-rays up to about 80 keV. However, the energy band in which we can build high-energy optics remains pretty limited, and the hard X/soft gamma band is still mainly studied with direct-view instruments.

The need for new technologies to overcome today's limits is arising, and here we describe a technique which could help us to overcome this challenge: Laue lenses, focusing optics based on Bragg's law of diffraction. We will also describe a concept mission based on a Laue lens optics: ASTENA, the Advanced Surveyor for Transients Events and Nuclear Astrophysics, which was submitted to the ESA Call "Voyage 2050".

1.4.1 The Laue lens concept

Laue lenses are innovative X and gamma-ray optics based on Bragg's law of diffraction in crystals [Zachariasen, 1945]:

$$2d_{hkl} \sin\theta_B = n\frac{hc}{E} \tag{1.29}$$

where θ_B is the Bragg's angle, which is the angle between the diffraction planes of the crystal and the diffracted beam, d_{hkl} is the inter-planar spacing of the diffraction planes of the crystal with Miller indexes (hkl), E is the energy of the diffracted photon, n is the diffraction order and hc corresponds to 12.39 keV·Å. The crystals can be arranged in such a way that the X-ray beam can be reflected by a thin, superficial layer of the crystal (Bragg, or Reflection, geometry), or it can cross the whole crystal and be transmitted over it (Laue, or Transmission geometry).

Optics based on Bragg's law of diffraction in Laue configuration can be of great interest in the astrophysical context because (i) Bragg's diffraction is effective up to energies of few MeV and (ii) the transmission configuration can be exploited to increase the effective area of the optics. A Laue lens is exactly based on this concept: it can be visualised as a spherical cap of radius R covered by crystal tiles oriented in such a way that the radiation coming from the sky is transmitted through the crystals and sent to the focal point. The focal distance of the lens f is equal to half the curvature radius of the spherical cap [Frontera and von Ballmoos, 2010] (Fig. 1.13).

There are different configurations for the crystals on the cap which can be chosen to optimise the effective area in different ways; the simplest one is to place the crystals in concentric rings at a distance r from the axis of the lens. From Bragg's equation, we can see that the centroid of the energy spectrum of the photons diffracted by each ring can be expressed as [Frontera and von Ballmoos, 2010]:

$$E = \frac{hc}{2d_{hkl}} \sin\left[\frac{1}{2}\arctan\left(\frac{f}{r}\right)\right] \sim \frac{hc}{d_{hkl}}\frac{f}{r} \tag{1.30}$$

where the approximation holds for small Bragg's angle, which is the case of hard X and gamma-rays. Higher energy photons are diffracted from crystals in the inner region of the lens, while lower energy photons interact with the outermost regions of the optics (Fig. 1.15). The pass-band $[E_{min}, E_{max}]$ of a spherical Laue lens can then be expressed as:

$$\begin{cases} E_{min} = \frac{hc}{d_{hkl}}\frac{f}{r_{max}} \\ E_{max} = \frac{hc}{d_{hkl}}\frac{f}{r_{min}} \end{cases} \tag{1.31}$$

where r_{min} and r_{max} are the inner and outer radius of the lens. By setting the focal lens and the radii of the Laue lens, it is possible to build a broad-band, high-energy radiation concentrator, which can effectively serve as the optics of an X/gamma ray telescope. The downside of those

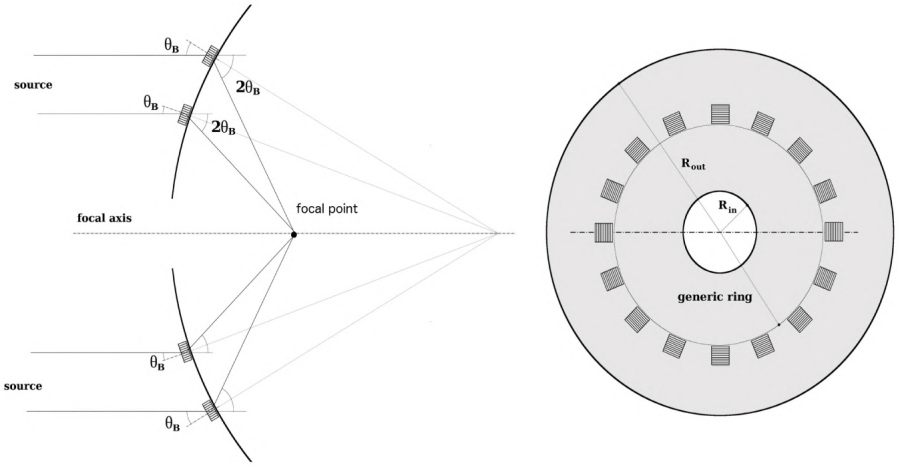

Figure 1.13: Side and top view of a Laue lens. The crystals are positioned on a spherical support in such a way that the radiation coming from the sky, parallel to the optical axis of the lens, interacts with the crystals and is focused. The diffraction planes of the crystals are oriented in such a way that the angle between them and the incoming X-ray beam is equal to the Bragg's angle θ_B, so the angle between the diffracted beam and the incoming beam is $2\theta_B$. The focal lens is equal to half the curvature radius of the spherical cap.

types of Laue lenses is that they do not satisfy the Abbe sine condition [Abbe Hon., 1881]. The Abbe condition was developed in the context of microscopy and gives a mathematical condition that an optical system must satisfy to avoid coma aberration:

$$\frac{h}{\sin\alpha} = \text{const} \tag{1.32}$$

Where h is the distance between the optical axis and the light-ray impinging on an optics and α is the arrival angle of the photon. For Laue lenses (Fig. 1.14), we can see that:

$$\sin\alpha = \sin(\pi/2 - 2\theta_B) = \cos 2\theta_B \tag{1.33}$$

where θ_B is the Bragg's angle of the interaction, and

$$h = F\tan\alpha = F\cot 2\theta_B \tag{1.34}$$

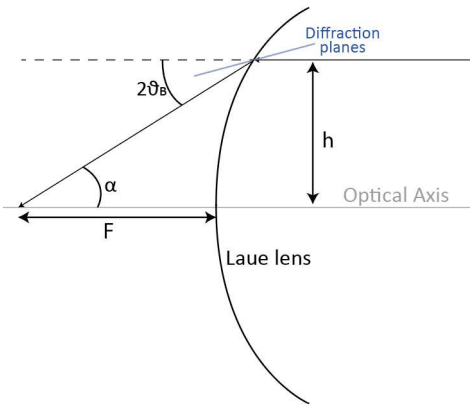

Figure 1.14: The Abbe sine condition applied to Laue lenses. F is the focal distance of the lens, h is the distance between the incoming photon and the optical axis, θ_B is the Bragg's angle.

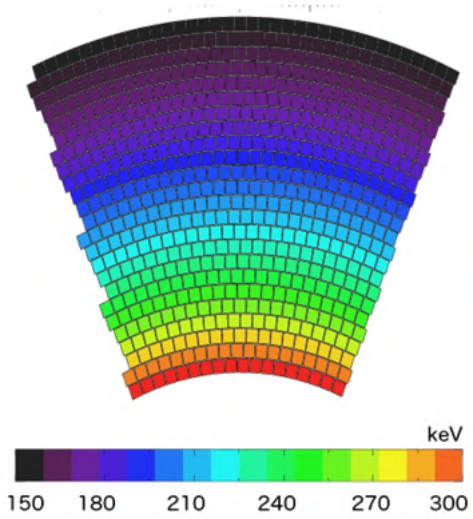

Figure 1.15: In a spherical Laue lens, all the crystals at the same radial distance from the centre of the lens are sensitive to the same energy range, so by nesting multiple rings it is possible to build a broad-band Laue lens. The highest energies are focused by the innermost crystals, while the lower energies are focused by the outermost crystals.

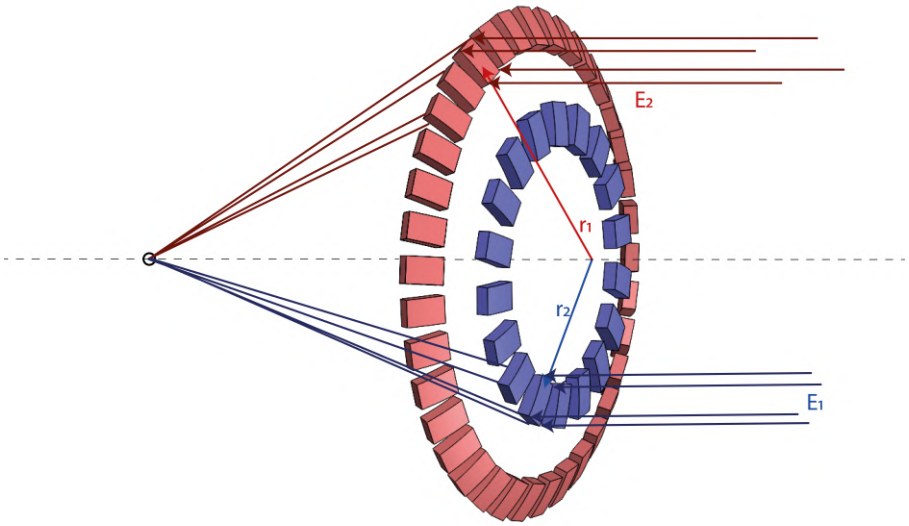

Figure 1.16: Schematics of Laue lens. Several crystal tiles must be arranged in concentric rings and oriented according to Bragg's law, to focus the radiation at the common focal point where a 3D position sensitive detector is positioned. Different rings are sensitive to different energy bands

where F is the focal of the lens. If we evaluate the Abbe condition, we obtain:

$$\frac{h}{\sin\alpha} = \frac{F}{\sin 2\theta_B} \neq \text{const} \tag{1.35}$$

This means that Laue lenses are prone to coma aberration for off-axis sources. As a result, their field of view is usually limited to a few arcminutes.

1.4.2 Crystals for Laue lenses

The choice of crystals for a Laue lens is crucial since the lens's performance and capabilities depend heavily on them. In our work, we studied two different types of crystals, perfect or

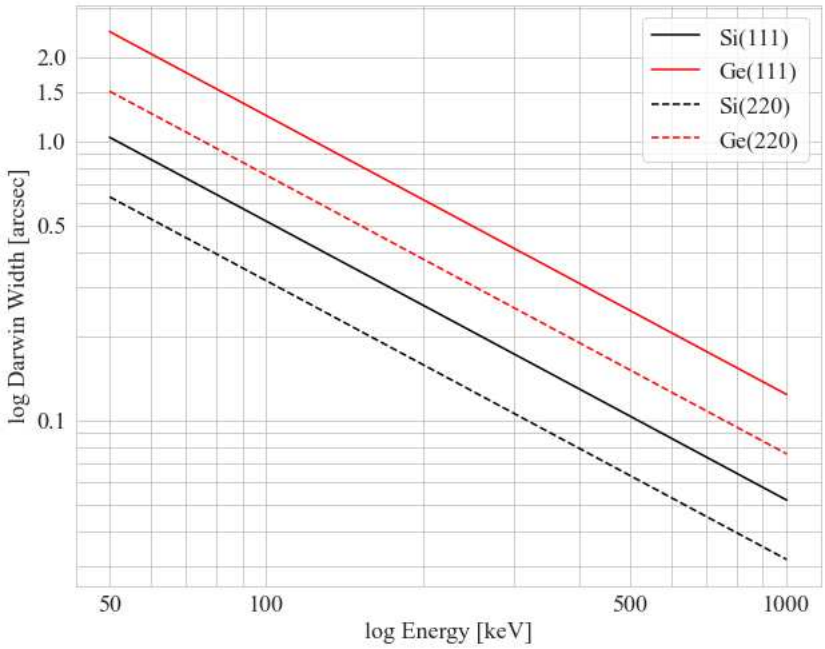

Figure 1.17: Darwin width vs energy for Silicon (black) and Germanium (red) for (111) diffracting planes (solid line) and (220) diffracting planes (dashed line).

mosaic, and two different geometries for the diffraction planes, flat or bent.

The diffraction properties of a crystal in a chosen energy interval are typically characterised by the measurement of its rocking curve. The rocking curve is the measurement of the diffracted beam intensity as a function of the angle between an impinging beam and the crystal. The shape of the rocking curve is directly linked to the crystals' underlying diffraction planes' structure. Thus, rocking curve measurements are one of the most used characterisation techniques to describe crystalline structures.

In this section, we will describe some different types of crystals that can be used to build Laue lenses, their properties, and their advantages and disadvantages in relation to optimizing the efficiency of a spherical, broadband, astrophysical Laue lens.

Perfect flat crystals

A perfect crystal is defined as a crystal whose lattice structure does not show any point-like, linear or planar defect [Cullity, 1957]. From a practical point of view, a crystal is considered perfect when it lacks linear/planar defects and is dislocation-free.

For a flat, perfect crystal, the rocking curve is a very narrow Gaussian peak centred on the angle satisfying Bragg's law and whose FWHM is called Darwin width [Zachariasen, 1945]. The Darwin width δ_W is linked to the lattice properties of the crystals and the diffraction energy through the relation:

$$\delta_W = \frac{d}{\Lambda} \quad \text{with} \quad \Lambda = \frac{\pi V \cos\theta_B}{r_e \lambda C |F_h|} \tag{1.36}$$

in which Λ and V are respectively the extinction length and the volume of the unitary cell of the crystal, θ_B, λ, and C are the Bragg's angle, the wavelength, and the polarisation factor of the incoming photons, and, finally, $|F_h|$ is the structure factor of the diffracting planes of the crystal.

At high energies (>50 keV), crystals of Silicon and Germanium have a Darwin width of about <5 arcsec, decreasing with energy (see Fig. 1.17).

This means that perfect flat crystals, for high energies, are typically sensitive only to a very narrow energy band. Thus, they are ideal monochromators and are a good solution for

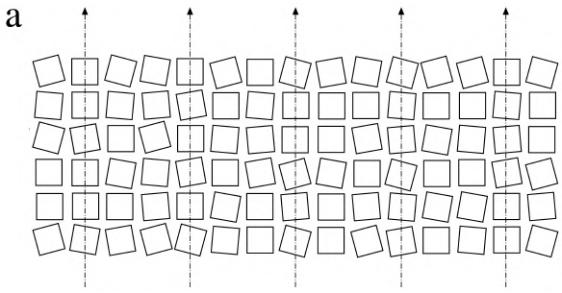

Figure 1.18: Schematic picture of a flat mosaic crystal (section view). The crystallites (black squares) are all misaligned with respect to an average direction (black arrows), which is the same at every point of the crystal.

narrowband Laue lenses. However, they are not suitable for a broadband Laue lens since it would be impossible to build a lens of this type with a smooth effective area without the use of very small crystals. Finally, the last important limitation of perfect flat crystals is that their reflectivity cannot be higher than 50% [Zachariasen, 1945]. This comes from the fact that a photon traversing a crystal has the same probability of undergoing an even or odd number of diffraction processes, limiting the maximum efficiency theoretically achievable. When working with low fluxes, which is the case for astrophysical sources, this can strongly limit the amount of photons we can collect, thus hindering the performance of the lens.

Mosaic flat crystals

A mosaic crystal can be seen as a crystal composed of a mosaic of small, perfect crystals of dimensions of the order of 10–100 μm, called crystallites [Darwin, 1914a,b, Zachariasen, 1945]. The diffraction planes of the crystallites are distributed according to a Gaussian distribution W(δ) whose FWHM is called mosaicity of the crystals (Fig. 1.18):

$$W(\delta) = \frac{1}{\sqrt{2\,\pi\,\eta}} \exp\left(-\frac{\delta^2}{2\eta^2}\right) \tag{1.37}$$

where δ is the misalignment from the average direction of the crystallites and the mosaicity is defined as $\beta = 2.35\eta$. The mosaicity is typically larger than the Darwin width, and this reflects on the rocking curve of the crystal itself, which is enlarged to the value of the mosaicity, increasing the energy band of a mosaic crystal w.r.t a flat one.

From the point of view of radiation concentration, mosaicity brings a downside: the distribution of the crystallites induces an angular dispersion of the diffracted radiation, which means that the image of the diffracted beam will appear as surrounded by a halo of out-of-focus radiation (Fig. 1.19).

In Laue configuration, when the diffraction planes are perpendicular to the irradiated surface of the crystal, the reflectivity of a mosaic crystal R(δ, E) can be written as [Zachariasen, 1945]:

$$R(\delta, E) = \frac{1}{2}(1 - e^{-2\,\sigma\,T})e^{-\mu\frac{T}{\gamma_0}} \tag{1.38}$$

where μ and T are respectively the X-ray self-absorption coefficient and the thickness of the crystal, γ_0 is the cosine of the angle between the direction of the incoming beam and the normal vector to the crystal surface, and σ is expressed as:

$$\sigma = W(\delta)\; Q(E)\; f(A) \tag{1.39}$$

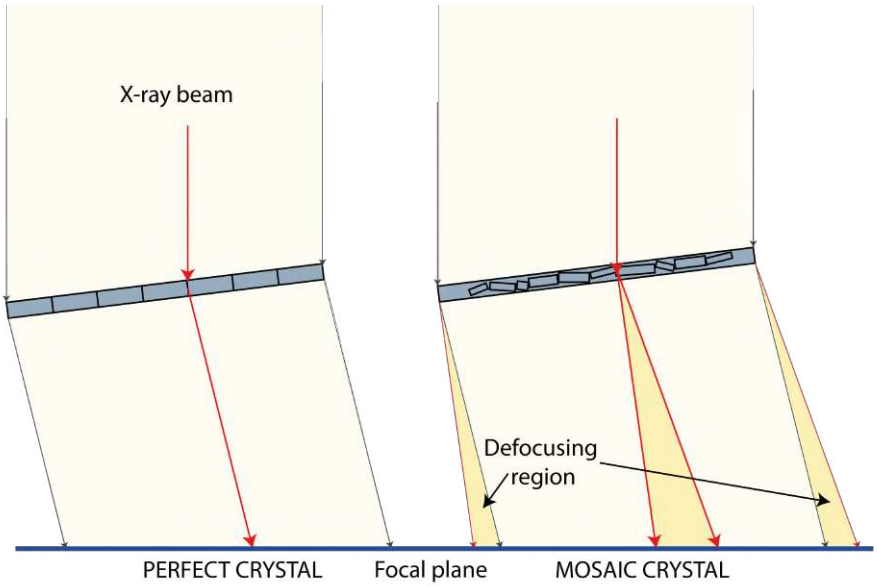

Figure 1.19: Representation of the mosaic defocusing effect induced by mosaic crystals. In the case of a perfect crystal (left) hit by a polychromatic beam, only the photons satisfying Bragg's condition are diffracted and redirected to the focal plane since the diffraction planes are exactly parallel to each other. In a mosaic crystal (right), instead, each point of the crystal can diffract a wider energy band because of the dispersion of the crystallites' planes. However, the diffracted beam will come out of the crystals with an angular distribution that reflects the distribution of the crystallites. This results in a de-focused and enlarged image.

where:

$$Q(E) = r_e^2 \left| \frac{F_h}{V} \right|^2 \lambda^3 \frac{1 + \cos^2(2\theta_B)}{2 \sin 2\theta_B} \tag{1.40}$$

in which the quantities have the same meaning as defined for Eq. 1.36 and, finally:

$$f(A) = \frac{B_0(2A) + |\cos 2\theta_B| \, B_0(2A|\cos 2\theta_B|)}{2A(1 + \cos^2 \theta_B)} \quad \text{with} \quad A = \frac{\pi t_0}{\Lambda \cos \theta_B} \tag{1.41}$$

where B_0 is the 0-th order Bessel's function integrated between 0 and 2A, t_0 is the crystallite's thickness and Λ is the extinction length of the crystal. The highest reflectivity is obtained when $t_0 \ll \Lambda$, in which case $f(A) \sim 1$. Even in this case, the reflection efficiency can never exceed 50% [Zachariasen, 1945].

Mosaic bent crystals

A bent crystal is a crystal which has been mechanically or permanently deformed to a curved shape. The easiest type of shape that can be obtained is usually a cylindrical shape, which is the case of the bent crystals that we considered for our Laue lenses. From now on, when talking about bent crystals, we will always assume that they are bent in a cylindrical shape.

Bent crystals can be especially useful for Laue lenses since they can act as true concentrators of radiation thanks to the continuous variation of the angle between the incident beam and the diffraction planes. This is not possible with flat crystals, which redirect the radiation, but do not possess concentration capabilities, so the footprint of the diffracted beam will be comparable to the size of the crystals themselves, thus limiting the minimum size of the PSF of the lens to the size of the crystal.

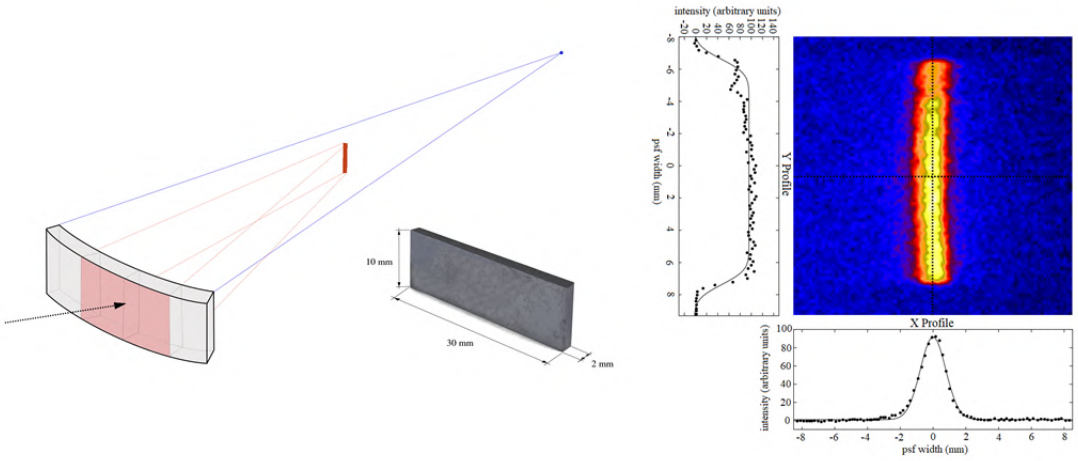

Figure 1.20: *Right:* Representation of the radiation concentration effect attainable with a cylindrically curved crystal. The crystal (white) squeezes an impinging beam (red rectangle) in a smaller area on the focal plane, at a distance equal to half the curvature radius of the crystal itself (bold, red line). *Left:* Real, concentrated image of a polychromatic beam obtained at the LARIX-A facility. A GaAs crystal (size = $30 \times 10 \times 2$ cm^3) was used to concentrate a 10×10 cm^2 beam into an image of size $\sim 1 \times 10$ cm^2. Diffraction performed at 130 keV.

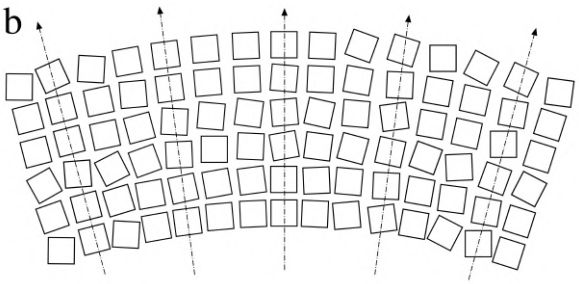

Figure 1.21: Schematic picture of a bent mosaic crystal (section view). The average direction (black arrows) of the crystallites varies continuously along the length of the crystal due to the curvature.

This has been experimentally verified at the LARIX facility, in which bent crystals of gallium arsenide (GaAs), silicon and germanium have been used to perform different X-ray concentration experiments (Fig. 1.20) [Ferro et al., 2022, Virgilli et al., 2014, Virgilli et al., 2016, Virgilli et al., 2019]. For a mosaic crystal, the bending has the effect of changing continuously the average direction of the crystallites (Fig. 1.21).

Another advantage of bent crystals is that the presence of a curvature radius contributes to the increase of the crystal's energy pass-band. We can see this by differentiating the Bragg's equation on both sides:

$$2d_{hkl} \cos\theta_B \, \mathrm{d}\theta = -n\frac{hc}{E^2} \, \mathrm{d}E \tag{1.42}$$

Since for X and gamma rays, Bragg's angles are very small, we can approximate the Bragg's equation and its derivative as:

$$\begin{cases} 2d_{hkl}\theta_B = n\frac{hc}{E} \\ 2d_{hkl} \, \mathrm{d}\theta = -n\frac{hc}{E^2} \, \mathrm{d}E \end{cases} \tag{1.43}$$

then we divide the derivative for Bragg's equation and we obtain:

$$\frac{\mathrm{d}\theta}{\theta_B} = -\frac{\mathrm{d}E}{E} \tag{1.44}$$

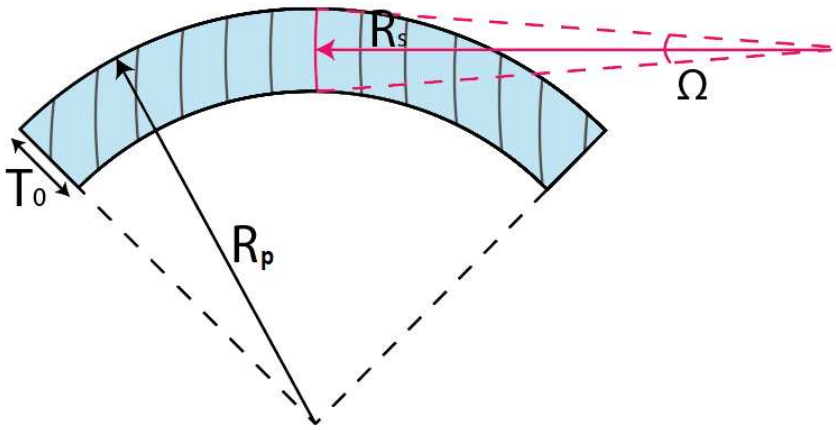

Figure 1.22: Schematic representation of the structure of a perfect bent crystal.When a crystal is bent to an external curvature R_p, some specific plane families can acquire a secondary curvature radius R_s. This is due to the anisotropic elastic behaviour of the crystal along different directions. T_0 is the thickness of the crystal, while Ω is the quasi-mosacity.

So, as a first approximation, we can say that a variation of the Bragg's angle $\Delta\theta$ due to the presence of a curvature radius will be linked to an enlargement of the pass-band ΔE of the crystal around the average value E as:

$$\frac{|\Delta\theta|}{\theta_B} = \frac{|\Delta E|}{E} \tag{1.45}$$

This means that, for mosaic crystals, the energy pass-band is further enlarged with respect to a flat mosaic crystal, in which only the mosaicity contributes to the increase of the band. It is worth noticing that ΔE increases with the energy, so the higher the crystal's average diffraction energy, the larger its energy pass-band will be.

From the point of view of the crystal's diffraction efficiency, it is still debated whether the efficiency of a bent mosaic crystal could be higher than the efficiency of an equivalent, flat crystal. Some authors found a possible linear correlation between curvature and efficiency in both perfect and mosaic crystals [Buffagni et al., 2015], however, such results still need to be confirmed or disputed by further experiments.

Perfect bent crystals

In the case of perfect crystals, the bending of the crystal to an external curvature radius (called primary radius) induces a secondary curvature radius on some families of diffraction planes. This means that the diffraction planes show an angular spread, which is called quasi-mosaicity. (Fig. 1.22). As in the case of mosaic crystals, perfect bent crystals act as radiation concentrators and their energy band is enlarged w.r.t. flat crystals.

The most interesting property of bent perfect crystals is that, according to the dynamical theory of diffraction, their efficiency should exceed the limit of 50% of flat perfect crystals [Authier and Malgrange, 1998]. The theory describing the diffraction inside perfect, homogeneously bent crystals in transmission configuration was developed by Malgrange [Malgrange, 2002] from the dynamical theory of diffraction and is confirmed by experimental results [Bellucci et al., 2013, Camattari et al., 2015, Keitel et al., 1999].

The distortion of the diffraction planes is called strain gradient β_s, which can be expressed as:

$$\beta_s = \frac{\Omega}{T_0(\delta_w/2)} \tag{1.46}$$

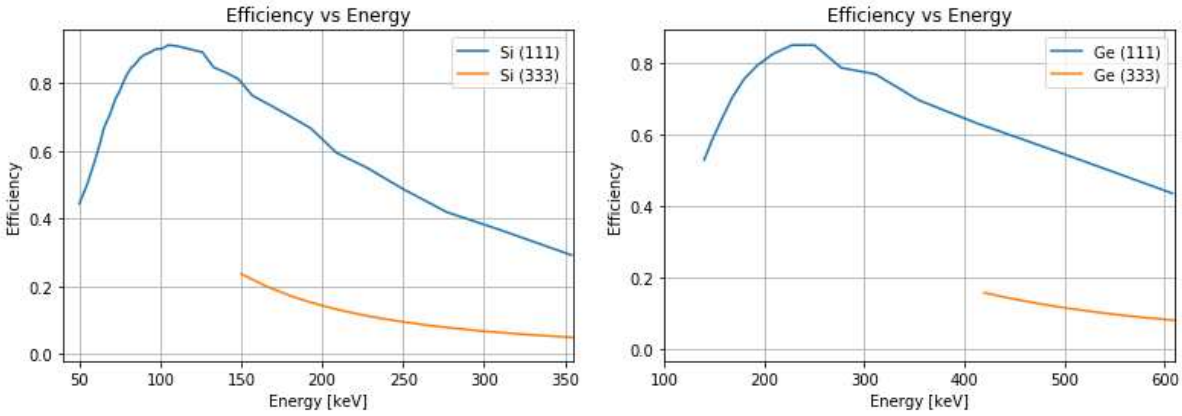

Figure 1.23: Bragg's diffraction efficiency vs energy for Si(111), first and third order of diffraction (left), and Ge(111), first and third order of diffraction (right). The thickness of the crystals is optimized to obtain a higher efficiency. Reprinted from Ferro [2020]

where T_0 is the thickness of the crystal, Ω is the induced quasi-mosaicity and δ_w is the Darwin width. Then we define the critical strain β_C and the critical radius R_C:

$$\begin{cases} \beta_C = \frac{\pi}{2\Lambda} \\ R_C = \frac{2\Lambda}{\delta_w \pi} = \frac{2\Lambda^2}{d_{hkl}\pi} \end{cases} \tag{1.47}$$

When $\beta_s \gg \beta_C$, or analogously when the secondary curvature radius R_s is way smaller than R_C, the peak reflectivity of the crystal can be expressed as:

$$R^{peak} = \left(1 - e^{-\frac{\pi^2 \, d_{hkl} \, R_s}{\Lambda^2}}\right) e^{-\frac{\mu \, \Omega \, R_s}{\cos\theta_B}} \tag{1.48}$$

in which μ and Λ are, again, the self-absorption coefficient and the extinction length of the crystal. In the limit $R_s/R_C \to 0$, we can linearly approximate the peak reflectivity as:

$$R^{peak} \simeq \frac{\pi^2 d_{hkl}}{\Lambda^2} R_s \tag{1.49}$$

When $R_s \sim R_C$, Eq. 1.48 does not hold any more, however, we can state that in the limit $R_s \gg R_C$, i.e. for an asymptotically flat crystal, the peak reflectivity must be 0.5, as expected for a flat crystal.

In past works, we evaluated the diffraction efficiency for Si and Ge by combining Malgrange's equation for bent perfect crystals and a semi-analytical calculation technique [Bellucci et al., 2013] based on the dynamical theory of diffraction. Results for the first and third order of diffraction for Si(111) and Ge(111) crystals are shown in Fig. 1.23 [Ferro, 2020]. The efficiency obtained has been used to evaluate the performance of full Laue lenses made by Si and Ge crystals.

1.4.3 ASTENA: a Laue lens-based mission concept for High Energy Astrophysics

The Advanced Surveyor for Transient Events and Nuclear Astrophysics (ASTENA) is a concept mission proposed to the ESA Call "Voyage 2050" by an international team of scientists led by the University of Ferrara and INAF-OAS Bologna. Two white papers [Frontera et al., 2021, Guidorzi et al., 2021] were submitted to the call.

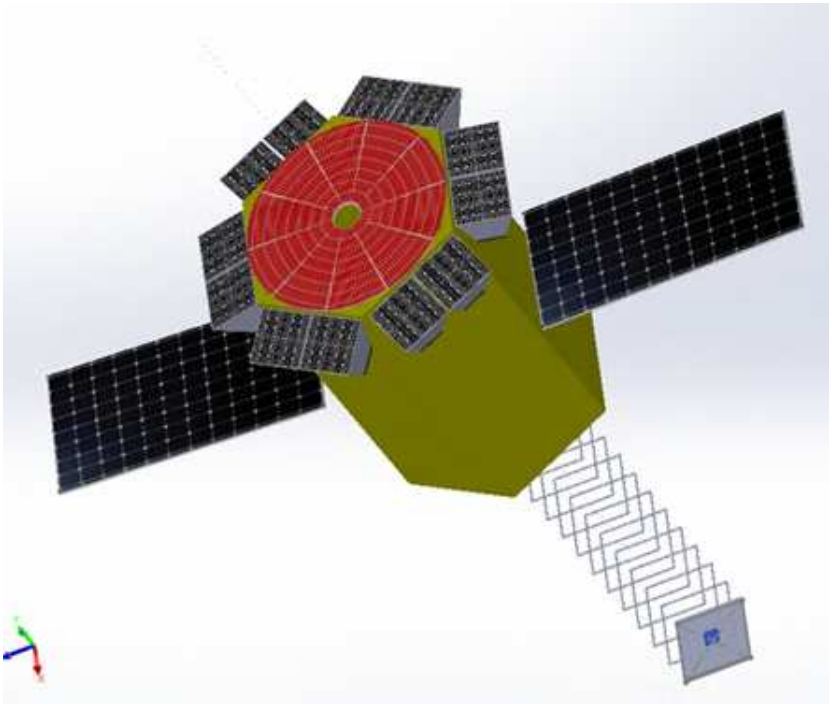

Figure 1.24: Representation of ASTENA's in-flight configuration. In red, the NFT's Laue lens is shown on the top of the spacecraft, surrounded by six WFM cameras (dark grey).

ASTENA is based on the unique synergy between its two instruments: the Wide Field Monitor (WFM), which works in the 2 keV - 20 MeV energy band and will be an evolution of the THESEUS/XGIS, and the Narrow Field Telescope (NFT), which will be a high energy telescope working in the energy band 50-700 keV, based on a Laue lens optics. The WFM will provide a rough source localisation-accuracy and on-board triggers for the NFT, which will act as a follow-up telescope. Both instruments will be capable of performing spectroscopic and polarisation measurements, meaning that ASTENA will be a multipurpose, high-energy facility, able to address the open problem described before, with a great synergy with the future gravitational waves and follow-up observatories.

The Wide Field Monitor

ASTENA's Wide Field Monitor will work in the energy band 2 keV - 20 MeV and consists of twelve camera units disposed in pairs around the main body of ASTENA's spacecraft, misaligned by 15° with respect to the axis of the lens. Each camera unit is made by a Position Sensitive Detector (PSD) surmounted by a double-scaled coded mask (Fig. 1.25). The PSD is an array of 4×8 modules, each module made by 205 hexagonal scintillator bars (5 mm between flats, length to be optimised). The scintillators are readout on top by linear silicon drift detectors and on bottom by hexagonal SDDs. The WFM is based on the same siswhich system used for THESEUS/XGIS and constitutes an evolution of this instrument. The material for the scintillator bars will be chosen among CsI(Tl), BGO, or GAGG:Ce, depending on which will ensure the best performances.

The ASTENA's WFM will use a coded mask system consisting of a low-energy mask (<30 keV) and a higher-energy mask (30-150 keV). The combination of the two masks enables the WFM to locate point sources with an accuracy of 1 arcmin within a fully coded Field of View (FoV) of 0.27 sr and a full width at zero response FoV of 2 sr. Above 150 keV, the WFM will function as a full sky spectrometer, with limited localisation achieved through Compton imaging

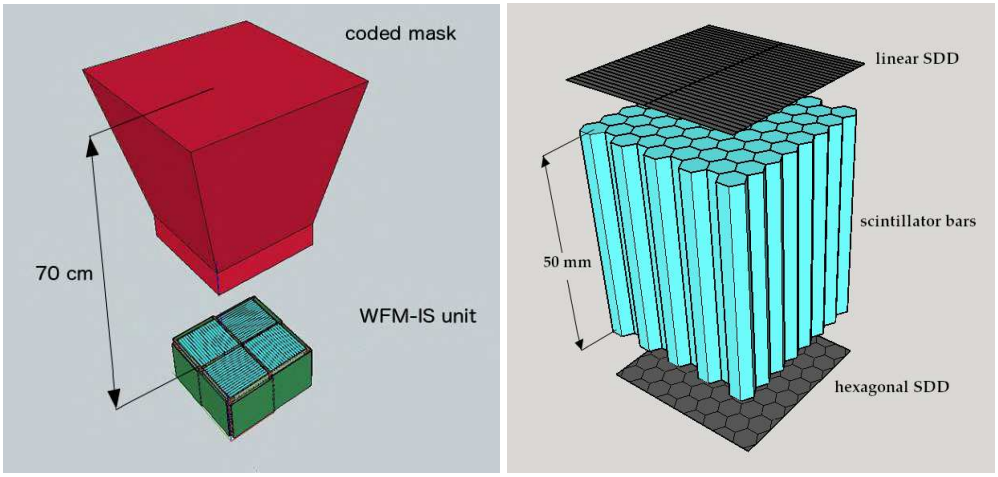

Figure 1.25: *Left*: Schematic of one of WFM's twelve cameras. Each camera is composed of a position-sensitive detector (bottom) surmounted by a coded mask (red). *Right*: Schematic of one of the modules which compose each of WFM's PSDs. Each PSD is made by hexagonal scintillator bars read-out on top and bottom by silicon drift detectors. The length of the scintillator bars has not been finalised and may be changed after further performance optimisation studies. Reprinted from Frontera et al. [2021].

and/or triangulation using the signal detected on the different units.

The Narrow Field Telescope

The Narrow Field Telescope [Virgilli et al., 2019] will be a revolutionary hard X/soft gamma-ray focusing telescope working in the energy band 50-700 keV based on the technology of Laue lenses (Fig. 1.24). The NFT will be composed of a Laue lens optics of 3 m diameter and 20 m focal length. The lens will be made by ~19500 crystal tiles of perfect Si(111) and Ge(111), bent to a curvature radius of 40 m (Fig 1.26, left). The crystals tiles will have a cross-section of 30 × 10 mm^2, while the thickness will be 2 mm for the Si tiles and varying between 2 and 5 mm for the Ge tiles to optimise the diffraction efficiency. The simulated PSF of the NFT is shown in Fig. 1.26, right. The focal plane detector is expected to be a pixelated CdZnTe spectral-imager detector, with a size of 8×8×8 cm^3, a pitch of 300 μm and an efficiency >80% in the whole energy band of NFT.

The combination of the optics and detector characteristics will grant NFT an unprecedented angular resolution in the sub-MeV energy range of 30 arcsec and a point source localisation accuracy <10 arcsec, with a Field of View of 4 arcmin. NFT will bring a leap in sensitivity of two orders of magnitude with respect to the best current instruments working in the same energy bands (Fig. 1.27), opening a new range of possibilities for high-energy astronomical observations.

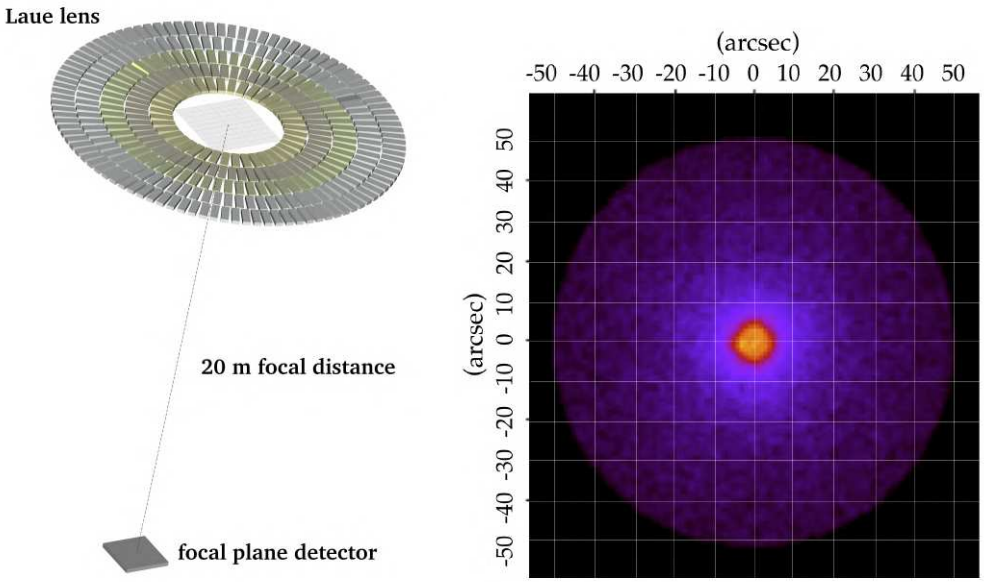

Figure 1.26: *Left*: Schematics (not on scale) of the Narrow Field Telescope onboard ASTENA. *Right*: Simulated PSF of NFT for an on-axis source, assuming an ideal focal plane detector. Reprinted from Frontera et al. [2021].

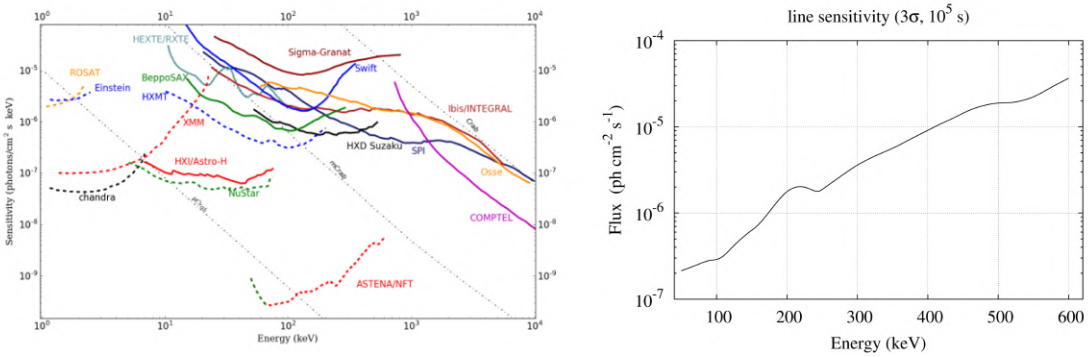

Figure 1.27: ASTENA's NFT continuum sensitivity (left) and line sensitivity (right), both at 3σ confidence level and for 100 ks observation time. Reprinted from Frontera et al. [2021]

Chapter 2

Current status and next advancements of the Laue lens technology

At the University of Ferrara, we have been working on advancing the Laue lens technology for many years. The development of Laue lenses started with the HAXTEL (HArd X-ray TELescope) project, which led to a patented technique to build short-focal Laue lenses with flat, mosaic crystals of copper [Ferrari et al., 2009, Frontera et al., 2007, Frontera et al., 2008]. Next, with the LAUE project [Frontera et al., 2012, Virgilli et al., 2018], the LARge Italian X-ray (LARIX) facility was built at the University of Ferrara. The LARIX facility[1] was developed with the aim to create a flexible X-ray facility equipped with a low divergence beam line specially designed to test high energy X-ray optics [Loffredo et al., 2005]. The most recent project devoted to advancing the Laue lens technology was TRILL (Technological Readiness Level Increase for Laue Lenses), aiming to develop a reliable technique to build long focal Laue lenses. In this chapter, we will describe the main results of the TRILL project and the steps we are taking to improve the Laue lens technology further.

2.1 The TRILL project and its results

The TRILL project (Technological Readiness Level Increase for Laue Lenses) was funded by the Italian Space Agency through the National Institute for Astrophysics, with the aim to increase the technological readiness level (TRL) of Laue lenses. The TRILL project aimed to develop the technologies and techniques to build a section of a Laue lens made of bent crystals and test this prototype section with a suitable focal plane detector. To do so, we opted for a modular approach: the full lens is ideally divided into spherical sectors, and then each sector is divided into smaller modules, which contain about 30 crystals each (Fig. 2.1).

In the context of the project, three main tasks have been defined:

1. Define a reliable and repeatable technique to bend Silicon and Germanium crystals at a curvature radius of 40 ± 2 m without deterioration of the properties of the crystals.
2. Define a reproducible assembly technique to bond a sample of crystal tiles to an adequate substrate with an angular orientation accuracy < 10 arcsec and long-term stability.
3. Test the performance of the Laue lens prototype with a spectra-imager focal plane detector to reach an overall maturity of the lens + detector system.

The requirement on the curvature radius accuracy and the orientation misalignment of the crystals are necessary to ensure that the PSF of the complete Laue lens will be within 30 arcsec.

[1] https://larixfacility.unife.it/

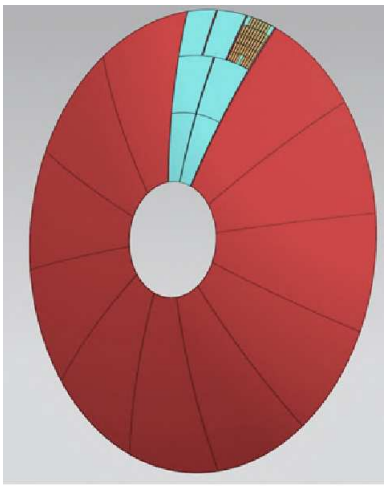

Figure 2.1: Left: Schematic CAD model of a full Laue lens. The lens is divided into spherical sectors called petals (red), and each petal is divided into a series of modules (cyan). The crystals are fixed on each module.

2.1.1 Crystals manufacturing and bending

The crystals are cut at the CNR/IMEM institute (Parma, IT) starting from 4 inches dislocation-free silicon and germanium wafers. From each wafer, about 15 crystals of size $30 \times 10 \times 2$ mm^3 are cut in such a way that the (220) diffraction planes are parallel to the 10×2 mm^2 with a miscut angle < 0.2 deg.

The crystals are bent through the surface lapping technique [Buffagni et al., 2015, Ferrari et al., 2013] to achieve a cylindrical curvature radius of 40 m. The lapping method consists of exerting controlled mechanical damages on one surface of the sample, which introduces defects in a superficial layer of a few microns, providing a highly compressive strain which bends the crystal in a self-standing way. The requirement for the curvature radius was obtained by experimental tests on a first sample of GaAs crystals bent via surface lapping. The curvature radius of the GaAs(220) crystals and their PSF width at the lens nominal focal distance were measured at LARIX. If a crystal is bent to the nominal curvature radius, the focal distance of the lens will correspond to its best focus position and the size of the image I will only depend on the mosaic defocussing of the crystals:

$$I = 2\beta F \tag{2.1}$$

where β is the mosaicity of the crystal, and F is the focal length. If the curvature radius is smaller or bigger than the expected value, the focal length of the crystal does not correspond to the focal of the lens, so the image will be enlarged due to being out of focus. From geometrical consideration, it is possible to determine the defocusing radial contribution as follows:

$$I = \frac{d}{F}|F_N - F| \tag{2.2}$$

where d is the length of the side of the crystal in the focusing direction, F = R/2 is the focal length of the deformed crystals, equal to half its curvature radius R. From our measurements, we can see that the mosaic defocussing prevails on the radial distortion as long as the curvature radius of the crystal is close enough to the nominal curvature radius, in which case the size of the PSF is independent of the curvature of the crystal. The critical values of the curvature radius which delimits the two regions can be obtained as:

$$2\,\beta\,F = \frac{d}{R_c}|R_N - R_c| \rightarrow R_c = \frac{R_N}{1 \pm \frac{2\beta F}{d}} \tag{2.3}$$

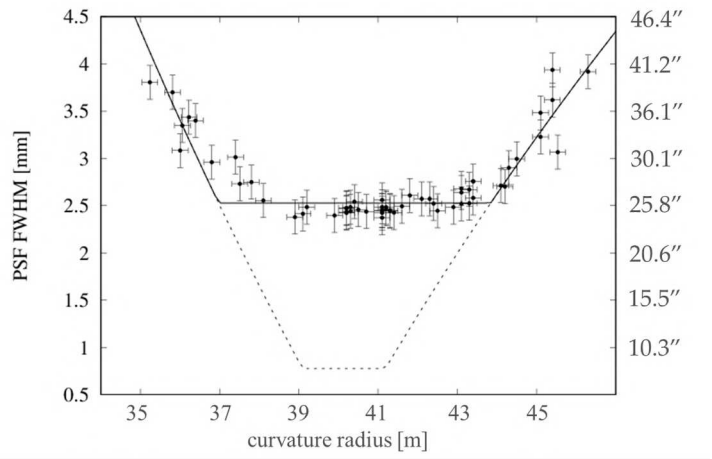

Figure 2.2: *Black points*: the measured size of PSF of a sample of GaAs crystals versus their curvature radius. It can be seen that in the range 38–43 m, the deformation of the crystals' curvature radius from the optimal value does not affect the size of the PSF. *Black solid line*: fit of the data points. *Black dashed line*: Theoretical PSF FWHM vs curvature radius curve for a Ge(111) crystal with quasi-mosaicity of 5 arcsec. The region in which the defocusing prevails on the radial deformation is reduced to about 2 m around the optimal value of 40 m.

In the case of a crystal with a nominal curvature radius of 40 m, mosaicity of 10 arcsec and length of the non-focussing side of 30 mm, we obtain two values of R_c: $R_c^+ = 38$ m and $R_c^- = 43$ m (Fig. 2.2). We can then conclude that we can accept an error on the value of the curvature radius of the crystals up to ±2 m without degradation of the quality of the final image of the Laue lens.

The surface lapping technique was then tested with Ge(220) crystals. The average value of the curvature radii distribution of the Ge sample is 39.7 ± 0.2 m, with an estimate of the standard deviation of 1 m (Fig. 2.3), meaning that all the crystals are within our requirements. The curvatures of the crystals were measured at CNR/IMEM with a Phillips X'Pert PRO high-resolution X-ray diffractometer equipped with a Cu Kα source. The average value of the final thickness of the crystals after the lapping procedure is 1.656 ± 0.002 mm (Fig. 2.3).

The surface lapping technique emerged as a very accurate, reliable, and repeatable procedure for bending crystals for Laue lenses. However, it shows two significant downsides: (1) part of the material needs to be removed, therefore the thickness of the crystals significantly decreased with respect to the initial thickness, and (2), to date, crystals with thickness higher than 2 mm are not bendable at the nominal 40 m radius, which poses a constraint on the size of the tiles, thus limiting their diffraction efficiency and mechanical properties.

2.1.2 Manufacturing of a Laue lens model

The crystals used to realise the sector are made of Germanium tiles (thickness S = 1676 ÷ 1775 μm) with cross-section 30 × 10 mm^2 (Fig. 2.4, left) and diffraction planes (220). The crystal tiles are cut such that the diffraction planes are parallel to the 10 × S mm^2 faces within a miscut angle < 0.2°.

Crystals are bent in a cylindrical shape with a radius of curvature of 40 m. Due to the variability of the amount of material removed by the surface lapping process, the thickness of the crystals is not uniform, as reported in Table 2.1. in the same table we also report the achieved curvature radius for each crystal. The planes (220) do not acquire a secondary curvature, as can be expected with other families of planes [Authier and Malgrange, 1998] however, the

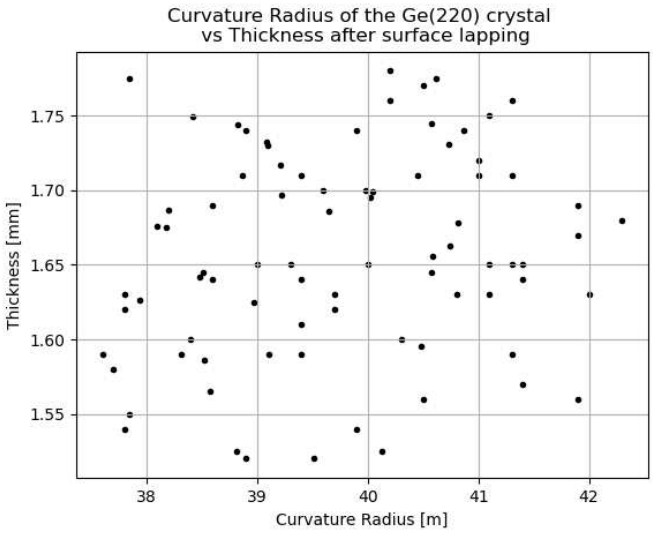

Figure 2.3: Curvature radius of the sample of 82 bent crystals of Ge(220) vs their thickness after the surface lapping procedure. Each point represents a crystal. All the curvature radii are within the limit ±2 m from the nominal curvature radius of 40 m.

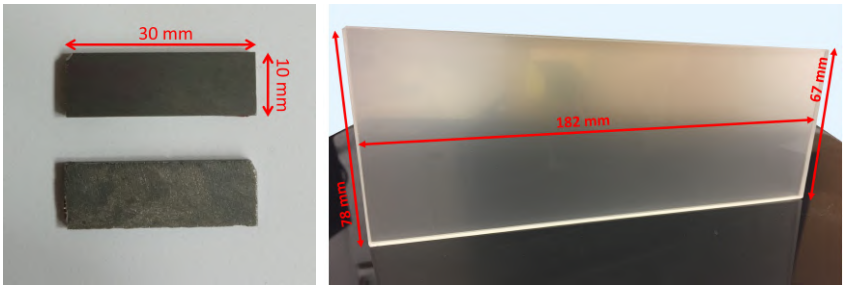

Figure 2.4: Left: Two Germanium crystal tiles used to build the lens prototype; the bottom crystal shows the polished side. The crystals are bent along the long side. Right: The quartz glass that we used as the substrate for the bonded crystals.

external bending of the crystals allows the X-ray radiation coming from a parallel beam to be concentrated onto a focal point at a distance equal to half their radius of curvature [Virgilli et al., 2014] .

The adhesive used to realise the lens sector is the OP 61 LS by DYMAX, a UV-curable adhesive with a linear shrinkage factor of 0.03%. A low value of the adhesive shrinkage is fundamental for reducing unwanted positioning displacements after curing. For our substrate, we used fused quartz with a trapezoid shape (Fig. 2.4, right). The choice of quartz for the substrate is due to its low coefficient of thermal expansion and its transparency to the UV light, which is required for the adhesive curing process. One of the two surfaces of the quartz glass has been worked to be flat, while the surface on which the crystals are bonded has been polished to achieve a curvature radius of 40 m to better match the shape of the crystals. This reduces the non-homogeneities in the glue deposition between crystals and substrate. The substrate is 5 mm thick, and the diffraction process is carried out at about 130 keV. At this energy, and based on the density and attenuation coefficient of quartz glass, the beam transmitted through the substrate is about 84% of the diffracted beam.

The prototype was built in the 100-meter-long tunnel (LARIX-T) of the LARIX laboratory at the University of Ferrara. A scheme of the facility is shown in Fig. 2.5, top. The facility consists of a 26.5 m beamline working in the 50 – 320 keV energy range. The X-ray beam is

Crystal ID	Curvature Radius (m)	Thickness (μm)
25A	40.0 ± 0.4	1700 ± 5
26A	39 ± 1	1717 ± 5
26B	37.8 ± 0.3	1775 ± 5
26C	38.8 ± 0.8	1744 ± 5
28B	40.62 ± 0.04	1775 ± 5
29A	39.08 ± 0.01	1732 ± 5
29B	38.4 ± 0.9	1749 ± 5
30A	38.1 ± 0.6	1676 ± 5
31A	40.6 ± 0.1	1745 ± 5
32C	40.7 ± 0.7	1731 ± 5
33B	40.8 ± 0.3	1678 ± 5

Table 2.1: Curvature radius and thickness of the crystals used in the TRILL prototype. The variation in the reported errors on the curvature radius is due to the different deviations with respect to a perfect curvature for the crystals. Measurements performed at CNR-IMEM (Parma) with a Cu-α X-ray diffractometer.

produced by an X-ray tube equipped with a tungsten anode (Fig. 2.5, top left) with a focal spot size of 0.4 mm. A 20 mm thick tungsten plate with a 3 mm diameter hole and a 50 mm thick lead shield with a 1 mm diameter hole are both placed in front of the exit window to reduce the beam divergence; the two collimator plates are immediately in front of the X-ray tube exit window. The X-ray beam passes inside a 21 m long vacuum pipe and then through a motorised slit collimator with four independently motorised 20 mm thick tungsten blades (Fig. 2.5, top right). For this experiment, the collimator aperture was set to obtain a beam dimension of 10 $\times$ 10 mm^2. Given the distance of 26.5 m between the X-ray source and quartz substrate and the beam size, the divergence of the X-ray source over the crystal area is about 78 arcsec. This setup is designed to reduce the divergence of the incident beam to approximate the illumination conditions from a source placed at an infinite distance from the target [Virgilli et al., 2014].

The crystals are positioned using a customised holder, which is mounted on a high precision 6-axis Hexapod HXP100-MECA from Newport (translation accuracy of 1 μm and rotation accuracy of 2×10^{-5} rad) (Fig. 2.5, bottom left). The customised holder, visible in Fig. 2.5, supports the crystals from the back, top side, and right side without exerting any force, while a small, movable bar supports the crystals from the bottom and can be adjusted in such a way that the crystal is clamped between the top and bottom part of the holder. The collimator and the hexapod are placed inside an ISO8 clean room. An INVAR steel frame is also installed on the same hexapod carriage. This frame hosts the quartz glass, used as the substrate for the Laue lens module under realisation. Both the quartz glass and the INVAR steel have been chosen for their extremely low thermal expansion coefficients (0.55ppm/^{o}C and 1.2ppm/^{o}C, respectively).

A further carriage is placed on a movable rail, which allows the detector to be moved from a minimum distance from the lens frame of $\sim$ 8 m to a maximum distance of $\sim$ 23 m. A Perkin Elmer Cesium Iodide (CsI(Tl)) digital X-ray flat panel detector with 1024 $\times$ 1024 pixels, 200 μm pixel size and sensitive in the broad energy range 20 keV — 15 MeV has been used to detect the diffracted signals by each crystal and for their mutual alignment (Fig. 2.5, bottom right).

Given the divergence of the beam, the imager is placed at a distance F_D from the crystals, obtained by [Virgilli et al., 2016]:

$$\frac{1}{F_D} = \frac{1}{D} + \frac{2}{R_c} \tag{2.4}$$

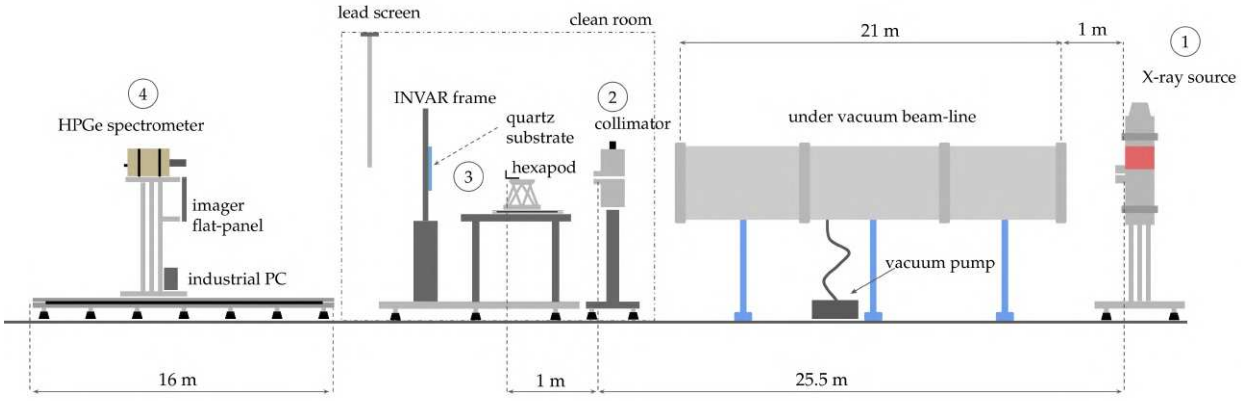

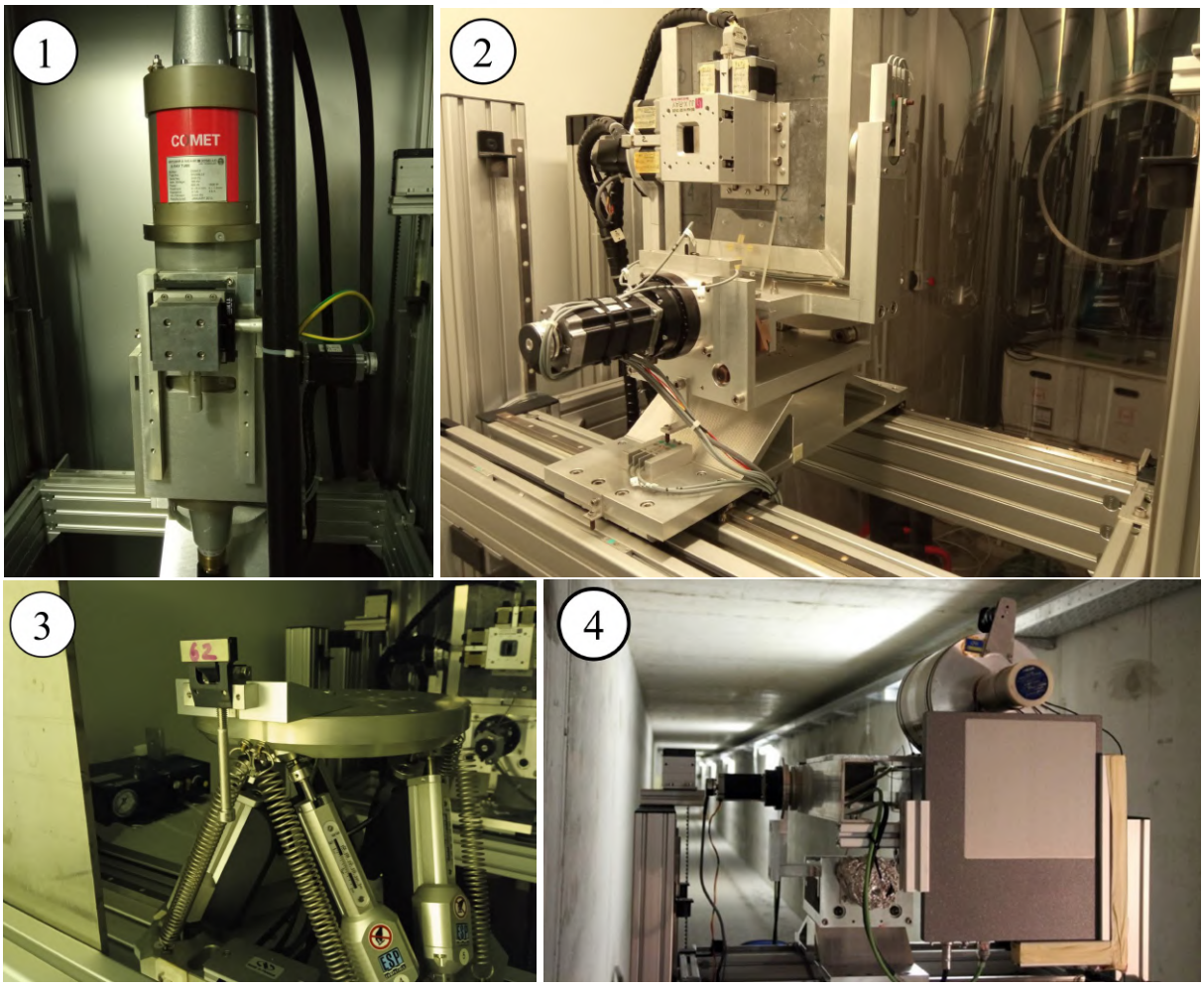

Figure 2.5: *Top*: Sketch (not at scale) of the LARIX-T facility at the University of Ferrara, where the Laue lens module has been assembled and tested. *Centre left*: the collimated X-ray source. *Centre right*: the remotely controllable lead and tungsten collimator. *Bottom left*: the hexapod we used to orient the crystals; the custom crystal holder, with a crystal mounted, is also visible. *Bottom right*: the suite of available detectors: an HPGe spectrometer and a flat-panel imager Perkin-Elmer (200 μm spatial resolution).

where D is the distance between the source and the sample holder and R_c is the curvature radius of the crystals. In the ideal case of a crystal with a curvature radius of 40.0 m, F_D is 11.4 m instead of 20.0 m. Note that X-rays get diffracted only once in the Laue lens configuration; therefore, the beam divergence reduces the focal length.

The main objective of this research is to fabricate a test module consisting of 12 bent

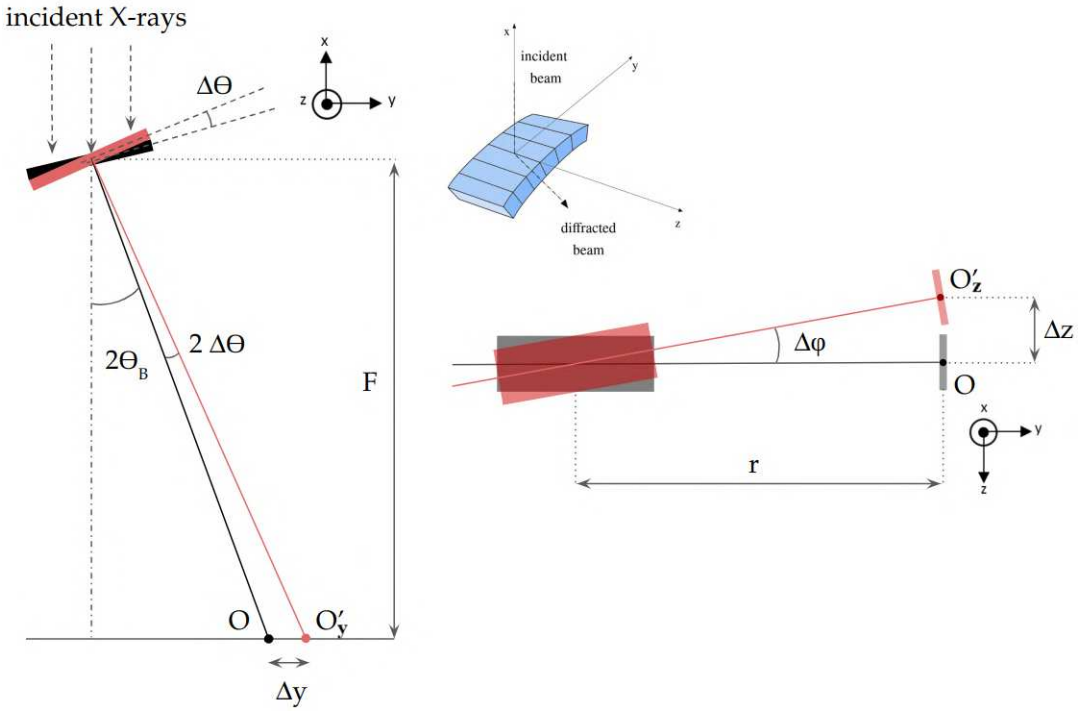

Figure 2.6: Scheme showing how the deviation of one crystal from the nominal positioning angles (θ and ϕ) affect the position of the diffracted beam. Black points O represent the nominal diffracted position. The variation $\Delta\theta$ along the Bragg angle θ_B (left) shifts the diffracted signal in O'_y by $\Delta y = F \tan(2\Delta\theta)$. The variation $\Delta\phi$ of the polar angle with respect to the nominal position results in a shift of the diffracted beam from O to O'_z by an amount $\Delta z = r \tan\Delta\phi$ (right).

germanium crystals. With reference to Fig. 2.6, for a parallel beam impinging on the lens, the proper orientation of the diffracted beam towards the Laue lens focus is achieved by adjusting the crystal with respect to the θ angle, which is related to the Bragg angle, and to the polar, or radial, angle ϕ. We aim to be able to build an astrophysical Laue lens with a PSF of the order of 30 arcsec Half Power Diameter (HPD) in all its energy band, which means that we require to position the Bragg's angle of the crystal with an accuracy <10 arcsec [Frontera et al., 2021]. The misplacement of the image of a crystal due to a wrong incident angle scales with the focal of the lens, so, with a long focal such as our case, it is very important to keep this type of misalignment as small as possible. On the polar angle, instead, we can have a less strict requirement of an accuracy of at least 2 arcmin since the misplacement of the image induced by a polar angle misalignment scales with the radius of the lens, which is about one order of magnitude smaller than the focal length. Even with a limited number of crystals, such a cluster is representative of the elemental module that constitutes a complete Laue lens. The position of each crystal is set under the control of the X-ray beam to align the positions of the centroid of their images all on the same point on the detector. Each crystal is bonded to the substrate through the following procedure:

1. the crystal is mounted on the hexapod, and the collimator is positioned in such a way that the central part of the crystal is illuminated.

2. The position of the diffracted signal is measured with the flat panel. From the difference between the nominal and measured positions of the diffracted signal, the Bragg and polar angles are evaluated and provided to the hexapod to orient the crystal correctly.

3. A drop of glue is dispensed on the substrate in correspondence to the central part of the

crystal. The polished side of the crystal is then pressed in contact with the adhesive. We chose to apply the adhesive on the polished side to avoid the glue inducing excessive stress on the crystals, possibly changing their curvature radii. The typical distance between crystal and substrate is about 150-200 μm. A final check of the position of the diffracted signal is made. By fitting the diffraction profile in both directions, the measurable positional accuracy is better than 0.5 pixels, i.e., of about 2 arcsec.

4. The glue is cured from the back of the quartz substrate using a DYMAX BlueWave 75 UV lamp, with a light guide. We alternated between short light shots and longer dark times. The idea below this procedure is that the light shots partially cure the glue, so during the dark times, there is still room to correct the position of the crystal in case the expected shrinkage of the glue moves the crystal from its optimal position. For each crystal, we performed 60 cycles of 0.5 s of light and 45 s of dark, then 20 cycles of 2 s of light and 45 s of dark. The total light time given to each crystal is 70 s, while the total dark time is 3600 s, so the curing process of each crystal takes 1 hour.

5. the crystal is released from the hexapod, and the position of the centroid of its diffracted image is measured. The release of the crystal is typically the most crucial phase of the bonding process since the combined effects of the adhesive force of the glue, gravity, and backlash from the release of the crystal clamp can drastically change the position of the crystal if the bonding process is not performed properly. The position of the diffracted signal for each crystal is monitored at regular time intervals, with a particular interest in evaluating its long-term stability.

2.1.3 Performance of the Laue lens module prototype

The assembled Laue lens module is shown in Fig. 2.7 (left), while the image of the crystals illuminated together is shown in Fig. 2.7 (right). The bonding procedure is quite time-consuming since continuous checks on the position of the crystals are needed throughout the process. Of the ten days that passed from the bonding of the first to the last crystals, seven were working days, resulting in the bonding of 1-2 crystals a day. To check the positional stability of the crystals in the assembled module, we repeated the measurement of the position of the diffracted beam from each crystal daily for 31 (21) days after the assembly of the first (last) crystal. After this period, we noted that the crystals' position remained stable for at least one week, after which we stopped the daily measurements. The final sector was made by 11 crystals instead of 12 because the crystal 26B got detached from its original position due to an assembly mishap and left a white spot of cured glue on the quartz substrate (clearly visible in Fig. 2.7), which rendered it impossible to bond another crystal on the same position without risks of damage to the assembly. Finally, the profile of the image along the focusing direction is shown in Fig. 2.8, left, and the profile along the non-focusing direction is shown in Fig. 2.8, right. The images shown in Fig. 2.7 have been taken 31 days after bonding the first crystal. Seven of the 11 crystals are aligned in the central peak of the image, while four crystals (30A, 26C, 31A, 28B) are strongly misaligned along the focusing direction. We can see that the width of the diffracted peaks produced by the crystals 26C, 31A, and 28B are twice the width of the peak generated by the crystal 30A. We believe this effect can be ascribed to the stress generated by the glue on the crystals, which can be strong enough to deform their curvature radius. In the focusing direction, we can cleary see the five distinc peanks in the combined image of the crystals. The most prominent peak is centred at a distance of 45 arcsec from the expected position (see Fig. 2.8) and has a FWHM of 88 arcsec. The position and FWHM of every peak are reported in Table 2.2. On the non-focusing direction, the profile of the image can be fitted by a box shape centred on 9.2 ± 0.3 arcsec from

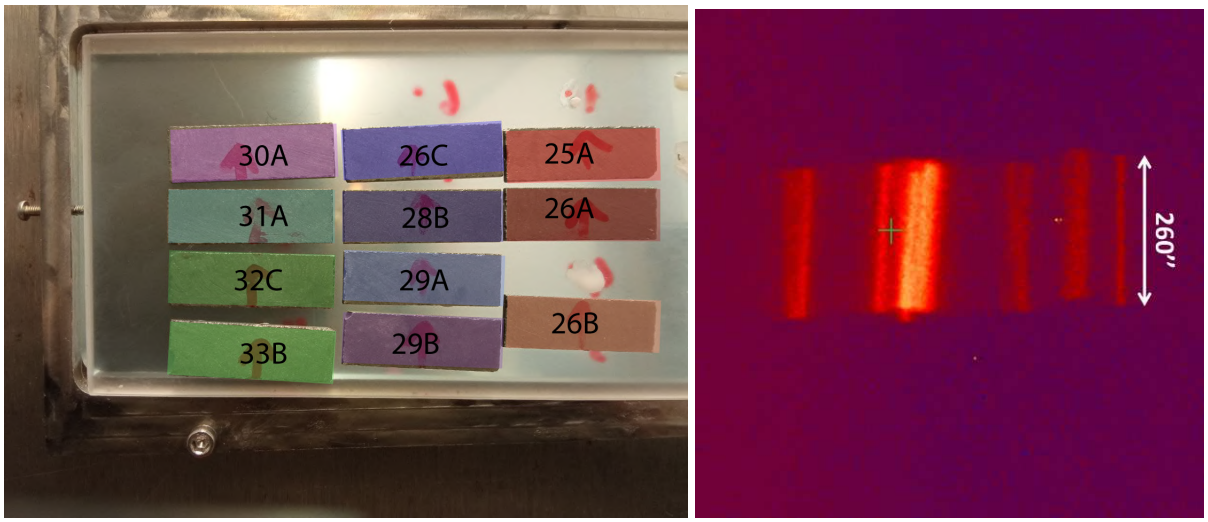

Figure 2.7: *Left*: The eleven crystals bonded on the quartz substrate fixed on the INVAR support. The colour overlapped on each crystal corresponds to the colours used to distinguish each crystal on the plots in Fig. 2.9. *Right*: diffracted image produced by the 11 crystals fixed on the substrate and illuminated simultaneously. The centre of the green cross was the target position on which we tried to align the image of each crystal.

Peak Number	Normalization	Mean [arcsec]	FWHM [arcsec]
1	0.341 ± 0.009	−160.5 ± 0.9	64 ± 2
2	0.96 ± 0.03	45 ± 1	88 ± 3
3	0.181 ± 0.006	230 ± 1	67 ± 3
4	0.226 ± 0.009	336 ± 1	60 ± 3
5	0.22 ± 0.01	414.2 ± 0.8	25 ± 2

Table 2.2: Fit parameters of the five peaks forming the combined image of the 11 crystals bonded on glass, projected along the focusing direction. The peaks are numbered in increasing order, from left to right.

the target position and with a width of 267 ± 7 arcsec, which corresponds to a linear width on the detector of 15 mm at the distance of 11.4 m, compatible with the expected crystal footprint taking into account the divergence of the X-ray beam. The time stability of the assembly has been evaluated by measuring the position of the centroid of every crystal daily after the cure. Time stability measurements on both the Bragg and polar angle can be seen in Fig. 2.9. After 31 days from the cure of the first crystal, the average misalignment value in the Bragg's angle is 100 ± 50 arcsec, while the average misalignment value in the polar angle is 2 ± 3 arcsec. The amplitude of Bragg's angle distribution is 9.58 ± 0.03 arcmin, while the amplitude of the polar angle distribution is 30 ± 7 arcsec. Taking into account that the angle with respect to the incoming direction of the photons is twice the angle between the diffraction planes and the beam [Frontera and von Ballmoos, 2010] in transmission configuration, the assembly misalignment of the crystals is then obtained by dividing the angular misalignment we measured by two. This means that the average Bragg's angles' assembly misalignment is 50 ± 25 arcsec and the width of the distribution is 4.79 ± 0.02 arcmin, while the average polar angles' assembly misalignment is 1.0 ± 1.5 arcsec.

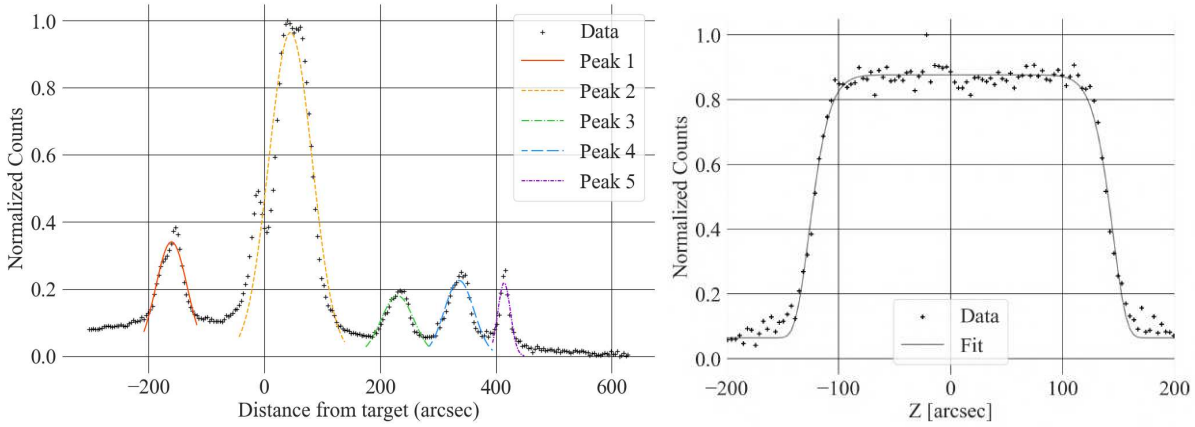

Figure 2.8: *Left*: Profile along the focusing direction of the image produced by the assembled Laue lens module. The main peak includes the overlapped images of 7 crystals. *Right*: Profile along the non-focusing direction of the image produced by the assembled Laue lens module.

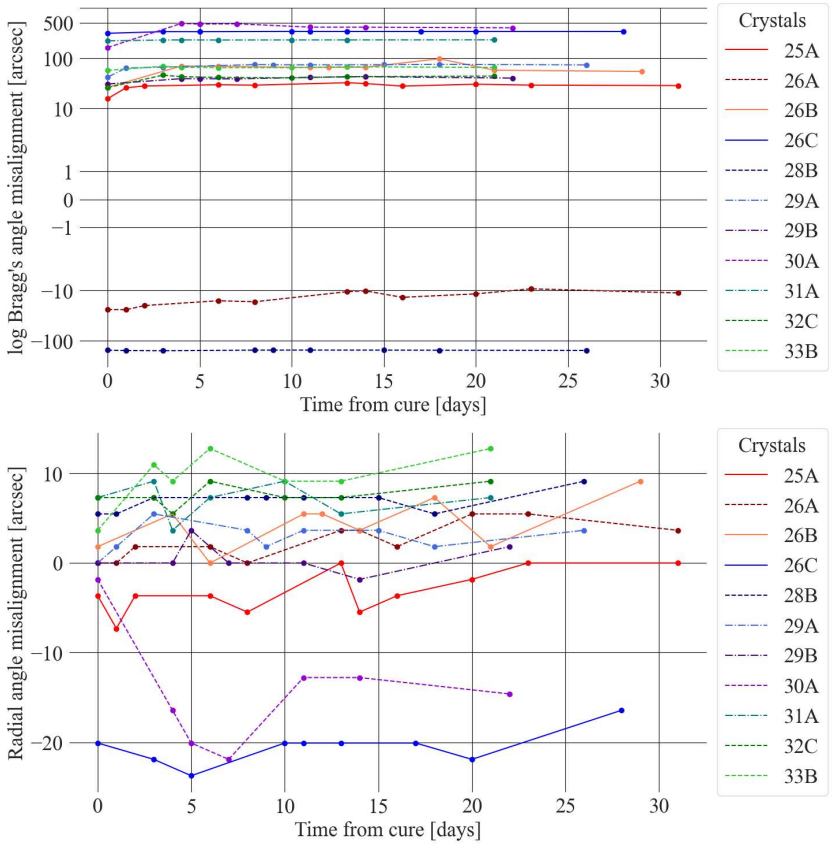

Figure 2.9: Measured misalignments in the Bragg's angle (top) and polar angle (bottom) of each crystal as a function of time after bonding.

2.1.4 Model validation and full lens simulation

The mean and width of the distribution of misalignment angles and the uncertainty of the radius of curvature were used to simulate both a sector and a whole Laue lens. For this purpose, the *Laue Lens Library* (LLL) [Virgilli et al., 2017] was used. The LLL is a hybrid analytical + ray-tracing Monte Carlo tool developed to simulate different configurations of Laue lenses and evaluate their performance. At present, the Laue simulation tool assumes that the curvature radius of the crystals, as well as the angles θ and ϕ, can be distributed according to a uniform or Gaussian profile with respect to an average value. However, the model does not include the effect of the variation of the curvature radius, which may occur during the curing process due to the aforementioned stresses. The simulated mosaicity of the crystals is set to 10 arcsec, as required for the batch of crystals used in the experimental campaign.

Module of a Laue lens: laboratory configuration

First, a Laue lens module made from bent Ge (220) was simulated, assuming a uniform distribution of misalignment errors on the Bragg's and polar angles of the crystals. The mean and width of these distributions are the same as measured from the assembled module. In addition, we included in the simulation a uniform random distribution of the curvature radius of the crystal, with a mean value of 39.7 m and width of 1.0 m. These values were obtained from the measurements of the curvature radius of a sample of 82 bent crystals of Ge(220) prepared explicitly for this project and measured at CNR-IMEM [Ferro et al., 2022] . The 11 crystals used for this demonstration prototype are part of the same batch of samples. Each crystal's assembly misalignment angles and curvature radius were sampled from those random distributions.

In the simulations, we used the geometrical configuration of source–lens prototype–detector system in our experimental setup, so we simulated a source-lens distance of 26.5 m, lens-detector distance of 11.4 m and source size of 0.4 mm.

We also simulated the performance of a sector consisting of 12 perfect crystals of Ge(220), all bent with a radius of curvature of 40 m and with no misalignment error from the ideal position. This nominal module is taken as a reference for comparison with the experimental module. Along the focusing direction (Y direction), the profile of the combined image from the 12 crystals has a Gaussian profile with a FWHM of 36.6 ± 0.1 arcsec. Along the non-focusing direction (Z direction), no focalisation is expected due to the cylindrical curvature of the sample. The data are fitted with a box profile centred on 0.01 ± 0.02 arcsec with width of 257 ± 7 arcsec. The image and the profiles along the Z and Y directions of the ideal configuration sector are shown in Fig. 2.10, left.

Images and profiles along the Z and Y directions for the distorted/misaligned configurations are shown in Fig. 2.10, right. In the latter condition, the overall image of the crystals projected along the focusing direction shows six separate peaks which can be fitted with Gaussian profiles. The parameters used to fit the peaks are reported in Table 2.3. Along the non-focusing direction, the data are fitted again by a box profile, with centre on 0.96 ± 0.08 arcsec and with a width of 260 ± 7 arcsec. Interestingly, along the Z direction, which is less affected by assembly errors, the width of the simulated realistic image is perfectly consistent with the width of the real image of the prototype along the vertical direction.

Module of Laue lens: astrophysical configuration

To assess the impact of the beam divergence, we simulated the prototype's behaviour in an astrophysical configuration, i.e., with a lens-detector distance of 20 m and a point-like source at an infinite distance. Even in this case, we simulated both an ideal lens sector and a sector

Peak Number	Normalization	Mean [arcsec]	FWHM [arcsec]
1	0.98 ± 0.01	−242.5 ± 0.2	49.7 ± 0.7
2	0.284 ± 0.005	−167.6 ± 0.2	35.5 ± 0.7
3	0.282 ± 0.005	−54.0 ± 0.2	36.7 ± 0.7
4	0.344 ± 0.005	130.7 ± 0.2	35.7 ± 0.5
5	0.88 ± 0.01	218.5 ± 0.2	37.5 ± 0.6
6	0.259 ± 0.004	273.3 ± 0.2	37.0 ± 0.7

Table 2.3: Fit parameters of the six peaks forming the combined image of the 12 Ge(220) crystals composing the simulated sector, projected along the focusing direction, in the laboratory configuration.

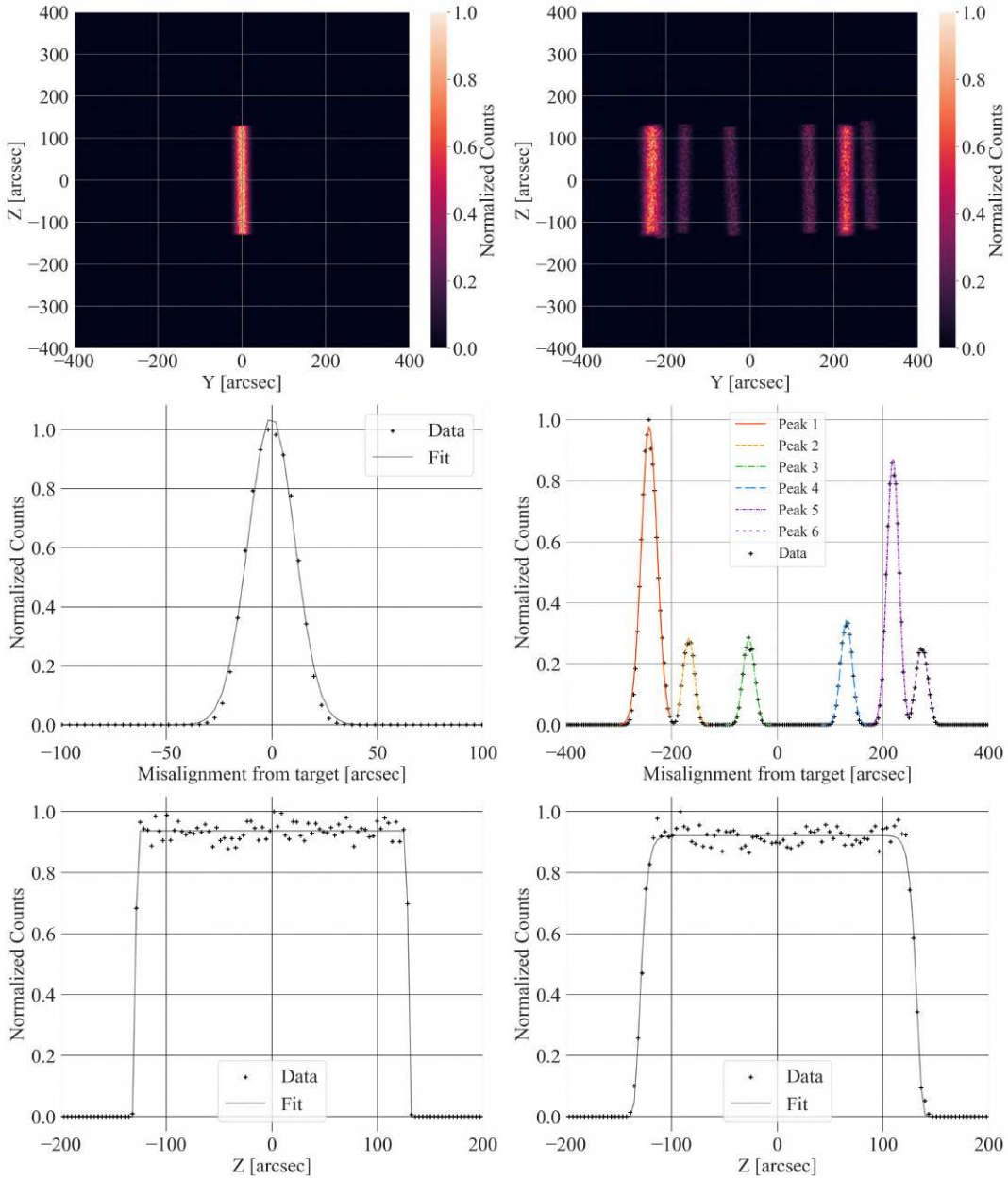

Figure 2.10: Comparison of the simulated images and profiles in the case of ideal crystal alignment configuration (left) and a configuration reproducing the laboratory setup with the observed alignment error (right). *Top*: Focal plane images of an ideal and a real sector. *Centre*: Profiles along the focusing direction. *Bottom*: Profiles along the non-focusing direction.

Peak Number	Normalization	Mean [arcsec]	FWHM [arcsec]
1	0.89 ± 0.03	−135.0 ± 0.6	61 ± 2
2	0.82 ± 0.01	88.5 ± 0.2	37.6 ± 0.6
3	0.91 ± 0.01	149.8 ± 0.2	52.4 ± 0.9
4	0.437 ± 0.007	208.6 ± 0.2	36.0 ± 0.7
5	0.903 ± 0.008	276.4 ± 0.1	38.9 ± 0.4

Table 2.4: Fit parameters of the five peaks forming the combined image of the 12 Ge(220) crystals composing the simulated sector, projected along the focusing direction, in an astrophysical configuration (point-like source at infinity).

with the same curvature radius distribution of the crystals and assembly error distribution as we measured on the prototype.

In the ideal lens case, the profile of the combined image from the 12 crystals along the focusing direction has a Gaussian profile with a FWHM of 36.0 ± 0.1 arcsec. Along the non-focusing direction, the data are fitted with a box profile centred on −0.01 ± 0.03 arcsec with a width of 104 ± 4 arcsec. Images and profiles along the Z and Y direction from both the simulated configurations are shown in Fig. 2.11.

In the realistic configuration, due to the random sampling of the misalignment distributions, the overall image of the crystals along the focusing direction shows five separate peaks. These peaks can be fitted with Gaussian profiles whose parameters are reported in Table 2.4. Along the non-focusing direction, the data are fitted again by a box profile, with centre on 3.05 ± 0.03 arcsec and with a width of 103 ± 4 arcsec. Again, this is compatible with the expected angular size of the 10 mm long non-focusing side at a distance of 20 m for a parallel beam.

Full Laue lens

With the same set of parameters characterising the astrophysical configuration, we simulated a full Laue lens made of ~13700 Ge(220) crystals working in the energy range 100 - 500 keV, in the ideal case of no errors on the curvature radius of the crystals and no misalignment errors. Results from the simulations are shown in Fig. 2.12, left. For the ideal configuration case, the PSF's HPD is 54 ± 4 arcsec, mainly due to the mosaicity of the crystals. By adding a uniform distribution of alignment and curvature radius errors and reproducing the parameter spread measured on our prototype, we obtain the results in Fig. 2.12, right. In this case, the PSF is broadened to a Half-Power diameter of 289 ± 4 arcsec.

2.1.5 Discussion of the results

For this prototype, we obtained an average assembly misalignment in the Bragg's angle value of 50 ± 25 arcsec and an average misalignment in the polar angle position of 1.0 ± 1.5 arcsec, which means that we were able to reach a good accuracy in the polar angle positioning alignment. In contrast, the misalignment in the Bragg's angle is two orders of magnitudes larger. We observed that the position of the crystals is subjected to fluctuations in the first 3–4 days after the glueing procedure; however, it settles afterwards.

Simulations based on our physical model of the Laue lens corroborate these observations and can reproduce a typical observed PSF produced by a single sector when the experimental setup is adopted, namely the source-lens geometrical configuration, the number of crystals and the alignment error distribution. Note that the presence of different features between observed and

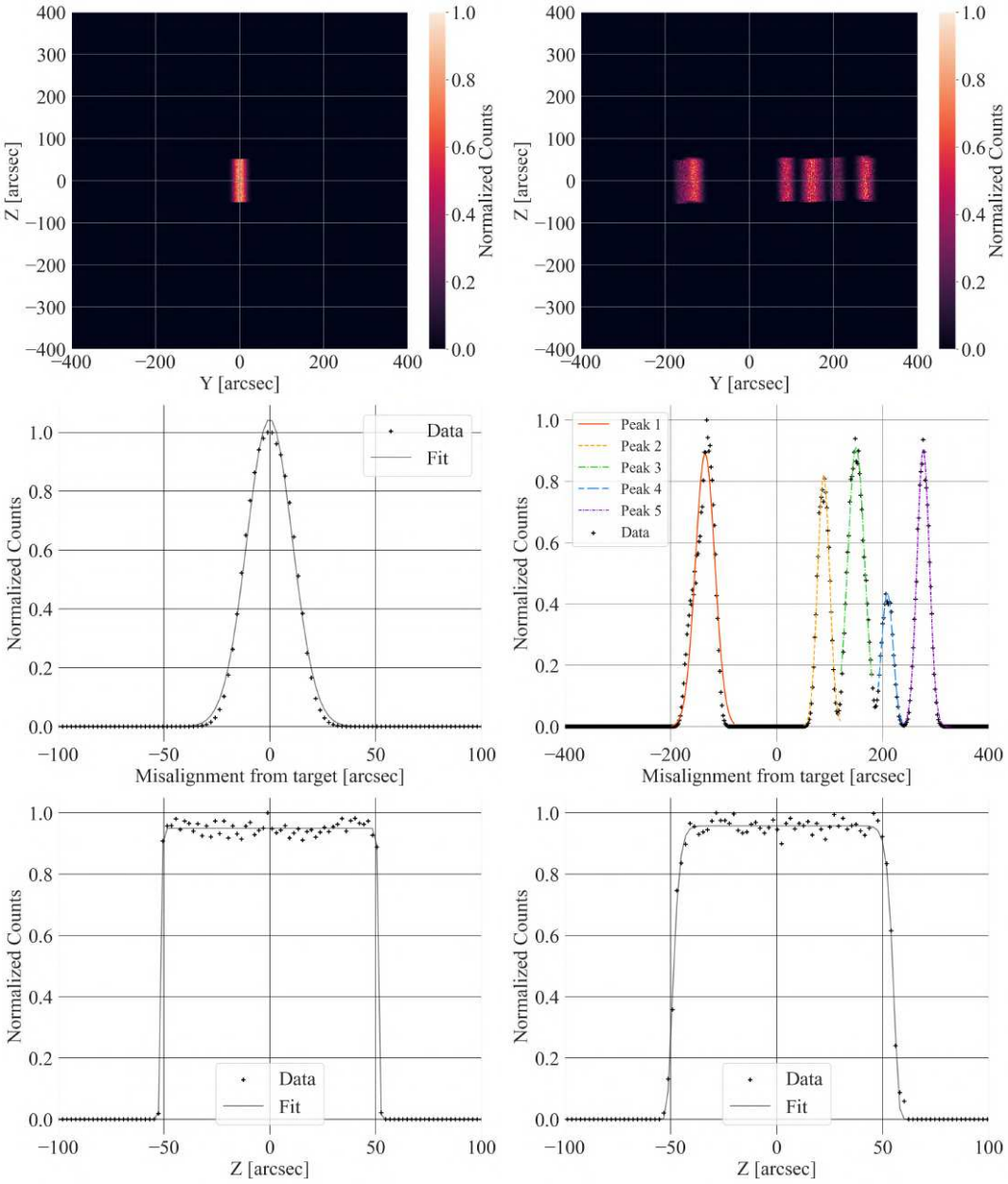

Figure 2.11: Comparison of the simulated images and profiles in the case of ideal sector configuration (left) and real configuration (right), with an astrophysical source. *Top*: Focal plane images of an ideal and a real sector. *Centre*: Profiles along the focusing direction. *Bottom*: Profiles along the non-focusing direction.

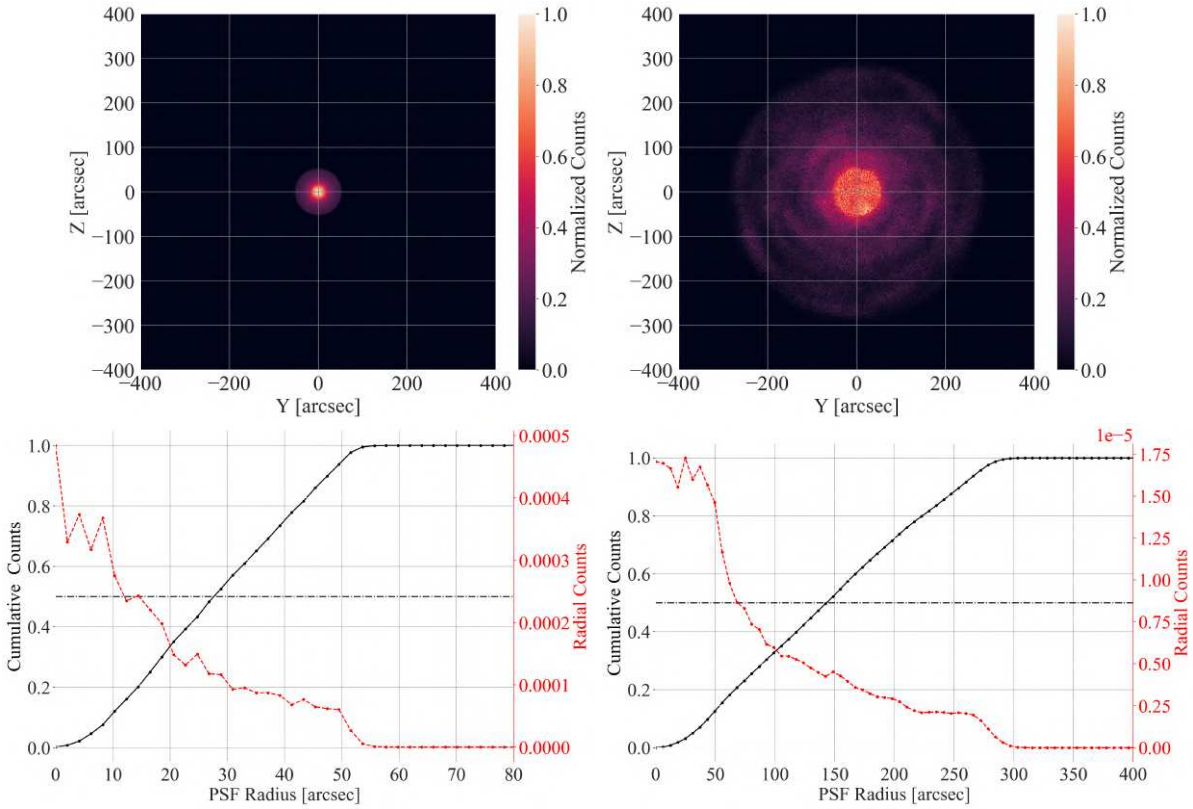

Figure 2.12: *Left*: (top) image produced by a simulated ideal full Laue lens built with Ge(220) crystals working in the 100-500 keV energy band; (bottom) radial (red curve) and cumulative (black curve) counts from the centre of the PSF. All the crystals are bent with the same curvature radius of 40 m, and no misalignment errors are present. The black dot-dashed line in the middle represents the 50% integrated counts level. *Right*: same as in the left panel, but with a real Laue lens in which the curvature radius of the crystals are distributed according to the measured uniform distribution (centre = 39.7 m, width = 1.0 m) and the misalignment errors are uniformly distributed as observed (centre = 101 arcsec, width = 161 arcsec for the Bragg angles; centre = 2 arcsec, width = 9 arcsec for the radial positioning angles). The black dot-dashed horizontal line represents the 50% cumulative counts.

simulated sector PSF is due to the randomisation of the angular misalignments performed by the LLL code, which at the moment cannot be supplied with the measured errors.

By extrapolating these performances to a whole Laue lens assembly, adopting a uniform distribution of misalignment errors, simulations show a final PSF with an HPD = 289 ± 4 arcsec. This is our best result in building a long-focal Laue lens prototype with adhesive-based bonding techniques. The Narrow Field Telescope on board the ASTENA mission has a PSF requirement of 30 arcsec, which would call for a reduction of at least one order of magnitude in the Bragg's angle misalignment with respect to what we have obtained to date. The most significant source of misalignment in our process is the unpredictability of the volumetric shrinkage of the glue, which, combined with the release of heat during the cure, makes it challenging to position the crystal with the desired level of accuracy.

To address the challenges of the bonding technique outlined above, we are currently investigating various alternative approaches. The final goal is to robustly bond the crystals while ensuring their precise alignment. As previously emphasised, the role of the adhesive is critical, especially when its thickness lacks uniformity, leading to uneven shrinkage during the curing phase. By reducing the miscut angle to a few arcseconds and, more importantly, by using crystals with a uniform miscut, one could significantly reduce the adhesive thickness between the crystals and the substrate, thus alleviating the stress induced by the curing process.

Our research so far shows that the level of positional accuracy of bent crystals achieved with UV-curable adhesives allows a long-focal length Laue lens to focus hard X-ray radiation onto a spot with a half-power diameter of 4.8 arcmin. With such a performance for the entire lens, even though it is still far from the 0.5-1 arcmin goal, one could build a narrow-field telescope for high energy spectro-polarimetry capable of obtaining a significant jump in sensitivity in the 50-600 keV band, when compared to current non-focusing instrumentation, thereby opening a new window in hard X and soft gamma-ray astrophysics.

The results of this work were published in the Journal of Astronomical Telescopes, Instruments, and Systems (JATIS) and the paper is reported in the Appendix.

2.2 New techniques for Laue lens building

The experience of assembling the Laue lens prototype highlighted some criticalities that must be addressed to reach the assembly accuracy desired for ASTENA/NFT's optics. In particular:

1. Our current assembly technique relies heavily on human input; automatised bonding equipment is not used yet. This makes the process very time-consuming and subjected to many uncontrollable sources of errors.

2. The presence of a miscut angle on the planes of the crystals makes it necessary to perform the alignment under an X-ray beam since the surface of the tiles cannot be used as an optical reference. This means that, at the moment, the process requires very specific equipment and facilities and is not ideal for industrial production.

3. Since the X-ray beam of the facility is horizontal, we need to perform our bonding vertically, limiting our choice of adhesives to high-viscosity glues.

In this chapter, I will describe further experiments and techniques we investigated to progress the limits of Laue lens technology above the level we reached with TRILL.

2.2.1 Automatized placement tests

In collaboration with the Institute for Data Processing and Electronics (IPE)[2] of the Karlsruhe Institute of Technology (KIT), we tested the possibility of automating the bonding process with dedicated equipment. The group of Electronics at IPE has years-long experience in bonding techniques for microelectronics, from standard wire bonding [Harman and Harman, 2010] to flip-chip techniques, bump bonding and more [Lau, 2016]. The IPE's group worked on the bonding of the detector sensors of the Compact Muon Solenoid (CMS) experiment at CERN [Caselle et al., 2016], of the Compressed Baryonic Matter (CBM) [Pfistner et al., 2019] experiment at FAIR facility (GSI, Germany)[3], and of the PANDA (anti-Proton ANnihilations at DArmstadt) experiment at GSI[4]. IPE's laboratory is equipped with cutting-edge machinery to perform different types of bonding and test their properties. With the supervision of Dr. Michele Caselle of IPE, we performed two different bonding experiments in which we bonded Germanium crystals to two different substrates (Zerodur and fused quartz glass) with the use of the *FINEPLACER Femto* automatic die bonder by *Finetech*[5].

The experiment aims to test the quality and uniformity of the bonding process. Diffraction alignment is not possible at KIT since it needs to be performed under an X-ray beam. Still, it is possible to obtain an idea of the repeatability of the bonding, the long-term stability of the alignment, and its applicability to our type of crystals.

Materials and experimental set-up

The 16 tiles used for this experiment are again Ge(220) crystal tiles with cross-section 30×10 mm^2, with thickness S = 1.54 − 1.77 mm, and they are cut such that the diffraction planes are parallel to the $10 \times$ S mm^2. The curvature radius and the thickness of the crystals are shown in Table 2.5.

We tested two different substrates: a circular, fused quartz substrate (diameter = 100 mm, thickness = 5 mm) and a trapezoid (long base = 78 mm, short base = 67 mm, height = 182

[2] https://www.ipe.kit.edu/english/index.php
[3] https://www.gsi.de/en/researchaccelerators/fair
[4] https://panda.gsi.de/
[5] https://finetech.de/products/fineplacer-femto-2/

Crystal ID	Curvature Radius (m)	Thickness (μm)	Prototype
29	39.4 ± 0.1	1.59 ± 0.01	1
30	37.8 ± 0.1	1.63 ± 0.01	1
33	41.0 ± 0.1	1.72 ± 0.01	2
34	41.4 ± 0.1	1.57 ± 0.01	2
35	41.1 ± 0.1	1.63 ± 0.01	2
36	40.2 ± 0.1	1.76 ± 0.01	1
37	41.3 ± 0.1	1.71 ± 0.01	2
39	37.8 ± 0.1	1.62 ± 0.01	2
40	40.5 ± 0.1	1.77 ± 0.01	1
41	40.3 ± 0.1	1.60 ± 0.01	1
44	41.1 ± 0.1	1.65 ± 0.01	1
45	41.1 ± 0.1	1.75 ± 0.01	1
47	39.7 ± 0.1	1.63 ± 0.01	1
48	39.7 ± 0.1	1.62 ± 0.01	2
49	39.9 ± 0.1	1.54 ± 0.01	2
50	41.4 ± 0.1	1.64 ± 0.01	1

Table 2.5: Curvature radius and thickness of the batch of crystals used for the assembly test at the KIT institute.

mm, thickness = 4 mm) Zerodur substrate, remainder of unused substrates from the TRILL experiment. The glue used is again OP 61 LS by DYMAX.

The bonding is performed with the use of the *FINEPLACER Femto* bonding machine (Fig. 2.13, A). The machine is an automatic flip-chip die bonder with pick-and-place technology. The machine can pick up a die, orient it according to a predefined reference and bond it to the desired position on the substrate through a pattern recognition algorithm, which can be programmed to recognise specific patterns on the die and the substrate. In this way, the machine can orient and position the die with an accuracy of 0.5 microns on the horizontal plane.

The working plate of the machine is divided into two trays (Fig. 2.13, B): one is for the dice, and the other is for the substrate. The dice are placed on a Gel-Pak substrate, and then the Gel-Pak is placed on the dice tray. When the machine is operative, vacuum is applied below both trays so that the Gel-Pak and substrate are kept in position, and the dice are released from the gel tray.

The machine picks up a die with a movable arm (Fig. 2.13, C) equipped with a flat, rotating head. The die is rotated to the desired position and then positioned on the substrate. Vacuum is applied on the head of the arm to keep the die in position during the whole process. Finally, the die is bonded with the desired bonding technique. For this purpose, the machine can heat up and press the sample, work in different atmospheres, and be equipped with attachments for specific bonding methods. A schematic of a general bonding procedure is shown in Fig. 2.14.

The head of the vacuum arm and the bonding plate of the machine are properly adjusted to a high degree of parallelism. For our scope, the machine, at the moment, has an important limit: it orients the crystal only in the horizontal direction, so crystals and substrate are bound to be parallel between each other, meaning that it is not possible to set the crystals at a specific Bragg's angle by tilting the crystal with respect to the substrate. However, it is still possible to obtain a rough idea of the potentiality of an automatised bonding process by comparing the dispersion

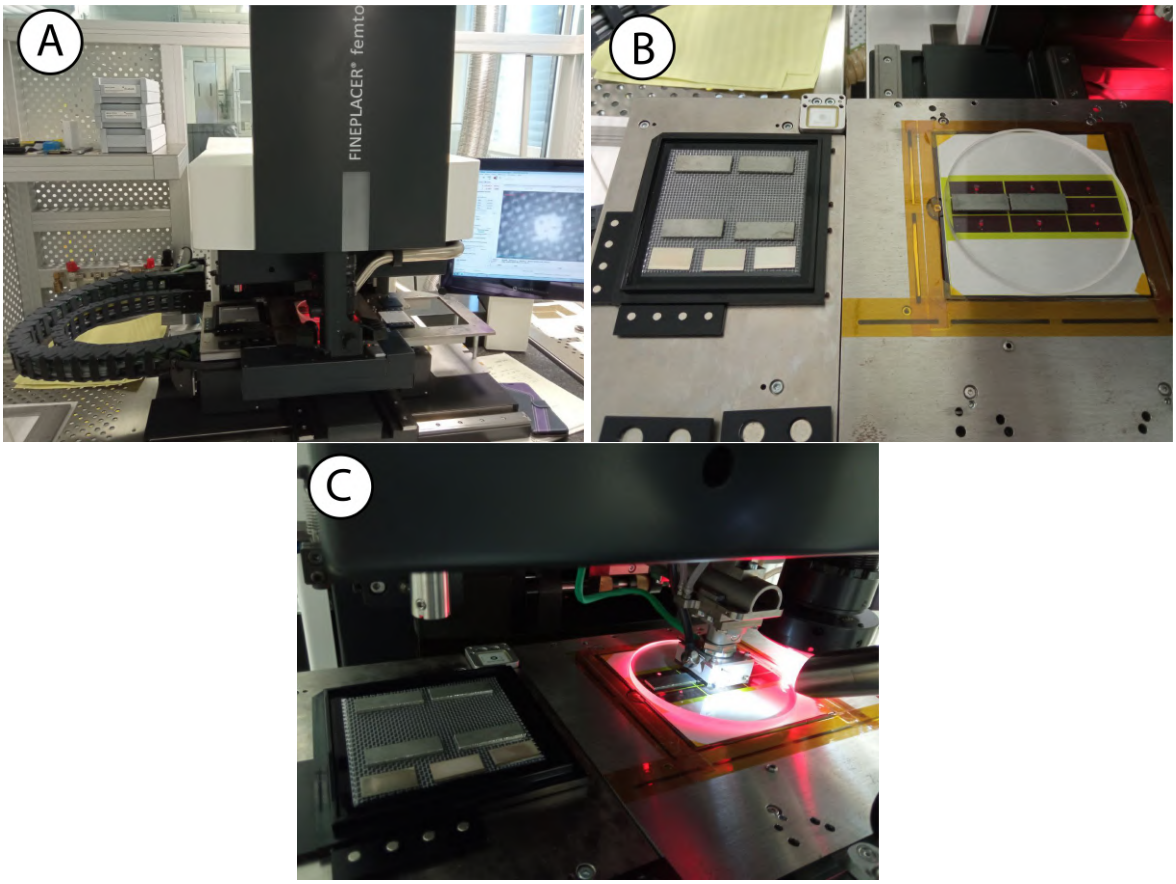

Figure 2.13: *A:* The *FINEPLACER femto* machine by *Finetech* available at KIT. *B:* The working plate of the machine. The Gel-Pak with the dice to bond is visible on the left, while the substrate tray, with a circular glass substrate on top, is visible on the right. *C:* The movable arm of the machine is visible on the right, bent on the substrate to keep a die in position.

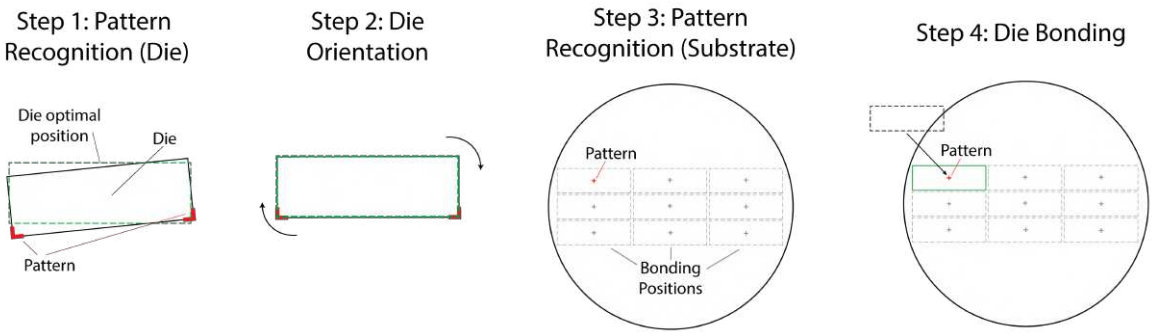

Figure 2.14: Step-by-step schematics of an example bonding process with the Finetech bonding machine available at KIT. Step 1: the machine recognises a specific pattern on the die to bond (in this example, the corners of the sample) and picks up the die. Step 2: while the machine's movable arm holds the die, the pattern is used to rotate and orient the die to the desired direction (green dashed line), defined through an automation code. Step 3: the machine recognises a pattern on the substrate that defines the bonding position (in this example, the red cross). Step 4: the machine bonds the die on the substrate in the desired position.

of the diffracted images of the crystals bonded at KIT with the dispersion we can expect due to the different miscut among the crystals: if the former is compatible with the latter, it means that the alignment errors introduced by an automatised bonding are compatible or smaller with the crystals' miscut angles distribution.

Bonding procedure

In the first experiment, we bonded nine Ge(220) crystals to a circular substrate. The crystals used for this test are marked in Table 2.5. For this first module, we decided to position the crystals on a 3 x 3 grid. We set up the crystals on the Gel-Pak and programmed the machine to recognise the corner edges of the tiles and use them as a reference for the orientation. Then we set up the substrate on its tray and, for each crystal, we followed those steps:

1. The machine picks up and orients the crystal. Each crystal is oriented so that the bottom edge is parallel to the bottom edge of the substrate holder tray. In this way, all the crystals should be equally distanced from each other.

2. A drop of glue is deposited on the substrate. At the time of the experiment, the glue was dispensed manually by an operator; however, it is possible to upgrade the machine with an automatic glue dispenser.

3. The crystal is moved to the desired bonding position and put in contact with the glue. The machine is programmed to hold the crystal in position while exerting 5 N of force toward the substrate for 120 seconds while the glue is cured. The glue is cured with a UV beam coming from the side of the substrate since the back was covered by the machine tray and inaccessible.

4. the crystal is released, and the procedure is repeated with the next crystal until all the crystals are bonded to the substrate.

The same procedure was repeated with the Zerodur substrate, on which we bonded the remaining crystals.

Prototypes' testing

The aims of the tests on the prototype are:

1. to verify that bent crystals could withstand the bonding procedure, i.e., their shape was not deformed in the process.

2. To test the capability to evenly space the crystals, meaning that we can co-align the crystals on the substrate plane.

3. At LARIX, test whether the distribution of the diffracted images is compatible with the expected spread due to the crystals' miscut.

At KIT, we performed a first visual inspection of the two prototypes (Fig. 2.15). From the assembled modules, it is visible that the machine could not reach a high level of accuracy in the positioning of the crystal. This is due to the jagged corners of the tiles (Fig. 2.16), which are the result of the surface lapping process. This reduces the accuracy of the pattern recognition process, inducing a rotation error. In future experiments, we will take this into account and search for a technique to obtain clean, sharp edges on all the crystal tiles. A possible solution is

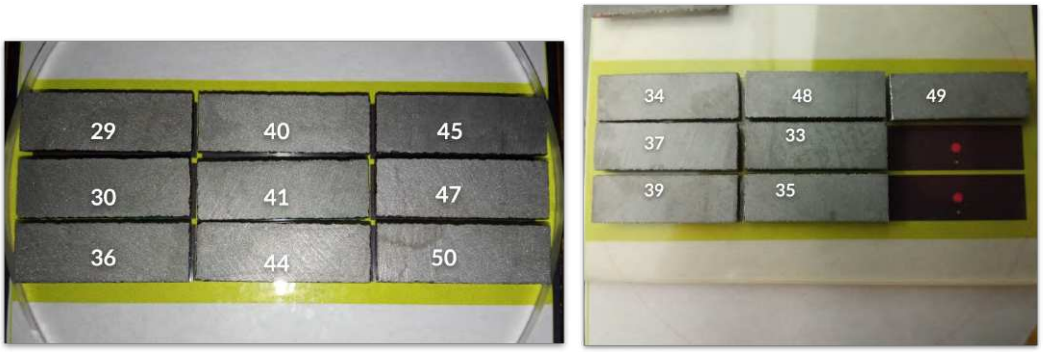

Figure 2.15: The two Laue lens prototypes assembled at KIT. *Left*: first prototype, made by nine crystals of germanium bonded on a glass substrate. *Right*: second prototype, made by seven crystals bonded on a Zerodur substrate. The numbers on the crystals correspond with the identification numbers in Table 2.5

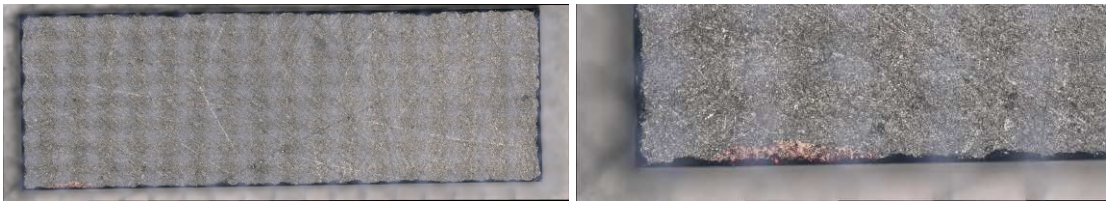

Figure 2.16: Microscopic image of crystal 29 (left) and detail of the bottom-left corner (right). The edges of the crystals appear jagged due to the lapping process, making it hard for the bonding machine to reconstruct the shape of the tile properly.

to pot the crystals in resin, which can be modelled to get very sharp edges without damaging the crystal. However, this requires tests to verify (1) that the resin and its mechanical machining do not change the crystals' curvature radius, (2) that the resin does not reduce excessively the diffraction efficiency of the crystals, and (3) how accurately we can orient the crystals inside the resin.

After this first inspection at KIT, the two prototypes were tested at the LARIX-T facility. The setup for the prototypes' tests at LARIX is analogous to the setup described in Sect. 2.1, which was used for the TRILL project prototype. Both the trapezoid and the circular substrates were mounted on the hexapod: the first was fixed via steel brackets, while the second was placed in a 3-D printed circular sample holder. The samples were fully illuminated with the polychromatic X-ray beam (voltage = 200 V, current = 4 mA), and the assemblies were rotated until all the crystals produced a diffracted image on the detector simultaneously. Then, we set the aperture of the collimator to 8×8 mm^2 and illuminate the position of each single crystal separately. In this way, it is possible to record the misalignment of the crystals day by day and test the time stability of the assembly.

From the tests on the Zerodur substrate, we observed that the crystals could sustain the bonding process. The angular spread of the crystals along the θ-direction results to be 15 arcmin, which is remarkably similar to the typical value of miscut of 0.25 deg for standard, factory-produced Germanium wafers. This indicates that this type of bonding process is already very accurate without X-ray control, introducing an error <15 arcmin on the position of the crystal. Remarkably, at the LARIX facility, we cannot reach this level of accuracy without using the X-ray beam to perform a first rough alignment of the crystals. If we could obtain/produce crystals with a very low miscut, it would be possible to use this type of machine to bond them with a very high accuracy level.

Less positive results were obtained on the crystals bonded to the glass substrate, for which almost all the diffracted images were misshaped, indicating that a deformation of the structure of

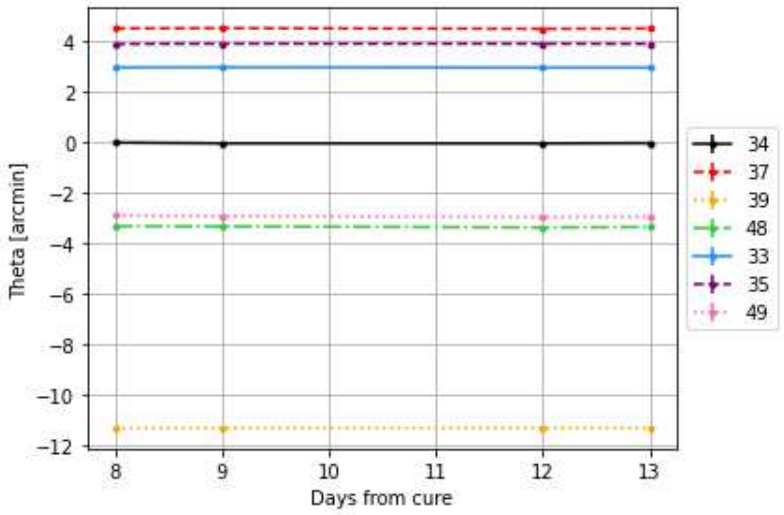

Figure 2.17: Crystals' relative misalignment angles with respect to crystal 34 (reference), vs days from cure.

the crystals occurred during the bonding process. Results of this experiment suggest that that the substrate choice for this process is crucial; we believe that Zerodur's very low coefficient of thermal expansion and higher Young's modulus with respect to fused quartz were responsible for reducing the amount of deformation transferred to the crystal during the bonding process. More tests are needed to understand which substrate materials are the best for this procedure. Still, Zerodur seems to be a promising material, but it has the disadvantage of being more expensive than fused quartz/silica glass. Finally, this bonding process showed a very high time stability, way higher than the stability we obtained with the TRILL prototype. Stability data were collected for the Zerodur prototype and are shown in Fig. 2.17. For the Bragg's angle misalignment error, we fixed one of the crystals (crystal 34) as a reference and evaluated the misalignment of the image of the other crystals with respect to the image of crystal 34. Even though it was impossible to test the first days immediately after the bonding, the high assembly stability reached with this technique is evident.

Conclusion and prospects

In conclusion, this experiment at KIT confirmed that it is necessary to invest in technologies to automate and perfect the process to overcome the limits reached with glue-based bonding. The advantages of a more controlled environment are visible both from the point of view of the time stability of the assembly and from the amount of time necessary to build one sample. More research can be performed toward automating the process at LARIX and/or increasing the synergy with KIT and other institutions to exploit high-precision bonding techniques and push further the maximum accuracy which can be achieved with adhesive-based bonding.

We also want to remark that, at the moment, we are also exploring other techniques not based on the use of adhesives, which are anodic bonding for Laue lenses [Mazzolari et al., 2023], the development of tunable Laue lenses, and the SiLC (Silicon Laue Component) technology [Barrière et al., 2023], in collaboration with *cosine Measurements Solutions*[6].

Anodic bonding is a well-established semiconductor physics technique used to perform direct bonding between silicon wafers and within silicon and suitable glass [Knowles and van Helvoort, 2006]. In collaboration with the semiconductor physics group of the University of Ferrara, we

[6] https://www.cosine.nl/

are developing the technology to bond flat, super-polished, very low miscut (<15 arcsec) silicon tiles to bent glass substrates in such a way to simultaneously bend the crystals to the desired curvature radius and bond them to the suitable substrate. Tests will be performed to extend this technology to germanium crystals.

Adjustable Laue lenses, instead, have already been proposed by different authors [Lund, 2021], and they solve the problem of properly orienting the crystals by changing approach and using tunable systems, such as micrometric screws or piezoelectric motors to finely position each single crystals, potentially performing active adjustments of the lens while in use. A possible solution, which exploits the deformation of an elastic support through piezo motors to orient crystals, has been proposed for a proof of concept study at the INAF institute.

Finally, we are collaborating with *cosine* to test SiLC modules at LARIX. SiLCs have been developed as a heritage of the Silicon Pore Optics developed for the ATHENA space mission by ESA [Girou et al., 2023, Keek et al., 2023], and consist of stacks of silicon wedged plates, curved in two directions to provide radial and azimuthal focusing. They can be a great solution to build Laue lenses working up to 150 keV, and a SiLC test campaign is foreseen at LARIX, in which we will test the focalisation capabilities of a SiLC module and its diffraction efficiency.

Chapter 3

ASTENA as a high energy polarimetry observatory

Polarimetry of hard X-rays and soft gamma-rays is a key observational parameter to investigate the emission mechanisms and geometry of a wide number of cosmic objects and events such as GRBs, pulsars, binary black holes, and AGNs, whose emissions are expected to be polarised. In the last two decades, missions such as RHESSI [Lin and RHESSI Team, 2002], INTEGRAL, AstroSat [Chattopadhyay et al., 2019], POLAR [Kole and Polar Collaboration, 2017, Kole et al., 2020], and PoGO+ [Friis et al., 2018] brought a great contribution to the field. However, our knowledge of the polarimetric properties of high-energy sources is still limited, and new instruments with enhanced polarimetric capabilities are needed. In this chapter, we will describe the very basics of polarimetry with Compton interaction, which is typically the dominant type of interaction between radiation and matter in the soft gamma-ray energy band, then we will present the results of our study devoted to understanding how ASTENA can contribute to the field of high energy polarimetry.

3.1 Compton polarimetry basics

The Klein-Nishina [Klein and Nishina, 1929] differential cross-section of Compton interaction, for a linearly polarised beam, can be written as:

$$\frac{d\sigma}{d\Omega} = \frac{r_0^2 \epsilon^2}{2}\left(\frac{1}{\epsilon} + \epsilon - 2\sin^2\theta\cos^2\phi\right) \tag{3.1}$$

where r_0^2 is the classical electron radius, ϵ is the ratio between the energy of the scattered photon and the energy of the incoming photon, θ is called *Compton scattering angle* and is measured with respect to the direction of the incident photon, while ϕ is the azimuth scattering angle, measured with respect to the direction of the electric field vector of the incident photon (Fig. 3.1, left). The Klein-Nishina cross-section foresees that, for linearly polarised radiation, the probability distribution of the azimuthal angle has a maximum along the direction orthogonal to the polarisation direction and a minimum in the parallel, while all the directions should be equally probable for an unpolarised beam (Fig. 3.1, right). The azimuthal scattering distribution also shows a strong dependence on the energy, and its asymmetry reduces with the increase of the energy of the scattered beam (Fig. 3.2).

Exploiting this property of Compton interaction, it is possible to infer the polarisation intensity and direction of a linearly polarised beam by analysing the distribution of photons scattered on a detection plate. For a Compton polarimeter, then, the number of detected events

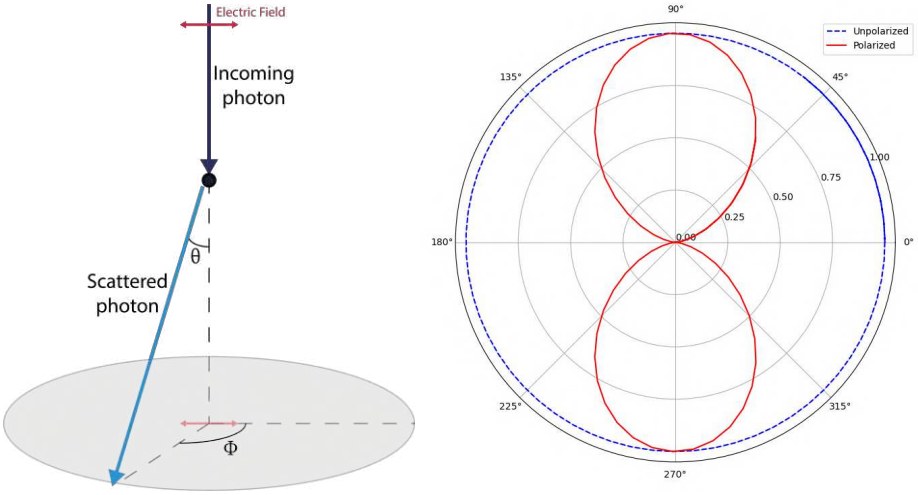

Figure 3.1: *Left:*Schematics of the typical Compton scattering geometry. The angle θ is the Compton scattering angle, while ϕ is the azimuth scattering angle. *Right:* Klein-Nishina normalised probability distribution on the azimuthal plane for a 300 keV scattered beam. The red solid line is the probability distribution for a 100% polarised beam, the blue dashed line is the distribution for an unpolarised beam.

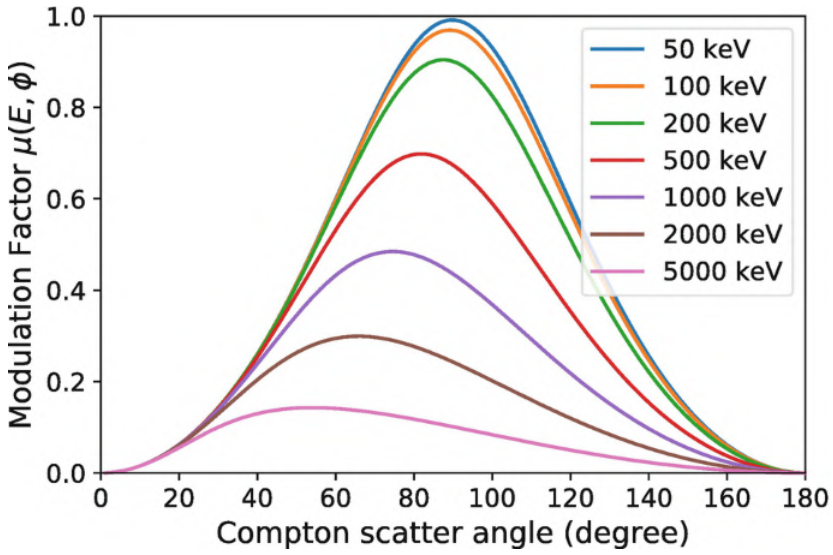

Figure 3.2: Maximum theoretical modulation factor vs Compton scattering angle, for different energies. The higher the modulation factor, the higher the degree of polarisation. Reprinted from Kierans et al. [2022].

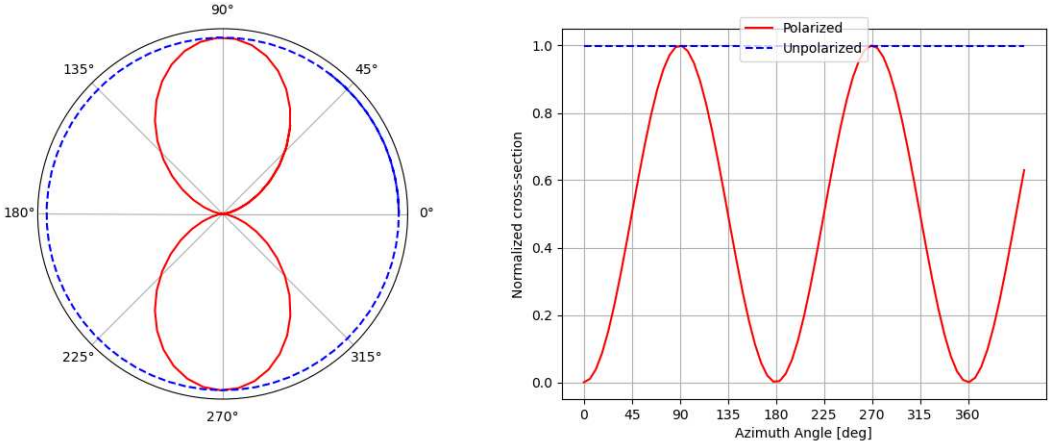

Figure 3.3: Compton scattering cross-section expressed as modulation function (left) for polarised (red) and unpolarised (blue) radiation. In the case of an unpolarised beam, the modulation curve appears completely flat, while for a polarised beam, it shows the typical cosine behaviour.

as a function of the azimuth angle can be written as:

$$N(\phi) = N_0(1 + Q\cos(2(\phi - P + \pi/2)) \tag{3.2}$$

This function is usually called modulation curve, in which N_0 is a normalisation factor, Q is the so-called modulation factor, and P represents the polarisation angle. This means that, by fitting the distribution of the scattered photons, it is possible to obtain information on both the polarisation level and the polarisation angle of the incoming radiation (Fig. 3.3).

Segmented detectors, with 2D/3D spatial resolution, can be ideal Compton polarimeters, since each segment of the detector can act both as a scattering and a detection unit by exploiting a coincidence event logic, thus allowing us to reconstruct the photons' distribution. However, the pixelisation of the detector induces systematic effects on the shape of the modulation plot, which can lead us to overestimate the polarisation level. To take this into account and remove the effects of systematics in the modulation plot, we correct the polarised modulation curve $N(\phi)$ with the unpolarised modulation curve $N_{unpol}(\phi)$ measured in the same conditions: [Lei et al., 1997]

$$N_{corr}(\phi) = \frac{N(\phi)}{N_{unpol}(\phi)} N^{max}_{unpol} \tag{3.3}$$

where $N_{corr}(\phi)$ is the corrected polarised modulation curve and N^{max}_{unpol} is the maximum of the unpolarised modulation curve. Once the correction is done, it is possible to fit the corrected modulation curve and extract the polarimetric information from the curve.

3.2 Optmization of ASTENA/NFT and ASTENA/WFM polarimetric capabilities

Even though they are based on different technologies, the detector of ASTENA/NFT and the ASTENA/WFM are both segmented detectors with 3D spatial resolution. Given the importance of polarimetry in high-energy astrophysics, we decided to investigate the polarimetric capabilities of those instruments. The first part of our work focused on testing and optimising different configurations for both instruments. Then, once we determined an optimised configuration, we simulated realistic astrophysical sources to test the capabilities of both instruments. In both cases, the analysis procedure followed the same logic:

1. We implemented a Monte Carlo model of the instruments using the MEGAlib tools [Zoglauer, 2019], a Geant4-based software designed to easily simulate gamma-ray detectors, perform event reconstruction, and high-level analysis. MEGAlib is specialised in Compton telescopes, but its high flexibility makes it a very good tool to simulate different types of high-energy detectors, not limited to astrophysical applications.

2. We simulated different types of sources and their interactions with the detector model, then we used the REVAN software [Zoglauer, 2005] of the MEGAlib tools to reconstruct the Compton events happening inside the detectors. For each source, we simulated both a polarised and unpolarised beam variant, in such a way that we could use the unpolarised modulation curve to correct for the geometrical systematics of the detectors. The REVAN software reconstructs all the events occurring in the detector and flags them according to the type of interaction (photoelectric, Compton scattering, pair production, etc.)

3. We used a custom Python tool[1] to analyze both polarized and unpolarized reconstructed event data. From the reconstructed events, the software creates a scattering matrix and a modulation curve using only events that satisfy some selection criteria, then it corrects the polarised modulation curve with the unpolarized data. Finally, the Python software outputs the modulation factor, the polarisation angle, and the number of events used to construct the modulation curves.

Optimising the configuration means finding the one that allows us to obtain the lowest MDP, and this strongly depends on the value of the modulation factor Q and the detection efficiency of Compton interactions. In this section, we will describe the first part of our work, which was to optimise the configurations of NFT and WFM.

3.2.1 ASTENA/NFT Monte Carlo model and source model

First, we implement a simplified Monte Carlo model for the NFT based on its requirements and the most recent developments in the technology of 3D CdZnTe spectra-polarimeters [Abbene et al., 2020]. The model was implemented with the MEGAlib/Geomega package and consisted of a stack of 4 thick layers of CZT separated by 10 mm thick layers of a PCB-type passive material, representative of the read-out electronics (Fig. 3.4, left). The spectroscopic response of the detector was modelled by previous measurements on CZT drift-strips spectrometers, (Fig. 3.4, right), and the low energy threshold for the detector was set to 5 keV, which is a reasonable value at room temperature [Kuvvetli, 2003]. Each CZT layer has a volume of $80 \times 80 \times 20$ mm^3 and was divided into voxels, i.e. 3D cubic pixels, the size of which was representative of the 3D spatial resolution of the detector. Since we were interested in understanding the influence of the spatial resolution of the instrument on its polarimetric performance, we defined five models with different voxels' side length: 0.25 mm, 0.5 mm, 1.0 mm, 2.5 mm, and 5.0 mm.

To simulate the focalised X-ray beam coming from the Laue lens, we defined an on-axis source placed at 20 m from the detector model, aligned with the centre of the detector. The spatial profile of the source is a Gaussian-profile cone beam, with a FWHM of 1.5 mm, equal to the expected PSF-HPD of NFT.

This is an approximation of the real beam; the true beam coming from the Laue lens will be inclined with respect to the lens axis of 0.4 deg @700 keV up to 4.5 deg @50 keV. We expect, however, that due to the cylindrical symmetry of the lens, for each off-axis beam, there will be a symmetric beam with opposite off-axis angle, such that any possible systematic errors coming from the effect of impinging on the detector with off-axis beams, will be cancelled out. We

[1] https://github.com/Lisa9584/PolSoftware.git

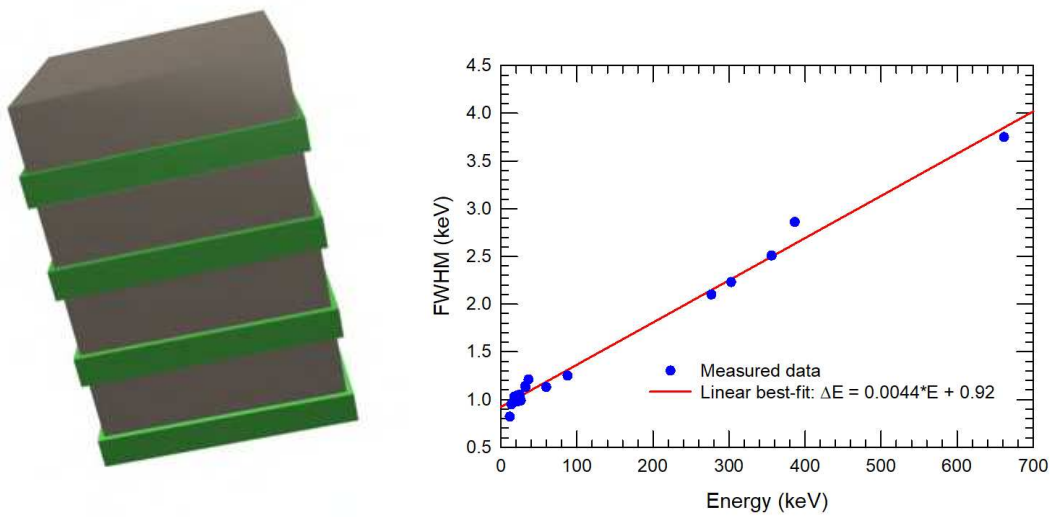

Figure 3.4: *Left*: Simplified Monte Carlo model of ASTENA/NFT used to optimise the detector geometry. The grey layers are CZT, while the green layers are PCB. *Right*: Interpolated energy resolution used for the Monte Carlo model. Data from Kuvvetli [2003].

performed a systematic study to validate this assumption: we simulated pairs of symmetric off-axis beam sources, varying the number of paired beams from 2 to 128, reconstructed the modulation curve of the radiation, and evaluated the distribution of the modulation factors. We evaluated a standard deviation on the value of the modulation factor of 0.02 from the central value, comparable with the errors (Fig. 3.5). Hence, we adopted the on-axis approximation to simplify the code and speed up the simulations without compromising the results.

Finally, the baseline event selection logic is as follows:

1. events flagged as Compton which are not compatible with Compton kinematics are rejected;

2. events for which the scattering and detection points are closer than 2 voxels are rejected. This is to reduce the systematic effect induced by the first neighbour voxels, for which, due to the detector's pixelisation, it is impossible to measure the Compton angle with enough accuracy.

3. After the first Compton interaction, further interactions of the same type can happen. We call multiplicity M the total number of interactions composing an event flagged as Compton, being two the minimum. We accept all the events with M > 2 but use only the first two interaction points to reconstruct the modulation curve.

Polarimetric capabilities characterisation and optimisation

The first thing we investigated was the multiplicity of the detected Compton scattering events as a function of the energy and the voxels' size. For this test, we illuminated each of the five detector models with monochromatic beams of energies 150 keV, 300 keV, 500 keV and 1 MeV. For each energy, we simulated the behaviour of the detector both for polarised and unpolarised radiation. The simulations are run with the MEGAlib/Cosima tool, then pre-processed by the MEGAlib/REVAN tool, and finally, they are analysed with our Python software, in which we implemented the event selection logic. We evaluated the modulation plot for the polarised and unpolarised data by splitting the scattering plane into 24 angular bins, and then we used the unpolarised data to correct the polarised modulation curve. Finally, the corrected curve is

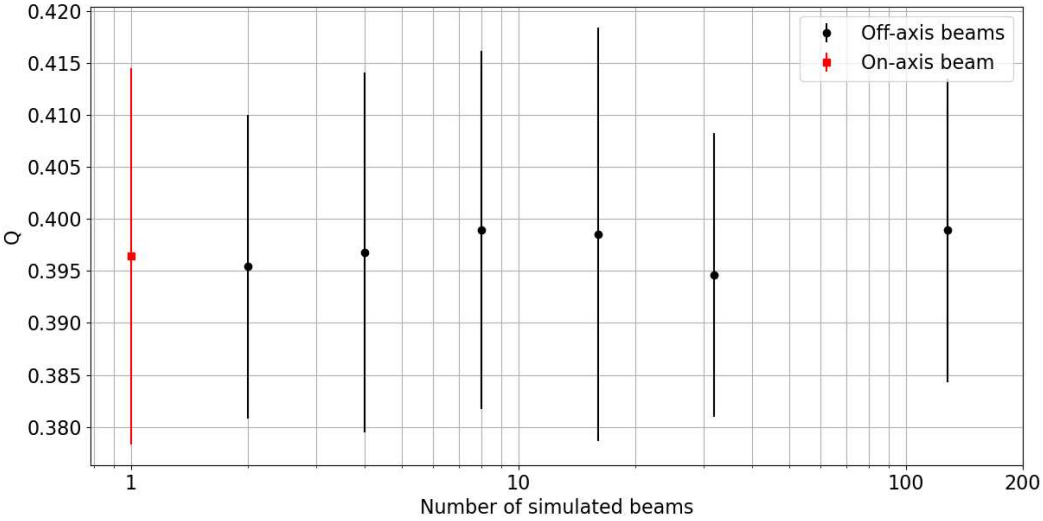

Figure 3.5: Modulation factor Q evaluated for an on-axis, cone beam (red) and for an increasing number of pairs of symmetric off-axis sources (black). The evaluated modulation factors are compatible within the errors.

fitted with Eq. 3.2 to extract the modulation factor and the reconstructed polarisation angle. An example of the pixelised scattering maps and modulation plots obtained in this process are shown in Fig. 3.6. If we compare the scattering map and modulation plot of polarised and non-polarised radiation, the difference in the spatial distribution of the photon on the detector plane is evident. Notably, we can see the systematic effects due to the square shape of the voxels in the modulation plot of the unpolarised radiation, which shows four spikes. We can also see how effective the correction technique that we applied is since the corrected modulation plot does not show any geometrical systematic errors anymore.

Results are shown in Fig. 3.7. Independently from the voxel scale, we can see that, by increasing the energy, the number of events with M > 2 increases. This is to be expected: the higher the energy of the impinging beam, the higher the probability that the scattered photon is still very energetic and can undergo further Compton scattering. Interestingly, we can see that by decreasing the voxel size, the number of events with higher multiplicity increases. This is a direct effect of the increase of the spatial resolution of the detector: smaller resolutions allow the detector to separate better multiple interactions happening very close to each other, increasing the average multiplicity of the events.

Then, we tested the variation of the modulation factor Q as a function of the voxel scale. Results are shown in Fig. 3.8, left. The best results at every energy are obtained for values of the voxel scale ≤ 0.5 mm, compatible with the requirements of ASTENA/NFT. Detection efficiency, instead, does not depend on the voxel scale, but only on the volume of active detection material. In Fig. 3.8, right, we report the evaluated detection efficiency **without** event selection, for different multiplicities.

We chose the configuration with 0.25 mm side voxels since it is closer to the spatial resolution requirements of ASTENA/NFT (<0.3 mm). In this configuration, we performed a finer evaluation of the modulation factor and the detection efficiency, this time **after** the event selection. Results are shown in Fig. 3.9.

Finally, we tested our capability to reconstruct the polarisation level and the polarisation direction from the measured modulation plot. We simulated beams with 1%, 3%, 5%, 10%, 30%, and 50% polarisation levels (polarisation angle = 0 deg), and we compared the injected value of

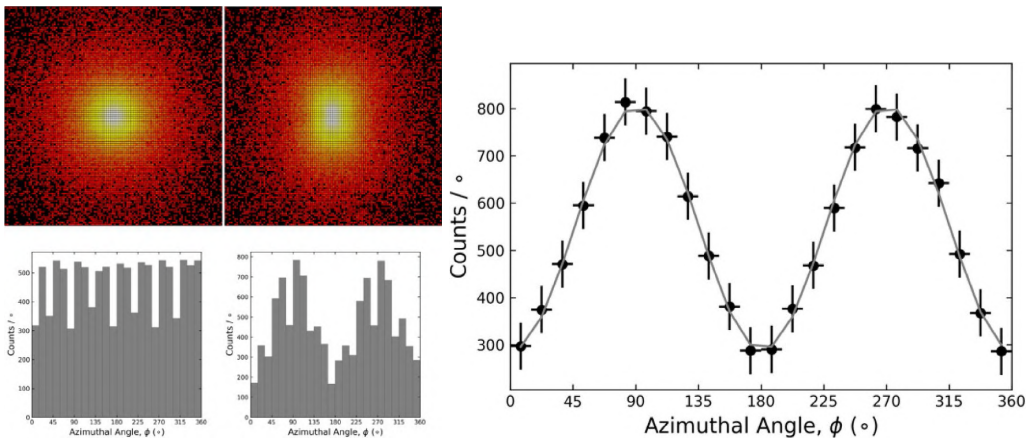

Figure 3.6: *Left*: Side-by-side comparison of the scattering map and the modulation curve for an unpolarised and a 100% polarised beam. In both cases, the beam energy is 300 keV and the voxel size is 0.25 mm. *Right:* Corrected polarised modulation curve of the same data. We can see how applying the correction removed the systematic effects. Reprinted from Moita et al. [2023].

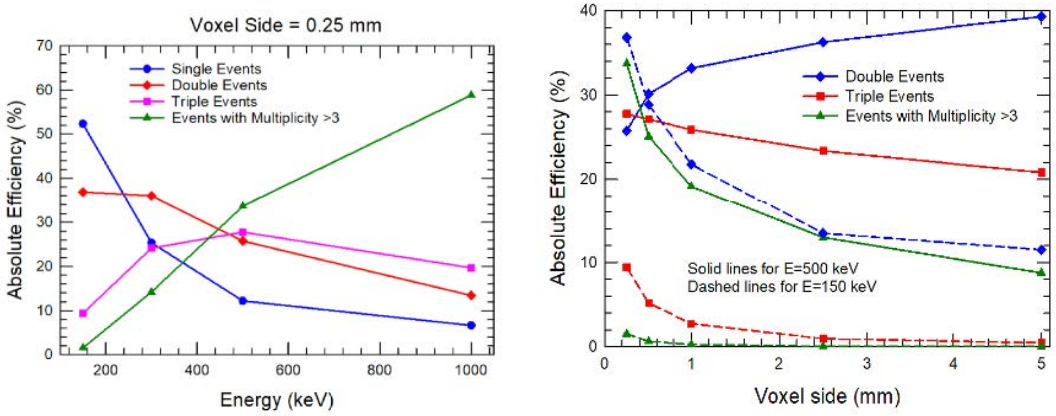

Figure 3.7: *Left*: Absolute efficiency of events with different multiplicities vs energy, in the case of 0.25 mm voxel resolution. Event chains made by one single interaction point, which are not Compton events, are also included. *Right:* Absolute efficiency of events with different multiplicities vs voxel scale, for two different values of energy. Reprinted from [Moita et al., 2020]

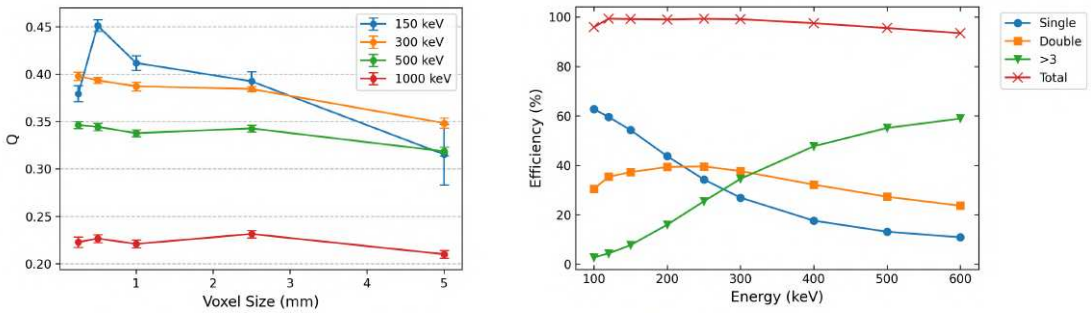

Figure 3.8: *Left*: Modulation factor vs voxel size for different values of energy. *Right*: NFT's detection efficiency (without event selection) vs energy.

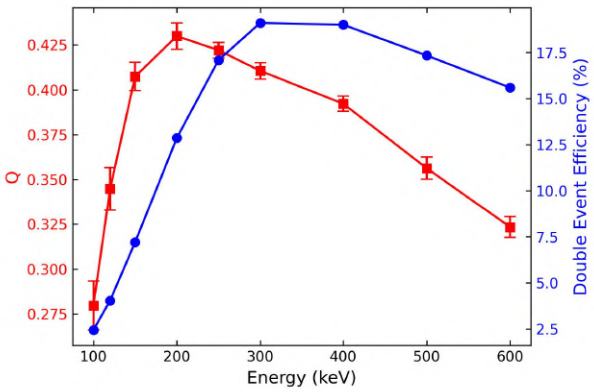

Figure 3.9: Modulation factor (red) and Compton events selection efficiency (blue) vs energy for a voxel side of 0.25 mm. Reprinted from Moita et al. [2021].

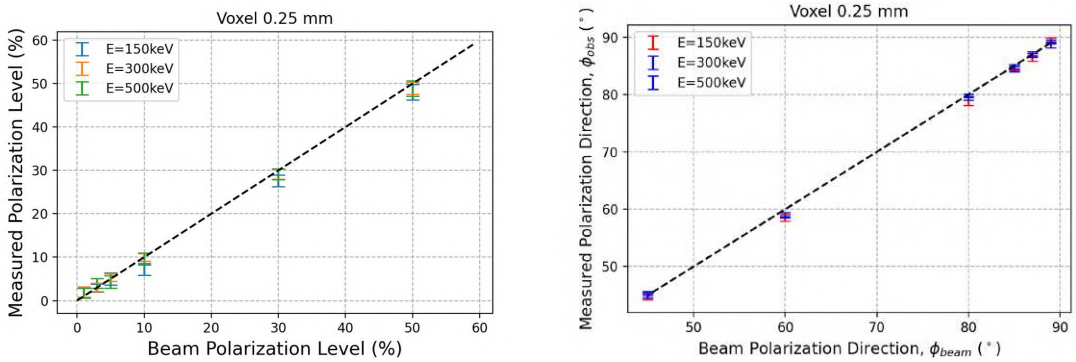

Figure 3.10: *Left*: Measured polarisation level vs simulated for three different energy values. *Right*: Measured polarisation angle vs simulated for three energy angles.

the polarisation level with what we obtained by fitting the modulation curve. In the same way, we simulated beams with 45 deg, 60 deg, 80 deg, 85 deg, 87 deg, and 90 deg polarisation angles (polarisation level = 100%) and compared the reconstructed angle with the simulated. Results are shown in Fig. 3.10. We can see that both the polarisation level and the polarisation angle can be well reconstructed.

NFT final Monte Carlo model

Based on this study and the current developments in spectra-imager, high-resolution CZT technologies [Caroli et al., 2022], we defined a more realistic model of the NFT detector. The full detector is now split into a stack of several detector units. Each unit consists of a CZT crystal with anode electrodes oriented in one direction on the largest side and strip cathodes oriented in the perpendicular direction on the other side (Fig. 3.11, left). With current technologies, it is possible to realise CZT wafers 5 mm thick, with 20×30 mm^2 cross-section. The PCB material now has an "L" shape, 1 mm thick, with outer edges dimensions of 40 mm (bottom) and 30 mm (side), and is connected to the sensor crystal in such a way that the top and one of the sides of the CZT are free. 24 units are stacked together in the so-called Photons Transverse Field (PTF) configuration [Kuvvetli et al., 2010] and constitute one of the four layers of the full detector 3.11, right). The full NFT model has a detection area of 60×60 mm^2 and a CZT thickness of 80 mm. From the signal acquired at the anodes and cathodes, and from the ratio between them, it is possible to evaluate the three coordinates of interaction with the sub-millimetric accuracy required for NFT.

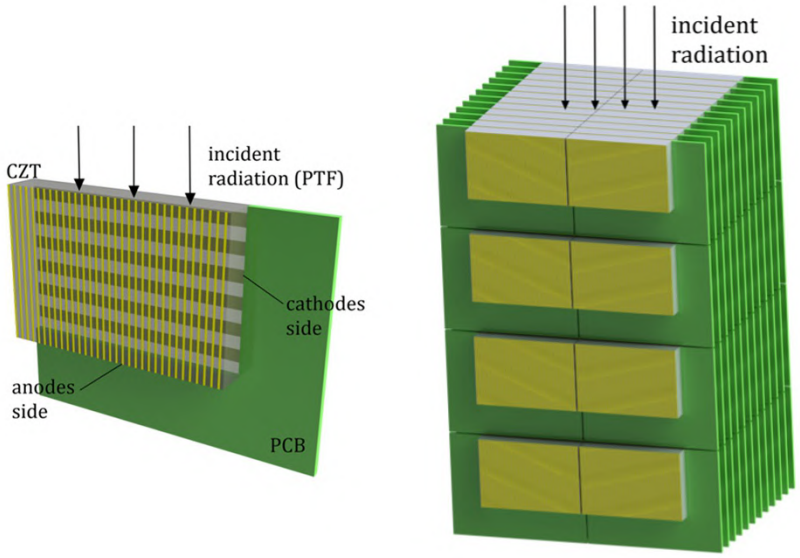

Figure 3.11: *Left*: Single CZT detection unit composing the full model of the NFT detector. *Right*: The full NFT detector model, which is composed of several units stacked together to form a stack of four layers. Reprinted from Moita et al. [2023].

3.2.2 ASTENA/WFM Monte Carlo model and source model

The Monte Carlo model of each WFM unit consists of an array of 40×40 hexagonal scintillator bars of CsI, for a total of 205 bars. The distance between flats of each hexagon is 5 mm, while the length of each bar was set to 50 mm. To mimic the depth resolution of the WFM, each scintillator bar was segmented into 10 sections of 5 mm each. The model includes the read-out SDDs: a 0.4 mm linear SDD on top, and a single anode, 0.4 mm thick hexagonal SSD on bottom (Fig. 3.12, left). Finally, the model of the full WFM was obtained by arranging twelve units, in pairs, on a hexagonal configuration around the axis of the lens, with at a distance from the lens axis of 1.5 m. The units are all tilted by 15 deg with respect to the lens axis (Fig. 3.12, right).

For now, our optimization efforts focused on the NFT model, so we did not implement different models for the WFM and adhered to the structure described in ASTENA's white papers. In the future, we will also try to optimize the WFM model by testing different lengths of the scintillator bars and different scintillator materials. At the time of writiig, we characterised the polarisation capabilities of this baseline model.

In the case of the WFM, the incoming radiation beam was simulated using the Far Field Point Source type of MEGAlib. This source type mimics the behaviour of a point source coming from an infinite distance and corresponds to a divergence-less radiation front impinging on the detector. Finally, from the point of view of event selection, we kept the same baseline selection logic we defined for NFT and adopted the same data analysis technique.

The main difference with respect to NFT is that now the scintillators show a hexagonal geometry instead of the cubic geometry of NFT's voxels, which results in a different structure of the systematic error on the unpolarised and uncorrected polarised modulation curves (Fig. 3.13).

Polarimetric capabilities characterisation

First, we used the WFM model to simulate the effective area of the instrument vs energy. The effective area was evaluated as the ratio between the reconstructed Compton events and the total number of simulated events, multiplied by the surface area from which the simulated events were generated. The simulated effective area is shown in Fig. 3.14, left. Then we evaluated the

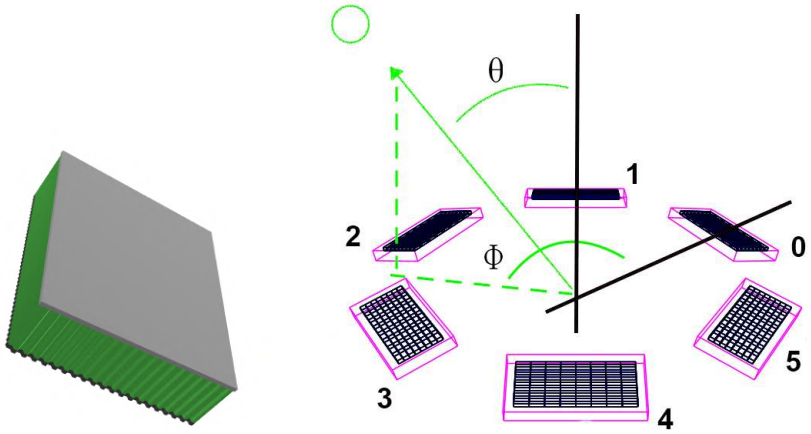

Figure 3.12: *Left*: Monte Carlo model of a single camera of the Wide Field Monitor. The green bars are the hexagonal scintillator, while the top SSD is shown in grey and the bottom SSD in black. *Right*: Model of the full WFM configuration, with the twelve cameras arranged in six pairs around the axis of the lens. Reprinted from Ferro et al. [2023].

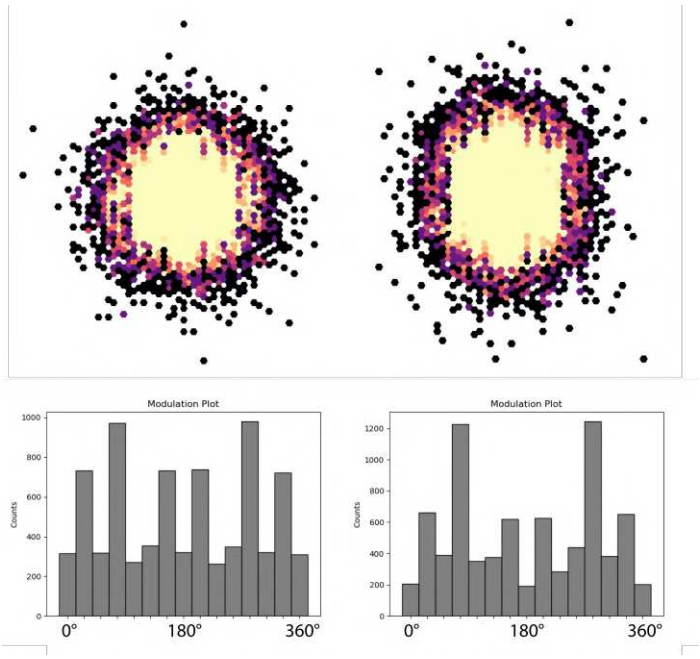

Figure 3.13: Scattering maps and modulation plots obtained for a 500 keV unpolarised beam (left), and for a 100% polarised beam (right).

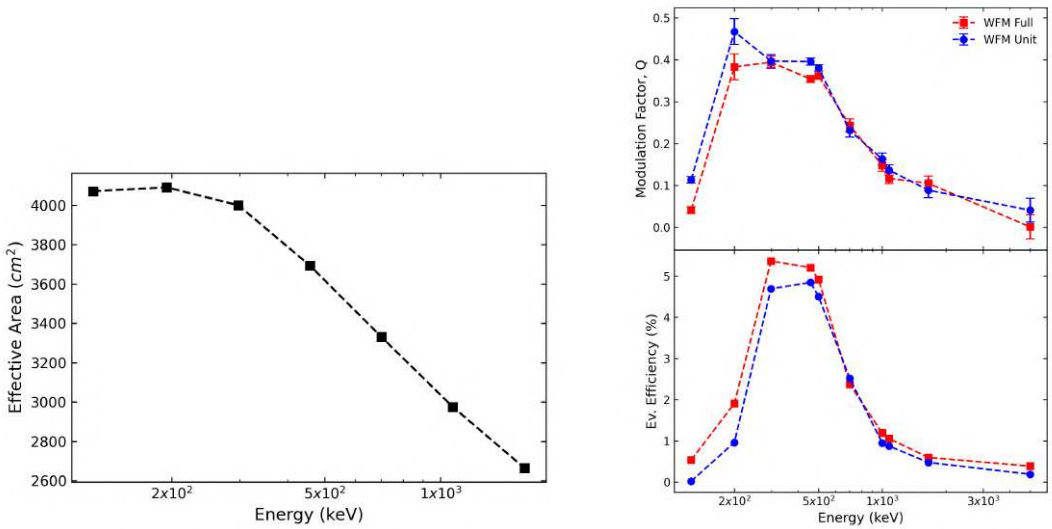

Figure 3.14: *Left*: Simulated effective area of ASTENA/WFM vs beam energy. *Right*: Modulation factor (top) and double event efficiency (bottom) evaluated for a single WFM module and the complete WFM instrument. Reprinted from Moita et al. [2021]

modulation factor and the selected event efficiency for a single unit and the full WFM assembly. Results are shown in Fig. 3.14, right. We can see that the instrument can be used as a polarimeter up to 1 MeV, while, above this limit, both the modulation factor and the select event efficiency become very low due to the reduction of the overall efficiency of Compton interaction. A way to overcome this limit would be to implement a pair-production polarimetry reconstruction model along with the Compton polarimetry model; however, this requires further investigation.

3.3 ASTENA polarisation capabilities study

After the characterisation of ASTENA/NFT and ASTENA/WFM, we concentrated on some scientific cases, for which we tried to evaluate the minimum detectable polarisation with NFT and/or with WFM. For each astrophysical source, we simulated a source object with the same spectral characteristics of the astrophysical source in analysis and evaluated the respective modulation factor and the selected events efficiency. By combining those with the effective area of NFT and WFM, and the background model for both instruments, we evaluated the minimum detectable polarisation. Here, we describe the results we obtained from some astrophysical sources, which are just a small sample of the types of sources that can be observed with ASTENA.

The effective area of NFT was evaluated in previous works [Ferro, 2020, Frontera et al., 2021] and is shown in Fig. 3.15, while the background for both instruments was simulated with MEGAlib by combining the background models for different types of background sources, including cosmic-rays, atmospheric neutrinos, Earth's X-ray albedo, and the hard X-ray atmospheric and extra-terrestrial X-ray backgrounds [Churazov et al., 2008, Kole et al., 2015, Mizuno et al., 2004, Sazonov et al., 2007, Türler et al., 2010]. The simulated background for both NFT and WFM are shown in Fig. 3.16.

3.3.1 Crab Nebula

The first realistic case we analysed was the Crab pulsar nebula. The Crab pulsar is one of the most famous supernova remnants, and it is a neutron star surrounded by a nebula. It is a typical example of a young, rapidly spinning, strongly magnetised neutron star that generates broad-band

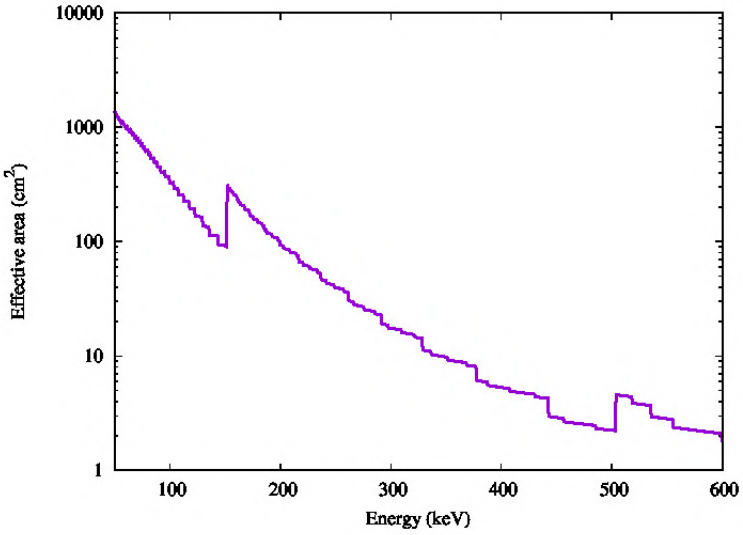

Figure 3.15: Effective area of ASTENA/NFT re-binned at 1 keV. Reprinted from Ferro [2020].

electromagnetic radiation by particle acceleration in its magnetosphere [Hester, 2008]. The hard X and gamma-ray spectrum of the nebula can be interpreted as a combination of synchrotron emission and inverse Compton scattering [Burn, 1973, Haymes et al., 1968]. The details of this emission process are poorly understood, and polarisation measurements in gamma-rays, particularly as a function of pulse phase, can be a key element to unravel the mystery of pulsar radiation [Pétri, 2013].

We evaluated the MDP of a Crab-like source in different energy bands for ASTENA/NFT and ASTENA/WFM. To do so, we started by estimating the modulation factor and event efficiency for a Crab-type source. As we did before, for the NFT, we simulated an on-axis beam with a Gaussian profile to mimic the image of the Laue lens, while for WFM, we simulated a far-field point source. In both cases, we assumed an energy distribution of the photons equal to the typical Crab's nebula spectrum, which is a power-law distribution with a normalisation index of 10.74 photons s^{-2} cm^{-2} and photon index of 2.17. The simulated energy range was compatible with the instruments' energy pass bands, i.e. 50 - 600 keV for the NFT, and 150 keV - 1 MeV for the WFM. We analysed the data as before, extracting the modulation factor and selected event detection efficiency, and then we evaluated the MDP for both instruments. The MDP as a function of the energy for a 100 mCrab source observed for 100 ks is shown in Fig. 3.17. For energies < 200 keV, the NFT presents MDP values $\sim$1%, however, the MDP degrades very fast above that energy. The WFM-IS achieves the maximum MDP for energies between 300 and 600 keV, so this means that the instruments can complement each other.

3.3.2 Magnetars

Magnetars are another possible target of interest for a survey with NFT. Magnetars are neutron stars with ultra-strong magnetic fields that can reach up to 10^{11} T and, in some cases, emit X/gamma-rays. There are about 30 confirmed known magnetars [Olausen and Kaspi, 2014], many of which are detectable only during periods of enhanced activity. At present, hard X-ray emission has been reported in about one-third of magnetars. They can be a good candidate for a polarisation study with NFT, providing a new way to investigate their magnetic fields'

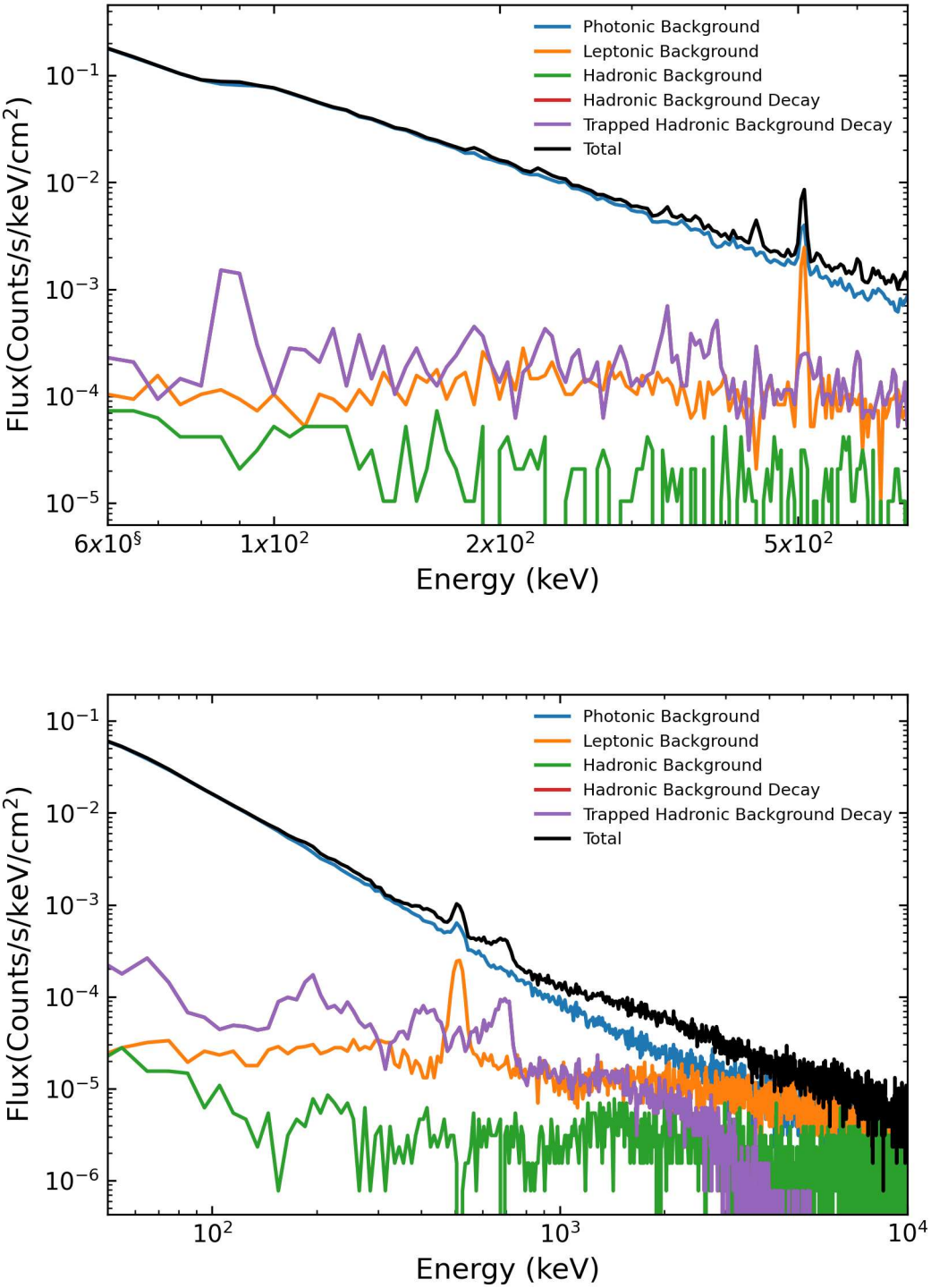

Figure 3.16: Evaluated total background (black) and split for component types for ASTENA/NFT (top) and ASTENA/WFM (bottom).

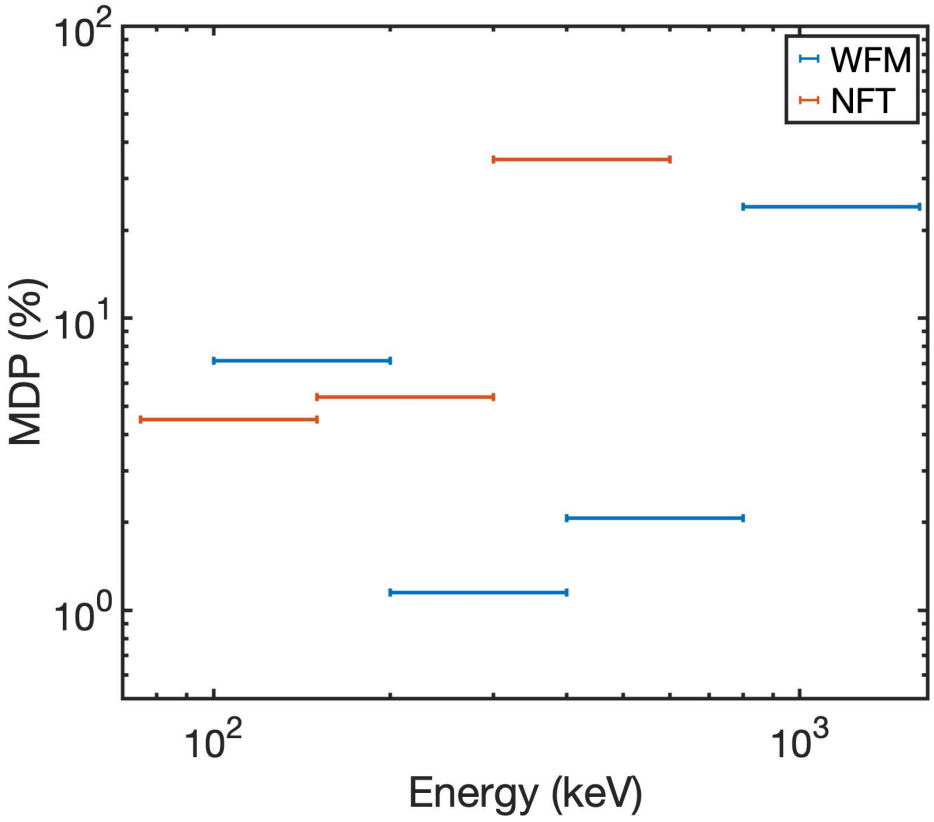

Figure 3.17: MPD for a Crab-like source as a function of the energy band, for ASTENA/NFT (blue), and ASTENA/WFM (orange). Observation time = 100 ks.

distributions and surface properties.

We focused on magnetar 4U 0142+61, an anomalous X-ray pulsar which was well investigated in the soft and hard X-ray bands with INTEGRAL, NuSTAR and Swift [Weng and Göğüş, 2015], and recently with IXPE [Taverna et al., 2022]. IXPE measured the linear polarisation properties of this magnetar properties at low energies, finding a polarisation degree of $15.0 \pm 1.0\%$ @ 2–4 keV, no significant polarisation in 4–5 keV, and $35.2 \pm 7.1\%$ @ 5.5-8 keV. This is a remarkably strange behaviour, and further investigations on this source are required to understand its magnetic properties better. We simulated a magnetar-like source by extrapolating the spectrum of 4U 0142+61 measured with NuSTAR [Tendulkar et al., 2014] to higher energies and we evaluated the MDP as a function of the observation time obtainable with NFT. The results, split for three different energy bands, are shown in Fig. 3.18.

3.3.3 Gamma Ray Bursts

As described in the first chapter, polarisation measurements are a fundamental tool for investigating the physics of GRB prompt and afterglow emissions. Studies over the last few years have been extremely fruitful in the field of GRB polarimetry science: measurements from POLAR [Zhang et al., 2019] and AstroSat [Chattopadhyay et al., 2019] have almost tripled the GRB prompt emission polarisation sample. However, the results are not in agreement and are difficult to interpret based on prompt emission models of polarisation. Polarisation observations on a larger sample covering different GRB properties are still required to investigate the prompt emission polarisation better. An innovative instrument such as ASTENA could give an important contribution to solving this ambiguity and significantly increase the number of measured GRB

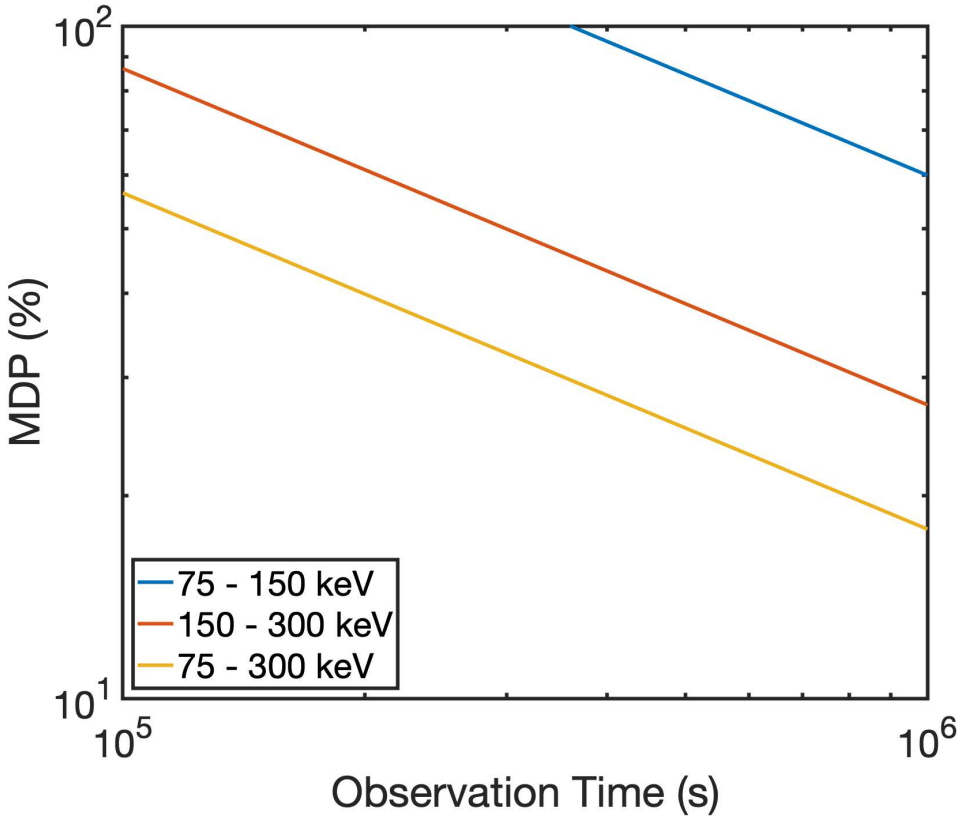

Figure 3.18: Evaluated MDP for magnetar 4U 0142+61 vs observation time, for three different energy bands.

prompt polarisation, specifically with the WFM instrument, which has the potential to detect GRBs and perform prompt polarimetric measurements quickly.

GRBs can appear in any part of the WFM field of view, so studying the influence of the source off-axis angle on the modulation curve is crucial. To do so, we simulated a far-field point source with photon energy distributed as the typical Band spectrum of GRBs' prompt emission [Band et al., 1993]. For the parameters of the band function, we used the average from the parameters reported in Poolakkil et al. [2021], so we set the low energy index to -0.46, the high energy index to -2.98 and the peak energy to 413 keV. The modulation factor as a function of the source off-axis polar angle for different fixed azimuth angles is shown in Fig. 3.19. We can notice a significant decrease of the modulation factor, which decreases up to ~50% of its maximum value for off-axis polar angles >30 deg. Due to the asymmetrical geometry of the single WFM units, we can see that also the source azimuth angle influences the value of the modulation factor. This effect is slightly reduced for the full WFM assembly, which has a greater symmetry than the single unit but is still present.

As a last scientific case, we investigate GRB afterglows, which are suitable candidates for a follow-up performed with NFT. In this case, the starting time of the observation after the GRB trigger is crucial to collecting enough photons to allow us to obtain good-quality measurements, so we must also take this into account in our simulations. To do so, we simulated the emission of a GRB afterglow at different epochs and tested how the MPD varies as a function of the observation time and the observation start time. The first GRB we considered was 130427A, which was detected in April 2013. It originated from a relatively close galaxy, and its prompt emission registered the highest recorded GRB fluence up to that point in time [Ackermann et al., 2014, Fan et al., 2013].

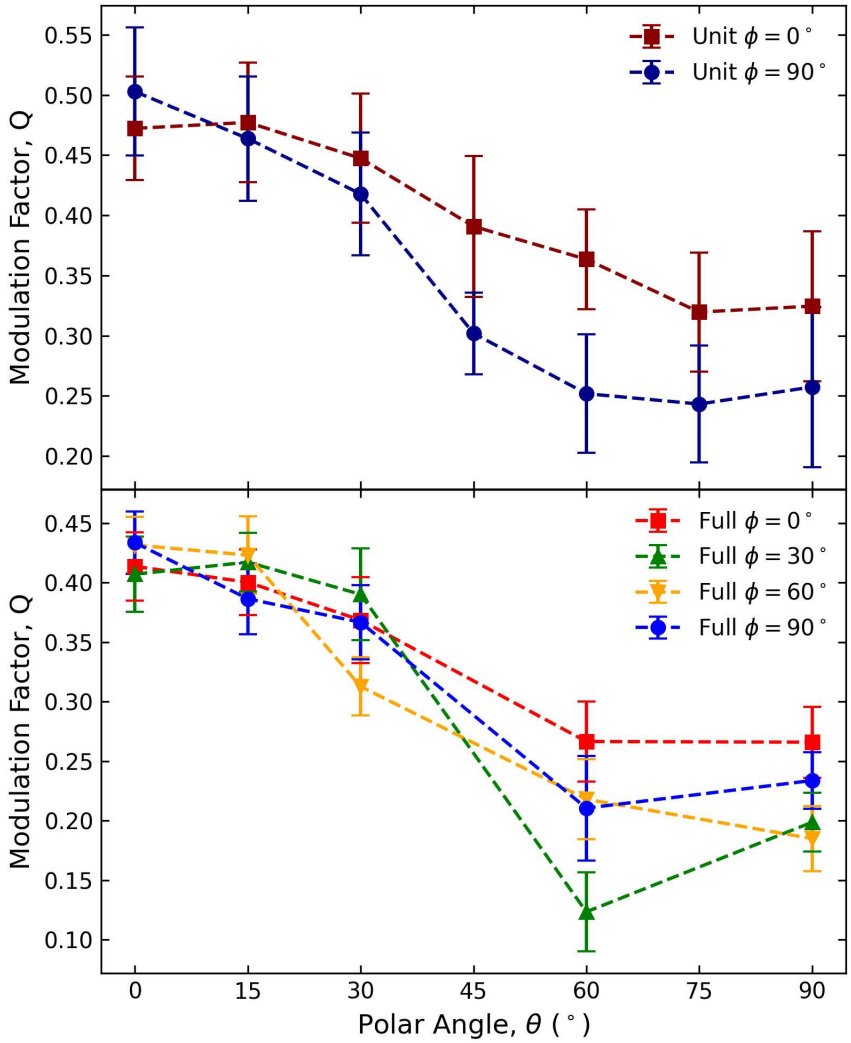

Figure 3.19: Modulation factor as a function of the source off-axis angle for a single WFM unit (top), and the full WFM (bottom). Each curve represents a different value of the source azimuth angle with respect to the lens axis.

Its afterglow was observed in different energy [Aliu et al., 2014, Levan et al., 2014, van der Horst et al., 2014] bands and remained luminous enough to be observed by NuSTAR within the 3–79 keV energy range for up to 5 days after the prompt [Kouveliotou et al., 2013]. The afterglow spectrum model is a broken power law with spectral indices -1.67 and -2.17, with a break energy of 70 keV. Instead, the temporal decay of the GRB's flux exhibited a power-law behaviour with a temporal index of -1.30. The afterglow spectra as seen by NFT, and the total flux in NFT's energy band, were evaluated using the XSPEC spectral fitting package [2] in a previous work [Ferioli, 2021], then those results were used to evaluate the MDP as function of the observation time and start time from the GRB's trigger. Results are shown in Fig. 3.20, top. Results are quite promising, however, 130427A was quite an exceptional GRB, so we also tested the case of a GRB with a more typical flux, such as 190114C. The long-lived afterglow emission of 190114C, at $z = 0.42$, was observed by different instruments, such as Fermi/GBM, Fermi/LAT, Swift/XRT, and Swift/UVOT [D'Elia et al., 2019, Gropp et al., 2019, Hamburg et al., 2019, Kocevski et al., 2019, Krimm et al., 2019]. In particular, prompt TeV emission was detected by the MAGIC detectors [MAGIC Collaboration et al., 2019]. For our analysis, we used the data detected by Swift/XRT [Beardmore, 2019], in which the energy spectrum after 150s of observation is best fitted with a broken power law with indexes -1.71 and -2.11, and a break energy of 5.52 keV, while the flux decayed as a simple power law with index -1.10. The MDP evaluated for this GRB is shown in Fig. 3.20, bottom. In this case, NFT's ability to detect the afterglow polarisation is way worse. Only for the most luminous GRBs we can expect to be able to detect the polarisation of the afterglow; however, this is still a good result since, at the time of writing, polarisation measurements of the hard X/soft gamma afterglow are still missing.

[2] https://heasarc.gsfc.nasa.gov/xanadu/xspec/

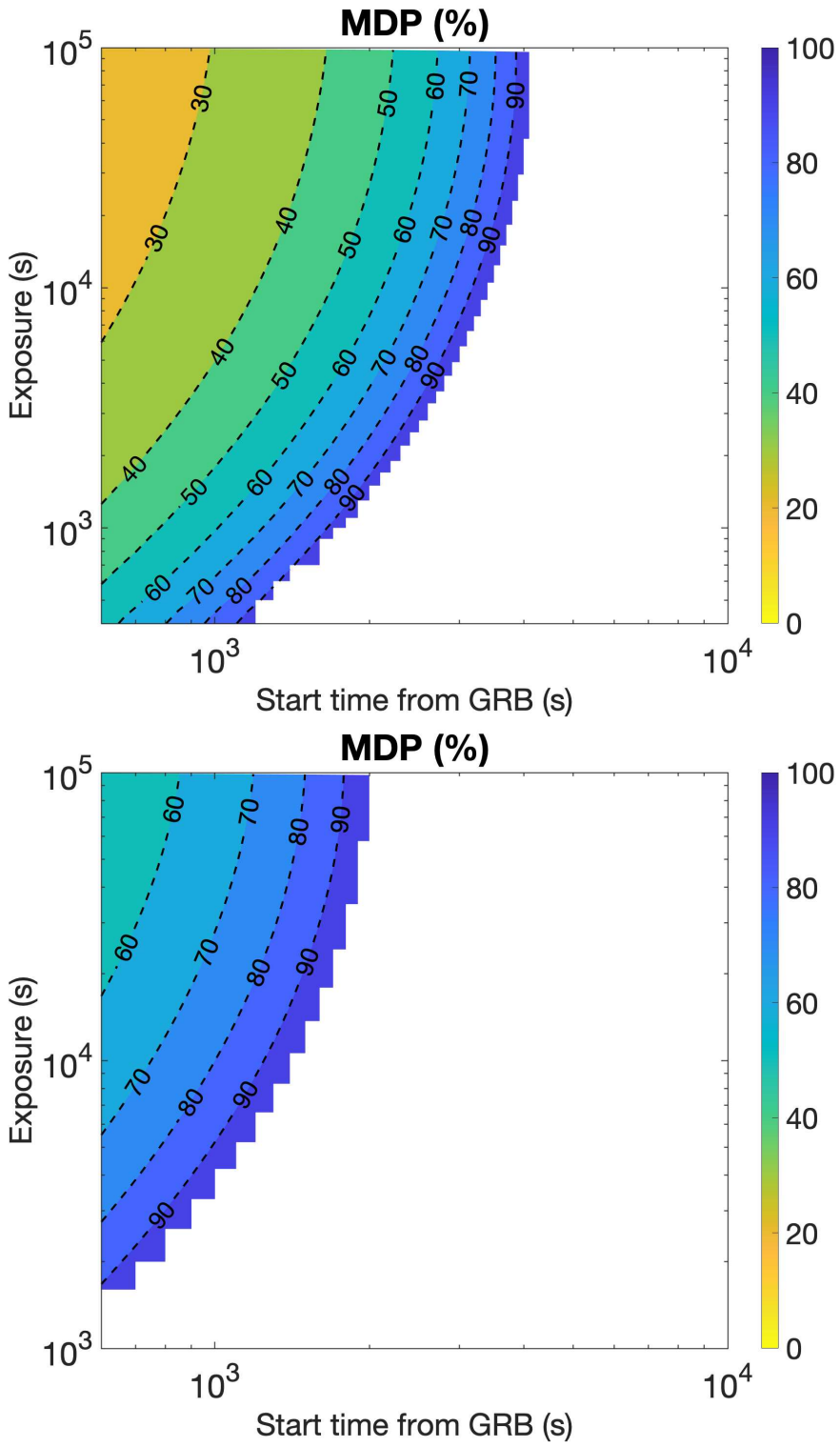

Figure 3.20: MDP vs exposure time and start time of observation with respect to the trigger for GRB130427A (top) and GRB190114C (bottom).

Chapter 4

Machine learning applied to GRBs: optimisation of light curve models

In the previous chapters, we described how we worked to advance different technologies that can be applied to high-energy astrophysics. However, methodological advancements are also needed, and we worked in this direction by searching for a new solution to a persistent challenge in GRB physics: finding a robust and reliable simulation model that can generate realistic GRB prompt emission light curves. Such a model would greatly help the experimental high-energy astrophysics community since it would make the characterisation of new missions, either nanosat spacecraft like HERMES or monolithic satellites like THESEUS, way easier and more reliable. In this chapter, we will quickly summarise the main properties of GRB light curves. Then, we will illustrate a stochastic pulse avalanche model developed during the Compton Gamma-Ray Observatory/Burst And Transient Source Experiment (CGRO/BATSE) era and how we exploited a machine-learning (ML) algorithm to optimise the parameters of the model to simulate realistic light curves. Our aim is to obtained a reliable code to simulate LCs, that we will heavily exploit to characterise ASTENA/WFM's performances.

4.1 GRB prompt light curves and their main properties

GRB prompt emission is the initial gamma-ray emission that triggers a GRB detector. It can reach an isotropic-equivalent luminosity in the range 10^{47} – 10^{54} erg/s, and a total emitted isotropic-equivalent energy from 10^{49} to 10^{55} erg [Zhang, 2019]. GRB LCs show a wide array of morphologies, ranging from highly structured curves with completely erratic behaviour, comprised by tens of overlapped pulses, to simple profiles composed by one or few pulses (Fig. 4.1, Fishman and Meegan [1995]). The pulses composing the LCs are typically described with Fast Rising, Exponential Decaying (FRED) profiles [Norris et al., 1996]. The duration of a light curve is usually defined as the time T_{90}, during which the detector collects 5% and 95% of the total fluence, and it can range from some tens of milliseconds up to several minutes. Notably, some GRBs also show a precursor emission, usually tens of seconds before the bulk emission, followed by a quiescent time before the rest of the emission [Zhang et al., 2016].

Great efforts have been made to find common properties of prompt LCs, which allowed the GRB community to understand that:

- GRB light curves are not periodic [Beloborodov et al., 1998, 2000, Guidorzi et al., 2012]. There have been indications of quasi-periodic oscillations (QPOs) in the light curves of three GRBs detected by Fermi [Guidorzi et al., 2016], one of which was also detected by Swift and XMM-Newton [Cenko et al., 2010, De Luca et al., 2010]. Additionally, two

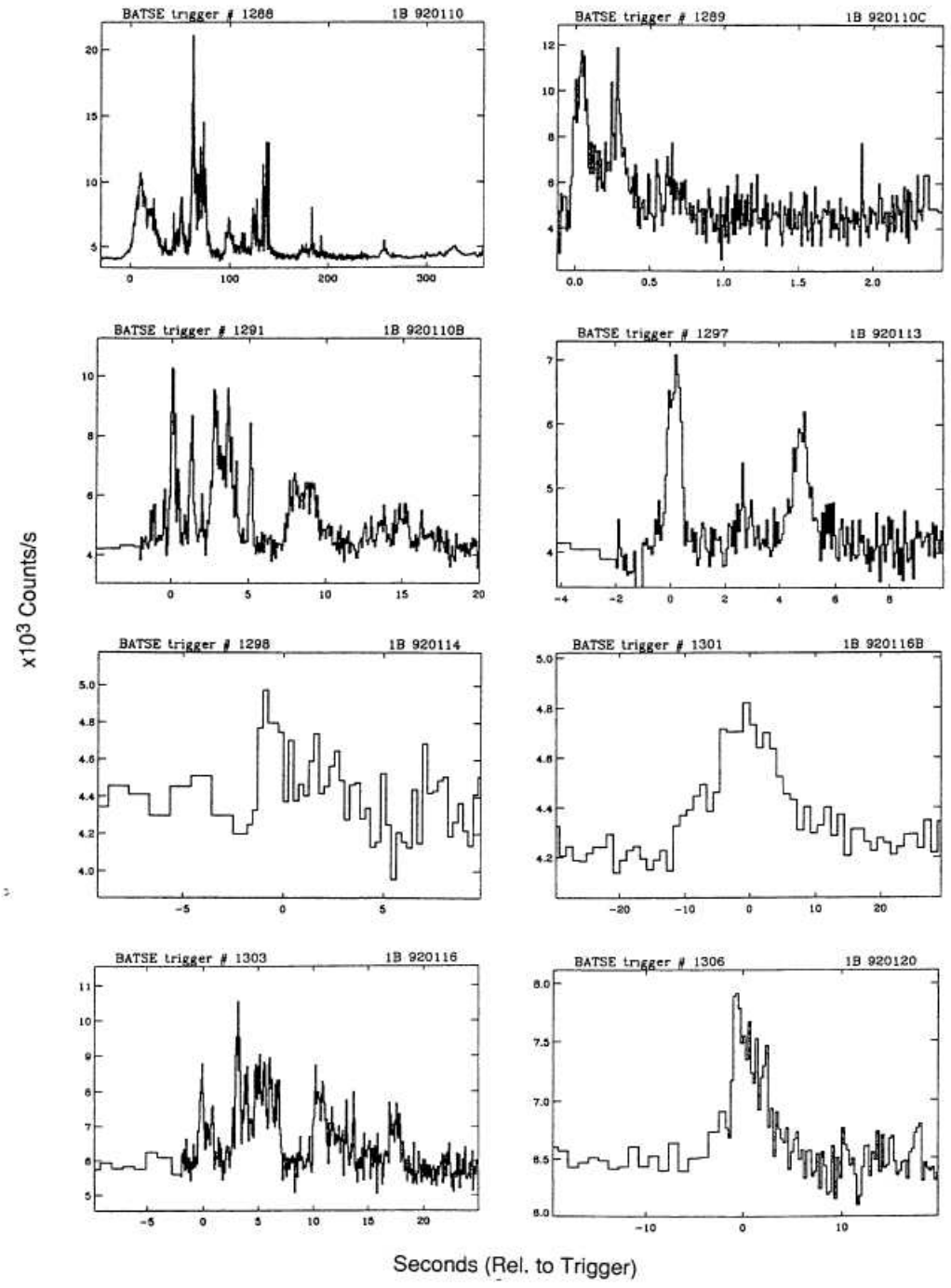

Figure 4.1: Eight different GRB prompt LCs detected by BATSE, showing very different morphologies. Reprinted from Fishman and Meegan [1995]

short GRBs in the BATSE catalogue have shown indications of QPOs [Chirenti et al., 2023], but no conclusive pieces of evidence have been found yet.

- The peak features of the LCs show a dependence on the energy: the harder the energy band, the narrower the peaks.
- For GRB detected by the CGRO/BATSE, the average power density spectrum of a large sample of bursts is a power-law with index a ∼-5/3 and a break above ∼1 Hz [Beloborodov et al., 2000]. These results were also confirmed for the GRBs detected by the Gamma-ray Burst Monitor (GRBM) onboard BeppoSAX [Dichiara et al., 2013]. In the case of the bursts detected by Swift, however, the slope of the power-law is steeper and does not show a break [Guidorzi et al., 2012, 2016].
- Typical energy spectra can be described by the Band function. This is an empirical model, consisting of two smoothly connected power-law profiles [Band et al., 1993]. In some cases, GRB prompt emission can also include a quasi-thermal component [Guiriec et al., 2011], or a power-law component extending to high energies [Ackermann et al., 2010].
- A correlation between variability and minimum variability timescale, as well as a correlation between luminosity and initial Lorentz factor of the outflow, exists (Camisasca et al. [2023] and references therein).

Nevertheless, a unifying scheme able to explain the large diversity of LCs in terms of duration, number of pulses, energy distribution, and waiting times between pulses has not been found yet. At the time of writing, the nature of the dissipation mechanism responsible for the GRB prompt emission is still an open issue. In the case of Long GRBs (LGRBs), which were the main subject of our study, the great variety observed in their LCs is thought to be the result of the variability imprinted to the relativistic outflow by the inner engine left over by the collapsar, either a millisecond magnetised neutron star or a black hole, along with the effects of the propagation of the jet within the stellar envelope [Geng et al., 2016, Gottlieb and Globus, 2021, Gottlieb et al., 2020, Morsony et al., 2010], although some models ascribe the possible presence of subsecond variability to magnetic reconnection events taking place at larger radii [Zhang and Yan, 2011].

Either way, no simulation algorithms based on those physical models can reproduce the variability and features of real LCs. This means that current physical models still lack some key elements to describe GRB physics properly. From an instrument-design point of view, this also makes characterising soft gamma-ray detectors particularly hard since we lack a way to generate realistic template GRBs to test the performances of our instrumentation. The alternative approach is using LCs detected by other instruments as a template. However, one must preliminarily filter the genuine GRB signal from the Poisson noise affecting the measurements, which cannot be rescaled for a different instrument without altering its statistical properties.

Both approaches can be pursued to obtain template LCs that can be used to test and characterise forthcoming detectors. We opted for the first solution, which is generating ex-novo light curves from a model, with the secondary aim of reviving an interesting "toy model" laid out by Stern and Svensson [1996] (hereafter SS96) exploiting modern ML algorithms. This model was also used in Greiner et al. [2022] to assess the localisation capabilities of a proposed network of GRB detectors on the global navigation satellite system Galileo G2.

SS96 proposed a stochastic process built on a pulse avalanche mechanism and tried to reproduce some of the observed properties of BATSE LCs. At that time, the cosmological distances of GRBs and the nature of the two classes of GRB progenitors were yet to be solidly established, with the first afterglow discoveries secured from 1997 [Costa et al., 1997]. By manually guessing the values of the seven model parameters, SS96 came up with a process

operating in a nearly critical regime and with a remarkably good capability of reproducing the variety of observed BATSE LCs.

To fit the parameters of the model was too complicated at the time. Nowadays, advanced statistical and ML techniques are available and could be used to fit the parameters of SS96 not only on the BATSE data, but also on different catalogues such as the one of Swift/BAT.

4.2 Light-curve simulations with a stochastic pulse avalanche process

The model proposed in Stern and Svensson [1996] is a branching process, a type of process which describes the development of a population whose members reproduce according to a random process [Harris, 1963]. It is based on the assumptions that (i) GRB LCs can be seen as different, random realisations of the same stochastic process, within narrow parameter ranges; (ii) the stochastic process is scale-invariant in time; (iii) the stochastic process works near its critical regime.

The model describes LCs as a series of primary, or "parent", pulses, which can give rise to secondary, or "child", pulses. Secondary pulses can generate further pulses until the process reaches sub-critical conditions and stops. Each pulse is described as a Norris pulse [Norris et al., 1996], a commonly used FRED profile which consists of a Gaussian rise followed by a simple exponential decay:

$$f(t) = \begin{cases} A \exp\left\{-[(t-t_p)/\tau_r]^2\right\}, & \text{for } t < t_p \\ A \exp\left\{-(t-t_p)/\tau\right\}, & \text{for } t > t_p \end{cases} \tag{4.1}$$

in which:

- t_p is the peak time.
- τ is the peak time constant.
- τ_r is a fraction of τ. For distributions of real pulses, $\tau_r \sim 0.3 - 0.5\tau$ [Norris et al., 1996]. As in SS96, we assumed $\tau_r = 0.5\tau$.
- A is a normalisation factor. SS96 performed a uniform random sample of A in the interval U[0, 1]. In our implementation, instead, each time we generate a LC we sample a value $A_{\max}$ from the distribution of the peak count rates of the real observed LCs, and then the amplitude of each pulse composing that LC is sampled in U[0, $A_{\max}$].

As described in SS96, the LC generation process works as follows:

1. A random number of parent pulses is sampled from a Poisson distribution with average value μ_0.
2. The distribution of the time constant τ_0 of each parent pulse is assumed to be of the type $p(\tau_0) \propto 1/\tau_0$. This means that the logarithm of τ_0 must be sampled uniformly between two limit values τ_{min} and τ_{max}. τ_{min} must be smaller than the simulated LC time resolution.
3. Each parent pulse gives rise to a random number of child pulses sampled from a Poisson distribution with average value μ.
4. Each child pulse is delayed with respect to its parent by a quantity Δt sampled by an exponential distribution of the type: $p(\Delta t) = 1/(\alpha\tau_0)\exp(-t/\alpha\tau_0)$, where α is a delay parameter, the same for every pulse, and τ_0 is the time constant of the parent pulse.

5. the time constant τ of each child pulse is a fraction of the time constant of their parent pulse τ_p. The quantity $\log(\tau/\tau_p)$ is sampled in a uniform probability space with limits δ_1 and δ_2, with the constraints $\delta_1 < 0$, $\delta_2 \geq 0$, $|\delta_1| > |\delta_2|$.

The process has seven free parameters: the average number of parent pulses μ_0, the average number of child pulses per parent μ, the delay parameter α, the limits of the distribution of the parents' time constants, τ_{min} and τ_{max}, and the values δ_1 and δ_2. In SS96, the authors proposed an educated guess on the value of the seven parameters based on known properties of GRB LCs, shown in Table 4.1.

In our work, we used an open source Python implementation[1] of the model by SS96, with which we generated ex-novo light curves. Then we added the effect of the simulated statistical noise of BATSE and Swift/BAT on the simulated LCs. In the case of BATSE sample, we added a uniform background noise with a rate of 2.9 cnt $s^{-1}cm^{-2}$, corresponding to the median of the value of the real BATSE LCs. Then we obtained the final LC as a Poisson realisation of the model. We then subtracted the noise level to obtain simulated background-subtracted BATSE LCs.

In the case of Swift/BAT, whose background-subtracted LCs result from the deconvolution of the detected signal with the pattern of the mask, the rate in each bin can be modelled as a Gaussian variable. We simulated BAT LCs by sampling the rates from a Gaussian distribution centred on the noise-free model, and with standard deviation randomly sampled from the distribution of errors of the real BAT LCs.

We then implemented a genetic algorithm, a type of machine learning algorithm, to optimise the value of the seven parameters of the model on both datasets.

4.3 Genetic algorithms

Genetic algorithms (GAs) are a specific type of machine learning algorithms in the family of the so-called evolutionary algorithms [Aggarwal, 2021, Hurbans, 2020, Rojas, 1996, Russell and Norvig, 2021], where a Darwinian evolution process is simulated to find the parameters that maximise a function.

In GAs, each solution to an optimisation problem can be seen as an individual, with the "fitness" of that individual being determined by the objective function value of the corresponding solution. These solutions are points in the domain of the function to be optimised.

In our work, each individual is represented by a genome made of seven genes, which are the parameters of the SS96 model. At each generation, a new set of individuals is created. Over time, the points belonging to the new generations gradually converge towards local maxima of the fitness function. The typical life cycle of a GA, made up of a succession of the so-called *generations*, includes the following steps:

1. Population initialisation: generating randomly a population of potential solutions;
2. Evaluating fitness: assessing the quality of each individual by employing a fitness function that assigns scores to evaluate their fitness;
3. Parent selection: choosing pairs of parents for reproduction based on their fitness score;
4. Offspring creation: producing offspring by combining genetic information from parents, and introducing random mutations;

[1] https://github.com/anastasia-tsvetkova/lc_pulse_avalanche

5. Generation advancement: selecting individuals and offspring from the population to progress to the next generation.

Genetic algorithms are particularly useful when no information about the function's gradient at the evaluated points is available. Indeed, GA can effectively handle functions that are not continuous or differentiable [Rojas, 1996].

In our work, we used a GA to optimise the value of the seven parameters of the model by SS96 on a both the BATSE LCs datased and the Swift/BAT LCs dataset. A similar technique, in which the parameters of a physical model were optimised through the application of a GA, was recently applied by Vargas et al. [2022] to model the shock propagation in the supernova SN2014C progenitor star and ejecta, in which the GA was used to optimise a hydrodynamic and radiation transfer model.

4.4 Process parameters optimisation and results

4.4.1 Statistical metrics

SS96 tested how their model could reproduce the properties of real LCs by comparing the ensemble-average properties of a sample of real BATSE LCs and simulated LCs. The four metrics taken into consideration are:

1. the average peak-aligned post-peak time profile [Mitrofanov, 1996], evaluated for the first 150 s after the LCs' most intense peak. This is evaluated by averaging the normalised flux of all the LCs in the sample, i.e., $\langle F/F_p \rangle$, F_p being the peak flux [Stern, 1996].

2. The average peak-aligned third moment of post-peak time profiles $\langle (F/F_p)^3 \rangle$, evaluated for the first 150 s after the peak.

3. The average auto-correlation function (ACF) of the GRBs, evaluated for time profiles subjected to Poisson noise [Link et al., 1993]. The ACF is evaluated from a minimum time lag of 0 s to a maximum of 150 s.

4. The distribution of the duration of the GRBs. SS96 defined the duration of a GRB as the interval in which the detected signal exceeds 20% of the peak counts. Henceforth, we will call this proxy of the duration $T_{20\%}$.

We integrated those metrics in the optimisation algorithm, such that the GA will search for a set of parameters which generates families of LCs whose average properties are as close as possible to the sample of real GRBs with which they are compared.

4.4.2 Sample Selection

The GA needs to compare the generated families of LCs with a reference family, which, in our case, is constituted by a sample of real BATSE LCs, or real Swift/BAT LCs.

Unlike SS96, we restrict our analysis to long GRBs, whose progenitor is thought to be a collapsar, to preserve the homogeneity of the putative GRB inner engines as much as possible. For $\sim 30\%$ of the *Swift* sample with measured redshift, it is possible to carry out the same analysis in the GRB rest frame. However, we did not consider this option, since the cosmological dilation correction by (1 + z) is partly counteracted by other energy-dependent effects, which make the final correction milder and less obvious (Camisasca et al. [2023] and references therein).

The BATSE sample is a selection of 64-ms time profiles that were made available by the BATSE team[2] contained in the BATSE 4B catalogue [Paciesas et al., 1999]. The GRBs were observed with the BATSE eight Large Area Detectors (LADs) and the data are the result of a concatenation of three standard BATSE types: DISCLA, PREB, and DISCSC, available in four energy channels: 25–55, 55–110, 110–320, and > 320 keV. We used the total passband LCs. For each GRB, the background was interpolated with polynomials of up to fourth degree, and we used the background-subtracted LCs in our analysis.

From an initial sample of 2024 GRBs we selected only those that satisfy the following requirements:

- $T_{90} > 2$ s, that is, only long GRBs;
- data available for at least 150 s after the brightest peak;
- signal-to-noise ratio of the total net counts within the duration of the event greater than 70. This value was chosen as a trade-off between the number of GRBs and the statistical quality of the LCs in the sample.

Following the definition of duration of SS96, we evaluated the S2N in $T_{20\%}$ interval, instead of the typical used T_{90}. Before evaluating the $T_{20\%}$, the LCs were first filtered with a Savitzky-Golay smoothing filter [Savitzky and Golay, 1964], using a moving window of size $T_{90}/15$. Accordingly, we defined the S2N of a GRB as the sum of the net counts in the whole $T_{20\%}$ interval, divided by the corresponding error. We ended up with 585 long GRBs satisfying the aforementioned properties.

We also considered a second dataset made by Swift/BAT LCs detected from January 2005 to November 2023. BAT data are available in four energy channels (15–25, 25–50, 50–100 and 100–150 keV). We used the total passband LCs, with 64–ms bin time. The LCs are mask-weighted background-subtracted LCs, obtained following the standard procedure recommended by the BAT team.[3] From an initial sample of 1389 GRBs observed in burst mode, 531 passed the selection based on the same criteria adopted for BATSE, except for the value of the S2N threshold, which was lowered to 15 to obtain a sample of size comparable to the BATSE one, but still ensuring the required statistical quality.

4.4.3 Genetic algorithm optimisation

We implemented the genetic algorithm using the `PyGAD`[4] library, an open-source Python library which implements several machine learning algorithms [Gad, 2023]. The seven parameters to be optimised were constrained within the intervals in Table 4.1.

The GA generates a number $N_{\rm gen}$ of generations, each consisting of a population with $N_{\rm pop} = 2000$ individual sets of the seven parameters. Each set of parameters, hereafter referred to as an individual, is used to generate $N_{\rm grb} = 2000$ LCs. For each of the $N_{\rm pop}$ individuals, we evaluate the statistical metrics over the corresponding $N_{\rm grb}$ LCs and compare them with the values obtained from the real datasets by computing the $L2$ loss between these four observables. The average of these quantities is the final loss associated with a given individual.

Then, the individuals are ranked based on their loss, and the next generation is obtained by mixing the value of the seven parameters, i.e. the "genes" of the evolution process, of the

[2] https://heasarc.gsfc.nasa.gov/FTP/compton/data/batse/ascii_data/64ms/
[3] https://swift.gsfc.nasa.gov/analysis/threads/bat_threads.html.
[4] https://github.com/ahmedfgad/GeneticAlgorithmPython

Parameter	Lower bound	Upper bound	SS96
μ	0.80	1.7	1.20
μ_0	0.80	1.7	1.00
α	1	15	4.00
δ_1	-1.5	-0.30	-0.5
δ_2	0	0.30	0
$\tau_{\rm min}$	0.01 s	`bin_time` s	0.02 s
$\tau_{\rm max}$	1 s	50 s	26.0 s

Table 4.1: Region of exploration during the GA optimisation and educated guess by SS96 of the seven parameters of stochastic pulse avalanche model.

fittest individuals in the current generation. We set the elitism[5] to zero, then the offsprings are obtained by randomly sampling two individuals among the top 15% in the current generation, and assigning to each parameter in the seven parameters set the value of one of the two parents, with equal probability.

We set a 4% probability of random mutation, which means that, during the mating step, each of the seven parameters has this probability of undergoing mutation. This means that its value is not inherited from one of the parents but instead randomly sampled from the parameter's exploration range. The optimisation process stops when the loss and, thus, the value of the seven parameters reach convergence. The GA ran for 30 generations on both the BATSE and the Swift sample.

4.4.4 Optimisation results

The results of our GA optimisation on the BATSE and Swift/BAT dataset compared with the seven parameter values suggested by SS96 are shown in Table 4.2. We also indicate the achieved values of the loss function evaluated on the training set (both in terms of the best parameter configuration and by averaging on the corresponding population) as well as on a test set of 5000 simulated GRB LCs obtained with the optimised parameters. The individual contribution of each metric to the test loss is also indicated.

The final optimised values of the seven parameters are obtained by taking the median value in the whole population of the last GA generation. The uncertainty in the values of the parameters is estimated at the 1σ level.

Figure 4.2 displays the comparison of the four observables between the simulated and the real BATSE curves. In particular, the panels show the average profiles obtained from the 585 useful BATSE events (blue), the ones estimated from 5000 simulated GRBs with optimised parameters (red), and the ones estimated from 5000 LCs simulated using the parameter values guessed by SS96 (green). Figure 4.3 shows the analogous comparison between the simulated and the real Swift curves.

We find an excellent agreement for three out of the four metrics computed from real and simulated BATSE LCs, in particular for the average post-peak time profile, its third moment, and the average auto-correlation, whose $L2$ loss values are smaller than the corresponding ones estimated with SS96 non-optimised parameters. The $T_{20\%}$ distribution holds the most significant contribution to the loss, yet it slightly improves the SS96 performance. Compared with SS96, our GA-optimised results on BATSE data better reproduce the observed distributions.

[5]The elitism is defined as the percentage of the fittest individuals which are passed to the next generation without undergoing the mating process.

Parameter	SS96	BATSE	Swift/BAT
μ	1.20	$1.10^{+0.03}_{-0.02}$	$1.34^{+0.03}_{-0.02}$
μ_0	1.00	$0.91^{+0.06}_{-0.07}$	$1.16^{+0.18}_{-0.10}$
α	4.00	$2.57^{+0.07}_{-0.52}$	$2.53^{+0.25}_{-0.01}$
δ_1	-0.50	$-1.28^{+0.16}_{-0.05}$	$-0.75^{+0.11}_{-0.29}$
δ_2	0	$0.28^{+0.01}_{-0.03}$	$0.27^{+0.01}_{-0.02}$
$\tau_{\rm min}$	0.02 s	$0.02^{+0.02}_{-0.01}$ s	$0.03^{+0.02}_{-0.02}$ s
$\tau_{\rm max}$	26.0 s	$40.2^{+0.9}_{-1.2}$ s	$56.8^{+0.4}_{-1.3}$ s
Loss (*Train* best)	–	0.72	0.38
Loss (*Train* avg.)	–	0.98	0.66
Loss (*Test*)	1.47	0.88	0.56
Loss (*Test*: $\langle F/F_p \rangle$)	1.01	0.67	0.46
Loss (*Test*: $\langle (F/F_p)^3 \rangle$)	0.40	0.20	0.20
Loss (*Test*: $\langle$ACF$\rangle$)	2.24	0.64	0.49
Loss (*Test*: $T_{20\%}$)	2.22	2.04	1.08

Table 4.2: Results of the GA optimisation on the BATSE and Swift datasets. Col. 2 presents the parameters given by SS96 (for the BATSE dataset), while Col. 3 and Col. 4 show the optimised ones obtained after 30 generations of the GA for BATSE and Swift/BAT, respectively. From the distribution of the seven parameters in the last generation we estimated their best-fitting values as the median, and their corresponding errors as the 16-th and 84-th percentiles. "Train best" is the loss of the best generation, while "Train avg." is the average loss in the last generation. The test set is a newly produced set of 5000 simulated LCs; the last four rows show all the single contributions to the "Test" loss.

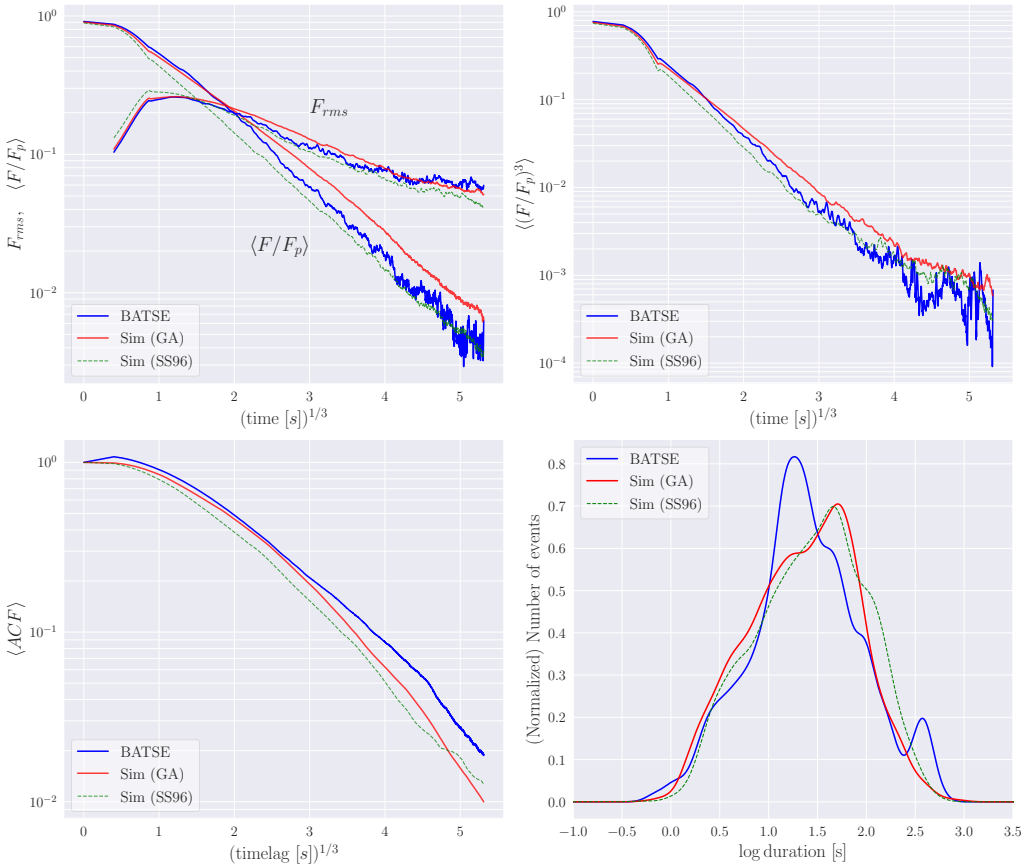

Figure 4.2: Average distributions of real (blue) and GA-optimised simulated (red) BATSE GRB profiles. For comparison, the analogous distributions of simulated profiles assuming the SS96 parameters are also shown (green). *Top left*: average peak-aligned post-peak normalised time profile, $\langle F/F_p \rangle$ vs. $t^{1/3}$, in the time range 0–150 s after the highest peak. The curve labelled $F_{\rm rms}$ instead is the r.m.s. deviation of the individual peak-aligned time profiles, $F_{\rm rms} \equiv \left[\langle (F/F_p)^2 \rangle - \langle F/F_p \rangle^2\right]^{1/2}$. *Top right*: average peak-aligned third moment test, $\langle (F/F_p)^3 \rangle$ vs. $t^{1/3}$. *Bottom left*: Average ACF of the GRBs, evaluated for time-lags in the interval 0–150 s. *Bottom right*: distribution of duration, measured at a level of 20% of the peak amplitude ($T_{20\%}$). In *top left* and *top right* panels, both real and simulated averaged curves were smoothed with a Savitzky-Golay filter (filter window of 21 bins) to reduce the effect of Poisson noise.

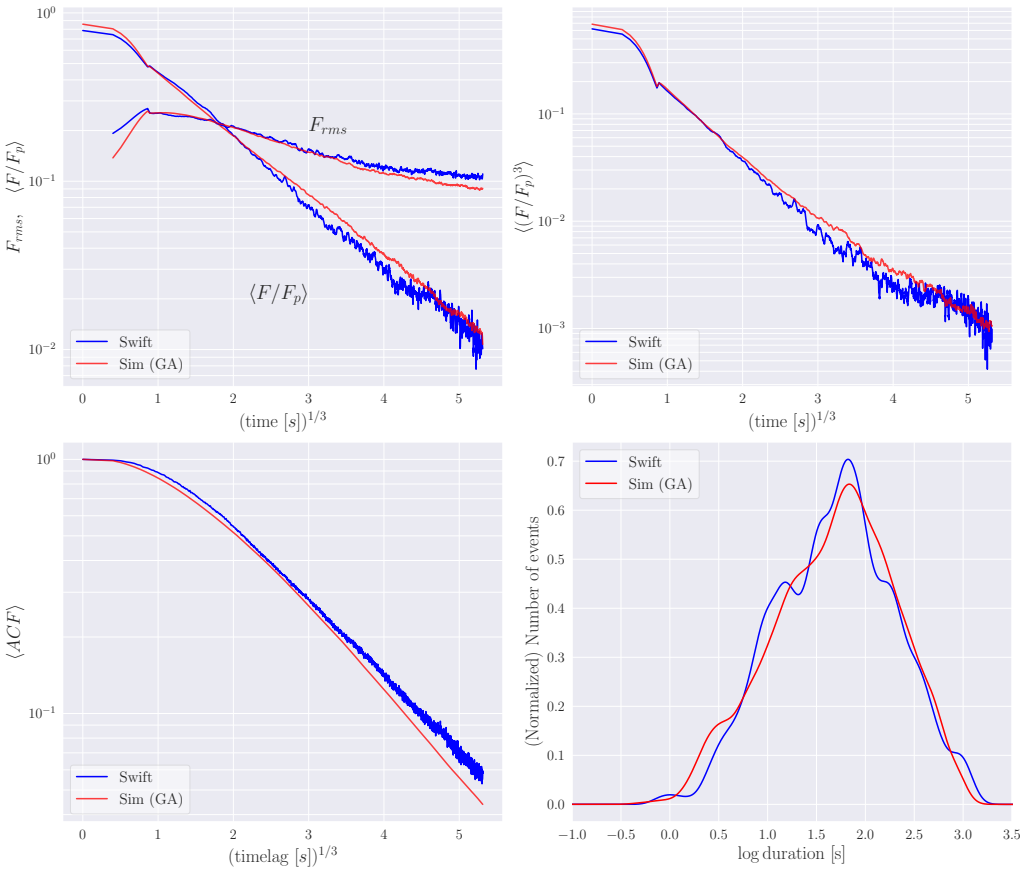

Figure 4.3: Comparison between the real Swift/BAT dataset and the corresponding simulated dataset on the same four metrics defined for the BATSE dataset, analogously to Figure 4.2.

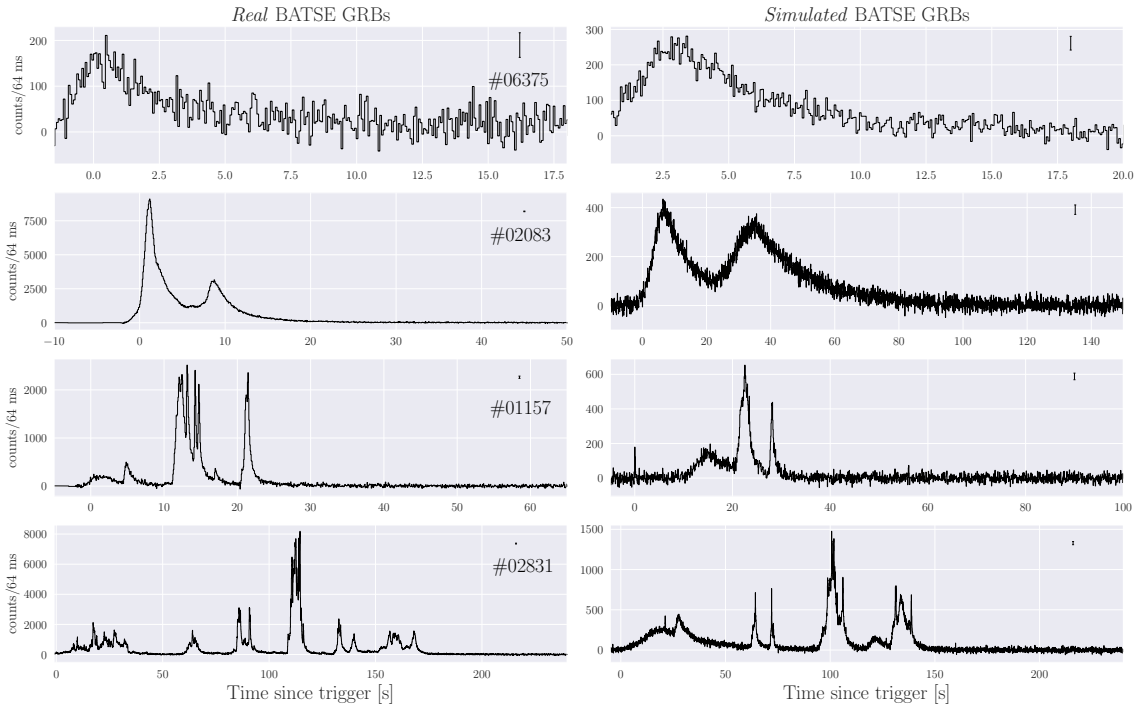

Figure 4.4: Four examples of as many classes of GRB LCs from the BATSE real sample (*left*) along with their trigger number, and the corresponding simulated one (*right*). Following the same qualitative classification adopted by SS96, from top to bottom the four classes are "single pulse", "blending of some pulses", "moderately structured", and "highly erratic". On the top right of each subplot is shown the average error on the counts of the corresponding LC.

The avalanche model appears to work well even in the case of Swift data: the results on the average ACF and third moment of peak-aligned profiles are comparably good, whereas the average peak-aligned profile and duration distributions are further improved with respect to the BATSE case.

Notably, the sets of best-fitting parameters optimised on the BATSE sample are not too different from the one guessed by SS96. The parameters whose optimised value differ most from SS96 are (δ_1, δ_2), $\tau_{\max}$, and α. The former pairs define the child-to-parent pulse duration ratio, and we can see that our values turn into broader dynamical ranges than SS96, instead, our best-fit values for α, which rules the time delay between parent and child, lean towards slightly shorter intervals than SS96. Finally, Fig. 4.4 presents the comparison of four real BATSE time profiles with four simulated LCs of similar morphology and complexity, sampled from the test set, generated using the best-fitting set of BATSE model parameters given above. Those results are quite remarkable, and for the first time in the GRB literature, we implemented and tested an ML technique to optimise the parameter of a stochastic model able to generate ex-novo realistic LCs.

This model allows us to simulate ex-novo realistic GRB profiles that can be used for the study of future experiments, such as HERMES, THESEUS/XGIS or ASTENA/WFM, avoiding the risk that arises from using renormalised LCs observed with other instruments.

This work showcases not only the potential of a simple toy model like the avalanche one conceived by SS96 but also how useful ML techniques can be for GRB studies. To further optimise the model, we will test the possibility of adding other metrics, such as the average number of peaks as a function, or the observed distribution of the number of peaks per GRB [Guidorzi et al., 2024], to study in more detail the dependence of the model parameters on the energy channels, and to carry out the same study in the comoving frame of a sample of GRBs with known redshift,

assuming the luminosity and released energy distributions of individual pulses [Maccary et al., 2024]. These efforts should end up with a reliable and accessible machine for simulating credible LGRB profiles with any experiment. Once the parameter of the pulse avalanche model will be properly calibrated, we will exploit our code to simulate realistic prompt GRB light-curves and test ASTENA/WFM's performances as a GRB monitor.

A paper summarising this work was submitted to Astronomy & Astrophysics, while the source code of our algorithm will be publicly released on GitHub[6]. The appendix contains the preprint version of the paper, as submitted to A&A.

[6] https://github.com/LBasz/geneticgrbs

Conclusions

This work has focused new technological and methodological advancements in the high-energy astrophysics domain to increase the breadth of outstanding scientific questions to be addressed by the high-energy astrophysics community.

We specifically aimed to advance the technology necessary to develop the ASTENA mission concept, by exploring new techniques to build a Laue lens and to advance the simulation software tools to characterise the satellite's performances. Our main results can be quickly summarised in the following points:

- we contributed to the **advancement of the Laue lens technology** by developing a technique to build long focal Laue lenses based on bent crystals bonded to a substrate with a UV adhesive. We built and tested a small Laue lens prototype made of eleven germanium(220) crystals, bent in a self-standing way, bonded on a quartz substrate with a UV-cured, low-shrinkage glue. We aimed to reach a positional accuracy of the crystals <15 arcsec on the Bragg's and polar angles of the crystal. We reached a positional accuracy on the Bragg's angle of 50 ± 25 arcsec and an accuracy on the polar angle of 1.0 ± 1.5 arcsec. We then validated the Laue lens simulation model developed at the University of Ferrara by simulating the experimental configuration of the prototype. We verified that the model can reproduce the results obtained at the LARIX laboratory. Finally, we used the simulation model to extrapolate the measured performances to a whole Laue lens assembly. We obtained a PSF half power diameter for a full Laue lens working in the energy range 100 keV - 500 keV of 289 ± 4 arcsec.

  This is still not at the level of accuracy required for ASTENA, for which we set an ambitious requirement of an angular resolution <30 arcsec over all its energy band; however, it can be a starting point for the study of smaller Laue lens-based spectrometers and polarimeters. In any case, we are working on further reducing the assembly error obtained by exploring different bonding and alignment techniques to increase the technological readiness of Laue lenses.

- We performed an extensive **polarimetric characterisation study of ASTENA/WFM and ASTENA/NFT**. Within this study, we defined the instruments' physical models, optimised the configuration of the focal plane detector of the Narrow Field Telescope onboard ASTENA, and developed a flexible Python analysis tool which can be easily adapted to different detector configurations. We evaluated the instruments' quality as Compton polarimetry in terms of their modulation factor, detection efficiency and polarisation reconstruction capabilities. We also used the physical models to evaluate the effective area as a function of the energy of ASTENA/WFM, the WFM response for off-axis sources, and the expected background for both instruments based on physical models defined in the literature. Then, we evaluated the polarimetric performances of WFM and NFT for the scientific cases of pulsars, magnetars and GRB events.

  We observed that the NFT works best in the 100-300 keV energy range, while the WFM

performs optimally in the 200 keV - 1 MeV range. These two instruments are complementary and can be used together to study persistent sources across a broad energy spectrum. For a source similar to the Crab Nebula, the NFT can detect polarisation with a minimum detectable level of less than 7% up to 300 keV, which then degrades to less than 40% up to the limits of its passband (observation time = 100 ks). On the other hand, the WFM can detect polarisation with a minimum detectable level of less than 2% up to 800 keV, which then degrades to less than 20% up to 2 MeV (observation time = 100 ks). The WFM performs better than the NFT due to its larger effective area, essential for collecting enough photons to perform polarimetric measurements.

- Finally, we developed an innovative **simulation model for GRB prompt emission light curves** based on a stochastic pulse avalanche model optimised through a genetic algorithm. We optimised a stochastic model created during the BATSE experiment era to generate ex-novo long GRB light curves whose characteristics are compatible with the light curves detected by BATSE and by the BAT instrument onboard Swift. Following the authors of the model, the similarity between the generated LCs and the real LCs has been evaluated based on four metrics: the average normalised post-peak profile of the population, the third moment of the post-peak profile, the average autocorrelation function and the distribution of the durations. We saw that the model optimised through our genetic algorithm performs very well, meaning that the population generated by the pulse avalanche model with the optimised parameters is similar in terms of the four metrics to the real populations of the long GRBs in the catalogues of BATSE and BAT.

  The model is already capable of simulating ex-novo light curves that, once the effect of the instrumental noise is added, are remarkably similar to real light curves of BATSE and BAT. Our next step is to refine the optimisation process further by adding additional metrics and studying the model in the comoving frame of GRBs with known redshift. In particular, we want to implement a fifth metric to enforce that the population of GRBs produced by the pulse avalanche algorithm is compatible with the real population in terms of signal-to-noise. Ultimately, we will end up with an accessible and reliable code that will be made public and allow us, and the whole GRB community, to quickly produce GRB light curves to simulate instrument performances, test data analysis algorithms, and investigate GRB physics from a stochastic perspective.

This thesis has led to the development of new technology for high-energy astrophysics and paved the way for the realisation of innovative soft gamma-ray optics and their application on the ASTENA mission concept. Our plans for the future are to push further the limits we obtained for Laue lens optics by testing new, state-of-the-art bonding technologies based on anodic bonding techniques. In the meantime, we will study the possible applications of Laue lenses to short and mid-term small missions devoted to soft gamma spectroscopy and polarimetry. Finally, we will maintain and upgrade the polarimetric analysis software and the GRB simulation software developed and used in the contest of this work. Both software are open-source and can be used by the whole high-energy community.

We are currently living in an exciting time for high-energy astrophysics with the beginning of the multi-messenger era, advancements in X-ray polarimetry, and the emergence of new satellite and nanosatellite missions. Ultimately, this thesis is the result of our best efforts to keep up with the constant demand for instrumentation progress and prepare ourselves for the upcoming era of discoveries in the high-energy field.

Bibliography

E. Abbe Hon. Vii.—on the estimation of aperture in the microscope. Journal of the Royal Microscopical Society, 1(3):388–423, 1881. doi: https://doi.org/10.1111/j.1365-2818.1881.tb05909.x. URL https://onlinelibrary.wiley.com/doi/abs/10.1111/j.1365-2818.1881.tb05909.x.

L. Abbene, G. Gerardi, F. Principato, A. Buttacavoli, S. Altieri, N. Protti, E. Tomarchio, S. Del Sordo, N. Auricchio, M. Bettelli, N. S. Amadè, S. Zanettini, A. Zappettini, and E. Caroli. Recent advances in the development of high-resolution 3D cadmium–zinc–telluride drift strip detectors. Journal of Synchrotron Radiation, 27(6):1564–1576, Nov 2020. doi: 10.1107/S1600577520010747. URL https://doi.org/10.1107/S1600577520010747.

B. P. Abbott, R. Abbott, T. D. Abbott, F. Acernese, K. Ackley, C. Adams, T. Adams, P. Addesso, R. X. Adhikari, and e. a. Adya. Multi-messenger Observations of a Binary Neutron Star Merger. ApJ, 848(2):L12, Oct. 2017. doi: 10.3847/2041-8213/aa91c9.

H. Abe, T. Akutsu, M. Ando, A. Araya, N. Aritomi, H. Asada, and e. a. Aso. The Current Status and Future Prospects of KAGRA, the Large-Scale Cryogenic Gravitational Wave Telescope Built in the Kamioka Underground. Galaxies, 10(3):63, Apr. 2022. doi: 10.3390/galaxies10030063.

M. Ackermann, K. Asano, W. B. Atwood, M. Axelsson, L. Baldini, J. Ballet, G. Barbiellini, M. G. Baring, D. Bastieri, K. Bechtol, R. Bellazzini, B. Berenji, P. N. Bhat, E. Bissaldi, R. D. Blandford, E. D. Bloom, E. Bonamente, A. W. Borgland, A. Bouvier, J. Bregeon, A. Brez, M. S. Briggs, M. Brigida, P. Bruel, S. Buson, G. A. Caliandro, R. A. Cameron, P. A. Caraveo, S. Carrigan, J. M. Casandjian, C. Cecchi, Ö. Çelik, E. Charles, J. Chiang, S. Ciprini, R. Claus, J. Cohen-Tanugi, V. Connaughton, J. Conrad, C. D. Dermer, F. de Palma, B. L. Dingus, E. d. C. e. Silva, P. S. Drell, R. Dubois, D. Dumora, C. Farnier, C. Favuzzi, S. J. Fegan, J. Finke, W. B. Focke, M. Frailis, Y. Fukazawa, P. Fusco, F. Gargano, D. Gasparrini, N. Gehrels, S. Germani, N. Giglietto, F. Giordano, T. Glanzman, G. Godfrey, J. Granot, I. A. Grenier, M. H. Grondin, J. E. Grove, S. Guiriec, D. Hadasch, A. K. Harding, E. Hays, D. Horan, R. E. Hughes, G. Jóhannesson, W. N. Johnson, T. Kamae, H. Katagiri, J. Kataoka, N. Kawai, R. M. Kippen, J. Knödlseder, D. Kocevski, C. Kouveliotou, M. Kuss, J. Lande, L. Latronico, M. Lemoine-Goumard, M. Llena Garde, F. Longo, F. Loparco, B. Lott, M. N. Lovellette, P. Lubrano, A. Makeev, M. N. Mazziotta, J. E. McEnery, S. McGlynn, C. Meegan, P. Mészáros, P. F. Michelson, W. Mitthumsiri, T. Mizuno, A. A. Moiseev, C. Monte, M. E. Monzani, E. Moretti, A. Morselli, I. V. Moskalenko, S. Murgia, H. Nakajima, T. Nakamori, P. L. Nolan, J. P. Norris, E. Nuss, M. Ohno, T. Ohsugi, N. Omodei, E. Orlando, J. F. Ormes, M. Ozaki, W. S. Paciesas, D. Paneque, J. H. Panetta, D. Parent, V. Pelassa, M. Pepe, M. Pesce-Rollins, F. Piron, R. Preece, S. Rainò, R. Rando, M. Razzano, S. Razzaque, A. Reimer, S. Ritz, A. Y. Rodriguez, M. Roth, F. Ryde, H. F. W. Sadrozinski, A. Sander, J. D. Scargle, T. L. Schalk, C. Sgrò, E. J. Siskind, P. D. Smith, G. Spandre, P. Spinelli, M. Stamatikos, F. W. Stecker,

M. S. Strickman, D. J. Suson, H. Tajima, H. Takahashi, T. Takahashi, T. Tanaka, J. B. Thayer, J. G. Thayer, D. J. Thompson, L. Tibaldo, K. Toma, D. F. Torres, G. Tosti, A. Tramacere, Y. Uchiyama, T. Uehara, T. L. Usher, A. J. van der Horst, V. Vasileiou, N. Vilchez, V. Vitale, A. von Kienlin, A. P. Waite, P. Wang, C. Wilson-Hodge, B. L. Winer, X. F. Wu, R. Yamazaki, Z. Yang, T. Ylinen, and M. Ziegler. Fermi Observations of GRB 090510: A Short-Hard Gamma-ray Burst with an Additional, Hard Power-law Component from 10 keV TO GeV Energies. ApJ, 716(2):1178–1190, June 2010. doi: 10.1088/0004-637X/716/2/1178.

M. Ackermann, M. Ajello, K. Asano, W. B. Atwood, M. Axelsson, L. Baldini, J. Ballet, G. Barbiellini, M. G. Baring, D. Bastieri, K. Bechtol, R. Bellazzini, E. Bissaldi, E. Bonamente, J. Bregeon, M. Brigida, P. Bruel, R. Buehler, J. M. Burgess, S. Buson, G. A. Caliandro, R. A. Cameron, P. A. Caraveo, C. Cecchi, V. Chaplin, E. Charles, A. Chekhtman, C. C. Cheung, J. Chiang, G. Chiaro, S. Ciprini, R. Claus, W. Cleveland, J. Cohen-Tanugi, A. Collazzi, L. R. Cominsky, V. Connaughton, J. Conrad, S. Cutini, F. D'Ammando, A. de Angelis, M. DeKlotz, F. de Palma, C. D. Dermer, R. Desiante, A. Diekmann, L. Di Venere, P. S. Drell, A. Drlica-Wagner, C. Favuzzi, S. J. Fegan, E. C. Ferrara, J. Finke, G. Fitzpatrick, W. B. Focke, A. Franckowiak, Y. Fukazawa, S. Funk, P. Fusco, F. Gargano, N. Gehrels, S. Germani, M. Gibby, N. Giglietto, M. Giles, F. Giordano, M. Giroletti, G. Godfrey, J. Granot, I. A. Grenier, J. E. Grove, D. Gruber, S. Guiriec, D. Hadasch, Y. Hanabata, A. K. Harding, M. Hayashida, E. Hays, D. Horan, R. E. Hughes, Y. Inoue, T. Jogler, G. Jóhannesson, W. N. Johnson, T. Kawano, J. Knödlseder, D. Kocevski, M. Kuss, J. Lande, S. Larsson, L. Latronico, F. Longo, F. Loparco, M. N. Lovellette, P. Lubrano, M. Mayer, M. N. Mazziotta, J. E. McEnery, P. F. Michelson, T. Mizuno, A. A. Moiseev, M. E. Monzani, E. Moretti, A. Morselli, I. V. Moskalenko, S. Murgia, R. Nemmen, E. Nuss, M. Ohno, T. Ohsugi, A. Okumura, N. Omodei, M. Orienti, D. Paneque, V. Pelassa, J. S. Perkins, M. Pesce-Rollins, V. Petrosian, F. Piron, G. Pivato, T. A. Porter, J. L. Racusin, S. Rainò, R. Rando, M. Razzano, S. Razzaque, A. Reimer, O. Reimer, S. Ritz, M. Roth, F. Ryde, A. Sartori, P. M. S. Parkinson, J. D. Scargle, A. Schulz, C. Sgrò, E. J. Siskind, E. Sonbas, G. Spandre, P. Spinelli, H. Tajima, H. Takahashi, J. G. Thayer, J. B. Thayer, D. J. Thompson, L. Tibaldo, M. Tinivella, D. F. Torres, G. Tosti, E. Troja, T. L. Usher, J. Vandenbroucke, V. Vasileiou, G. Vianello, V. Vitale, B. L. Winer, K. S. Wood, R. Yamazaki, G. Younes, H. F. Yu, S. J. Zhu, P. N. Bhat, M. S. Briggs, D. Byrne, S. Foley, A. Goldstein, P. Jenke, R. M. Kippen, C. Kouveliotou, S. McBreen, C. Meegan, W. S. Paciesas, R. Preece, A. Rau, D. Tierney, A. J. van der Horst, A. von Kienlin, C. Wilson-Hodge, S. Xiong, G. Cusumano, V. La Parola, and J. R. Cummings. Fermi-LAT Observations of the Gamma-Ray Burst GRB 130427A. Science, 343(6166):42–47, Jan. 2014. doi: 10.1126/science.1242353.

C. C. Aggarwal. Artificial Intelligence: A Textbook. Springer, 2021.

I. Ahmad, J. P. Greene, E. F. Moore, S. Ghelberg, A. Ofan, M. Paul, and W. Kutschera. Improved measurement of the ^{44}Ti half-life from a 14-year long study. Phys. Rev. C, 74:065803, Dec 2006. doi: 10.1103/PhysRevC.74.065803. URL https://link.aps.org/doi/10.1103/PhysRevC.74.065803.

M. Ajello, M. Arimoto, M. Axelsson, L. Baldini, G. Barbiellini, D. Bastieri, R. Bellazzini, P. N. Bhat, E. Bissaldi, R. D. Blandford, R. Bonino, J. Bonnell, E. Bottacini, J. Bregeon, P. Bruel, R. Buehler, R. A. Cameron, R. Caputo, P. A. Caraveo, E. Cavazzuti, S. Chen, C. C. Cheung, G. Chiaro, S. Ciprini, D. Costantin, M. Crnogorcevic, S. Cutini, M. Dainotti, F. D'Ammando, P. de la Torre Luque, F. de Palma, A. Desai, R. Desiante, N. Di Lalla, L. Di Venere, F. Fana Dirirsa, S. J. Fegan, A. Franckowiak, Y. Fukazawa, S. Funk, P. Fusco, F. Gargano, D. Gasparrini, N. Giglietto, F. Giordano, M. Giroletti, D. Green, I. A. Grenier, J. E. Grove, S. Guiriec, E. Hays, J. W. Hewitt, D. Horan, G. Jóhannesson, D. Kocevski, M. Kuss, L. Latronico, J. Li,

F. Longo, F. Loparco, M. N. Lovellette, P. Lubrano, S. Maldera, A. Manfreda, G. Martí-Devesa, M. N. Mazziotta, I. Mereu, M. Meyer, P. F. Michelson, N. Mirabal, W. Mitthumsiri, T. Mizuno, M. E. Monzani, E. Moretti, A. Morselli, I. V. Moskalenko, M. Negro, E. Nuss, M. Ohno, N. Omodei, M. Orienti, E. Orlando, M. Palatiello, V. S. Paliya, D. Paneque, M. Persic, M. Pesce-Rollins, V. Petrosian, F. Piron, S. Poolakkil, H. Poon, T. A. Porter, G. Principe, J. L. Racusin, S. Rainò, R. Rando, M. Razzano, S. Razzaque, A. Reimer, O. Reimer, T. Reposeur, F. Ryde, D. Serini, C. Sgrò, E. J. Siskind, E. Sonbas, G. Spandre, P. Spinelli, D. J. Suson, H. Tajima, M. Takahashi, D. Tak, J. B. Thayer, D. F. Torres, E. Troja, J. Valverde, P. Veres, G. Vianello, A. von Kienlin, K. Wood, M. Yassine, S. Zhu, and S. Zimmer. A Decade of Gamma-Ray Bursts Observed by Fermi-LAT: The Second GRB Catalog. ApJ, 878(1):52, June 2019. doi: 10.3847/1538-4357/ab1d4e.

A. Alexis, P. Jean, P. Martin, and K. Ferrière. Monte Carlo modelling of the propagation and annihilation of nucleosynthesis positrons in the Galaxy. A&A, 564:A108, Apr. 2014. doi: 10.1051/0004-6361/201322393.

E. Aliu, T. Aune, A. Barnacka, M. Beilicke, W. Benbow, K. Berger, J. Biteau, J. H. Buckley, V. Bugaev, K. Byrum, J. V. Cardenzana, M. Cerruti, X. Chen, L. Ciupik, V. Connaughton, W. Cui, H. J. Dickinson, J. D. Eisch, M. Errando, A. Falcone, S. Federici, Q. Feng, J. P. Finley, H. Fleischhack, P. Fortin, L. Fortson, A. Furniss, N. Galante, G. H. Gillanders, S. Griffin, S. T. Griffiths, J. Grube, G. Gyuk, N. Håkansson, D. Hanna, J. Holder, G. Hughes, T. B. Humensky, C. A. Johnson, P. Kaaret, P. Kar, M. Kertzman, Y. Khassen, D. Kieda, H. Krawczynski, F. Krennrich, M. J. Lang, A. S. Madhavan, G. Maier, S. McArthur, A. McCann, K. Meagher, J. Millis, P. Moriarty, R. Mukherjee, D. Nieto, A. O'Faoláin de Bhróithe, R. A. Ong, A. N. Otte, N. Park, M. Pohl, A. Popkow, H. Prokoph, E. Pueschel, J. Quinn, K. Ragan, J. Rajotte, L. C. Reyes, P. T. Reynolds, G. T. Richards, E. Roache, G. H. Sembroski, K. Shahinyan, A. W. Smith, D. Staszak, I. Telezhinsky, J. V. Tucci, J. Tyler, A. Varlotta, V. V. Vassiliev, S. Vincent, S. P. Wakely, O. M. Weiner, A. Weinstein, R. Welsing, A. Wilhelm, D. A. Williams, B. Zitzer, J. E. McEnery, J. S. Perkins, P. Veres, and S. Zhu. Constraints on Very High Energy Emission from GRB 130427A. ApJ, 795(1):L3, Nov. 2014. doi: 10.1088/2041-8205/795/1/L3.

L. Amati, P. T. O'Brien, D. Götz, E. Bozzo, A. Santangelo, N. Tanvir, F. Frontera, S. Mereghetti, J. P. Osborne, A. Blain, S. Basa, M. Branchesi, L. Burderi, M. Caballero-García, A. J. Castro-Tirado, L. Christensen, R. Ciolfi, A. De Rosa, V. Doroshenko, A. Ferrara, G. Ghirlanda, L. Hanlon, P. Heddermann, I. Hutchinson, C. Labanti, E. Le Floch, H. Lerman, S. Paltani, V. Reglero, L. Rezzolla, P. Rosati, R. Salvaterra, G. Stratta, C. Tenzer, and Theseus Consortium. The THESEUS space mission: science goals, requirements and mission concept. Experimental Astronomy, 52(3):183–218, Dec. 2021. doi: 10.1007/s10686-021-09807-8.

L. Amati, C. Labanti, S. Mereghetti, F. Frontera, R. Campana, N. Auricchio, G. Baldazzi, P. Bellutti, G. Bertuccio, M. Branchesi, R. C. Butler, M. D. Caballero-Garcia, A. E. Camisasca, A. J. Castro-Tirado, L. Cavazzini, R. Ciolfi, A. De Rosa, F. Evangelisti, R. Farinelli, L. Ferro, F. Ficorella, M. Fiorini, F. Fuschino, J. L. Gasent-Blesa, G. Ghirlanda, M. Grassi, C. Guidorzi, P. Hedderman, I. Kuvvetli, G. La Rosa, P. Lorenzi, P. Malcovati, E. Marchesini, M. Marisaldi, M. Melchiorri, F. Mele, M. Mikhalska, M. Orlandini, P. Orleanski, S. M. Pedersen, R. Piazzolla, A. Rachevski, I. Rashevskaya, P. Rosati, V. Reglero, S. Ronchini, A. Santangelo, R. Salvaterra, P. Sarra, F. Sortino, G. Sottile, G. Stratta, S. Squerzanti, J. B. Stephen, C. Tenzer, L. Terenzi, A. Trois, A. Vacchi, E. Virgilli, A. Volpe, M. Winkler, G. Zampa, N. Zampa, and A. Zdziarski. The X/Gamma-ray Imaging Spectrometer (XGIS) for THESEUS and other mission opportunities. In J.-W. A. den Herder, S. Nikzad, and K. Nakazawa, editors, Space Telescopes and Instrumentation 2022: Ultraviolet to Gamma Ray, volume 12181 of Society

of Photo-Optical Instrumentation Engineers (SPIE) Conference Series, page 1218126, Aug. 2022. doi: 10.1117/12.2630178.

G. Amelino-Camelia, J. Ellis, N. E. Mavromatos, D. V. Nanopoulos, and S. Sarkar. Tests of quantum gravity from observations of γ-ray bursts. Nature, 395(6701):525–525, Oct 1998. ISSN 1476-4687. doi: 10.1038/26793. URL https://doi.org/10.1038/26793.

W. B. Atwood, A. A. Abdo, M. Ackermann, W. Althouse, B. Anderson, M. Axelsson, L. Baldini, J. Ballet, D. L. Band, G. Barbiellini, J. Bartelt, D. Bastieri, B. M. Baughman, K. Bechtol, D. Bédérède, F. Bellardi, R. Bellazzini, B. Berenji, G. F. Bignami, D. Bisello, E. Bissaldi, R. D. Blandford, E. D. Bloom, J. R. Bogart, E. Bonamente, J. Bonnell, A. W. Borgland, A. Bouvier, J. Bregeon, A. Brez, M. Brigida, P. Bruel, T. H. Burnett, G. Busetto, G. A. Caliandro, R. A. Cameron, P. A. Caraveo, S. Carius, P. Carlson, J. M. Casandjian, E. Cavazzuti, M. Ceccanti, C. Cecchi, E. Charles, A. Chekhtman, C. C. Cheung, J. Chiang, R. Chipaux, A. N. Cillis, S. Ciprini, R. Claus, J. Cohen-Tanugi, S. Condamoor, J. Conrad, R. Corbet, L. Corucci, L. Costamante, S. Cutini, D. S. Davis, D. Decotigny, M. DeKlotz, C. D. Dermer, A. de Angelis, S. W. Digel, E. do Couto e Silva, P. S. Drell, R. Dubois, D. Dumora, Y. Edmonds, D. Fabiani, C. Farnier, C. Favuzzi, D. L. Flath, P. Fleury, W. B. Focke, S. Funk, P. Fusco, F. Gargano, D. Gasparrini, N. Gehrels, F.-X. Gentit, S. Germani, B. Giebels, N. Giglietto, P. Giommi, F. Giordano, T. Glanzman, G. Godfrey, I. A. Grenier, M.-H. Grondin, J. E. Grove, L. Guillemot, S. Guiriec, G. Haller, A. K. Harding, P. A. Hart, E. Hays, S. E. Healey, M. Hirayama, L. Hjalmarsdotter, R. Horn, R. E. Hughes, G. Jóhannesson, G. Johansson, A. S. Johnson, R. P. Johnson, T. J. Johnson, W. N. Johnson, T. Kamae, H. Katagiri, J. Kataoka, A. Kavelaars, N. Kawai, H. Kelly, M. Kerr, W. Klamra, J. Knödlseder, M. L. Kocian, N. Komin, F. Kuehn, M. Kuss, D. Landriu, L. Latronico, B. Lee, S.-H. Lee, M. Lemoine-Goumard, A. M. Lionetto, F. Longo, F. Loparco, B. Lott, M. N. Lovellette, P. Lubrano, G. M. Madejski, A. Makeev, B. Marangelli, M. M. Massai, M. N. Mazziotta, J. E. McEnery, N. Menon, C. Meurer, P. F. Michelson, M. Minuti, N. Mirizzi, W. Mitthumsiri, T. Mizuno, A. A. Moiseev, C. Monte, M. E. Monzani, E. Moretti, A. Morselli, I. V. Moskalenko, S. Murgia, T. Nakamori, S. Nishino, P. L. Nolan, J. P. Norris, E. Nuss, M. Ohno, T. Ohsugi, N. Omodei, E. Orlando, J. F. Ormes, A. Paccagnella, D. Paneque, J. H. Panetta, D. Parent, M. Pearce, M. Pepe, A. Perazzo, M. Pesce-Rollins, P. Picozza, L. Pieri, M. Pinchera, F. Piron, T. A. Porter, L. Poupard, S. Rainò, R. Rando, E. Rapposelli, M. Razzano, A. Reimer, O. Reimer, T. Reposeur, L. C. Reyes, S. Ritz, L. S. Rochester, A. Y. Rodriguez, R. W. Romani, M. Roth, J. J. Russell, F. Ryde, S. Sabatini, H. F.-W. Sadrozinski, D. Sanchez, A. Sander, L. Sapozhnikov, P. M. S. Parkinson, J. D. Scargle, T. L. Schalk, G. Scolieri, C. Sgrò, G. H. Share, M. Shaw, T. Shimokawabe, C. Shrader, A. Sierpowska-Bartosik, E. J. Siskind, D. A. Smith, P. D. Smith, G. Spandre, P. Spinelli, J.-L. Starck, T. E. Stephens, M. S. Strickman, A. W. Strong, D. J. Suson, H. Tajima, H. Takahashi, T. Takahashi, T. Tanaka, A. Tenze, S. Tether, J. B. Thayer, J. G. Thayer, D. J. Thompson, L. Tibaldo, O. Tibolla, D. F. Torres, G. Tosti, A. Tramacere, M. Turri, T. L. Usher, N. Vilchez, V. Vitale, P. Wang, K. Watters, B. L. Winer, K. S. Wood, T. Ylinen, and M. Ziegler. The large area telescope on thefermi gamma-ray space telescopemission. The Astrophysical Journal, 697(2):1071–1102, May 2009. ISSN 1538-4357. doi: 10.1088/0004-637x/697/2/1071. URL http://dx.doi.org/10.1088/0004-637X/697/2/1071.

K. Auchettl, M. Trenti, M. Thomas, and F. Fiore. The SpIRIT mission: Multiwavelength detection and follow-up of cosmic explosions with an Australian space telescope. In AAS/High Energy Astrophysics Division, volume 54 of AAS/High Energy Astrophysics Division, page 305.02, Apr. 2022.

A. Authier and C. Malgrange. Diffraction physics. Acta Crystallographica Section A, 54(6 Part

1):806–819, Nov 1998. doi: 10.1107/S0108767398011271. URL https://doi.org/10.1107/S0108767398011271.

D. Band, J. Matteson, L. Ford, B. Schaefer, D. Palmer, B. Teegarden, T. Cline, M. Briggs, W. Paciesas, G. Pendleton, G. Fishman, C. Kouveliotou, C. Meegan, R. Wilson, and P. Lestrade. BATSE Observations of Gamma-Ray Burst Spectra. I. Spectral Diversity. ApJ, 413:281, Aug. 1993. doi: 10.1086/172995.

N. M. Barrière, L. Abalo, M. J. Collon, D. Girou, R. Günther, B. Landgraf, J. Tomsick, and M. W. Beijersbergen. Laue lens made of SiLCs for hard x-ray polarimetry. In S. L. O'Dell, J. A. Gaskin, G. Pareschi, and D. Spiga, editors, Optics for EUV, X-Ray, and Gamma-Ray Astronomy XI, volume 12679 of Society of Photo-Optical Instrumentation Engineers (SPIE) Conference Series, page 126790J, Oct. 2023. doi: 10.1117/12.2677653.

S. D. Barthelmy, L. M. Barbier, J. R. Cummings, E. E. Fenimore, N. Gehrels, D. Hullinger, H. A. Krimm, C. B. Markwardt, D. M. Palmer, A. Parsons, G. Sato, M. Suzuki, T. Takahashi, M. Tashiro, and J. Tueller. The burst alert telescope (bat) on the swift midex mission. Space Science Reviews, 120(3–4):143–164, Oct. 2005. ISSN 1572-9672. doi: 10.1007/s11214-005-5096-3. URL http://dx.doi.org/10.1007/s11214-005-5096-3.

M. Bassan. Advanced Interferometers and the Search for Gravitational Waves, volume 404. Springer Cham, 11 2013. ISBN 978-3-319-03791-2. doi: 10.1007/978-3-319-03792-9.

A. Beardmore. The Swift-XRT WT mode spectrum of GRB190114C. GRB Coordinates Network, 23736:1, Jan. 2019.

V. Bellucci, V. Guidi, R. Camattari, and I. Neri. Calculation of diffraction efficiency for curved crystals with arbitrary curvature radius. Journal of Applied Crystallography, 46(2):415–420, 2013. doi: https://doi.org/10.1107/S0021889813000162. URL https://onlinelibrary.wiley.com/doi/abs/10.1107/S0021889813000162.

A. M. Beloborodov, B. E. Stern, and R. Svensson. Self-Similar Temporal Behavior of Gamma-Ray Bursts. ApJ, 508(1):L25–L27, Nov. 1998. doi: 10.1086/311710.

A. M. Beloborodov, B. E. Stern, and R. Svensson. Power Density Spectra of Gamma-Ray Bursts. ApJ, 535(1):158–166, May 2000. doi: 10.1086/308836.

S. Bhandari, E. M. Sadler, J. X. Prochaska, S. Simha, S. D. Ryder, L. Marnoch, K. W. Bannister, J.-P. Macquart, C. Flynn, R. M. Shannon, N. Tejos, F. Corro-Guerra, C. K. Day, A. T. Deller, R. Ekers, S. Lopez, E. K. Mahony, C. Nuñez, and C. Phillips. The Host Galaxies and Progenitors of Fast Radio Bursts Localized with the Australian Square Kilometre Array Pathfinder. ApJ, 895(2):L37, June 2020. doi: 10.3847/2041-8213/ab672e.

S. Bhandari, K. E. Heintz, K. Aggarwal, L. Marnoch, C. K. Day, J. Sydnor, S. Burke-Spolaor, C. J. Law, J. Xavier Prochaska, N. Tejos, K. W. Bannister, B. J. Butler, A. T. Deller, R. D. Ekers, C. Flynn, W.-f. Fong, C. W. James, T. J. W. Lazio, R. Luo, E. K. Mahony, S. D. Ryder, E. M. Sadler, R. M. Shannon, J. Han, K. Lee, and B. Zhang. Characterizing the Fast Radio Burst Host Galaxy Population and its Connection to Transients in the Local and Extragalactic Universe. AJ, 163(2):69, Feb. 2022. doi: 10.3847/1538-3881/ac3aec.

G. S. Bisnovatyi-Kogan and A. S. Pozanenko. Can Flare Stars Explain the Annihilation Line from the Galactic Bulge? Astrophysics, 60(2):223–227, June 2017. doi: 10.1007/s10511-017-9477-6.

C. Bœhm. The dark matter interpretation of the 511 keV line. New Journal of Physics, 11(10): 105009, Oct. 2009. doi: 10.1088/1367-2630/11/10/105009.

C. Boehm, D. Hooper, J. Silk, M. Casse, and J. Paul. MeV Dark Matter: Has It Been Detected? Phys. Rev. Lett., 92(10):101301, Mar. 2004. doi: 10.1103/PhysRevLett.92.101301.

L. Bouchet, A. Strong, E. Jourdain, J. P. Roques, T. Porter, I. Moskalenko, R. Diehl, and E. Orlando. A complete all-sky survey with INTEGRAL/SPI: sources census, hard X-ray diffuse emission and annihilation line. In The Extreme Sky: Sampling the Universe above 10 keV, page 16, Jan. 2009. doi: 10.22323/1.096.0016.

E. Buffagni, E. Bonnini, C. Ferrari, E. Virgilli, and F. Frontera. X-ray characterization of curved crystals for hard x-ray astronomy. In R. Hudec and L. Pina, editors, EUV and X-ray Optics: Synergy between Laboratory and Space IV, volume 9510 of Society of Photo-Optical Instrumentation Engineers (SPIE) Conference Series, 2015.

L. Burderi, A. Sanna, T. Di Salvo, L. Amati, G. Amelino-Camelia, M. Branchesi, S. Capozziello, E. Coccia, M. Colpi, E. Costa, N. D'Amico, P. De Bernardis, M. De Laurentis, M. Della Valle, H. Falcke, M. Feroci, F. Fiore, F. Frontera, A. F. Gambino, G. Ghisellini, K. C. Hurley, R. Iaria, D. Kataria, C. Labanti, G. Lodato, B. Negri, A. Papitto, T. Piran, A. Riggio, C. Rovelli, A. Santangelo, F. Vidotto, and S. Zane. GrailQuest: hunting for atoms of space and time hidden in the wrinkle of Space-Time. Experimental Astronomy, 51(3):1255–1297, June 2021. doi: 10.1007/s10686-021-09745-5.

B. J. Burn. A synchrotron model for the continuum spectrum of the Crab Nebula. MNRAS, 165: 421, Jan. 1973. doi: 10.1093/mnras/165.4.421.

D. N. Burrows, J. E. Hill, J. A. Nousek, J. A. Kennea, A. Wells, J. P. Osborne, A. F. Abbey, A. Beardmore, K. Mukerjee, A. D. T. Short, G. Chincarini, S. Campana, O. Citterio, A. Moretti, C. Pagani, G. Tagliaferri, P. Giommi, M. Capalbi, F. Tamburelli, L. Angelini, G. Cusumano, H. W. Bräuninger, W. Burkert, and G. D. Hartner. The swift x-ray telescope. Space Science Reviews, 120(3–4):165–195, Oct. 2005. ISSN 1572-9672. doi: 10.1007/s11214-005-5097-2. URL http://dx.doi.org/10.1007/s11214-005-5097-2.

R. Camattari, V. Guidi, V. Bellucci, and A. Mazzolari. The 'quasi-mosaic' effect in crystals and its applications in modern physics. Journal of Applied Crystallography, 48, 08 2015. doi: 10.1107/S1600576715009875.

A. E. Camisasca, C. Guidorzi, L. Amati, F. Frontera, X. Y. Song, S. Xiao, S. L. Xiong, S. N. Zhang, R. Margutti, S. Kobayashi, C. G. Mundell, M. Y. Ge, A. Gomboc, S. M. Jia, N. Jordana-Mitjans, C. K. Li, X. B. Li, R. Maccary, M. Shrestha, W. C. Xue, and S. Zhang. GRB minimum variability timescale with Insight-HXMT and Swift. Implications for progenitor models, dissipation physics, and GRB classifications. A&A, 671:A112, Mar. 2023. doi: 10.1051/0004-6361/202245657.

X. Cao, W. Jiang, B. Meng, W. Zhang, T. Luo, S. Yang, C. Zhang, Y. Gu, L. Sun, X. Liu, J. Yang, X. Li, Y. Tan, S. Liu, Y. Du, F. Lu, Y. Xu, J. Guan, S. Zhang, H. Wang, T. Li, C. Zhang, X. Wen, J. Qu, L. Song, X. Li, M. Ge, Y. Zhou, S. Xiong, S. Zhang, Y. Zhang, Z. Cheng, F. Zhang, M. Li, X. Liang, M. Gao, E. Yang, X. Liu, H. Liu, Y. Yang, and F. Zhang. The Medium Energy X-ray telescope (ME) onboard the Insight-HXMT astronomy satellite. Science China Physics, Mechanics, and Astronomy, 63(4):249504, Apr. 2020. doi: 10.1007/s11433-019-1506-1.

E. Caroli, L. Abbene, A. Zappettini, N. Auricchio, G. Benassi, M. Bettelli, A. Buttacavoli, G. Gargano, S. Del Sordo, F. Principato, J. B. Stephen, S. Zanettini, and N. Zambelli. 3DCaTM: a 3D Cadmium Zinc Telluride spectroscopic module for hard X- and γ-ray astronomy. In Memorie della Societa Astronomica Italiana, volume 93, page 201, Nov. 2022. doi: 10.36116/MEMSAIT_93N2_3.2022.26.

M. Caselle, T. Blank, F. Colombo, A. Dierlamm, U. Husemann, S. Kudella, and M. Weber. Low-cost bump-bonding processes for high energy physics pixel detectors. Journal of Instrumentation, 11(01):C01050, jan 2016. doi: 10.1088/1748-0221/11/01/C01050. URL https://dx.doi.org/10.1088/1748-0221/11/01/C01050.

L. Cavazzini. Experimental tests and simulations for the performance assessment of theseus/xgis and astena/wfm-is as compton imagers in the high-energy regime. Master's thesis, University of Ferrara, Department of Physics and Earth Science, Master's Degree in Physics, 2021.

A. Celotti and R. D. Blandford. On the Formation of Jets. In L. Kaper, E. P. J. V. D. Heuvel, and P. A. Woudt, editors, Black Holes in Binaries and Galactic Nuclei, page 206, Jan. 2001. doi: 10.1007/10720995_43.

S. B. Cenko, N. R. Butler, E. O. Ofek, D. A. Perley, A. N. Morgan, D. A. Frail, J. Gorosabel, J. S. Bloom, A. J. Castro-Tirado, J. Cepa, P. Chandra, A. de Ugarte Postigo, A. V. Filippenko, C. R. Klein, S. R. Kulkarni, A. A. Miller, P. E. Nugent, and D. L. Starr. Unveiling the origin of grb 090709a: Lack of periodicity in a reddened cosmological long-duration gamma-ray burst. The Astronomical Journal, 140(1):224, jun 2010. doi: 10.1088/0004-6256/140/1/224. URL https://dx.doi.org/10.1088/0004-6256/140/1/224.

S. Chatterjee, C. J. Law, R. S. Wharton, S. Burke-Spolaor, J. W. T. Hessels, G. C. Bower, J. M. Cordes, S. P. Tendulkar, C. G. Bassa, P. Demorest, B. J. Butler, A. Seymour, P. Scholz, M. W. Abruzzo, S. Bogdanov, V. M. Kaspi, A. Keimpema, T. J. W. Lazio, B. Marcote, M. A. McLaughlin, Z. Paragi, S. M. Ransom, M. Rupen, L. G. Spitler, and H. J. van Langevelde. A direct localization of a fast radio burst and its host. Nature, 541(7635):58–61, Jan. 2017. doi: 10.1038/nature20797.

T. Chattopadhyay. Hard X-ray polarimetry—an overview of the method, science drivers, and recent findings. Journal of Astrophysics and Astronomy, 42(2):106, Oct. 2021. doi: 10.1007/s12036-021-09769-5.

T. Chattopadhyay, S. V. Vadawale, E. Aarthy, N. P. S. Mithun, V. Chand, A. Ratheesh, R. Basak, A. R. Rao, V. Bhalerao, S. Mate, A. B., V. Sharma, and D. Bhattacharya. Prompt emission polarimetry of gamma-ray bursts with theAstroSat CZT imager. The Astrophysical Journal, 884(2):123, oct 2019. doi: 10.3847/1538-4357/ab40b7. URL https://doi.org/10.3847%2F1538-4357%2Fab40b7.

Y. Chen, W. Cui, W. Li, J. Wang, Y. Xu, F. Lu, Y. Wang, T. Chen, D. Han, W. Hu, Y. Zhang, J. Huo, Y. Yang, M. Li, B. Lu, Z. Zhang, T. Li, S. Zhang, S. Xiong, S. Zhang, R. Xue, X. Zhao, Y. Zhu, Y. Zhu, H. Liu, Y. Yang, and F. Zhang. The Low Energy X-ray telescope (LE) onboard the Insight-HXMT astronomy satellite. Science China Physics, Mechanics, and Astronomy, 63(4):249505, Apr. 2020. doi: 10.1007/s11433-019-1469-5.

CHIME/FRB Collaboration, M. Amiri, B. C. Andersen, K. Bandura, S. Berger, M. Bhardwaj, M. M. Boyce, P. J. Boyle, C. Brar, D. Breitman, T. Cassanelli, P. Chawla, T. Chen, J. F. Cliche, A. Cook, D. Cubranic, A. P. Curtin, M. Deng, M. Dobbs, F. A. Dong, G. Eadie, M. Fandino,

E. Fonseca, B. M. Gaensler, U. Giri, D. C. Good, M. Halpern, A. S. Hill, G. Hinshaw, A. Josephy, J. F. Kaczmarek, Z. Kader, J. W. Kania, V. M. Kaspi, T. L. Landecker, D. Lang, C. Leung, D. Li, H.-H. Lin, K. W. Masui, R. McKinven, J. Mena-Parra, M. Merryfield, B. W. Meyers, D. Michilli, N. Milutinovic, A. Mirhosseini, M. Münchmeyer, A. Naidu, L. Newburgh, C. Ng, C. Patel, U.-L. Pen, E. Petroff, T. Pinsonneault-Marotte, Z. Pleunis, M. Rafiei-Ravandi, M. Rahman, S. M. Ransom, A. Renard, P. Sanghavi, P. Scholz, J. R. Shaw, K. Shin, S. R. Siegel, A. E. Sikora, S. Singh, K. M. Smith, I. Stairs, C. M. Tan, S. P. Tendulkar, K. Vanderlinde, H. Wang, D. Wulf, and A. V. Zwaniga. The First CHIME/FRB Fast Radio Burst Catalog. ApJS, 257(2):59, Dec. 2021a. doi: 10.3847/1538-4365/ac33ab.

CHIME/FRB Collaboration, M. Amiri, B. C. Andersen, K. Bandura, S. Berger, M. Bhardwaj, M. M. Boyce, P. J. Boyle, C. Brar, D. Breitman, T. Cassanelli, P. Chawla, T. Chen, J.-F. Cliche, A. Cook, D. Cubranic, A. P. Curtin, M. Deng, M. Dobbs, F. A. Dong, G. Eadie, M. Fandino, E. Fonseca, B. M. Gaensler, U. Giri, D. C. Good, M. Halpern, A. S. Hill, G. Hinshaw, A. Josephy, J. F. Kaczmarek, Z. Kader, J. W. Kania, V. M. Kaspi, T. L. Landecker, D. Lang, C. Leung, D. Li, H.-H. Lin, K. W. Masui, R. Mckinven, J. Mena-Parra, M. Merryfield, B. W. Meyers, D. Michilli, N. Milutinovic, A. Mirhosseini, M. Münchmeyer, A. Naidu, L. Newburgh, C. Ng, C. Patel, U.-L. Pen, E. Petroff, T. Pinsonneault-Marotte, Z. Pleunis, M. Rafiei-Ravandi, M. Rahman, S. M. Ransom, A. Renard, P. Sanghavi, P. Scholz, J. R. Shaw, K. Shin, S. R. Siegel, A. E. Sikora, S. Singh, K. M. Smith, I. Stairs, C. M. Tan, S. P. Tendulkar, K. Vanderlinde, H. Wang, D. Wulf, and A. V. Zwaniga. The first chime/frb fast radio burst catalog. The Astrophysical Journal Supplement Series, 257(2):59, dec 2021b. doi: 10.3847/1538-4365/ac33ab. URL https://dx.doi.org/10.3847/1538-4365/ac33ab.

C. Chirenti, S. Dichiara, A. Lien, M. C. Miller, and R. Preece. Kilohertz quasiperiodic oscillations in short gamma-ray bursts. Nature, 613(7943):253–256, Jan. 2023. doi: 10.1038/s41586-022-05497-0.

F. E. Christensen and B. D. Ramsey. X-Ray Optics for Astrophysics: A Historical Review. In Handbook of X-ray and Gamma-ray Astrophysics, page 112. Springer Singapore, 2022. doi: 10.1007/978-981-16-4544-0_1-1.

E. Churazov, S. Sazonov, R. Sunyaev, and M. Revnivtsev. Earth X-ray albedo for cosmic X-ray background radiation in the 1-1000 keV band. MNRAS, 385(2):719–727, Apr. 2008. doi: 10.1111/j.1365-2966.2008.12918.x.

R. Churazov, E. Sunyaev, J. Isern, J. Knödlseder, P. Jean, F. Lebrun, N. Chugai, S. Grebenev, E. Bravo, S. Sazonov, and M. Renaud. Cobalt-56 γ-ray emission lines from the type ia supernova 2014j. Nature, 512(7515):406–408, Aug 2014. ISSN 1476-4687. doi: 10.1038/nature13672. URL https://doi.org/10.1038/nature13672.

M. Cinelli, S. Puccetti, M. Lavagna, P. Lunghi, and G. Pucacco. High Energy Modular Ensemble of Satellites Mission: Towards the final Full Constellation. Acta Astronautica, 189:129–142, Dec. 2021. doi: 10.1016/j.actaastro.2021.08.024.

E. Costa, F. Frontera, J. Heise, M. Feroci, J. in't Zand, F. Fiore, M. N. Cinti, D. Dal Fiume, L. Nicastro, M. Orlandini, E. Palazzi, M. Rapisarda#, G. Zavattini, R. Jager, A. Parmar, A. Owens, S. Molendi, G. Cusumano, M. C. Maccarone, S. Giarrusso, A. Coletta, L. A. Antonelli, P. Giommi, J. M. Muller, L. Piro, and R. C. Butler. Discovery of an X-ray afterglow associated with the γ-ray burst of 28 February 1997. Nature, 387:783–785, June 1997. doi: 10.1038/42885.

D. B. Cullity. Elements of X-ray Diffraction. Addison-Wesley, 1957.

K. Danzmann and the LISA study team. Lisa: laser interferometer space antenna for gravitational wave measurements. Classical and Quantum Gravity, 13(11A):A247, nov 1996. doi: 10.1088/0264-9381/13/11A/033. URL https://dx.doi.org/10.1088/0264-9381/13/11A/033.

C. Darwin. Xxxiv. the theory of x-ray reflexion. The London, Edinburgh, and Dublin Philosophical Magazine and Journal of Science, 27(158):315–333, 1914a. doi: 10.1080/14786440208635093. URL https://doi.org/10.1080/14786440208635093.

C. Darwin. Lxxviii. the theory of x-ray reflexion. part ii. The London, Edinburgh, and Dublin Philosophical Magazine and Journal of Science, 27(160):675–690, 1914b. doi: 10.1080/14786440408635139. URL https://doi.org/10.1080/14786440408635139.

A. De Luca, P. Esposito, G. L. Israel, D. Götz, G. Novara, A. Tiengo, and S. Mereghetti. XMM–Newton and Swift observations prove GRB 090709A to be a distant, standard, long GRB. Monthly Notices of the Royal Astronomical Society, 402(3):1870–1876, 02 2010. ISSN 0035-8711. doi: 10.1111/j.1365-2966.2009.16012.x. URL https://doi.org/10.1111/j.1365-2966.2009.16012.x.

V. D'Elia, A. D'Ai, B. Sbarufatti, D. N. Burrows, A. Tohuvavohu, K. L. Page, A. P. Beardmore, P. A. Evans, A. Melandri, and J. D. Gropp. GRB 190114C: Swift-XRT refined Analysis. GRB Coordinates Network, 23706:1, Jan. 2019.

S. Dichiara, C. Guidorzi, L. Amati, and F. Frontera. Average power density spectrum of long GRBs detected with BeppoSAX/GRBM and with Fermi/GBM. MNRAS, 431(4):3608–3617, June 2013. doi: 10.1093/mnras/stt445.

R. Diehl. Gamma rays from a supernova of type ia: Sn2014j. Astronomische Nachrichten, 336(5):464–470, 2015. doi: https://doi.org/10.1002/asna.201512179. URL https://onlinelibrary.wiley.com/doi/abs/10.1002/asna.201512179.

R. Diehl, T. Siegert, W. Hillebrandt, S. A. Grebenev, J. Greiner, M. Krause, M. Kromer, K. Maeda, F. Röpke, and S. Taubenberger. Early ^{56}Ni decay gamma rays from SN2014J suggest an unusual explosion. Science, 345(6201):1162–1165, Sept. 2014. doi: 10.1126/science.1254738.

Y. Evangelista, F. Fiore, F. Fuschino, R. Campana, F. Ceraudo, E. Demenev, A. Guzman, C. Labanti, G. La Rosa, M. Fiorini, M. Gandola, M. Grassi, F. Mele, G. Morgante, P. Nogara, R. Piazzolla, S. Pliego Caballero, I. Rashevskaya, F. Russo, G. Sciarrone, G. Sottile, D. Milankovich, A. Pál, F. Ambrosino, N. Auricchio, M. Barbera, P. Bellutti, G. Bertuccio, G. Borghi, J. Cao, T. Chen, G. Dilillo, M. Feroci, F. Ficorella, U. Lo Cicero, P. Malcovati, A. Morbidini, G. Pauletta, A. Picciotto, A. Rachevski, A. Santangelo, C. Tenzer, A. Vacchi, L. Wang, Y. Xu, G. Zampa, N. Zampa, N. Zorzi, L. Burderi, M. Lavagna, R. Bertacin, P. Lunghi, A. Monge, B. Negri, S. Pirrotta, S. Puccetti, A. Sanna, F. Amarilli, G. Amelino-Camelia, M. Bechini, M. Citossi, A. Colagrossi, S. Curzel, G. Della Casa, M. Cinelli, M. Del Santo, T. Di Salvo, C. Feruglio, F. Ferrandi, M. Fiorito, D. Gacnik, G. Galgóczi, A. F. Gambino, G. Ghirlanda, A. Gomboc, M. Karlica, P. Efremov, U. Kostic, A. Clerici, B. Lopez Fernandez, A. Maselli, L. Nava, M. Ohno, D. Ottolina, A. Pasquale, M. Perri, M. Piccinin, J. Prinetto, A. Riggio, J. Ripa, A. Papitto, S. Piranomonte, F. Scala, D. Selcan, S. Silvestrini, T. Rotovnik, E. Virgilli, I. Troisi, N. Werner, G. Zanotti, A. Anitra, A. Manca, and A. Clerici. The scientific payload on-board the HERMES-TP and HERMES-SP CubeSat missions. In J.-W. A. den Herder,

S. Nikzad, and K. Nakazawa, editors, Space Telescopes and Instrumentation 2020: Ultraviolet to Gamma Ray, volume 11444 of Society of Photo-Optical Instrumentation Engineers (SPIE) Conference Series, page 114441T, Dec. 2020. doi: 10.1117/12.2561018.

Y.-Z. Fan, P. H. T. Tam, F.-W. Zhang, Y.-F. Liang, H.-N. He, B. Zhou, R.-Z. Yang, Z.-P. Jin, and D.-M. Wei. High-energy Emission of GRB 130427A: Evidence for Inverse Compton Radiation. ApJ, 776(2):95, Oct. 2013. doi: 10.1088/0004-637X/776/2/95.

G. Ferioli. Simulazione di afterglow di grb alle alte energie con il narrow-field telescope a bordo della proposta di missione spaziale astena. Master's thesis, University of Ferrara, Department of Physics and Earth Science, Bachelor's Degree in Physics, 2021.

C. Ferrari, E. Buffagni, E. Bonnini, and A. Zappettini. X-ray diffraction efficiency of bent GaAs mosaic crystals for the LAUE project. In S. L. O'Dell and G. Pareschi, editors, Optics for EUV, X-Ray, and Gamma-Ray Astronomy VI, volume 8861, pages 568 – 575. SPIE, 2013.

F. Ferrari, F. Frontera, G. Loffredo, E. Virgilli, C. Guidorzi, V. Carassiti, F. Evangelisti, L. Landi, S. Chiozzi, S. Squerzanti, E. Caroli, J. B. Stephen, F. Schiavone, A. Basili, K. H. Andersen, and P. Courtois. New results on focusing of gamma-rays with Laue lenses. In S. L. O'Dell and G. Pareschi, editors, Optics for EUV, X-Ray, and Gamma-Ray Astronomy IV, volume 7437 of Society of Photo-Optical Instrumentation Engineers (SPIE) Conference Series, page 74370M, Aug. 2009. doi: 10.1117/12.829272.

L. Ferro. Simulations and experimental activity in support of the astena concept mission proposed to esa. Master's thesis, University of Ferrara, Department of Physics and Earth Science, Master's Degree in Physics, 2020. URL https://larixfacility.unife.it/wp-content/uploads/2023/07/Tesi_Magistrale_Lisa_Ferro-min.pdf.

L. Ferro, E. Virgilli, M. Moita, F. Frontera, P. Rosati, C. Guidorzi, C. Ferrari, R. Lolli, E. Caroli, N. Auricchio, J. B. Stephen, S. D. Sordo, C. Gargano, S. Squerzanti, M. Pucci, O. Limousin, A. Meuris, P. Laurent, and H. Allaire. The TRILL project: increasing the technological readiness of Laue lenses. In J.-W. A. den Herder, S. Nikzad, and K. Nakazawa, editors, Space Telescopes and Instrumentation 2022: Ultraviolet to Gamma Ray, volume 12181, page 121812K. International Society for Optics and Photonics, SPIE, 2022. doi: 10.1117/12.2629872. URL https://doi.org/10.1117/12.2629872.

L. Ferro, L. Cavazzini, M. Moita, E. Virgilli, F. Frontera, L. Amati, N. Auricchio, R. Campana, E. Caroli, C. Labanti, P. Rosati, C. Guidorzi, and J. B. Stephen. Imaging performance above 150 keV of the wide field monitor on board the ASTENA concept mission. In EUV and X-ray Optics: Synergy between Laboratory and Space VIII, volume 12576 of Society of Photo-Optical Instrumentation Engineers (SPIE) Conference Series, page 1257603, June 2023. doi: 10.1117/12.2665745.

D. P. Finkbeiner and N. Weiner. Exciting dark matter and the INTEGRAL/SPI 511keV signal. Phys. Rev. D, 76(8):083519, Oct. 2007. doi: 10.1103/PhysRevD.76.083519.

F. Fiore, A. Guzman, R. Campana, and Y. Evangelista. HERMES-Pathfinder. In Handbook of X-ray and Gamma-ray Astrophysics, page 38. Springer Singapore, 2022. doi: 10.1007/978-981-16-4544-0_35-1.

G. J. Fishman and C. A. Meegan. Gamma-Ray Bursts. ARA&A, 33:415–458, Jan. 1995. doi: 10.1146/annurev.aa.33.090195.002215.

M. Friis, M. Kiss, V. Mikhalev, M. Pearce, and H. Takahashi. The PoGO+ Balloon-Borne Hard X-ray Polarimetry Mission. Galaxies, 6(1):30, Mar. 2018. doi: 10.3390/galaxies6010030.

F. Frontera. Recent Results on Gamma-Ray Bursts with the Bepposax Satellite. In International Cosmic Ray Conference, volume 8 of International Cosmic Ray Conference, page 307, Jan. 1998. doi: 10.48550/arXiv.astro-ph/9802157.

F. Frontera. The key role of BeppoSAX in the GRB history. Rendiconti Lincei. Scienze Fisiche e Naturali, 30:171–184, Dec. 2019. doi: 10.1007/s12210-019-00766-z.

F. Frontera and P. von Ballmoos. Laue Gamma-Ray Lenses for Space Astrophysics: Status and Prospects. X-Ray Optics and Instrumentation 2010, 2010:215375, Jan. 2010. doi: 10.1155/2010/215375.

F. Frontera, G. Loffredo, A. Pisa, L. Milani, F. Nobili, N. Auricchio, V. Carassiti, F. Evangelisti, L. Landi, S. Squerzanti, K. H. Andersen, P. Courtois, L. Amati, E. Caroli, G. Landini, S. Silvestri, J. B. Stephen, J. M. Poulsen, B. Negri, and G. Pareschi. Development status of a Laue lens project for gamma-ray astronomy. In S. L. O'Dell and G. Pareschi, editors, Optics for EUV, X-Ray, and Gamma-Ray Astronomy III, volume 6688 of Society of Photo-Optical Instrumentation Engineers (SPIE) Conference Series, page 66880N, Sept. 2007. doi: 10.1117/12.736038.

F. Frontera, G. Loffredo, A. Pisa, F. Nobili, V. Carassiti, F. Evangelisti, L. Landi, S. Squerzanti, E. Caroli, J. B. Stephen, K. H. Andersen, P. Courtois, N. Auricchio, L. Milani, and B. Negri. Focusing of gamma-rays with Laue lenses: first results. In M. J. L. Turner and K. A. Flanagan, editors, Space Telescopes and Instrumentation 2008: Ultraviolet to Gamma Ray, volume 7011, pages 568 – 575. International Society for Optics and Photonics, SPIE, 2008. URL https://doi.org/10.1117/12.790484.

F. Frontera, E. Virgilli, V. Liccardo, V. Valsan, V. Carassiti, S. Chiozzi, F. Evangelisti, S. Squerzanti, M. Statera, V. Guidi, C. Ferrari, R. A. Zappettini, E. Caroli, N. Auricchio, S. Silvestri, R. Camattari, F. Cassese, L. Recanatesi, M. Pecora, S. Mottini, and B. Negri. Development status of the LAUE project. In T. Takahashi, S. S. Murray, and J.-W. A. den Herder, editors, Space Telescopes and Instrumentation 2012: Ultraviolet to Gamma Ray, volume 8443 of Society of Photo-Optical Instrumentation Engineers (SPIE) Conference Series, page 84430B, Sept. 2012. doi: 10.1117/12.926378.

F. Frontera, E. Virgilli, C. Guidorzi, P. Rosati, R. Diehl, T. Siegert, C. Fryer, L. Amati, N. Auricchio, R. Campana, E. Caroli, F. Fuschino, C. Labanti, M. Orlandini, E. Pian, J. B. Stephen, S. Del Sordo, C. Budtz-Jorgensen, I. Kuvvetli, S. Brandt, R. M. C. da Silva, P. Laurent, E. Bozzo, P. Mazzali, and M. D. Valle. Understanding the origin of the positron annihilation line and the physics of supernova explosions. Experimental Astronomy, 51(3):1175–1202, Jun 2021. ISSN 1572-9508. doi: 10.1007/s10686-021-09727-7. URL https://doi.org/10.1007/s10686-021-09727-7.

J. P. U. Fynbo, D. Watson, C. C. Thöne, J. Sollerman, J. S. Bloom, T. M. Davis, J. Hjorth, P. Jakobsson, U. G. Jørgensen, J. F. Graham, A. S. Fruchter, D. Bersier, L. Kewley, A. Cassan, J. M. C. Cerón, S. Foley, J. Gorosabel, T. C. Hinse, K. D. Horne, B. L. Jensen, S. Klose, D. Kocevski, J.-B. Marquette, D. Perley, E. Ramirez-Ruiz, M. D. Stritzinger, P. M. Vreeswijk, R. A. M. Wijers, K. G. Woller, D. Xu, and M. Zub. No supernovae associated with two long-duration γ-ray bursts. Nature, 444(7122):1047–1049, dec 2006. doi: 10.1038/nature05375. URL https://doi.org/10.1038%2Fnature05375.

A. F. Gad. Pygad: An intuitive genetic algorithm python library. Multimedia Tools and Applications, pages 1–14, 2023.

N. Gehrels, G. Chincarini, P. Giommi, K. O. Mason, J. A. Nousek, A. A. Wells, N. E. White, S. D. Barthelmy, D. N. Burrows, L. R. Cominsky, K. C. Hurley, F. E. Marshall, P. Mészáros, P. W. A. Roming, L. Angelini, L. M. Barbier, T. Belloni, S. Campana, P. A. Caraveo, M. M. Chester, O. Citterio, T. L. Cline, M. S. Cropper, J. R. Cummings, A. J. Dean, E. D. Feigelson, E. E. Fenimore, D. A. Frail, A. S. Fruchter, G. P. Garmire, K. Gendreau, G. Ghisellini, J. Greiner, J. E. Hill, S. D. Hunsberger, H. A. Krimm, S. R. Kulkarni, P. Kumar, F. Lebrun, N. M. Lloyd-Ronning, C. B. Markwardt, B. J. Mattson, R. F. Mushotzky, J. P. Norris, J. Osborne, B. Paczynski, D. M. Palmer, H.-S. Park, A. M. Parsons, J. Paul, M. J. Rees, C. S. Reynolds, J. E. Rhoads, T. P. Sasseen, B. E. Schaefer, A. T. Short, A. P. Smale, I. A. Smith, L. Stella, G. Tagliaferri, T. Takahashi, M. Tashiro, L. K. Townsley, J. Tueller, M. J. L. Turner, M. Vietri, W. Voges, M. J. Ward, R. Willingale, F. M. Zerbi, and W. W. Zhang. The Swift Gamma-Ray Burst Mission. ApJ, 611:1005–1020, Aug. 2004. doi: 10.1086/422091.

J.-J. Geng, B. Zhang, and R. Kuiper. Propagation of Relativistic, Hydrodynamic, Intermittent Jets in a Rotating, Collapsing GRB Progenitor Star. ApJ, 833(1):116, Dec. 2016. doi: 10.3847/1538-4357/833/1/116.

R. Giacconi, G. Branduardi, U. Briel, A. Epstein, D. Fabricant, E. Feigelson, W. Forman, P. Gorenstein, J. Grindlay, H. Gursky, F. R. Harnden, J. P. Henry, C. Jones, E. Kellogg, D. Koch, S. Murray, E. Schreier, F. Seward, H. Tananbaum, K. Topka, L. Van Speybroeck, S. S. Holt, R. H. Becker, E. A. Boldt, P. J. Serlemitsos, G. Clark, C. Canizares, T. Markert, R. Novick, D. Helfand, and K. Long. The Einstein (HEAO 2) X-ray Observatory. ApJ, 230: 540–550, June 1979. doi: 10.1086/157110.

D. Girou, L. Keek, R. K. Smith, R. L. McEntaffer, R. den Hartog, M. Bavdaz, I. Ferreira, N. M. Barrière, B. Landgraf, G. Vacanti, and M. Collon. Silicon pore optics: a mature and adaptable x-ray mirror technology. In S. L. O'Dell, J. A. Gaskin, G. Pareschi, and D. Spiga, editors, Optics for EUV, X-Ray, and Gamma-Ray Astronomy XI, volume 12679 of Society of Photo-Optical Instrumentation Engineers (SPIE) Conference Series, page 1267905, Oct. 2023. doi: 10.1117/12.2677388.

A. Goldwurm, P. Goldoni, A. Gros, J. Stephen, L. Foschini, F. Gianotti, L. Natalucci, G. De Cesare, and M. del Santo. Gamma-ray imaging with the coded mask IBIS telescope. In A. Gimenez, V. Reglero, and C. Winkler, editors, Exploring the Gamma-Ray Universe, volume 459 of ESA Special Publication, pages 497–500, Sept. 2001. doi: 10.48550/arXiv.astro-ph/0102386.

O. Gottlieb and N. Globus. The Role of Jet-Cocoon Mixing, Magnetization, and Shock Breakout in Neutrino and Cosmic-Ray Emission from Short Gamma-Ray Bursts. ApJ, 915(1):L4, July 2021. doi: 10.3847/2041-8213/ac05c5.

O. Gottlieb, O. Bromberg, C. B. Singh, and E. Nakar. The structure of weakly magnetized γ-ray burst jets. MNRAS, 498(3):3320–3333, Nov. 2020. doi: 10.1093/mnras/staa2567.

J. Granot, T. Piran, O. Bromberg, J. L. Racusin, and F. Daigne. Gamma-ray bursts as sources of strong magnetic fields. Space Science Reviews, 191(1-4):471–518, aug 2015. doi: 10.1007/s11214-015-0191-6. URL https://doi.org/10.1007%2Fs11214-015-0191-6.

J. Greiner, U. Hugentobler, J. M. Burgess, F. Berlato, M. Rott, and A. Tsvetkova. A proposed network of gamma-ray burst detectors on the global navigation satellite system Galileo G2. A&A, 664:A131, Aug. 2022. doi: 10.1051/0004-6361/202142835.

J. D. Gropp, J. A. Kennea, N. J. Klingler, H. A. Krimm, S. J. Laporte, A. Y. Lien, M. J. Moss, D. M. Palmer, B. Sbarufatti, and M. H. Siegel. GRB 190114C: Swift detection of a very bright burst with a bright optical counterpart. GRB Coordinates Network, 23688:1, Jan. 2019.

C. Guidorzi, R. Margutti, L. Amati, S. Campana, M. Orlandini, P. Romano, M. Stamatikos, and G. Tagliaferri. Average power density spectrum of Swift long gamma-ray bursts in the observer and in the source-rest frames. MNRAS, 422(2):1785–1803, May 2012. doi: 10.1111/j.1365-2966.2012.20758.x.

C. Guidorzi, S. Dichiara, and L. Amati. Individual power density spectra of Swift gamma-ray bursts. A&A, 589:A98, May 2016. doi: 10.1051/0004-6361/201527642.

C. Guidorzi, R. Margutti, D. Brout, D. Scolnic, W. Fong, K. D. Alexander, P. S. Cowperthwaite, J. Annis, E. Berger, P. K. Blanchard, R. Chornock, D. L. Coppejans, T. Eftekhari, J. A. Frieman, D. Huterer, M. Nicholl, M. Soares-Santos, G. Terreran, V. A. Villar, and P. K. G. Williams. Improved Constraints on H $_0$ from a Combined Analysis of Gravitational-wave and Electromagnetic Emission from GW170817. ApJ, 851(2):L36, Dec. 2017. doi: 10.3847/2041-8213/aaa009.

C. Guidorzi, F. Frontera, G. Ghirlanda, G. Stratta, C. G. Mundell, E. Virgilli, P. Rosati, E. Caroli, L. Amati, E. Pian, S. Kobayashi, G. Ghisellini, C. Fryer, M. D. Valle, R. Margutti, M. Marongiu, R. Martone, R. Campana, F. Fuschino, C. Labanti, M. Orlandini, J. B. Stephen, S. Brandt, R. C. d. Silva, P. Laurent, R. Mochkovitch, E. Bozzo, R. Ciolfi, L. Burderi, and T. Di Salvo. A deep study of the high–energy transient sky. Experimental Astronomy, 51 (3):1203–1223, Jun 2021. ISSN 1572-9508. doi: 10.1007/s10686-021-09725-9. URL https://doi.org/10.1007/s10686-021-09725-9.

C. Guidorzi, M. Sartori, R. Maccary, A. Tsvetkova, L. Amati, L. Bazzanini, M. Bulla, A. E. Camisasca, L. Ferro, F. Frontera, C. K. Li, S. L. Xiong, and S. N. Zhang. Distribution of number of peaks within a long gamma-ray burst. arXiv e-prints, art. arXiv:2402.17282, Feb. 2024. doi: 10.48550/arXiv.2402.17282.

S. Guiriec, V. Connaughton, M. S. Briggs, M. Burgess, F. Ryde, F. Daigne, P. Mészáros, A. Goldstein, J. McEnery, N. Omodei, P. N. Bhat, E. Bissaldi, A. Camero-Arranz, V. Chaplin, R. Diehl, G. Fishman, S. Foley, M. Gibby, M. M. Giles, J. Greiner, D. Gruber, A. von Kienlin, M. Kippen, C. Kouveliotou, S. McBreen, C. A. Meegan, W. Paciesas, R. Preece, A. Rau, D. Tierney, A. J. van der Horst, and C. Wilson-Hodge. Detection of a Thermal Spectral Component in the Prompt Emission of GRB 100724B. ApJ, 727(2):L33, Feb. 2011. doi: 10.1088/2041-8205/727/2/L33.

D. Götz, S. Basa, F. Pinsard, L. Martin, A. Arhancet, E. Bozzo, C. Cara, I. E. Sanz, P.-A. Frugier, J. Floriot, L. Genolet, P. Heddermann, E. L. Floc'h, I. L. Mer, S. Paltani, T. Pamplona, C. Paries, T. Prod'homme, B. Schneider, C. Tenzer, T. Tourrette, and H. Triou. The infra-red telescope (irt) on board the theseus mission, 2021.

C. J. Hailey, K. Mori, F. E. Bauer, M. E. Berkowitz, J. Hong, and B. J. Hord. A density cusp of quiescent X-ray binaries in the central parsec of the Galaxy. Nature, 556(7699):70–73, Apr. 2018. doi: 10.1038/nature25029.

R. Hamburg, P. Veres, C. Meegan, E. Burns, V. Connaughton, A. Goldstein, D. Kocevski, and O. J. Roberts. GRB 190114C: Fermi GBM detection. GRB Coordinates Network, 23707:1, Jan. 2019.

G. G. Harman and G. G. Harman. Wire bonding in microelectronics. McGraw-Hill New York, 2010.

D. I. Harp, C. C. Liebe, W. Craig, F. Harrison, K. Kruse-Madsen, and A. Zoglauer. NuSTAR: system engineering and modeling challenges in pointing reconstruction for a deployable x-ray telescope. In G. Z. Angeli and P. Dierickx, editors, Modeling, Systems Engineering, and Project Management for Astronomy IV, volume 7738 of Society of Photo-Optical Instrumentation Engineers (SPIE) Conference Series, page 77380Z, July 2010. doi: 10.1117/12.856626.

T. Harris. The Theory of Branching Processes. Grundlehren der mathematischen Wissenschaften. Springer Berlin Heidelberg, 1963. ISBN 9783540029861. URL https://books.google.it/books?id=_ORQAAAAMAAJ.

F. Harrison and NuSTAR Team. The Nuclear Spectroscopic Telescope Array Mission Overview and First Results. In AAS/High Energy Astrophysics Division #13, volume 13 of AAS/High Energy Astrophysics Division, page 201.01, Apr. 2013.

F. A. Harrison, F. E. Christensen, W. Craig, C. Hailey, W. Baumgartner, C. M. H. Chen, J. Chonko, W. R. Cook, J. Koglin, K.-K. Madsen, M. Pivavoroff, S. Boggs, and D. Smith. Development of the HEFT and NuSTAR focusing telescopes. Experimental Astronomy, 20(1-3):131–137, Dec. 2005. doi: 10.1007/s10686-006-9072-z.

F. A. Harrison, J. Aird, F. Civano, G. Lansbury, J. R. Mullaney, D. R. Ballantyne, D. M. Alexander, D. Stern, M. Ajello, D. Barret, F. E. Bauer, M. Baloković, W. N. Brandt, M. Brightman, S. E. Boggs, F. E. Christensen, A. Comastri, W. W. Craig, A. Del Moro, K. Forster, P. Gandhi, P. Giommi, B. W. Grefenstette, C. J. Hailey, R. C. Hickox, A. Hornstrup, T. Kitaguchi, J. Koglin, B. Luo, K. K. Madsen, P. H. Mao, H. Miyasaka, K. Mori, M. Perri, M. Pivovaroff, S. Puccetti, V. Rana, E. Treister, D. Walton, N. J. Westergaard, D. Wik, L. Zappacosta, W. W. Zhang, and A. Zoglauer. The NuSTAR Extragalactic Surveys: The Number Counts of Active Galactic Nuclei and the Resolved Fraction of the Cosmic X-Ray Background. ApJ, 831(2): 185, Nov. 2016. doi: 10.3847/0004-637X/831/2/185.

R. C. Haymes, D. V. Ellis, G. J. Fishman, J. D. Kurfess, and W. H. Tucker. Observation of Gamma Radiation from the Crab Nebula. ApJ, 151:L9, Jan. 1968. doi: 10.1086/180129.

J. J. Hester. The Crab Nebula : an astrophysical chimera. ARA&A, 46:127–155, Sept. 2008. doi: 10.1146/annurev.astro.45.051806.110608.

S. Hild, S. Chelkowski, and A. Freise. Pushing towards the et sensitivity using 'conventional' technology, 2008.

R. Hurbans. Grokking Artificial Intelligence Algorithms. Manning, 2020.

Jansen, F., Lumb, D., Altieri, B., Clavel, J., Ehle, M., Erd, C., Gabriel, C., Guainazzi, M., Gondoin, P., Much, R., Munoz, R., Santos, M., Schartel, N., Texier, D., and Vacanti, G. Xmm-newton observatory* - i. the spacecraft and operations. A&A, 365(1):L1–L6, 2001. doi: 10.1051/0004-6361:20000036. URL https://doi.org/10.1051/0004-6361:20000036.

I. Johnson, W. N., J. Harnden, F. R., and R. C. Haymes. The Spectrum of Low-Energy Gamma Radiation from the Galactic-Center Region. ApJ, 172:L1, Feb. 1972. doi: 10.1086/180878.

L. Keek, G. Vacanti, L. Abalo, N. Barrière, M. Bavdaz, M. Collon, B. Donovan, D. Girou, B. Landgraf, R. McEntaffer, A. Simionescu, R. Smith, J. Tomsick, and R. Willingale. Silicon Pore Optics for Athena and beyond. In AAS/High Energy Astrophysics Division, volume 55 of AAS/High Energy Astrophysics Division, page 103.31, Sept. 2023.

S. Keitel, C. Malgrange, T. Niemöller, and J. Schneider. Diffraction of 100 to 200 kev x-rays from an si1-xgex gradient crystal: Comparison with results from dynamical theory. Acta crystallographica. Section A, Foundations of crystallography, 55:855–863, 09 1999. doi: 10.1107/S010876739900313X.

C. Kierans, T. Takahashi, and G. Kanbach. Compton Telescopes for Gamma-Ray Astrophysics. Springer Nature Singapore, Singapore, 2022. ISBN 978-981-16-4544-0. doi: 10.1007/978-981-16-4544-0_46-1. URL https://doi.org/10.1007/978-981-16-4544-0_46-1.

R. W. Klebesadel, I. B. Strong, and R. A. Olson. Observations of Gamma-Ray Bursts of Cosmic Origin. ApJ, 182:L85, June 1973. doi: 10.1086/181225.

O. Klein and T. Nishina. Über die Streuung von Strahlung durch freie Elektronen nach der neuen relativistischen Quantendynamik von Dirac. Zeitschrift fur Physik, 52(11-12):853–868, Nov. 1929. doi: 10.1007/BF01366453.

D. A. Kniffen. The Gamma-Ray Observatory. Annals of the New York Academy of Sciences, 571:482–496, Dec. 1989. doi: 10.1111/j.1749-6632.1989.tb50535.x.

K. M. Knowles and A. T. J. van Helvoort. Anodic bonding. International Materials Reviews, 51 (5):273–311, 2006. doi: 10.1179/174328006X102501. URL https://doi.org/10.1179/174328006X102501.

D. Kocevski, N. Omodei, M. Axelsson, E. Burns, G. Vianello, E. Bissaldi, and F. Longo. GRB 190114C: Fermi-LAT detection. GRB Coordinates Network, 23709:1, Jan. 2019.

M. Kole and Polar Collaboration. First Results of POLAR: A dedicated Gamma-Ray Burst Polarimeter. In 35th International Cosmic Ray Conference (ICRC2017), volume 301 of International Cosmic Ray Conference, page 852, July 2017. doi: 10.22323/1.301.0852.

M. Kole, M. Pearce, and M. Muñoz Salinas. A model of the cosmic ray induced atmospheric neutron environment. Astroparticle Physics, 62:230–240, Mar. 2015. doi: 10.1016/j.astropartphys.2014.10.002.

M. Kole, N. D. Angelis, F. Berlato, J. M. Burgess, N. Gauvin, J. Greiner, W. Hajdas, H. C. Li, Z. H. Li, A. Pollo, N. Produit, D. Rybka, L. M. Song, J. C. Sun, J. Szabelski, T. Tymieniecka, Y. H. Wang, B. B. Wu, X. Wu, S. L. Xiong, S. N. Zhang, and Y. J. Zhang. The POLAR gamma-ray burst polarization catalog. Astronomy & Astrophysics, 644:A124, dec 2020. doi: 10.1051/0004-6361/202037915. URL https://doi.org/10.1051%2F0004-6361%2F202037915.

C. Kouveliotou, J. Granot, J. L. Racusin, E. Bellm, G. Vianello, S. Oates, C. L. Fryer, S. E. Boggs, F. E. Christensen, W. W. Craig, C. D. Dermer, N. Gehrels, C. J. Hailey, F. A. Harrison, A. Melandri, J. E. McEnery, C. G. Mundell, D. K. Stern, G. Tagliaferri, and W. W. Zhang. NuSTAR Observations of GRB 130427A Establish a Single Component Synchrotron Afterglow Origin for the Late Optical to Multi-GeV Emission. ApJ, 779(1):L1, Dec. 2013. doi: 10.1088/2041-8205/779/1/L1.

H. A. Krimm, S. D. Barthelmy, J. R. Cummings, J. D. Gropp, A. Y. Lien, C. B. Markwardt, D. M. Palmer, T. Sakamoto, M. Stamatikos, and T. N. Ukwatta. GRB 190114C: Swift-BAT refined analysis. GRB Coordinates Network, 23724:1, Jan. 2019.

P. Kumar and B. Zhang. The physics of gamma-ray bursts & relativistic jets. Phys. Rep., 561: 1–109, Feb. 2015. doi: 10.1016/j.physrep.2014.09.008.

I. Kuvvetli. Development of CdZnTe detector systems for space applications. PhD thesis, Technical University of Denmark, 2003.

I. Kuvvetli, C. Budtz-Jørgensen, E. Caroli, and N. Auricchio. CZT drift strip detectors for high energy astrophysics. Nuclear Instruments and Methods in Physics Research A, 624(2): 486–491, Dec. 2010. doi: 10.1016/j.nima.2010.03.172.

C. Labanti, G. Di Cocco, G. Ferro, F. Gianotti, A. Mauri, E. Rossi, J. B. Stephen, A. Traci, and M. Trifoglio. The Ibis-Picsit detector onboard Integral. A&A, 411:L149–L152, Nov. 2003. doi: 10.1051/0004-6361:20031356.

J. H. Lau. Recent advances and new trends in flip chip technology. Journal of Electronic Packaging, 138(3):030802, 2016.

D. Lazzati. X-ray polarization of gamma-ray bursts. In X-ray Polarimetry, pages 202–208. Cambridge University Press, jul 2010. doi: 10.1017/cbo9780511750809.031. URL https://doi.org/10.1017%2Fcbo9780511750809.031.

F. Lei, A. J. Dean, and G. L. Hills. Compton Polarimetry in Gamma-Ray Astronomy. Space Sci. Rev., 82:309–388, Nov. 1997. doi: 10.1023/A:1005027107614.

A. J. Levan, N. R. Tanvir, A. S. Fruchter, J. Hjorth, E. Pian, P. Mazzali, R. A. Hounsell, D. A. Perley, Z. Cano, J. Graham, S. B. Cenko, J. P. U. Fynbo, C. Kouveliotou, A. Pe'er, K. Misra, and K. Wiersema. Hubble Space Telescope Observations of the Afterglow, Supernova, and Host Galaxy Associated with the Extremely Bright GRB 130427A. ApJ, 792(2):115, Sept. 2014. doi: 10.1088/0004-637X/792/2/115.

M. Leventhal, C. J. MacCallum, and P. D. Stang. Detection of 511 keV positron annihilation radiation from the galactic center direction. ApJ, 225:L11–L14, Oct. 1978. doi: 10.1086/182782.

M. Leventhal, C. J. MacCallum, A. F. Huters, and P. D. Stang. Gamma-ray lines and continuum radiation from the galactic center direction. ApJ, 240:338–343, Aug. 1980. doi: 10.1086/158237.

C. K. Li, L. Lin, S. L. Xiong, M. Y. Ge, X. B. Li, T. P. Li, F. J. Lu, S. N. Zhang, Y. L. Tuo, Y. Nang, B. Zhang, S. Xiao, Y. Chen, L. M. Song, Y. P. Xu, C. Z. Liu, S. M. Jia, X. L. Cao, J. L. Qu, S. Zhang, Y. D. Gu, J. Y. Liao, X. F. Zhao, Y. Tan, J. Y. Nie, H. S. Zhao, S. J. Zheng, Y. G. Zheng, Q. Luo, C. Cai, B. Li, W. C. Xue, Q. C. Bu, Z. Chang, G. Chen, L. Chen, T. X. Chen, Y. B. Chen, Y. P. Chen, W. Cui, W. W. Cui, J. K. Deng, Y. W. Dong, Y. Y. Du, M. X. Fu, G. H. Gao, H. Gao, M. Gao, Y. D. Gu, J. Guan, C. C. Guo, D. W. Han, Y. Huang, J. Huo, L. H. Jiang, W. C. Jiang, J. Jin, Y. J. Jin, L. D. Kong, G. Li, M. S. Li, W. Li, X. Li, X. F. Li, Y. G. Li, Z. W. Li, X. H. Liang, B. S. Liu, G. Q. Liu, H. W. Liu, X. J. Liu, Y. N. Liu, B. Lu, X. F. Lu, T. Luo, X. Ma, B. Meng, G. Ou, N. Sai, R. C. Shang, X. Y. Song, L. Sun, L. Tao, C. Wang, G. F. Wang, J. Wang, W. S. Wang, Y. S. Wang, X. Y. Wen, B. B. Wu, B. Y. Wu, M. Wu, G. C. Xiao, H. Xu, J. W. Yang, S. Yang, Y. J. Yang, Y.-J. Yang, Q. B. Yi,

Q. Q. Yin, Y. You, A. M. Zhang, C. M. Zhang, F. Zhang, H. M. Zhang, J. Zhang, T. Zhang, W. Zhang, W. C. Zhang, W. Z. Zhang, Y. Zhang, Y. Zhang, Y. F. Zhang, Y. J. Zhang, Z. Zhang, Z. Zhang, Z. L. Zhang, D. K. Zhou, J. F. Zhou, Y. Zhu, Y. X. Zhu, and R. L. Zhuang. Hxmt identification of a non-thermal x-ray burst from sgr j1935+2154 and with frb 200428. Nature Astronomy, 5(4):378–384, Feb. 2021. ISSN 2397-3366. doi: 10.1038/s41550-021-01302-6. URL http://dx.doi.org/10.1038/s41550-021-01302-6.

E. Liang, B. Zhang, F. Virgili, and Z. G. Dai. Low-luminosity gamma-ray bursts as a unique population: Luminosity function, local rate, and beaming factor. The Astrophysical Journal, 662(2):1111–1118, jun 2007. doi: 10.1086/517959. URL https://doi.org/10.1086%2F517959.

O. Limousin, J. M. Duda, F. Lebrun, and J. P. Leray. The basic component of the ISGRI CdTe /γ-ray camera for space telescope IBIS on board the INTEGRAL satellite. Nuclear Instruments and Methods in Physics Research A, 428(1):216–222, June 1999. doi: 10.1016/S0168-9002(99)00009-1.

R. P. Lin and RHESSI Team. The Ramaty High Energy Solar Spectroscopic Imager (RHESSI) Mission. In American Astronomical Society Meeting Abstracts #200, volume 200 of American Astronomical Society Meeting Abstracts, page 76.01, May 2002.

B. Link, R. I. Epstein, and W. C. Priedhorsky. Prevalent Properties of Gamma-Ray Burst Variability. ApJ, 408:L81, May 1993. doi: 10.1086/186836.

C. Liu, Y. Zhang, X. Li, X. Lu, Z. Chang, Z. Li, A. Zhang, Y. Jin, H. Yu, Z. Zhang, M. Fu, Y. Chen, J. Ji, Y. Xu, J. Deng, R. Shang, G. Liu, F. Lu, S. Zhang, Y. Dong, T. Li, M. Wu, Y. Li, H. Wang, B. Wu, Y. Zhang, Z. Zhang, S. Xiong, Y. Liu, S. Zhang, H. Liu, Y. Yang, and F. Zhang. The High Energy X-ray telescope (HE) onboard the Insight-HXMT astronomy satellite. Science China Physics, Mechanics, and Astronomy, 63(4):249503, Apr. 2020. doi: 10.1007/s11433-019-1486-x.

T. Liu, P. Tozzi, J.-X. Wang, W. N. Brandt, C. Vignali, Y. Xue, D. P. Schneider, A. Comastri, G. Yang, F. E. Bauer, M. Paolillo, B. Luo, R. Gilli, Q. D. Wang, M. Giavalisco, Z. Ji, D. M. Alexander, V. Mainieri, O. Shemmer, A. Koekemoer, and G. Risaliti. X-ray spectral analyses of agns from the 7ms chandra deep field-south survey: The distribution, variability, and evolutions of agn obscuration. The Astrophysical Journal Supplement Series, 232(1):8, aug 2017. doi: 10.3847/1538-4365/aa7847. URL https://dx.doi.org/10.3847/1538-4365/aa7847.

G. Loffredo, F. Frontera, D. Pellicciotta, A. Pisa, V. Carassiti, S. Chiozzi, F. Evangelisti, L. Landi, M. Melchiorri, and S. Squerzanti. The Ferrara hard X-ray facility for testing/calibrating hard X-ray focusing telescopes. Experimental Astronomy, 20(1-3):413–420, Dec. 2005. doi: 10.1007/s10686-006-9049-y.

N. Lund. Technologies for tunable gamma-ray lenses. Experimental Astronomy, 51(1):165–179, Feb. 2021. doi: 10.1007/s10686-020-09683-8.

N. Lund, N. J. Westergaard, S. Brandt, A. Hornstrup, and C. Budtz-Jørgensen. The scientific role of JEM-X: The X-ray monitor on INTEGRAL. In M. L. McConnell and J. M. Ryan, editors, The Fifth Compton Symposium, volume 510 of American Institute of Physics Conference Series, pages 727–731, Apr. 2000. doi: 10.1063/1.1303295.

D. Lynden-Bell. Galactic nuclei as collapsed old quasars. Nature, 223(5207):690–694, Aug 1969. ISSN 1476-4687. doi: 10.1038/223690a0. URL https://doi.org/10.1038/223690a0.

R. Maccary, C. Guidorzi, L. Amati, L. Bazzanini, M. Bulla, A. E. Camisasca, L. Ferro, F. Frontera, and A. Tsvetkova. Distributions of energy, luminosity, duration, and waiting times of gamma-ray burst pulses with known redshift detected by Fermi/GBM. arXiv e-prints, art. arXiv:2401.14063, Jan. 2024. doi: 10.48550/arXiv.2401.14063.

MAGIC Collaboration, V. A. Acciari, S. Ansoldi, L. A. Antonelli, A. Arbet Engels, D. Baack, A. Babić, B. Banerjee, U. Barres de Almeida, J. A. Barrio, J. Becerra González, W. Bednarek, L. Bellizzi, E. Bernardini, A. Berti, J. Besenrieder, W. Bhattacharyya, C. Bigongiari, A. Biland, O. Blanch, G. Bonnoli, Ž. Bošnjak, G. Busetto, A. Carosi, R. Carosi, G. Ceribella, Y. Chai, A. Chilingaryan, S. Cikota, S. M. Colak, U. Colin, E. Colombo, J. L. Contreras, J. Cortina, S. Covino, G. D'Amico, V. D'Elia, P. da Vela, F. Dazzi, A. de Angelis, B. de Lotto, M. Delfino, J. Delgado, D. Depaoli, F. di Pierro, L. di Venere, E. Do Souto Espiñeira, D. Dominis Prester, A. Donini, D. Dorner, M. Doro, D. Elsaesser, V. Fallah Ramazani, A. Fattorini, A. Fernández-Barral, G. Ferrara, D. Fidalgo, L. Foffano, M. V. Fonseca, L. Font, C. Fruck, S. Fukami, S. Gallozzi, R. J. García López, M. Garczarczyk, S. Gasparyan, M. Gaug, N. Giglietto, F. Giordano, N. Godinović, D. Green, D. Guberman, D. Hadasch, A. Hahn, J. Herrera, J. Hoang, D. Hrupec, M. Hütten, T. Inada, S. Inoue, K. Ishio, Y. Iwamura, L. Jouvin, D. Kerszberg, H. Kubo, J. Kushida, A. Lamastra, D. Lelas, F. Leone, E. Lindfors, S. Lombardi, F. Longo, M. López, R. López-Coto, A. López-Oramas, S. Loporchio, B. Machado de Oliveira Fraga, C. Maggio, P. Majumdar, M. Makariev, M. Mallamaci, G. Maneva, M. Manganaro, K. Mannheim, L. Maraschi, M. Mariotti, M. Martínez, S. Masuda, D. Mazin, S. Mićanović, D. Miceli, M. Minev, J. M. Miranda, R. Mirzoyan, E. Molina, A. Moralejo, D. Morcuende, V. Moreno, E. Moretti, P. Munar-Adrover, V. Neustroev, C. Nigro, K. Nilsson, D. Ninci, K. Nishijima, K. Noda, L. Nogués, M. Nöthe, S. Nozaki, S. Paiano, J. Palacio, M. Palatiello, D. Paneque, R. Paoletti, J. M. Paredes, P. Peñil, M. Peresano, M. Persic, P. G. Prada Moroni, E. Prandini, I. Puljak, W. Rhode, M. Ribó, J. Rico, C. Righi, A. Rugliancich, L. Saha, N. Sahakyan, T. Saito, S. Sakurai, K. Satalecka, K. Schmidt, T. Schweizer, J. Sitarek, I. Šnidarić, D. Sobczynska, A. Somero, A. Stamerra, D. Strom, M. Strzys, Y. Suda, T. Surić, M. Takahashi, F. Tavecchio, P. Temnikov, T. Terzić, M. Teshima, N. Torres-Albà, L. Tosti, S. Tsujimoto, V. Vagelli, J. van Scherpenberg, G. Vanzo, M. Vazquez Acosta, C. F. Vigorito, V. Vitale, I. Vovk, M. Will, D. Zarić, and L. Nava. Teraelectronvolt emission from the γ-ray burst GRB 190114C. Nature, 575(7783):455–458, Nov. 2019. doi: 10.1038/s41586-019-1750-x.

E. Maiorano, N. Masetti, E. Palazzi, F. Frontera, P. Grandi, E. Pian, L. Amati, L. Nicastro, P. Soffitta, C. Guidorzi, R. Landi, E. Montanari, M. Orlandini, A. Corsi, L. Piro, L. A. Antonelli, E. Costa, M. Feroci, J. Heise, E. Kuulkers, and J. J. M. in 't Zand. The puzzling case of GRB 990123: multiwavelength afterglow study. Astronomy & Astrophysics, 438(3): 821–827, jul 2005. doi: 10.1051/0004-6361:20042534. URL https://doi.org/10.1051%2F0004-6361%3A20042534.

C. Malgrange. X-ray propagation in distorted crystals: From dynamical to kinematical theory. Crystal Research and Technology, 37(7):654–662, 2002. doi: https://doi.org/10.1002/1521-4079(200207)37:7<654::AID-CRAT654>3.0.CO;2-E. URL https://onlinelibrary.wiley.com/doi/abs/10.1002/1521-4079%28200207%2937%3A7%3C654%3A%3AAID-CRAT654%3E3.0.CO%3B2-E.

R. Margutti, E. Zaninoni, M. G. Bernardini, G. Chincarini, F. Pasotti, C. Guidorzi, L. Angelini, D. N. . Burrows, M. Capalbi, P. A. Evans, N. Gehrels, J. Kennea, V. Mangano, A. Moretti, J. Nousek, J. P. Osborne, M. Page, K. L. a nd Perri, J. Racusin, P. Romano, B. Sbarufatti, S. Stafford, and M. Stamatikos. The prompt-afterglow connection in gamma-ray bursts: a

comprehensive statistical analysis of Swift X-ray light curves. MNRAS, 428:729–742, Jan. 2013. doi: 10.1093/mnras/sts066.

M. Marisaldi, C. Labanti, and H. Soltau. A pulse shape discrimination gamma-ray detector based on a silicon drift chamber coupled to a CsI(Tl) scintillator: prospects for a 1 keV-1 MeV monolithic detector. IEEE Transactions on Nuclear Science, 51(4):1916–1922, 2004. doi: 10.1109/TNS.2004.832679.

A. Martin-Carrillo, L. Hanlon, M. Topinka, A. P. LaCluyzé, V. Savchenko, D. A. Kann, A. S. Trotter, S. Covino, T. Krühler, J. Greiner, S. McGlynn, D. Murphy, P. Tisdall, S. Meehan, C. Wade, B. McBreen, D. E. Reichart, D. Fugazza, J. B. Haislip, A. Rossi, P. Schady, J. Elliott, and S. Klose. GRB 120711A: an intense INTEGRAL burst with long-lasting soft γ-ray emission and a powerful optical flash. A&A, 567:A84, July 2014. doi: 10.1051/0004-6361/201220872.

J. M. Mas-Hesse, A. Giménez, A. Domingo, D. Rísquez, and M. D. Caballero. The Optical Monitoring Camera Onboard INTEGRAL. In The Obscured Universe. Proceedings of the VI INTEGRAL Workshop, volume 622 of ESA Special Publication, page 623, Jan. 2007.

A. Mazzolari, F. Frontera, M. Romagnoni, V. Guidi, M. Tamisari, L. Ferro, M. Moita, P. Rosati, C. Guidorzi, L. Bandiera, L. Malagutti, M. Orlandini, E. Virgilli, N. Auricchio, E. Caroli, J. Stephen, and R. Verbeni. Anodic bonding to manufacture LAUE lenses for high-energy astrophysics. In EUV and X-ray Optics: Synergy between Laboratory and Space VIII, volume 12576 of Society of Photo-Optical Instrumentation Engineers (SPIE) Conference Series, page 125760F, June 2023. doi: 10.1117/12.2665894.

M. L. McConnell. High energy polarimetry of prompt GRB emission. New Astronomy Reviews, 76:1–21, feb 2017. doi: 10.1016/j.newar.2016.11.001. URL https://doi.org/10.1016%2Fj.newar.2016.11.001.

C. Meegan, G. Lichti, P. N. Bhat, E. Bissaldi, M. S. Briggs, V. Connaughton, R. Diehl, G. Fishman, J. Greiner, A. S. Hoover, A. J. van der Horst, A. von Kienlin, R. M. Kippen, C. Kouveliotou, S. McBreen, W. S. Paciesas, R. Preece, H. Steinle, M. S. Wallace, R. B. Wilson, and C. Wilson-Hodge. The Fermi Gamma-ray Burst Monitor. ApJ, 702(1):791–804, Sept. 2009. doi: 10.1088/0004-637X/702/1/791.

S. Mereghetti, V. Savchenko, C. Ferrigno, D. Götz, M. Rigoselli, A. Tiengo, A. Bazzano, E. Bozzo, A. Coleiro, T. J.-L. Courvoisier, M. Doyle, A. Goldwurm, L. Hanlon, E. Jourdain, A. von Kienlin, A. Lutovinov, A. Martin-Carrillo, S. Molkov, L. Natalucci, F. Onori, F. Panessa, J. Rodi, J. Rodriguez, C. Sánchez-Fernández, R. Sunyaev, and P. Ubertini. Integral discovery of a burst with associated radio emission from the magnetar sgr 1935+2154. The Astrophysical Journal Letters, 898(2):L29, jul 2020. doi: 10.3847/2041-8213/aba2cf. URL https://dx.doi.org/10.3847/2041-8213/aba2cf.

A. Meuris, A. Arhancet, D. Bachet, F. Ceraudo, E. Doumayrou, L. Dumaye, A. Goetschy, D. Götz, B. Horeau, D. D. Huynh, T. Lavanant, M. Lortholary, I. L. Mer, F. Nico, F. Pinsard, M. Prieur, L. Provost, D. Renaud, N. Renault-Tinacci, B. Schneider, T. Tourrette, F. Visticot, K. Mercier, and N. Meidinger. Design and performance of the camera of the Micro-channel X-ray Telescope on-board the SVOM mission. Nuclear Instruments and Methods in Physics Research A, 1049:167908, Apr. 2023. doi: 10.1016/j.nima.2022.167908.

I. G. Mitrofanov. New statistics of gamma-ray bursts: average time histories and energy spectra. Mem. Soc. Astron. Italiana, 67:417, Jan. 1996.

T. Mizuno, T. Kamae, G. Godfrey, T. Handa, D. J. Thompson, D. Lauben, Y. Fukazawa, and M. Ozaki. Cosmic-Ray Background Flux Model Based on a Gamma-Ray Large Area Space Telescope Balloon Flight Engineering Model. ApJ, 614(2):1113–1123, Oct. 2004. doi: 10.1086/423801.

M. Moita, L. Ferro, E. Caroli, E. Virgilli, R. M. Curado da Silva, N. Auricchio, S. del Sordo, J. M. Maia, and J. B. Stephen. A monte carlo study of a 3d czt spectroscopic imager for scattering polarimetry. In 2020 IEEE Nuclear Science Symposium and Medical Imaging Conference (NSS/MIC), pages 1–6, 2020. doi: 10.1109/NSS/MIC42677.2020.9507808.

M. Moita, L. Ferro, E. Caroli, E. Virgilli, F. Frontera, J. B. Stephen, R. M. Curado Da Silva, J. M. Maia, and S. Del Sordo. Astena's polarimetric prospects. In 2021 IEEE Nuclear Science Symposium and Medical Imaging Conference (NSS/MIC), pages 1–7, 2021. doi: 10.1109/NSS/MIC44867.2021.9875607.

M. Moita, L. Ferro, E. Caroli, L. Cavazzini, R. M. C. da Silva, J. B. Stephen, and E. Virgilli. Monte Carlo study of a 3D CZT spectroscopic-imager for scattering polarimetry. Nuclear Instruments and Methods in Physics Research A, 1048:167870, Mar. 2023. doi: 10.1016/j.nima.2022.167870.

M. Molina, A. Malizia, L. Bassani, A. J. Bird, A. J. Dean, R. Landi, A. De Rosa, R. Walter, E. J. Barlow, D. J. Clark, A. B. Hill, and V. Sguera. Integral observations of active galactic nuclei obscured by the galactic plane. Monthly Notices of the Royal Astronomical Society, 371(2):821–828, Sept. 2006. ISSN 1365-2966. doi: 10.1111/j.1365-2966.2006.10715.x. URL http://dx.doi.org/10.1111/j.1365-2966.2006.10715.x.

B. J. Morsony, D. Lazzati, and M. C. Begelman. The Origin and Propagation of Variability in the Outflows of Long-duration Gamma-ray Bursts. ApJ, 723(1):267–276, Nov. 2010. doi: 10.1088/0004-637X/723/1/267.

M. Negro, N. D. Lalla, N. Omodei, P. Veres, S. Silvestri, A. Manfreda, E. Burns, L. Baldini, E. Costa, S. R. Ehlert, and e. a. Jamie A. Kennea. The ixpe view of grb 221009a. The Astrophysical Journal Letters, 946(1):L21, mar 2023. doi: 10.3847/2041-8213/acba17. URL https://dx.doi.org/10.3847/2041-8213/acba17.

L. Nicastro, C. Guidorzi, E. Palazzi, L. Zampieri, M. Turatto, and A. Gardini. Multiwavelength Observations of Fast Radio Bursts. Universe, 7(3):76, Mar. 2021. doi: 10.3390/universe7030076.

J. P. Norris, R. J. Nemiroff, J. T. Bonnell, J. D. Scargle, C. Kouveliotou, W. S. Paciesas, C. A. Meegan, and G. J. Fishman. Attributes of Pulses in Long Bright Gamma-Ray Bursts. ApJ, 459:393, Mar. 1996. doi: 10.1086/176902.

P. O'Brien, I. Hutchinson, H. N. Lerman, C. H. Feldman, M. McHugh, A. Lodge, R. Willingale, A. Beardmore, R. Speight, and P. Drumm. The soft x-ray imager on theseus: the transient high energy survey and early universe surveyor, 2021.

S. A. Olausen and V. M. Kaspi. The McGill Magnetar Catalog. ApJS, 212(1):6, May 2014. doi: 10.1088/0067-0049/212/1/6.

W. S. Paciesas, C. A. Meegan, G. N. Pendleton, M. S. Briggs, C. Kouveliotou, T. M. Koshut, J. P. Lestrade, M. L. McCollough, J. J. Brainerd, J. Hakkila, W. Henze, R. D.

Preece, V. Connaughton, R. M. Kippen, R. S. Mallozzi, G. J. Fishman, G. A. Richardson, and M. Sahi. The fourth batse gamma-ray burst catalog (revised). The Astrophysical Journal Supplement Series, 122(2):465, jun 1999. doi: 10.1086/313224. URL https://dx.doi.org/10.1086/313224.

Parisi, P., Masetti, N., Jiménez-Bailón, E., Chavushyan, V., Malizia, A., Landi, R., Molina, M., Fiocchi, M., Palazzi, E., Bassani, L., Bazzano, A., Bird, A. J., Dean, A. J., Galaz, G., Mason, E., Minniti, D., Morelli, L., Stephen, J. B., and Ubertini, P. Accurate classification of 17 agns detected with swift/bat*. A&A, 507(3):1345–1358, 2009. doi: 10.1051/0004-6361/200912931. URL https://doi.org/10.1051/0004-6361/200912931.

G. C. Perola, G. Matt, M. Cappi, F. Fiore, M. Guainazzi, L. Maraschi, P. O. Petrucci, and L. Piro. Compton reflection and iron fluorescence in bepposax observations of seyfert type 1 galaxies. Astronomy & Astrophysics, 389(3):802–811, July 2002. ISSN 1432-0746. doi: 10.1051/0004-6361:20020658. URL http://dx.doi.org/10.1051/0004-6361:20020658.

E. Petroff, J. W. T. Hessels, and D. R. Lorimer. Fast radio bursts at the dawn of the 2020s. A&A Rev., 30(1):2, Dec. 2022. doi: 10.1007/s00159-022-00139-w.

P. Pfistner, M. Caselle, T. Blank, and M. Weber. Novel production method for large double-sided microstrip detectors of the CBM Silicon Tracking System at FAIR. In Proceedings of Topical Workshop on Electronics for Particle Physics — PoS(TWEPP2018), volume 343, page 144, 2019. doi: 10.22323/1.343.0144.

M. M. Phillips. The Absolute Magnitudes of Type IA Supernovae. ApJ, 413:L105, Aug. 1993. doi: 10.1086/186970.

S. Poolakkil, R. Preece, C. Fletcher, A. Goldstein, P. N. Bhat, E. Bissaldi, M. S. Briggs, E. Burns, W. H. Cleveland, M. M. Giles, C. M. Hui, D. Kocevski, S. Lesage, B. Mailyan, C. Malacaria, W. S. Paciesas, O. J. Roberts, P. Veres, A. von Kienlin, and C. A. Wilson-Hodge. The Fermi-GBM Gamma-Ray Burst Spectral Catalog: 10 yr of Data. ApJ, 913(1):60, May 2021. doi: 10.3847/1538-4357/abf24d.

N. Prantzos, C. Boehm, A. M. Bykov, R. Diehl, K. Ferrière, N. Guessoum, P. Jean, J. Knoedlseder, A. Marcowith, I. V. Moskalenko, A. Strong, and G. Weidenspointner. The 511 keV emission from positron annihilation in the Galaxy. Reviews of Modern Physics, 83(3):1001–1056, July 2011. doi: 10.1103/RevModPhys.83.1001.

N. Produit, T. W. Bao, T. Batsch, T. Bernasconi, I. Britvich, F. Cadoux, I. Cernuda, J. Y. Chai, Y. W. Dong, N. Gauvin, W. Hajdas, M. Kole, M. N. Kong, R. Kramert, L. Li, J. T. Liu, X. Liu, R. Marcinkowski, S. Orsi, M. Pohl, D. Rapin, D. Rybka, A. Rutczynska, H. L. Shi, P. Socha, J. C. Sun, L. M. Song, J. Szabelski, I. Traseira, H. L. Xiao, R. J. Wang, X. Wen, B. B. Wu, L. Zhang, L. Y. Zhang, S. N. Zhang, Y. J. Zhang, and A. Zwolinska. Design and construction of the POLAR detector. Nuclear Instruments and Methods in Physics Research A, 877:259–268, Jan. 2018. doi: 10.1016/j.nima.2017.09.053.

W. R. Purcell, D. A. Grabelsky, M. P. Ulmer, W. N. Johnson, R. L. Kinzer, J. D. Kurfess, M. S. Strickman, and G. V. Jung. OSSE Observations of Galactic 511 keV Positron Annihilation Radiation: Initial Phase 1 Results. ApJ, 413:L85, Aug. 1993. doi: 10.1086/186965.

W. R. Purcell, L. X. Cheng, D. D. Dixon, R. L. Kinzer, J. D. Kurfess, M. Leventhal, M. A. Saunders, J. G. Skibo, D. M. Smith, and J. Tueller. OSSE Mapping of Galactic 511 keV Positron Annihilation Line Emission. ApJ, 491(2):725–748, Dec. 1997. doi: 10.1086/304994.

M. Pursiainen, M. Childress, M. Smith, S. Prajs, M. Sullivan, T. M. Davis, R. J. Foley, J. Asorey, J. Calcino, D. Carollo, C. Curtin, C. B. D'Andrea, K. Glazebrook, C. Gutierrez, and e. a. Hinton. Rapidly evolving transients in the Dark Energy Survey. MNRAS, 481(1):894–917, Nov. 2018. doi: 10.1093/mnras/sty2309.

J. Pétri. Phase-resolved polarization properties of the pulsar striped wind synchrotron emission. Monthly Notices of the Royal Astronomical Society, 434(3):2636–2644, Jul 2013. ISSN 1365-2966. doi: 10.1093/mnras/stt1214. URL http://dx.doi.org/10.1093/mnras/stt1214.

V. Ravi, M. Catha, L. D'Addario, S. G. Djorgovski, G. Hallinan, R. Hobbs, J. Kocz, S. R. Kulkarni, J. Shi, H. K. Vedantham, S. Weinreb, and D. P. Woody. A fast radio burst localized to a massive galaxy. Nature, 572(7769):352–354, Aug. 2019. doi: 10.1038/s41586-019-1389-7.

D. Reitze, R. X. Adhikari, S. Ballmer, B. Barish, L. Barsotti, G. Billingsley, D. A. Brown, Y. Chen, D. Coyne, R. Eisenstein, M. Evans, P. Fritschel, E. D. Hall, A. Lazzarini, G. Lovelace, J. Read, B. S. Sathyaprakash, D. Shoemaker, J. Smith, C. Torrie, S. Vitale, R. Weiss, C. Wipf, and M. Zucker. Cosmic explorer: The u.s. contribution to gravitational-wave astronomy beyond ligo, 2019.

A. Ridnaia, D. Svinkin, D. Frederiks, A. Bykov, S. Popov, R. Aptekar, S. Golenetskii, A. Lysenko, A. Tsvetkova, M. Ulanov, and T. L. Cline. A peculiar hard x-ray counterpart of a galactic fast radio burst. Nature Astronomy, 5(4):372–377, Apr 2021. ISSN 2397-3366. doi: 10.1038/s41550-020-01265-0. URL https://doi.org/10.1038/s41550-020-01265-0.

R. Rojas. Neural Networks: A Systematic Introduction. Springer Nature, 1996.

P. W. A. Roming, S. D. Hunsberger, C. Gronwall, J. A. Nousek, A. A. Breeveld, K. O. Mason, UVOT PSU Team, UVOT MSSL Team, and UVOT SwRI Team. The Swift Ultra-Violet/Optical Telescope. In American Astronomical Society Meeting Abstracts, volume 205 of American Astronomical Society Meeting Abstracts, page 160.03, Dec. 2004.

S. J. Russell and P. Norvig. Artificial Intelligence: a modern approach. Pearson, 4 edition, 2021.

O. S. Salafia and G. Ghirlanda. The structure of gamma ray burst jets, 2022.

A. Savitzky and M. J. E. Golay. Smoothing and differentiation of data by simplified least squares procedures. Analytical Chemistry, 36:1627–1639, Jan. 1964. doi: 10.1021/ac60214a047.

S. Sazonov, E. Churazov, R. Sunyaev, and M. Revnivtsev. Hard X-ray emission of the Earth's atmosphere: Monte Carlo simulations. MNRAS, 377(4):1726–1736, June 2007. doi: 10.1111/j.1365-2966.2007.11746.x.

S. Schanne, B. Cordier, P. Guillemot, A. Gros, N. Dagoneau, J.-L. Atteia, F. Château, F. Daly, and H. Le Provost. The gamma-ray burst trigger ECLAIRs on-board SVOM. In 42nd COSPAR Scientific Assembly, volume 42, pages E1.17–37–18, July 2018.

G. H. Share, M. D. Leising, D. C. Messina, and W. R. Purcell. Limits on a Variable Source of 511 keV Annihilation Radiation near the Galactic Center. ApJ, 358:L45, Aug. 1990. doi: 10.1086/185776.

T. Siegert. The Positron Puzzle. Ap&SS, 368(4):27, Apr. 2023. doi: 10.1007/s10509-023-04184-4.

T. Siegert, R. Diehl, A. C. Vincent, F. Guglielmetti, M. G. H. Krause, and C. Boehm. Search for 511 keV emission in satellite galaxies of the Milky Way with INTEGRAL/SPI. A&A, 595: A25, Oct. 2016. doi: 10.1051/0004-6361/201629136.

P. Soffitta, L. Baldini, R. Bellazzini, E. Costa, L. Latronico, F. Muleri, E. D. Monte, S. Fabiani, M. Minuti, M. Pinchera, C. Sgro', G. Spandre, A. Trois, F. Amici, H. Andersson, and e. a. Primo Attina'. The instrument of the imaging x-ray polarimetry explorer. The Astronomical Journal, 162(5):208, oct 2021. doi: 10.3847/1538-3881/ac19b0. URL https://doi.org/10.3847%2F1538-3881%2Fac19b0.

X.-Y. Song, S.-L. Xiong, S.-N. Zhang, C.-K. Li, X.-B. Li, Y. Huang, C. Guidorzi, F. Frontera, C.-Z. Liu, X.-F. Li, G. Li, J.-Y. Liao, C. Cai, Q. Luo, S. Xiao, Q.-B. Yi, Y.-G. Zheng, D.-K. Zhou, J.-C. Liu, W.-C. Xue, Y.-Q. Zhang, C. Zheng, Z. Chang, Z.-W. Li, X.-F. Lu, A.-M. Zhang, Y.-F. Zhang, Y.-J. Jin, T.-P. Li, F.-J. Lu, L.-M. Song, M. Wu, Y.-P. Xu, X. Ma, M.-Y. Ge, S.-M. Jia, B. Li, J.-Y. Nie, L.-J. Wang, J. Zhang, S.-J. Zheng, X.-J. Yang, and R.-J. Yang. The first insight-hxmt gamma-ray burst catalog: The first four years. The Astrophysical Journal Supplement Series, 259(2):46, mar 2022. doi: 10.3847/1538-4365/ac4d22. URL https://dx.doi.org/10.3847/1538-4365/ac4d22.

B. E. Stern. A Stretched Exponential Law for the Average Time History of Gamma-Ray Bursts and Their Time Dilations. ApJ, 464:L111, June 1996. doi: 10.1086/310113.

B. E. Stern and R. Svensson. Evidence for "chain reaction" in the time profiles of gamma-ray bursts. The Astrophysical Journal, 469(2):L109, 1996.

A. Summa, A. Ulyanov, M. Kromer, S. Boyer, F. K. Röpke, S. A. Sim, I. R. Seitenzahl, M. Fink, K. Mannheim, R. Pakmor, F. Ciaraldi-Schoolmann, R. Diehl, K. Maeda, and W. Hillebrandt. Gamma-ray diagnostics of Type Ia supernovae. Predictions of observables from three-dimensional modeling. A&A, 554:A67, June 2013. doi: 10.1051/0004-6361/201220972.

SVOM Collaboration, J. L. Atteia, B. Cordier, and J. Wei. The SVOM mission. In The Sixteenth Marcel Grossmann Meeting. On Recent Developments in Theoretical and Experimental General Relativity, Astrophysics, and Relativistic Field Theories, pages 104–132, July 2023. doi: 10.1142/9789811269776_0007.

M. Tavani, C. Casentini, A. Ursi, F. Verrecchia, A. Addis, L. A. Antonelli, A. Argan, G. Barbiellini, L. Baroncelli, G. Bernardi, G. Bianchi, A. Bulgarelli, P. Caraveo, M. Cardillo, P. W. Cattaneo, A. W. Chen, E. Costa, E. D. Monte, G. D. Cocco, G. D. Persio, I. Donnarumma, Y. Evangelista, M. Feroci, A. Ferrari, V. Fioretti, F. Fuschino, M. Galli, F. Gianotti, A. Giuliani, C. Labanti, F. Lazzarotto, P. Lipari, F. Longo, F. Lucarelli, A. Magro, M. Marisaldi, S. Mereghetti, E. Morelli, A. Morselli, G. Naldi, L. Pacciani, N. Parmiggiani, F. Paoletti, A. Pellizzoni, M. Perri, F. Perotti, G. Piano, P. Picozza, M. Pilia, C. Pittori, S. Puccetti, G. Pupillo, M. Rapisarda, A. Rappoldi, A. Rubini, G. Setti, P. Soffitta, M. Trifoglio, A. Trois, S. Vercellone, V. Vittorini, P. Giommi, and F. D. Amico. An x-ray burst from a magnetar enlightening the mechanism of fast radio bursts, 2020.

Tavani, M., Barbiellini, G., Argan, A., Boffelli, F., Bulgarelli, A., Caraveo, P., Cattaneo, P. W., Chen, A. W., Cocco, V., Costa, E., D'Ammando, F., Del Monte, E., De Paris, G., Di Cocco, G., Di Persio, G., Donnarumma, I., Evangelista, Y., Feroci, M., Ferrari, A., Fiorini, M., Fornari, F., Fuschino, F., Froysland, T., Frutti, M., Galli, M., Gianotti, F., Giuliani, A., Labanti, C., Lapshov, I., Lazzarotto, F., Liello, F., Lipari, P., Longo, F., Mattaini, E., Marisaldi, M., Mastropietro, M., Mauri, A., Mauri, F., Mereghetti, S., Morelli, E., Morselli, A., Pacciani,

L., Pellizzoni, A., Perotti, F., Piano, G., Picozza, P., Pontoni, C., Porrovecchio, G., Prest, M., Pucella, G., Rapisarda, M., Rappoldi, A., Rossi, E., Rubini, A., Soffitta, P., Traci, A., Trifoglio, M., Trois, A., Vallazza, E., Vercellone, S., Vittorini, V., Zambra, A., Zanello, D., Pittori, C., Preger, B., Santolamazza, P., Verrecchia, F., Giommi, P., Colafrancesco, S., Antonelli, A., Cutini, S., Gasparrini, D., Stellato, S., Fanari, G., Primavera, R., Tamburelli, F., Viola, F., Guarrera, G., Salotti, L., D'Amico, F., Marchetti, E., Crisconio, M., Sabatini, P., Annoni, G., Alia, S., Longoni, A., Sanquerin, R., Battilana, M., Concari, P., Dessimone, E., Grossi, R., Parise, A., Monzani, F., Artina, E., Pavesi, R., Marseguerra, G., Nicolini, L., Scandelli, L., Soli, L., Vettorello, V., Zardetto, E., Bonati, A., Maltecca, L., D'Alba, E., Patané, M., Babini, G., Onorati, F., Acquaroli, L., Angelucci, M., Morelli, B., Agostara, C., Cerone, M., Michetti, A., Tempesta, P., D'Eramo, S., Rocca, F., Giannini, F., Borghi, G., Garavelli, B., Conte, M., Balasini, M., Ferrario, I., Vanotti, M., Collavo, E., and Giacomazzo, M. The agile mission. A&A, 502(3):995–1013, 2009. doi: 10.1051/0004-6361/200810527. URL https://doi.org/10.1051/0004-6361/200810527.

R. Taverna, R. Turolla, F. Muleri, J. Heyl, S. Zane, L. Baldini, D. González-Caniulef, M. Bachetti, J. Rankin, I. Caiazzo, N. D. Lalla, V. Doroshenko, M. Errando, E. Gau, D. Kırmızıbayrak, H. Krawczynski, M. Negro, M. Ng, N. Omodei, A. Possenti, T. Tamagawa, K. Uchiyama, M. C. Weisskopf, I. Agudo, L. A. Antonelli, W. H. Baumgartner, R. Bellazzini, S. Bianchi, S. D. Bongiorno, R. Bonino, A. Brez, N. Bucciantini, F. Capitanio, S. Castellano, E. Cavazzuti, S. Ciprini, E. Costa, A. D. Rosa, E. D. Monte, L. D. Gesu, A. D. Marco, I. Donnarumma, M. Doviak, S. R. Ehlert, T. Enoto, Y. Evangelista, S. Fabiani, R. Ferrazzoli, J. A. Garcia, S. Gunji, K. Hayashida, W. Iwakiri, S. G. Jorstad, V. Karas, T. Kitaguchi, J. J. Kolodziejczak, F. L. Monaca, L. Latronico, I. Liodakis, S. Maldera, A. Manfreda, F. Marin, A. Marinucci, A. P. Marscher, H. L. Marshall, G. Matt, I. Mitsuishi, T. Mizuno, S. C. Ng, S. L. O'Dell, C. Oppedisano, A. Papitto, G. G. Pavlov, A. L. Peirson, M. Perri, M. Pesce-Rollins, M. Pilia, J. Poutanen, S. Puccetti, B. D. Ramsey, A. Ratheesh, R. W. Romani, C. Sgrò, P. Slane, P. Soffitta, G. Spandre, F. Tavecchio, Y. Tawara, A. F. Tennant, N. E. Thomas, F. Tombesi, A. Trois, S. S. Tsygankov, J. Vink, K. Wu, and F. Xie. Polarized x-rays from a magnetar. Science, 378:646–650, 11 2022. ISSN 10959203. doi: 10.1126/SCIENCE.ADD0080/SUPPL_FILE/SCIENCE.ADD0080_SM.PDF. URL https://www.science.org/doi/10.1126/science.add0080.

S. P. Tendulkar, C. Yang, V. M. Kaspi, R. Hascoet, and A. M. Beloborodov. Phase Resolved Observations of Magnetar 4U 0142+61 with NuSTAR. In AAS/High Energy Astrophysics Division #14, volume 14 of AAS/High Energy Astrophysics Division, page 114.02, Aug. 2014.

A. Tiengo, F. Pintore, B. Vaia, S. Filippi, A. Sacchi, P. Esposito, M. Rigoselli, S. Mereghetti, R. Salvaterra, B. Šiljeg, A. Bracco, Ž. Bošnjak, V. Jelić, and S. Campana. The Power of the Rings: The GRB 221009A Soft X-Ray Emission from Its Dust-scattering Halo. ApJ, 946(1): L30, Mar. 2023. doi: 10.3847/2041-8213/acc1dc.

M. Türler, M. Chernyakova, T. J. L. Courvoisier, P. Lubiński, A. Neronov, N. Produit, and R. Walter. INTEGRAL hard X-ray spectra of the cosmic X-ray background and Galactic ridge emission. A&A, 512:A49, Mar. 2010. doi: 10.1051/0004-6361/200913072.

A. J. van der Horst, Z. Paragi, A. G. de Bruyn, J. Granot, C. Kouveliotou, K. Wiersema, R. L. C. Starling, P. A. Curran, R. A. M. J. Wijers, A. Rowlinson, G. A. Anderson, R. P. Fender, J. Yang, and R. G. Strom. A comprehensive radio view of the extremely bright gamma-ray burst 130427A. MNRAS, 444(4):3151–3163, Nov. 2014. doi: 10.1093/mnras/stu1664.

F. Vargas, F. De Colle, D. Brethauer, R. Margutti, and C. G. Bernal. Survival of the fittest: Numerical modeling of sn 2014c. The Astrophysical Journal, 930(2):150, 2022.

G. Vedrenne, J. P. Roques, V. Schönfelder, P. Mandrou, G. G. Lichti, A. von Kienlin, B. Cordier, S. Schanne, J. Knödlseder, G. Skinner, P. Jean, F. Sanchez, P. Caraveo, B. Teegarden, P. von Ballmoos, L. Bouchet, P. Paul, J. Matteson, S. Boggs, C. Wunderer, P. Leleux, G. Weidenspointner, P. Durouchoux, R. Diehl, A. Strong, M. Cassé, M. A. Clair, and Y. André. SPI: The spectrometer aboard INTEGRAL. A&A, 411:L63–L70, Nov. 2003. doi: 10.1051/0004-6361:20031482.

F. J. Virgili, E.-W. Liang, and B. Zhang. Low-luminosity gamma-ray bursts as a distinct GRB population: a firmer case from multiple criteria constraints. MNRAS, 392:91–103, Jan. 2009. doi: 10.1111/j.1365-2966.2008.14063.x.

E. Virgilli, F. Frontera, V. Valsan, V. Liccardo, V. Carassiti, S. Squerzanti, M. Statera, M. Parise, S. Chiozzi, F. Evangelisti, E. Caroli, J. Stephen, N. Auricchio, S. Silvestri, A. Basili, F. Cassese, L. Recanatesi, V. Guidi, V. Bellucci, R. Camattari, C. Ferrari, A. Zappettini, E. Buffagni, E. Bonnini, M. Pecora, S. Mottini, and B. Negri. The laue project and its main results, 2014.

E. Virgilli, F. Frontera, P. Rosati, E. Bonnini, E. Buffagni, C. Ferrari, J. B. Stephen, E. Caroli, N. Auricchio, A. Basili, and S. Silvestri. Focusing effect of bent GaAs crystals for γ-ray Laue lenses: Monte Carlo and experimental results. Experimental Astronomy, 41(1-2):307–326, feb 2016. doi: 10.1007/s10686-015-9490-x.

E. Virgilli, V. Valsan, F. Frontera, E. Caroli, V. Liccardo, and J. B. Stephen. Expected performances of a Laue lens made with bent crystals. Journal of Astronomical Telescopes, Instruments, and Systems, 3(4):044001, 2017. doi: 10.1117/1.JATIS.3.4.044001. URL https://doi.org/10.1117/1.JATIS.3.4.044001.

E. Virgilli, F. Frontera, P. Rosati, E. Caroli, N. Auricchio, and J. B. Stephen. State-of-the-art of the hard X-/soft γ-ray focusing telescopes: The LAUE project status. In M. Bianchi, R. T. Jansen, and R. Ruffini, editors, Fourteenth Marcel Grossmann Meeting - MG14, pages 3289–3294, Jan. 2018. doi: 10.1142/9789813226609_0420.

E. Virgilli, F. Frontera, E. Caroli, J. B. Stephen, N. Auricchio, P. Rosati, V. Carassiti, S. Squerzanti, C. Guidorzi, L. Bassani, R. Campana, F. Fuschino, R. Gilli, C. Labanti, A. Malizia, M. Orlandini, L. Amati, S. Del Sordo, G. Stratta, G. Ghirlanda, I. Kuvvetli, S. Brandt, C. Budtz-Jørgensen, R. M. Curado da Silva, M. Moita, J. M. Maia, and P. Laurent. The Narrow Field Telescope on board the ASTENA mission. Mem. Soc. Astron. Italiana, 90:252, Jan. 2019.

E. Virgilli, G. Pareschi, L. Ferro, R. Hudec, C. Ferrari, S. Beretta, and V. Tichy. Double diffraction crystals for x-/gamma-ray optics (Conference Presentation). In S. L. O'Dell and G. Pareschi, editors, Optics for EUV, X-Ray, and Gamma-Ray Astronomy IX, volume 11119, page 111191D. International Society for Optics and Photonics, SPIE, 2019. doi: 10.1117/12.2529363. URL https://doi.org/10.1117/12.2529363.

G. Weidenspointner, G. Skinner, P. Jean, J. Knödlseder, P. von Ballmoos, G. Bignami, R. Diehl, A. W. Strong, B. Cordier, S. Schanne, and C. Winkler. An asymmetric distribution of positrons in the Galactic disk revealed by γ-rays. Nature, 451(7175):159–162, Jan. 2008. doi: 10.1038/nature06490.

M. C. Weisskopf, B. Brinkman, C. Canizares, G. Garmire, S. Murray, and L. P. Van Speybroeck. An Overview of the Performance and Scientific Results from the Chandra X-Ray Observatory. PASP, 114(791):1–24, Jan. 2002. doi: 10.1086/338108.

M. C. Weisskopf, R. F. Elsner, and S. L. O'Dell. On understanding the figures of merit for detection and measurement of x-ray polarization. In M. Arnaud, S. S. Murray, and T. Takahashi, editors, Space Telescopes and Instrumentation 2010: Ultraviolet to Gamma Ray, volume 7732 of Society of Photo-Optical Instrumentation Engineers (SPIE) Conference Series, page 77320E, July 2010. doi: 10.1117/12.857357.

X. Wen, J. Sun, J. He, R. Song, E. Wang, P. Zhou, Y. Dong, X. Liu, J. Liu, L. Li, H. Shi, R. Wang, B. Wu, L. Zhang, and S. Zhang. Calibration study of the Gamma-Ray Monitor onboard the SVOM satellite. Nuclear Instruments and Methods in Physics Research A, 1003:165301, July 2021. doi: 10.1016/j.nima.2021.165301.

S.-S. Weng and E. Göğüş. Broadband x-ray spectral investigations of magnetars, 4u 0142+61, 1e 1841-045, 1e 2259+586, and 1e 1048.1-5937. Astrophysical Journal, 815, 11 2015. doi: 10.1088/0004-637X/815/1/15. URL http://arxiv.org/abs/1511.06614http://dx.doi.org/10.1088/0004-637X/815/1/15.

C. Winkler, P. Barr, L. Hansson, R. Much, A. Orr, and A. N. Parmar. The Integral Science. ESA Bulletin, 111:72–78, Aug. 2002.

C. Winkler, T. J. L. Courvoisier, G. Di Cocco, N. Gehrels, A. Giménez, S. Grebenev, W. Hermsen, J. M. Mas-Hesse, F. Lebrun, N. Lund, G. G. C. Palumbo, J. Paul, J. P. Roques, H. Schnopper, V. Schönfelder, R. Sunyaev, B. Teegarden, P. Ubertini, G. Vedrenne, and A. J. Dean. The INTEGRAL mission. A&A, 411:L1–L6, Nov. 2003. doi: 10.1051/0004-6361:20031288.

H. Wolter. Spiegelsysteme streifenden Einfalls als abbildende Optiken für Röntgenstrahlen. Annalen der Physik, 445(1):94–114, Jan. 1952. doi: 10.1002/andp.19524450108.

S.-j. Yu, F. Gonzalez, J.-y. Wei, S.-n. Zhang, and B. Cordier. SVOM: a Joint Gamma-ray Burst Detection Mission. Chinese Astron. Astrophys., 44(2):269–282, Apr. 2020. doi: 10.1016/j.chinastron.2020.05.009.

W. H. Zachariasen. Theory of X-ray Diffraction in Crystals. Wiley, 1945.

B. Zhang. A burst of new ideas. Nature, 444(7122):1010–1011, Dec 2006. ISSN 1476-4687. doi: 10.1038/4441010a. URL https://doi.org/10.1038/4441010a.

B. Zhang. The physics of gamma-ray bursts. Cambridge University Press, 2019.

B. Zhang and H. Yan. The Internal-collision-induced Magnetic Reconnection and Turbulence (ICMART) Model of Gamma-ray Bursts. ApJ, 726:90, Jan. 2011. doi: 10.1088/0004-637X/726/2/90.

B.-B. Zhang, B. Zhang, and A. J. Castro-Tirado. Central Engine Memory of Gamma-Ray Bursts and Soft Gamma-Ray Repeaters. ApJ, 820(2):L32, Apr. 2016. doi: 10.3847/2041-8205/820/2/L32.

S.-N. Zhang, M. Kole, et al. Detailed polarization measurements of the prompt emission of five gamma-ray bursts. Nature Astronomy, 3(3):258–264, mar 2019. ISSN 2397-3366. doi: 10.1038/s41550-018-0664-0.

S.-N. Zhang, T. Li, F. Lu, L. Song, Y. Xu, C. Liu, Y. Chen, X. Cao, Q. Bu, Z. Chang, G. Chen, L. Chen, T. Chen, Y. Chen, Y. Chen, W. Cui, W. Cui, J. Deng, Y. Dong, Y. Du, M. Fu, G. Gao, H. Gao, M. Gao, M. Ge, Y. Gu, J. Guan, C. Gungor, C. Guo, D. Han, W. Hu, Y. Huang, J. Huo, S. Jia, L. Jiang, W. Jiang, J. Jin, Y. Jin, B. Li, C. Li, G. Li, M. Li, W. Li, X. Li, X. Li, X. Li, Y. Li, Z. Li, Z. Li, X. Liang, J. Liao, G. Liu, H. Liu, S. Liu, X. Liu, Y. Liu, Y. Liu, B. Lu, X. Lu, T. Luo, X. Ma, B. Meng, Y. Nang, J. Nie, G. Ou, J. Qu, N. Sai, R. Shang, G. Shen, L. Sun, Y. Tan, L. Tao, Y. Tuo, C. Wang, C. Wang, G. Wang, H. Wang, J. Wang, W. Wang, Y. Wang, X. Wen, B. Wu, B. Wu, M. Wu, G. Xiao, S. Xiong, L. Yan, J. Yang, S. Yang, Y. Yang, Q. Yi, B. Yuan, A. Zhang, C. Zhang, C. Zhang, F. Zhang, H. Zhang, J. Zhang, Q. Zhang, S. Zhang, S. Zhang, T. Zhang, W. Zhang, W. Zhang, W. Zhang, Y. Zhang, Y. Zhang, Y. Zhang, Y. Zhang, Z. Zhang, Z. Zhang, Z. Zhang, H. Zhao, X. Zhao, S. Zheng, J. Zhou, Y. Zhu, Y. Zhu, R. Zhuang, and Insight-HXMT Team. Overview to the Hard X-ray Modulation Telescope (Insight-HXMT) Satellite. Science China Physics, Mechanics, and Astronomy, 63(4):249502, Apr. 2020. doi: 10.1007/s11433-019-1432-6.

A. Zoglauer. FirstLightfortheNextGeneration ofComptonandPairTelescopes. PhD thesis, TechnischeUniversit´at M´unchen, 2005.

A. Zoglauer. MEGAlib: Medium Energy Gamma-ray Astronomy library. Astrophysics Source Code Library, record ascl:1906.018, June 2019.

Appendix A

Recent developments in Laue lens manufacturing and their impact on imaging performance

Paper published on the Journal of Astronomical Telescopes, Instruments, and Systems (January 2024)

JATIS Journal of Astronomical Telescopes, Instruments, and Systems

RESEARCH PAPER

Recent developments in Laue lens manufacturing and their impact on imaging performance

Lisa Ferro,[a,b,*] Enrico Virgilli,[b,c] Natalia Auricchio,[b] Claudio Ferrari,[d,e] Ezio Caroli,[b] Riccardo Lolli,[a,d] Miguel F. Moita,[a] Piero Rosati,[a,b,f] Filippo Frontera,[a,b] Mauro Pucci,[g] John B. Stephen,[b] and Cristiano Guidorzi[a,b,f]

[a]University of Ferrara, Department of Physics and Earth Science, Ferrara, Italy
[b]INAF/OAS of Bologna, Bologna, Italy
[c]INFN Section of Bologna, Bologna, Italy
[d]Institute of Materials for Electronics and Magnetism (CNR-IMEM), Parma, Italy
[e]INAF Osservatorio Astronomico di Brera - Merate, Merate, Italy
[f]INFN Section of Ferrara, Ferrara, Italy
[g]National Institute of Optics (CNR-INO), Florence, Italy

ABSTRACT. We report on recent progress in the development of Laue lenses for applications in hard X/soft gamma-ray astronomy. Here, we focus on the realization of a sector of such a lens made of 11 bent germanium crystals and describe the technological challenges involved in their positioning and alignment with adhesive-based bonding techniques. The accurate alignment and the uniformity of the curvature of the crystals are critical for achieving optimal X-ray focusing capabilities. We assessed how the errors of misalignment with respect to the main orientation angles of the crystals affect the point spread function (PSF) of the image diffracted by a single sector. We corroborated these results with simulations carried out with our physical model of the lens, based on a Monte Carlo ray-tracing technique, adopting the geometrical configuration of the Laue sector, the observed assembly accuracy, and the measured curvatures of the crystals. An extrapolation of the performances achieved on a single sector to an entire Laue lens based on this model shows that a PSF with a half-power-diameter of 4.8 arcmin can be achieved with current technology. This has the potential to lead to a significant improvement in the sensitivity of spectroscopic and polarimetric observations in the 50 to 600 keV band.

Keywords: Laue lenses; hard X-ray astronomy; soft gamma-ray astronomy; focusing optics

Paper 23122G received Oct. 10, 2023; revised Dec. 22, 2023; accepted Dec. 29, 2023; published Jan. 13, 2024.

1 Introduction

Laue lenses have emerged as a promising and unique technique for focusing hard X-/soft Gamma-ray radiation, offering the ability to achieve high angular resolution while providing large effective areas.[1,2] The fundamental principle of Laue lenses is the single diffraction of high energy photons by a number of crystals arranged in concentric rings [Fig. 1(a)]. By exploiting the diffractive properties of crystals, soft gamma rays can be focused onto a desired focal point, resulting in unparalleled focusing capabilities that can be extended, in principle, up to several hundreds of keV. In particular, our approach is based on the use of curved crystals that are bent to

*Address all correspondence to Lisa Ferro, frrlsi@unife.it

2329-4124/2024/$28.00 © 2024 SPIE

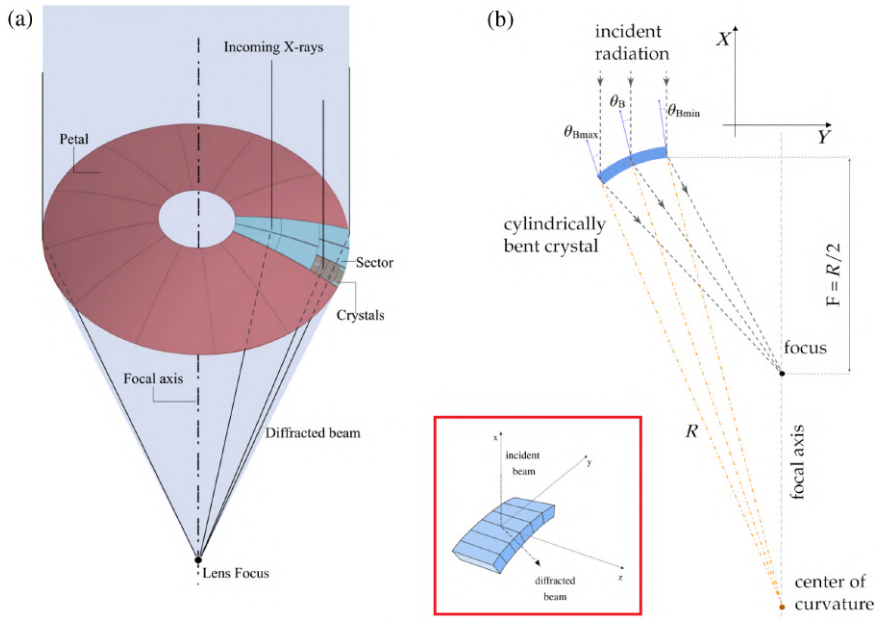

Fig. 1 (a) Concept of a Laue lens. A number of curved crystal tiles must be arranged in concentric rings and oriented according to the Bragg's law, along an overall curvature with a 40 m radius to focus the radiation at the common focal point where a 3D position-sensitive detector is placed. (b) Radial section of one of the bent crystals (blue arc) that composes the lens and acts as a radiation concentrator. The red inset shows a 3D drawing of the crystal including the diffraction planes (black lines) and their orientation.

an external cylindrical curvature in such a way that the average direction of the diffraction planes follows the curvature of the surface. In bent crystals, the Bragg's angle θ_B between the incoming radiation and the diffraction planes varies continuously, between a maximum ($\theta_{B_{max}}$) and a minimum ($\theta_{B_{min}}$), along the surface of the crystal [Fig. 1(b)]. Thus, the diffracted radiation is focused onto an area with a footprint that is smaller than the size of the crystal itself. The practical implementation of Laue lenses has, however, been limited to date by the ability to accurately align a large number of crystals so that their diffracted radiation is concentrated onto a common focal point. The accurate positioning of thousands of crystals within the lens assembly determines the sharpness of the point spread function (PSF), which is a key parameter, along with the overall throughput, when evaluating the scientific performance of the lens in high-energy astrophysics. Any deviation from the nominal positioning results in a reduced focusing ability, affecting the performance of the instrument. To address the difficulties encountered in crystal alignment, the choice of the materials that serve as substrates for the crystals plays a crucial role. These materials should possess low thermal expansion, exceptional mechanical stability, and high stiffness. In addition, they should exhibit a superior match with the crystal material to ensure an effective bonding between the crystal and substrate. If possible, these materials should already be space-proven or space-qualified. The introduction of these materials has the potential to significantly reduce alignment uncertainties and improve the overall performance of Laue lenses. From our experience, to realize a Laue lens made with numerous optical elements, a modular approach must be adopted. It is, therefore, necessary to build and align several modules with each other, each consisting of a few dozens of crystals. Within each module, the crystals must be aligned toward the common focus as accurately as possible because they cannot be further reoriented. The final objective of our R&D is to develop a Laue lens working in the 50 to 700 keV energy range as that of the narrow field telescope proposed for the ASTENA mission concept.[3,4] Such a Laue lens has an aperture diameter of ~3.2 m and an overall geometric area of 7 m^2 (Fig. 2).

In this paper, we report on the latest development in terms of crystals preparation, substrate choice, and, in particular, the realization of a test module of a Laue lens made of 12 crystals, aligned with respect to both the radial and azimuthal angles. The achieved positioning accuracy

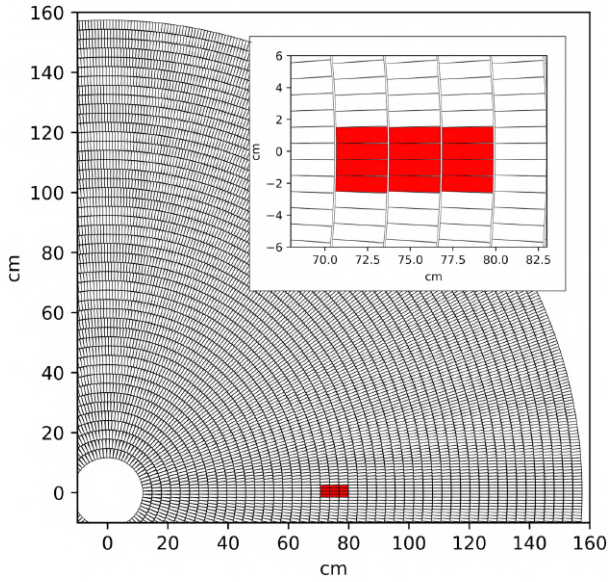

Fig. 2 Background image: scheme showing ~1/4 of the Laue lens designed for the NFT on board the ASTENA concept mission (internal radius $R_{in} = 12$ cm and external radius $R_{out} = 158$ cm). The inset shows a small sector made of 12 crystals of the prototype model that was built and presented in this work.

in setting these crystals is then used to predict the PSF of the entire Laue lens using a ray-tracing based physical model of the lens.

2 Experimental Activity

The goal of this research is to achieve an assembly accuracy that can meet the requirements of a Laue lens for astrophysical applications. In this section, we describe the relevant components of this endeavor, namely the selected crystals for diffraction, the choice of the substrate used to host the crystals, and the methodological steps of the assembly process in the X-ray facility.

2.1 Crystals and Substrate

The crystals used to realize the sector are made of germanium tiles (thickness $S = 1676 \div 1775$ μm) with cross-section 30×10 mm^2 [Fig. 3(a)] and diffraction planes (220). The crystal tiles are cut such that the diffraction planes are parallel to the $10 \times S$ mm^2 faces within a miscut angle <0.2 deg. In this work, we did not explore the impact of selecting

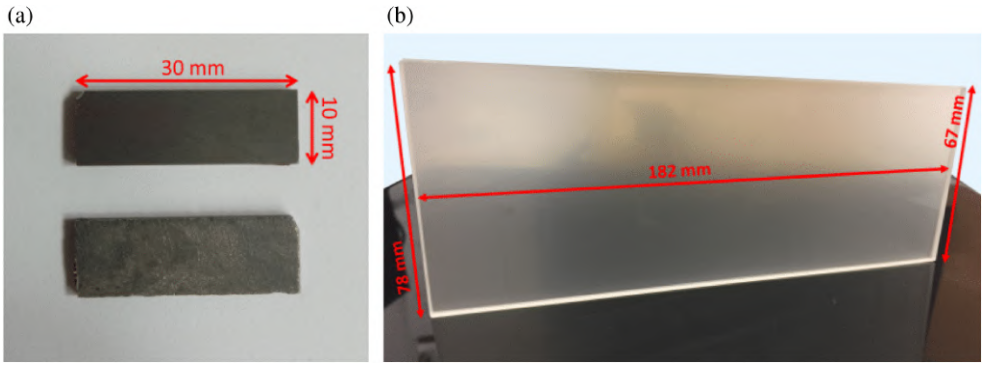

Fig. 3 (a) Two germanium crystal tiles used to build the lens prototype; the bottom crystal shows the polished side. The crystals are bent along the long side. (b) The quartz glass used as the substrate for the bonded crystals.

Table 1 Curvature radius and thickness of the crystals used to build the prototype. The variation in the reported errors on the curvature radius is due to the different deviations with respect to a perfect curvature for the crystals. Measurements done at CNR-IMEM (Parma) with a Cu $-\alpha$ X-ray diffractometer.

Crystal ID	Curvature radius (m)	Thickness (μm)
25A	40.0 ± 0.4	1700 ± 5
26A	39 ± 1	1717 ± 5
26B	37.8 ± 0.3	1775 ± 5
26C	38.8 ± 0.8	1744 ± 5
28B	40.62 ± 0.04	1775 ± 5
29A	39.08 ± 0.01	1732 ± 5
29B	38.4 ± 0.9	1749 ± 5
30A	38.1 ± 0.6	1676 ± 5
31A	40.6 ± 0.1	1745 ± 5
32C	40.7 ± 0.7	1731 ± 5
33B	40.8 ± 0.3	1678 ± 5

different diffraction planes on the lens performance. This aspect will be investigated in future research.

Crystals are bent in a cylindrical shape with a radius of curvature of 40 m. Such a curvature has been obtained through the so-called surface lapping technique,[5,6] which consists of controlled mechanical damaging on one surface of the sample. The procedure provides a highly compressive strain responsible for the convexity appearing on the worked side. Due to the variability of the amount of material removed by the surface lapping process, the thickness of the crystals is not uniform, as reported in Table 1, in which the achieved curvature radius for each crystal tile is also reported. The planes (220) do not acquire a secondary curvature, as is expected with other families of planes;[7] however, the external bending of the crystals allows the X-ray radiation coming from a parallel beam to be concentrated onto a focal point at a distance equal to half of their radius of curvature.[8]

The adhesive used to realize the lens sector is the OP 61 LS by DYMAX, an UV-curable adhesive with a linear shrinkage factor of 0.03%. A low value of the adhesive shrinkage is fundamental to reduce unwanted positioning displacements after curing. The substrate that we used is made of fused quartz with a trapezoid shape [Fig. 3(b)]. The choice of quartz as the material for the substrate is due to its low coefficient of thermal expansion and its transparency to the UV light, which is required for the adhesive curing process. One of the two surfaces of the quartz glass was worked to be flat, whereas the surface on which the crystals were bonded was polished to achieve a curvature radius of 40 m to better match the shape of the crystals. This reduces the inhomogeneities in the glue deposition between crystals and substrate. The substrate is 5 mm thick, and the diffraction process is carried out at about 130 keV. At this energy, and based on the density and attenuation coefficient of quartz glass, the beam transmitted through the substrate is about 84% of the diffracted beam.

2.2 Facility Set-up

The prototype was built in the 100 m long tunnel (LARIX-T) of the LARIX laboratory[9] of the University of Ferrara. A scheme of the facility is shown in Fig. 4(a). The facility consists of a 26.5 m beamline working in the 50 – 320 keV energy range. The X-ray beam is produced by an X-ray tube equipped with a tungsten anode [Fig. 4(b)] with a focal spot size of 0.4 mm. A 20 mm thick tungsten plate with a 3 mm diameter hole and a 50 mm thick lead shield with a 1 mm diameter hole are placed in front of the exit window to reduce the beam divergence; the two

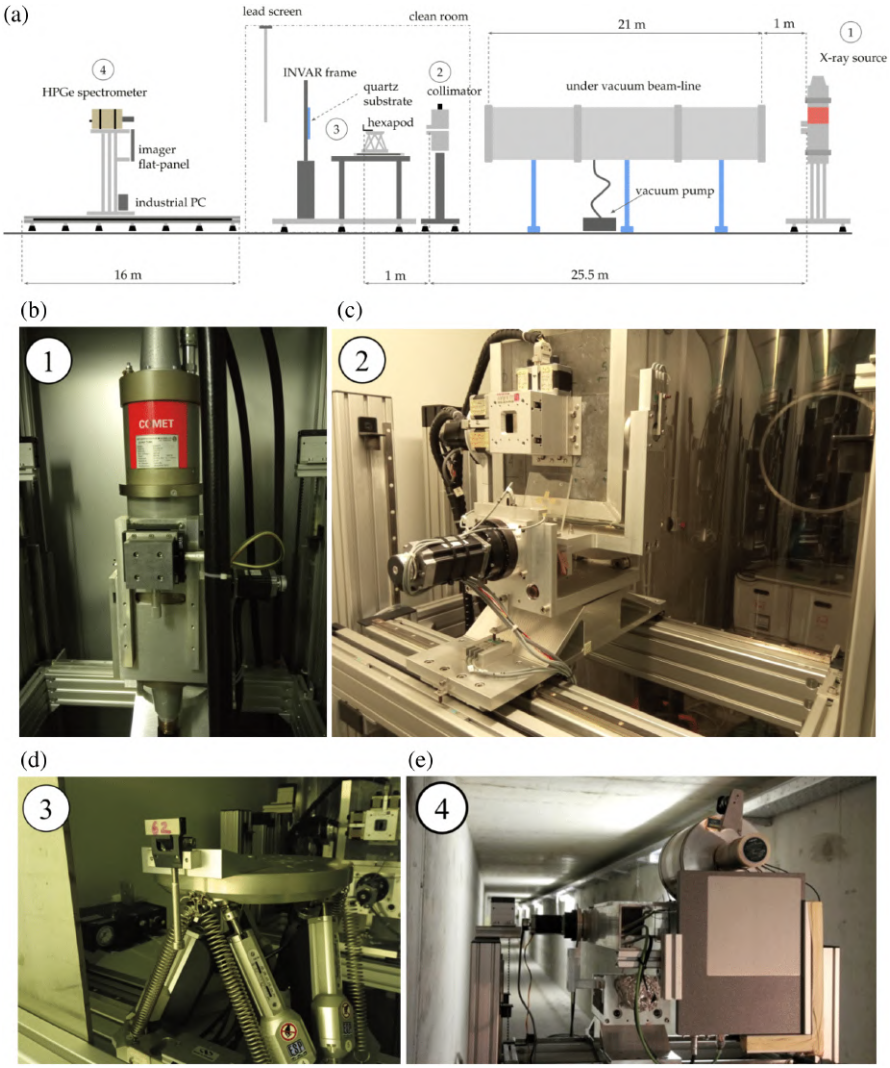

Fig. 4 (a) Sketch (not at scale) of the LARIX-T facility at the University of Ferrara, where the Laue lens module was assembled and tested. (b) The collimated X-ray source. (c) The remotely controllable lead and tungsten collimator. (d) The hexapod used to orient the crystals; the custom crystal holder is also visible with a mounted crystal. (e) The suite of the available detector, the HPGe spectrometer, and the flat-panel imager Perkin–Elmer (200 μm spatial resolution).

collimator plates are immediately in front of the X-ray tube exit window. The X-ray beam passes inside a 21 m long vacuum pipe and then through a motorized slit collimator with four independently motorized 20 mm thick tungsten blades [Fig. 4(c)]. In this experiment, the collimator aperture was set to obtain a beam dimension of 10×10 mm^2. Given the distance of 26.5 m between the X-ray source and quartz substrate and the beam size on the crystal, the divergence of the X-ray source over the crystal area is about 78 arcsec. This set-up is designed to reduce the divergence of the incident beam to approximate the illumination conditions from a source placed at an infinite distance from the target.[8]

The crystals are positioned using a customized holder, which is mounted on a high precision six-axis hexapod HXP100-MECA from Newport (with a translation accuracy of 1 μm and a rotation accuracy of 2×10^{-5} rad) [Fig. 4(d)]. The customized holder, visible in Fig. 4, supports the crystals from the back, top side, and right side without exerting any force, and a small, movable bar supports the crystals from the bottom and can be adjusted in such a way that the crystal is clamped between the top and bottom parts of the holder. The collimator and the hexapod are placed inside an ISO8 clean room. On the same carriage of the hexapod, an INVAR steel frame is

also installed. This frame hosts the quartz glass that is used as substrate for the module of the Laue lens under realization. Both the quartz glass and the INVAR steel were chosen for their extremely low thermal expansion coefficients (0.55 and 1.2 ppm/°C, respectively).

A further carriage is placed on a movable rail, which allows the detector to be moved from a minimum distance from the lens frame of ~8 m to a maximum distance of ~23 m. A Perkin Elmer cesium iodide (CsI(Tl)) digital X-ray flat panel detector with 1024 × 1024 pixels, 200 μm pixel size, and sensitive in the broad energy range of 20 keV to 15 MeV was used to detect the diffracted signals by each crystal and for their mutual alignment [Fig. 4(e)].

Given the divergence of the beam, the imager is placed at distance F_D from the crystals, obtained as[2]

$$\frac{1}{F_D} = \frac{1}{D} + \frac{2}{R_c}, \tag{1}$$

where D is the distance between the source and the sample holder and R_c is the curvature radius of the crystals. In the ideal case of a crystal with a curvature radius of 40.0 m, F_D is 11.4 m instead of 20.0 m. Note that X-rays get diffracted only once in the Laue lens configuration; therefore, the beam divergence contributes to reducing the focal length.

2.3 Prototype Assembly

The main objective of this research is to fabricate a test module consisting of 12 bent germanium crystals. With reference to Fig. 5, for a parallel beam impinging on the lens, the proper orientation of the diffracted beam toward the Laue lens focus is achieved by adjusting the crystal with respect to the θ angle, which is related to the Bragg's angle, and to the polar, or radial, angle ϕ. We aim to be able to build an astrophysical Laue lens with a PSF of the order of 30 arcsec half-power diameter (HPD) in its entire energy band, which means that we require positioning the Bragg's angle of the crystal with an accuracy of <10 arcsec.[3] The misplacement of the image of a crystal due to a wrong incident angle scales with the focal of the lens, so with a long focal such as our case, it is very important to keep this type of misalignment as small as possible. On the polar angle, we can have a less strict requirement of an accuracy of at least 5 arcmin because the misplacement of the image induced by a polar angle misalignment scales with the radius of the lens, which is about one order of magnitude smaller than the focal length. Even with a limited number of crystals, such a cluster is representative of the elemental module that constitutes a complete Laue lens. The position of each crystal is set under the control of the X-ray beam

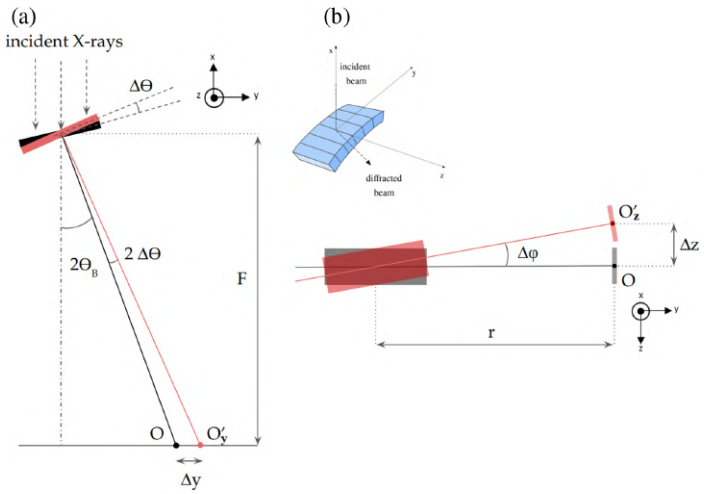

Fig. 5 Scheme showing how the deviation of one crystal from the nominal positioning angles (θ and ϕ) affects the position of the diffracted beam. Black points O represent the nominal diffracted position. (a) The variation $\Delta\theta$ along the Bragg's angle θ_B shifts the diffracted signal in O' by $\Delta y = F \tan(2\Delta\theta)$. (b) The variation $\Delta\phi$ of the polar angle with respect to the nominal position results in a shift of the diffracted beam from O to O' by an amount $\Delta z = r \tan\Delta\phi$.

to align the positions of the centroids of their images all on the same point on the detector. Each crystal is bonded to the substrate through the following procedure:

1. The crystal is mounted on the hexapod, and the collimator is positioned in such a way that the central part of the crystal is illuminated.
2. The position of the diffracted signal is measured with the flat panel. From the difference between the nominal and measured positions of the diffracted signal, the Bragg and polar angles are evaluated and provided to the hexapod to correctly orient the crystal.
3. A drop of glue is dispensed on the substrate in correspondence to the central part of the crystal. The polished side of the crystal is then pressed into contact with the adhesive. We chose to apply the adhesive on the polished side to avoid the glue inducing an excessive stress on the crystals, possibly changing their curvature radii. The typical distance between crystal and substrate is about 150 to 200 μm. A final check of the position of the diffracted signal is made. By fitting the diffraction profile in both directions, the measurable positional accuracy is better than 0.5 pixels, i.e., on the order of 1.5 to 2 arcsec.
4. The glue is cured from the back of the quartz substrate using the UV lamp DYMAX BlueWave 75 with the use of a light guide. We alternated between short light shots and longer dark times. The idea of this procedure is that the light shots partially cure the glue, so during the dark times, there is still room to correct the position of the crystal if the expected shrinkage of the glue moved the crystals from its desired position. For each crystal, we performed 60 cycles of 0.5 s of light and 45 s of dark and then 20 cycles of 2 s of light and 45 s of dark. The total light time given to each crystal is 70 s, and the total dark time is 3600 s, so the curing process of each crystal takes 1 h.
5. The crystal is released from the hexapod, and the position of the centroid of its diffracted image is measured. The release of the crystal is typically the most crucial phase of the bonding process because the combined effects of the adhesive force of the glue, gravity, and any backlash from the release of the crystal clamp can drastically change the position of the crystal if the bonding process was not performed properly. The position of the diffracted signal for each crystal is monitored at regular time intervals, with a particular interest in evaluating its long term stability.

3 Data Analysis and Results

The assembled module of the Laue lens is shown in Fig. 6(a), and the image of the crystals illuminated together is shown in Fig. 6(b). The bonding procedure is quite time-consuming because continuous checks are needed on the position of the crystals throughout the process.

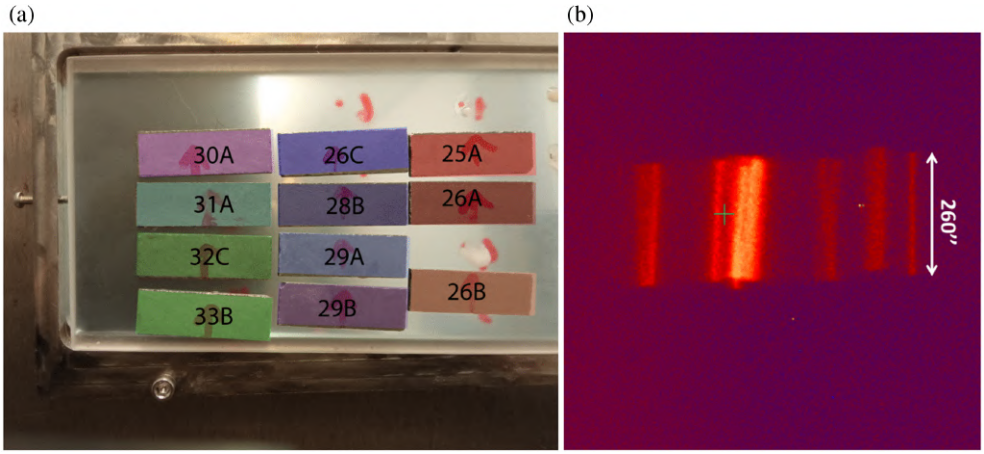

Fig. 6 (a) The 11 crystals bonded on the quartz substrate fixed on the INVAR support. The color overlapped on each crystal corresponds to the colors used to distinguish each crystal on the plots in Fig. 8. (b) Diffracted image produced by the 11 crystals fixed on the substrate and illuminated simultaneously. The center of the green cross was the target position on which we tried to align the image of each crystal.

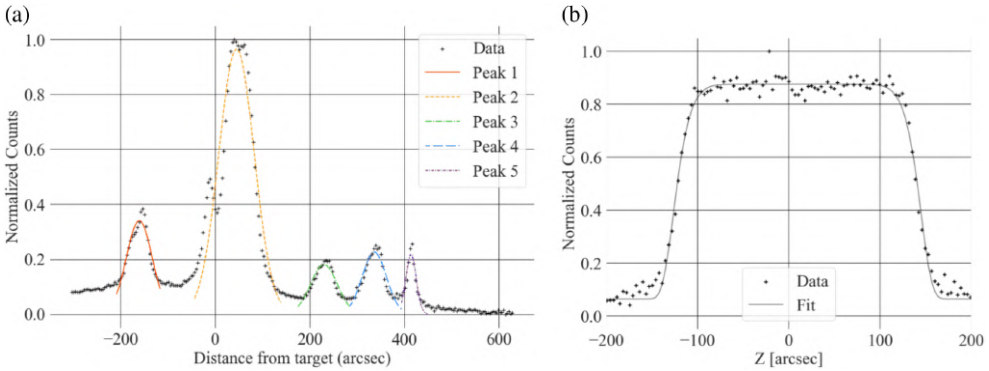

Fig. 7 (a) Profile along the focusing direction of the image produced by the assembled Laue lens module. The main peak includes the overlapped images of seven crystals. (b) Profile along the non-focusing direction of the image produced by the assembled Laue lens module.

Of the 10 days passed from the bonding of the first to the last crystals, seven were working days, resulting in the bonding of 1 to 2 crystals a day. To check the positional stability of the crystals in the assembled module, we repeated the measurement of the position of the diffracted beam from each crystal daily, for 31 (21) days after the assembly of the first (last) crystal. After this period, we noted that the crystals' position remained stable for at least 1 week, when we stopped the daily measurements. Very preliminary results of our assembled module were reported in a previous work.[10] The final sector was made by 11 crystals instead of 12 because the crystal 26B got detached from its original position due to an assembly mishap and left a white spot of cured glue on the quartz substrate (clearly visible in Fig. 6, which rendered it impossible to bond another crystal on the same position without risk of damage to the assembly). Finally, the profile of the image along the focusing direction is shown in Fig. 7(a), and the profile along the non-focusing direction is shown in Fig. 7(b). The images shown in Fig. 6 were taken 31 days after the bonding of the first crystal. Seven of the 11 crystals are aligned in the central peak of the image, and four crystals (30A, 26C, 31A, and 28B) are strongly misaligned along the focusing direction. We can see that the width of the diffracted peaks produced by crystals 26C, 31A, and 28B are twice the width of the peak generated by crystal 30A. We believe that this effect can be ascribed to the stress generated by the glue on the crystals, which in some cases can be strong enough to deform their curvature radius. In the focusing direction, the combined image of the crystals shows five distinct peaks: the major peak results from the combination of seven well-aligned crystals, it is centered at a distance of 45 arcsec from the expected position (see Fig. 7) and has an FWHM of 88 arcsec. The four smaller peaks are generated by the outlier crystals. The position and FWHM of every peak are reported in Table 2. On the non-focusing direction, the profile of the image can be fitted by a box shape centered 9.2 ± 0.3 arcsec from the target position and with a width of 267 ± 7 arcsec, which corresponds to a linear width on the detector of 15 mm at the distance of 11.4 m, compatible with the expected crystal footprint taking into account the divergence of the X-ray beam. The time stability of the assembly was evaluated by

Table 2 Fit parameters of the five peaks forming the combined image of the 11 crystals bonded on glass, projected along the focusing direction. The peaks are numbered in increasing order, from left to right.

Peak number	Normalization	Mean (arcsec)	FWHM (arcsec)
1	0.341 ± 0.009	-160.5 ± 0.9	64 ± 2
2	0.96 ± 0.03	45 ± 1	88 ± 3
3	0.181 ± 0.006	230 ± 1	67 ± 3
4	0.226 ± 0.009	336 ± 1	60 ± 3
5	0.22 ± 0.01	414.2 ± 0.8	25 ± 2

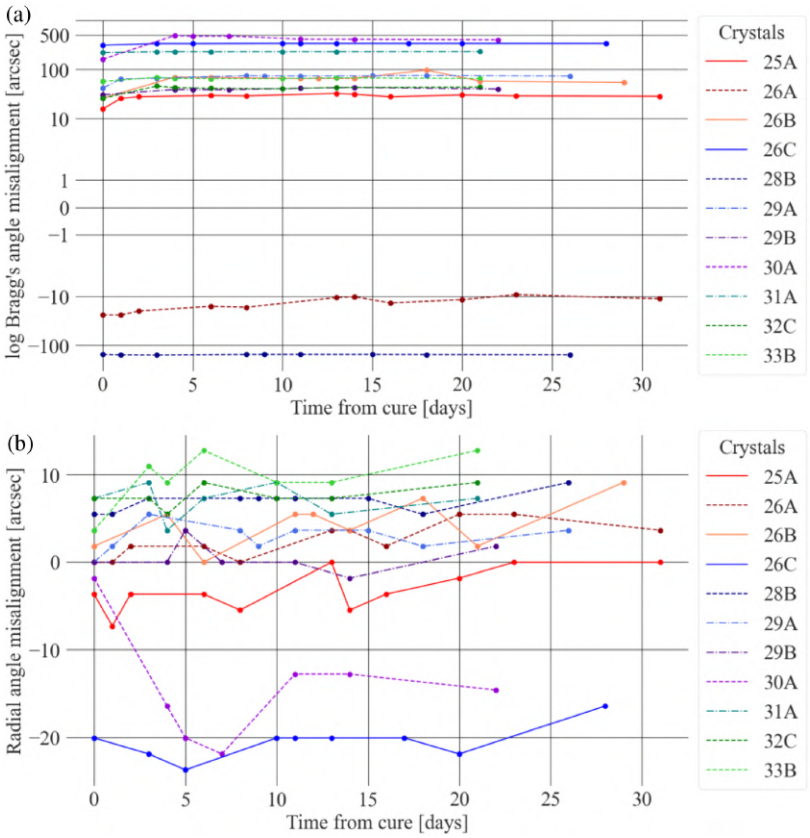

Fig. 8 Measured misalignment in (a) the Bragg's angle and (b) polar angle for every crystal as a function of time after bonding.

measuring the position of the centroid of every crystal day by day after the cure. Time stability measurements on both the Bragg's and polar angles are shown in Fig. 8. After 31 days from the cure of the first crystal, the average misalignment value in the Bragg's angle is 100 ± 50 arcsec, whereas the average misalignment value in the polar angle is 2 ± 3 arcsec. The amplitude of the Bragg's angle distribution is 9.58 ± 0.03 arcmin, whereas the amplitude of the polar angle distribution is 30 ± 7 arcsec. Taking into account that the angle with respect to the incoming direction of the photons is twice the angle between the diffraction planes and the beam[1] in the transmission configuration, the assembly misalignment of the crystals is then obtained by dividing the angular misalignment that we measured by two. This means that the average Bragg's angles' assembly misalignment is 50 ± 25 arcsec, and the width of the distribution is 4.79 ± 0.02 arcmin, whereas the average polar angles' assembly misalignment is 1.0 ± 1.5 arcsec.

4 Simulations

The mean and width of the distribution of misalignment angles and the uncertainty of the radius of curvature were used to simulate both a sector and a whole Laue lens. For this purpose, the Laue lens library (LLL), which is described elsewhere,[11] was used. The LLL is a hybrid analytical + ray-tracing Monte Carlo tool developed to simulate different configurations of Laue lenses and evaluate their performance. At present, the Laue simulation tools assume that the curvature radius of the crystals, as well as the angles θ and ϕ, can be distributed according to a uniform or Gaussian profile with respect to an average value. However, the model does not include the effect of the variation of the curvature radius that may occur during the curing process due to the aforementioned stresses.

The simulated mosaicity of the crystals is set to 10 arcsec, as required for the batch of crystals used in the experimental campaign.

4.1 Module of a Laue Lens: Laboratory Configuration

First, a Laue lens module made from bent Ge (220) was simulated, assuming a uniform distribution of misalignment errors on both the Bragg's and polar angles of the crystals. The mean and width of these distributions are the same as those measured from the assembled module. In addition, we included in the simulation a uniform random distribution of the curvature radius of the crystals, with a mean value of 39.7 m and a width of 1.0 m. These values were obtained from the measurements of the curvature radius of a sample of 82 bent crystals of Ge(220) specifically prepared for this project and measured at CNR-IMEM.[10] The set of 11 crystals used for this demonstration prototype is part of the same batch of samples. The assembly misalignment angles and curvature radius of each crystal were sampled from those random distributions.

In the simulations, we used the geometrical configuration of the source–lens prototype–detector system in our experimental setup, so we simulated a source–lens distance of 26.5 m, lens–detector distance of 11.4 m, and source size of 0.4 mm.

We also simulated the performance of a sector consisting of 12 perfect crystals of Ge(220), all bent with a radius of curvature of 40 m and with no misalignment error from the ideal position. This nominal module is taken as a reference for comparison with the experimental module. Along the focusing direction (Y direction), the profile of the combined image from the 12 crystals has a Gaussian profile with an FWHM of 36.6 ± 0.1 arcsec. Along the non-focusing direction (Z direction), due to the cylindrical curvature of the sample, no focalization is expected. The data are fitted with a box profile centered on 0.01 ± 0.02 arcsec with a width of 257 ± 7 arcsec. The image and the profiles along the Z and Y directions of the ideal configuration sector are shown in Fig. 9, left.

Images and profiles along the Z and Y directions for the distorted/misaligned configurations are shown in Fig. 9, right. In the latter condition, the overall image of the crystals projected along the focusing direction shows six separate peaks that can be fitted with Gaussian profiles. The parameters used to fit the peaks are reported in Table 3. Along the non-focusing direction, the data are fitted again by a box profile, with the center on 0.96 ± 0.08 arcsec and a width of 260 ± 7 arcsec. Interestingly, along the Z direction, which is less affected by assembly errors, the width of the simulated realistic image is perfectly consistent with the width of the real image of the prototype along the vertical direction.

4.2 Module of Laue Lens: Astrophysical Configuration

To assess the impact of the beam divergence, we simulated the behavior of the prototype in an astrophysical configuration, i.e., with a lens–detector distance of 20 m and a point-like source at an infinite distance. Even in this case, we simulated both an ideal lens sector and a sector with the same curvature radius distribution of the crystals and assembly error distribution as the one we measured on the prototype.

In the ideal lens case, the profile of the combined image from the 12 crystals along the focusing direction has a Gaussian profile with an FWHM of 36.0 ± 0.1 arcsec. Along the non-focusing direction, the data are fitted with a box profile centered on -0.01 ± 0.03 arcsec with a width of 103.6 ± 4 arcsec. Images and profiles along the Z and Y directions from both simulated configurations are shown in Fig. 10.

In the realistic configuration, as a result of the random sampling of the misalignment distributions, the overall image of the crystals along the focusing direction shows five separate peaks. These peaks can be fitted with Gaussian profiles, the parameters of which are reported in Table 4. Along the non-focusing direction, the data are fitted again by a box profile, with the center on 3.05 ± 0.03 arcsec and a width of 103 ± 4 arcsec. Again, this is compatible with the expected angular size of the 10 mm long non-focusing side, at a distance of 20 m, for a parallel beam.

4.3 Full Laue Lens

With the same set of parameters characterizing the astrophysical configuration, we simulated a full Laue lens made of ~13,700 Ge(220) crystals working in the energy range 100 to 500 keV, in the ideal case of no errors on the curvature radius of the crystals and no misalignment errors. Results from the simulations are shown in Fig. 11, left. For the ideal configuration case, the HPD of the PSF is 54 ± 4 arcsec, mainly due to the mosaicity of the crystals. By adding a uniform

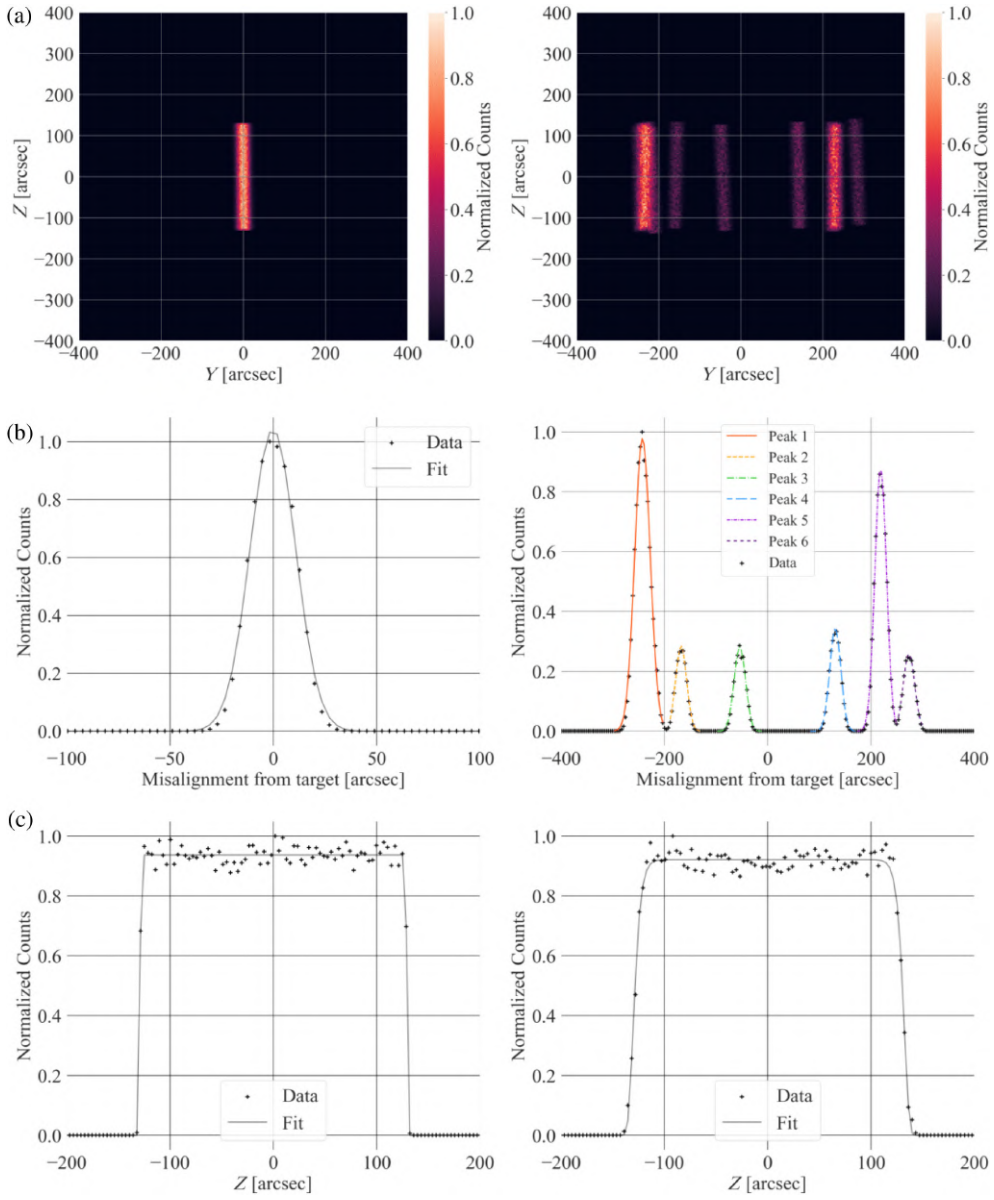

Fig. 9 (Left) Comparison of the simulated images and profiles in the case of ideal crystal alignment configuration and (right) a configuration reproducing the laboratory setup with the observed alignment error. (a) Focal plane images of an ideal and a real sector. (b) Profiles along the focusing direction. (c) Profiles along the non-focusing direction.

Table 3 Fit parameters of the six peaks forming the combined image of the 12 Ge(220) crystals composing the simulated sector, projected along the focusing direction, in the laboratory configuration.

Peak number	Normalization	Mean (arcsec)	FWHM (arcsec)
1	0.98 ± 0.01	-242.5 ± 0.2	49.7 ± 0.7
2	0.284 ± 0.005	-167.6 ± 0.2	35.5 ± 0.7
3	0.282 ± 0.005	-54.0 ± 0.2	36.7 ± 0.7
4	0.344 ± 0.005	130.7 ± 0.2	35.7 ± 0.5
5	0.88 ± 0.01	218.5 ± 0.2	37.5 ± 0.6
6	0.259 ± 0.004	273.3 ± 0.2	37.0 ± 0.7

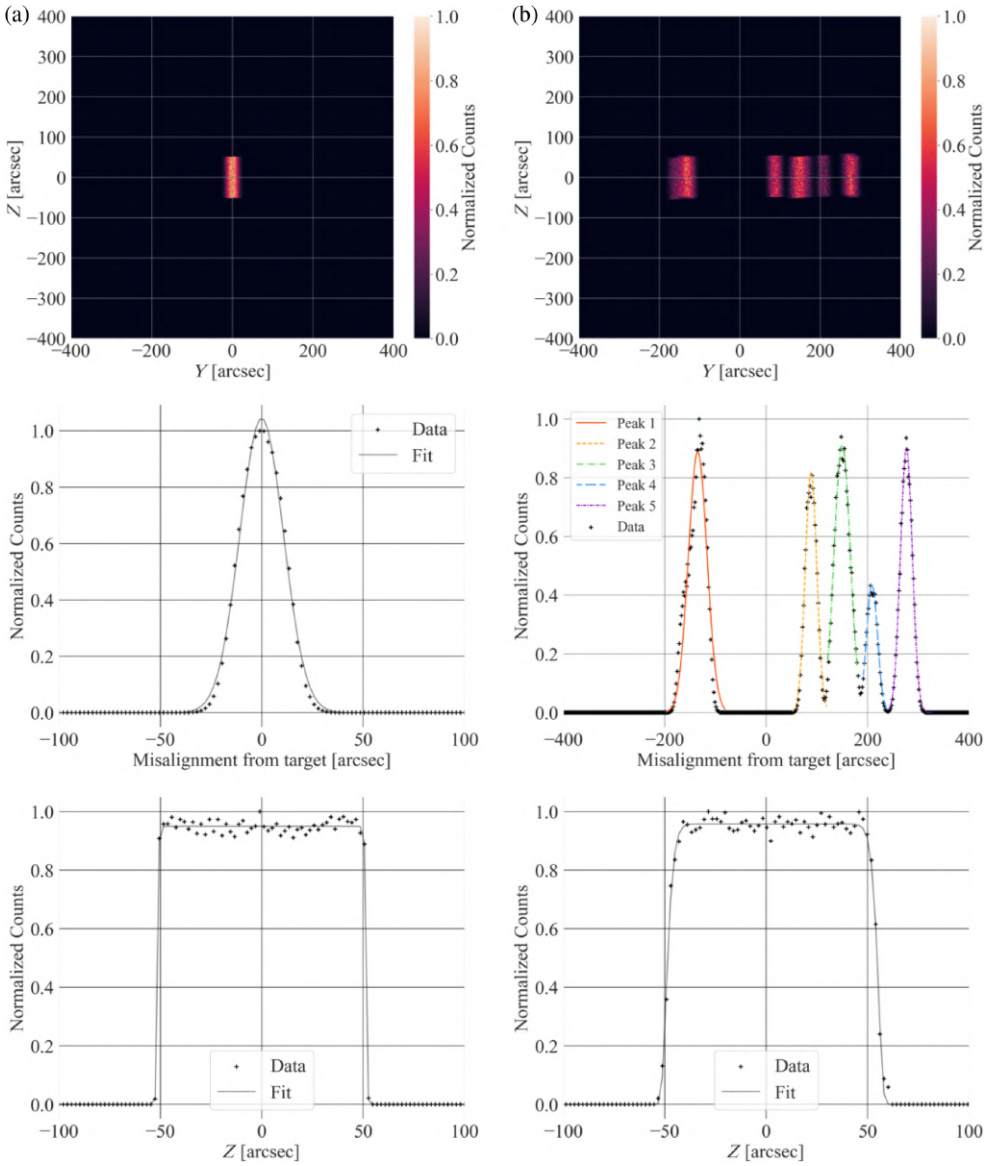

Fig. 10 Comparison of the simulated images and profiles in the case of (a) ideal sector configuration and (b) real configuration, with an astrophysical source. Top: Focal plane images of an ideal and a real sector. Center: Profiles along the focusing direction. Bottom: Profiles along the non-focusing direction.

Table 4 Fit parameters of the five peaks forming the combined image of the 12 Ge(220) crystals composing the simulated sector, projected along the focusing direction, in an astrophysical configuration (point-like source at infinity).

Peak number	Normalization	Mean (arcsec)	FWHM (arcsec)
1	0.89 ± 0.03	-135.0 ± 0.6	61 ± 2
2	0.82 ± 0.01	88.5 ± 0.2	37.6 ± 0.6
3	0.91 ± 0.01	149.8 ± 0.2	52.4 ± 0.9
4	0.437 ± 0.007	208.6 ± 0.2	36.0 ± 0.7
5	0.903 ± 0.008	276.4 ± 0.1	38.9 ± 0.4

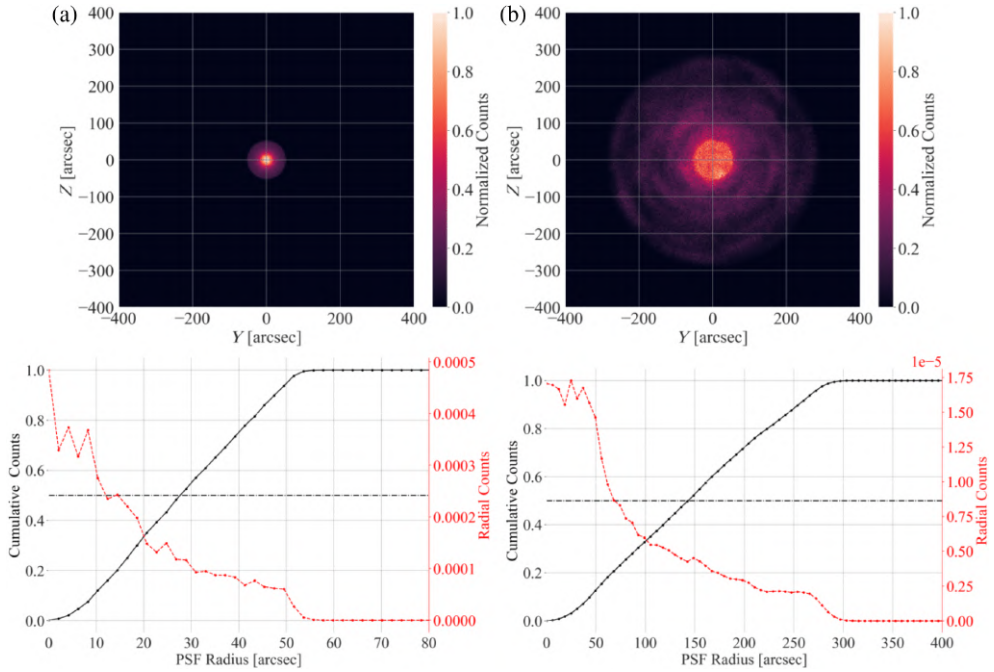

Fig. 11 (a) (top) Image produced by a simulated ideal full Laue lens built with Ge(220) crystals working in the 100 to 500 keV energy band; (bottom) radial (red curve) and cumulative (black curve) counts from the center of the PSF. All crystals are bent with the same curvature radius of 40 m and no misalignment errors are present. The black dot-dashed line in the middle represents the 50% integrated counts level. (b) Same as in the left panel, but with a real Laue lens in which the curvature radius of the crystals is distributed according to the measured uniform distribution (center = 39.7 m, width = 1.0 m) and the misalignment errors are uniformly distributed as observed (center = 101 arcsec, width = 161 arcsec for the Bragg's angles; center = 2 arcsec, width = 9 arcsec for the radial positioning angles). The black dot-dashed horizontal line represents the 50% cumulative counts.

distribution of alignment and curvature radius errors to reproduce the parameter spread measured on our prototype, we obtain the results in Fig. 11, right. In this case, the PSF is broadened to a HPD of 289 ± 4 arcsec.

5 Discussion and Conclusion

We built a prototype of a Laue lens sector made of 11 bent Ge(220) crystals bonded on a glass substrate by means of an UV-curable adhesive. From extensive testing, we obtained an average assembly misalignment in the Bragg's angle value of 50 ± 25 arcsec and an average misalignment in the polar angle position of 1.0 ± 1.5 arcsec. We were able to reach a good accuracy in the radial positioning alignment, whereas the misalignment in the Bragg's angle is two orders of magnitudes larger. We observed that the position of the crystals is subjected to fluctuations in the first 3 to 4 days after the gluing procedure; however, it settles afterward.

Simulations based on our physical model of the Laue lens corroborate these observations and well reproduce the observed PSF of the diffracted image by a single sector when the experimental setup is adopted; this includes the geometrical configuration of the source-lens, the number of crystals, and the alignment error distribution.

By extrapolating these performances to a full Laue lens assembly and adopting a uniform distribution of misalignment errors, the simulations show a final PSF with an HPD $= 289 \pm 4$ arcsec. This is the best result that we achieved in building a long focal Laue lens prototype with adhesive-based bonding techniques. The narrow field telescope on board the ASTENA mission has a PSF requirement of 30 arcsec, which would call for a reduction of at least one order of magnitude in the misalignment in the Bragg's angle with respect to what we have obtained to date. The most significant source of misalignment in our process is the

unpredictability of the volumetric shrinkage of the glue, which, combined with the release of heat during the cure, makes it difficult to position the crystal with the desired level of accuracy.

To address the challenges of the bonding technique outlined above, we are currently investigating various alternative approaches. The final goal is to achieve a robust bonding of the crystals while ensuring their precise alignment. As previously emphasized, the role of the adhesive is critical, particularly when its thickness lacks uniformity, leading to uneven shrinkage during the curing phase. By reducing the miscut angle to a few arcseconds and, more importantly, using crystals with a uniform miscut, one could achieve a significant reduction of the thickness of the adhesive between the crystals and the substrate, thus alleviating the stress induced by the curing process.

We are currently investigating alternatives that do not rely on traditional adhesives, specifically we are exploring either anodic or silicate bonding techniques, which are widely used in the field of electronics.

We are also studying the potential application of small mechanisms based on piezoelectric actuators. This technique would have the advantage to enable both the alignment of the crystals (or modules of crystals) with arcsecond accuracy and the periodic realignment of the system; however, the effect of the absorption of the material needed for the system must be evaluated. The latter is a feature not achievable with all bonding methods investigated thus far.

The research conducted so far shows that the level of positional accuracy of bent crystals achieved with UV-curable adhesives allows a long-focal length Laue lens to focus hard X-ray radiation onto a spot with a half-power diameter of 4.8 arcmin. With such a performance for the entire lens, even though it is still far from the 0.5 to 1 arcmin goal, one could build a narrow-field telescope for high energy spectro-polarimetry capable of obtaining a significant jump in sensitivity in the 50 to 600 keV band, when compared with current non-focusing instrumentation, thereby opening a new window in hard X and soft gamma-ray astrophysics.

Disclosures

The authors have no conflicts of interest to declare.

Code and Data Availability

The data and the simulation codes are accessible upon request to the authors.

Acknowledgments

This work was partly supported by the AHEAD-2020 Project Grant Agreement 871158 of the European Union's Horizon 2020 Program and by the ASI-INAF Agreement No. 2017-14-H.O "Studies for future scientific missions."

References

1. F. Frontera and P. V. Ballmoos, "Laue gamma-ray lenses for space astrophysics: status and prospects," *X-Ray Opt. Instrum.* **2010**, 215375 (2010).
2. E. Virgilli et al., "Focusing effect of bent GaAs crystals for γ-ray Laue lenses: Monte Carlo and experimental results," *Exp. Astron.* **41**, 307–326 (2016).
3. F. Frontera et al., "Understanding the origin of the positron annihilation line and the physics of supernova explosions," *Exp. Astron.* **51**, 1175–1202 (2021).
4. C. Guidorzi et al., "A deep study of the high–energy transient sky," *Exp. Astron.* **51**, 1203–1223 (2021).
5. C. Ferrari et al., "X-ray diffraction efficiency of bent GaAs mosaic crystals for the LAUE project," *Proc. SPIE* **8861**, 88610D (2013).
6. E. Buffagni et al., "X-ray characterization of curved crystals for hard x-ray astronomy," *Proc. SPIE* **9510**, 951006 (2015).
7. A. Authier and C. Malgrange, "Diffraction physics," *Acta Crystallogr. Sect. A* **54**, 806–819 (1998).
8. E. Virgilli et al., "The LAUE project and its main results," arXiv:1401.4948 (2014).
9. E. Virgilli et al., "The LARIX Facility website," https://larixfacility.unife.it/ (accessed 1 September 2023).

10. L. Ferro et al., "The TRILL project: increasing the technological readiness of Laue lenses," *Proc. SPIE* **12181**, 121812K (2022).
11. E. Virgilli et al., "Expected performances of a Laue lens made with bent crystals," *J. Astron. Telesc. Instrum. Syst.* **3**(4), 044001 (2017).

Lisa Ferro is a PhD student in physics at the University of Ferrara (UniFe), under the supervision of P. Rosati, F. Frontera, and C. Guidorzi from UniFe, and E. Virgilli from INAF-OAS of Bologna. Her main research topics are the development of focusing optics for hard X and Gamma-rays, especially Laue lenses, and instrumentation for high energy astrophysics.

Biographies of the other authors are not available.

Appendix B

Long gamma–ray burst light curves as the result of a common stochastic pulse–avalanche process

Preprint paper submitted to Astronomy & Astrophysics

Astronomy & Astrophysics manuscript no. output
March 27, 2024

Long gamma–ray burst light curves as the result of a common stochastic pulse–avalanche process

L. Bazzanini[1,2,⋆], L. Ferro[1,2], C. Guidorzi[1,2,3], G. Angora[1,4], L. Amati[2], M. Brescia[4,5], M. Bulla[1,3,6], F. Frontera[1,2], R. Maccary[1], M. Maistrello[1], P. Rosati[1,2,3], and A. Tsvetkova[7,2,8]

[1] Department of Physics and Earth Science, University of Ferrara, via Saragat 1, I–44122, Ferrara, Italy
[2] INAF – Osservatorio di Astrofisica e Scienza dello Spazio di Bologna, Via Piero Gobetti 101, I-40129 Bologna, Italy
[3] INFN – Sezione di Ferrara, via Saragat 1, I–44122, Ferrara, Italy
[4] INAF – Osservatorio Astronomico di Capodimonte, Salita Moiariello 16, I-80131 Napoli, Italy
[5] Dipartimento di Fisica "E. Pancini", Università di Napoli "Federico II", Via Cinthia 21, I-80126 Napoli, Italy
[6] INAF, Osservatorio Astronomico d'Abruzzo, via Mentore Maggini snc, 64100 Teramo, Italy
[7] Department of Physics, University of Cagliari, SP Monserrato-Sestu, km 0.7, 09042 Monserrato, Italy
[8] Ioffe Institute, Politekhnicheskaya 26, 194021 St. Petersburg, Russia

Received xxx; accepted xxx

ABSTRACT

Context. The complexity and variety exhibited by the light curves of long gamma–ray bursts (GRBs) enclose a wealth of information that still awaits being fully deciphered. Despite the tremendous advance in the knowledge of the energetics, structure, and composition of the relativistic jet that results from the core collapse of the progenitor star, the nature of the inner engine, how it powers the relativistic outflow, and the dissipation mechanisms remain open issues.
Aims. A promising way to gain insights is describing GRB light curves as the result of a common stochastic process. In the Burst And Transient Source Experiment (BATSE) era, a stochastic pulse avalanche model was proposed and tested through the comparison of ensemble-average properties of simulated and real light curves. Here we aim to revive and further test this model.
Methods. We apply it to two independent data sets, BATSE and *Swift*/BAT, through a machine learning approach: the model parameters are optimised using a genetic algorithm.
Results. The average properties are successfully reproduced. Notwithstanding the different populations and passbands of both data sets, the corresponding optimal parameters are interestingly similar. In particular, for both sets the dynamics appears to be close to a critical state, which is key to reproduce the observed variety of time profiles.
Conclusions. Our results propel the avalanche character in a critical regime as a key trait of the energy release in GRB engines, which underpins some kind of instability.

Key words. Gamma-ray burst: general – Methods: statistical – machine learning – genetic algorithms

1. Introduction

Gamma–ray bursts (GRBs) are the most powerful explosions on stellar scale in the Universe. At least two kinds of progenitors are known: (i) so-called 'collapsar' (Woosley 1993; Paczyński 1998; MacFadyen & Woosley 1999), that is a hydrogen-stripped massive star, whose core collapses to a compact object, which launches a relativistic ($\Gamma \sim 10^2$–10^3) jet; (ii) merger of a compact binary (Eichler et al. 1989; Paczynski 1991; Narayan et al. 1992), where at least one of the two objects is supposed to be a neutron star (NS) and which also results in a short-lived relativistic jet (see Kumar & Zhang 2015; Zhang 2018 for recent reviews). There are alternative models to the collapsar, such as the binary-driven hypernova model (BdHN; Rueda & Ruffini 2012; Becerra et al. 2019), in which the final collapse of a CO core of a massive star can trigger the collapse of a companion neutron star. Most GRBs due to (i) manifest themselves as long GRBs (LGRBs), lasting longer than ~ 2 s[1], while (ii) usually exhibit a subsecond spike occasionally followed by weak, long-lasting emission (Norris & Bonnell 2006), and are commonly referred to as short GRBs (SGRBs). Actually, the emerging picture is more complicated, as shown by the increasing number of cases with deceptive time profiles found in both classes (Gehrels et al. 2006; Rastinejad et al. 2022; Gompertz et al. 2023; Yang et al. 2022; Troja et al. 2022; Ahumada et al. 2021; Zhang et al. 2021; Rossi et al. 2022; Levan et al. 2023; Levan et al. 2024).

The nature of the dissipation mechanism that is responsible for the GRB prompt emission is still an open issue. The great variety observed in the light curves (LCs) of LGRBs is thought to be the result of the variability imprinted to the relativistic outflow by the inner engine left over by the collapsar, either a millisecond magnetised NS or a black hole (BH), along with the effects of the propagation of the jet within the stellar envelope (e.g., Morsony et al. 2010; Geng et al. 2016; Gottlieb et al. 2020b,a, 2021b,a), although some models ascribe the possible presence of subsecond variability to magnetic reconnection events taking place at larger radii (Zhang & Yan 2011). Some correlations were found between variability and minimum variability timescale on one side, as defined in a number of ways, and luminosity

⋆ bzzlnz[at]unife[dot]it
[1] This boundary value is from CGRO/BATSE GRB catalogue and slightly depends on the detector's passband.

and initial Lorentz factor of the outflow on the other side (e.g., see Camisasca et al. 2023 and references therein). However, apart from the study of average and of individual Fourier power density spectra of GRBs (Beloborodov et al. 1998; Guidorzi et al. 2012, 2016; Dichiara et al. 2013), the study of the waiting time distribution between pulses (Ramirez-Ruiz et al. 2001; Nakar & Piran 2002; Quilligan et al. 2002; Guidorzi et al. 2015), and the distribution of the number of peaks per GRB (Guidorzi et al. 2024), little progress has been made in deciphering and characterising the variety of LGRB LCs within a unifying scheme that could explain the large diversity (in terms of duration, number of pulses, distribution of energy and waiting times between pulses) and relate it to other key properties. Recent investigations found possible evidence that GRB engines emit as self-organised critical (SOC) systems (Wang & Dai 2013; Yi et al. 2017; Lyu et al. 2020; Wei 2023; Li & Yang 2023; Maccary et al. 2024), in which energy is released through avalanches whenever the system naturally reaches a critical point. Yet, the interpretation is not straightforward, since SOC dynamics is usually invoked for systems that are continuously fed by some energy input and are not characterised by the kind of irreversible evolution expected for a GRB inner engine. A successful description of the inner engine variability would help constrain the mechanism that powers the jetted outflow in GRBs and, ultimately, the nature of the compact object. Furthermore, it would provide the community with a reliable tool to simulate credible GRB LCs as they would be measured by future experiments, avoiding the pitfalls of using real noisy LCs (e.g., Sanna et al. 2020).

In this respect, an interesting attempt was laid out by Stern & Svensson (1996, hereafter SS96) in the Compton Gamma–Ray Observatory era (CGRO; 1991–2000) on the GRB catalogue of one of its experiments, the Burst And Transient Source Experiment (BATSE). These authors proposed a common stochastic process built on a pulse avalanche mechanism and tried to reproduce some of the observed distributions of BATSE GRB LCs. At that time, the cosmological distances of GRBs and the progenitors' nature of the two classes were yet to be firmly established, with the first afterglow discoveries starting from 1997 (Costa et al. 1997). By manually guessing the values of the seven model parameters, SS96 came up with a process operating in a nearly critical regime and capable of reproducing the variety of observed GRB LCs, as long as the chosen metrics are concerned. This approach of simulating GRB LCs was adopted in Greiner et al. (2022) to assess localisation capabilities of a proposed network of GRB detectors on the global navigation satellite system Galileo G2.

In the big data era, advanced statistical and machine learning (ML) techniques applied to astrophysics have become routine (e.g., see Feigelson et al. 2021 for a review). In this paper we aim to verify and improve the results obtained by SS96 on the BATSE data and, for the first time, apply their model to a sample from another detector operating in a softer energy band, such as the Burst Alert Telescope (BAT; Barthelmy et al. 2005) aboard the *Neil Gehrels Swift* Observatory (Gehrels et al. 2004). Specifically, we aim at optimising the model parameters using a genetic algorithm (GA; Rojas 1996).

A similar technique, in which the parameters of a physical model were optimised through the application of a GA, was recently applied by Vargas et al. (2022) to model the shock propagation in the supernova SN2014C progenitor star and ejecta, in which the GA was used to optimise a hydrodynamic and radiation transfer model.

Unlike SS96, we restrict our analysis to LGRBs, whose progenitor is thought to be a collapsar, to preserve as much as possible the homogeneity of the putative GRB inner engines. For $\sim 30\%$ of the *Swift* sample with measured redshift, in principle it is possible to carry out the same analysis in the GRB rest frame. However, we did not consider this option, since the cosmological dilation correction by $(1+z)$ is partly counteracted by other energy-dependent effects, which make the final correction milder and less obvious (see Camisasca et al. 2023 and references therein for a detailed explanation).

In this paper, we report the main results and implications. A companion and more ML-oriented paper will report all the technical details. The present work is organised as follows: in Section 2 we describe the data analysis and sample selection, while in Section 3 we illustrate the methods underpinning the avalanche model and the implementation of the genetic algorithm. Section 4 reports the results, whose discussion and conclusions are laid out in Section 5.

2. Data Analysis

2.1. Sample selection

From the BATSE 4B catalogue (Paciesas et al. 1999) we took the 64-ms time profiles that were made available by the BATSE team[2]. Observed with the BATSE eight Large Area Detectors (LADs), these data are the result of a concatenation of three standard BATSE types, DISCLA, PREB, and DISCSC, available in four energy channels: 25–55, 55–110, 110–320, and > 320 keV. We used the total passband LCs. For each GRB the background was interpolated with polynomials of up to fourth degree as prescribed by the BATSE team. In our analysis, we used the background-subtracted LCs.

From an initial sample of 2024 GRBs we selected only those that satisfy the following requirements:

- $T_{90} > 2$ s, that is, only *long* GRBs;
- data available for at least 150 s after the brightest peak;
- signal-to-noise ratio (S/N) of the total net counts within the duration of the event greater than 70.

In order to estimate the S/N, following SS96, rather than the commonly used T_{90}, we used as a proxy of the GRB duration the time interval from the first to the last time bin whose counts exceed the threshold of 20% of the peak counts, henceforth called $T_{20\%}$. Before evaluating the $T_{20\%}$, the LCs were first convolved with a Savitzky-Golay smoothing filter (Savitzky & Golay 1964), using a second order interpolating polynomial, and a moving window of size $T_{90}/15$. Accordingly, we defined the S/N of a GRB as the sum of the net counts in the whole $T_{20\%}$ interval, divided by the corresponding error. The value of the S/N threshold was the result of a trade-off between the number of GRBs and the statistical quality of the LCs in the sample. Furthermore, the $T_{20\%}$ is also used to compute the duration distribution of the LCs (Section 2.2).

We ended up with 585 long GRBs satisfying the aforementioned properties. Hereafter, this will be referred to as the BATSE sample.

As a second dataset, we considered the GRBs detected by *Swift*/BAT from January 2005 to November 2023 and covered in burst mode. We used the total 15–150 keV passband LCs, with 64-ms bin time; these were extracted as mask-weighted background-subtracted LCs, following the standard procedure recommended by the BAT team.[3] From an initial sample of 1389

[2] https://heasarc.gsfc.nasa.gov/FTP/compton/data/batse/ascii_data/64ms/

[3] https://swift.gsfc.nasa.gov/analysis/threads/bat_threads.html.

GRBs observed in burst mode, 531 passed the selection based on the same criteria adopted for BATSE, except for the value of the S/N threshold, which was lowered to 15 to obtain a sample of comparable size to the BATSE one, but still ensuring the required statistical quality. Hereafter, this will be referred to as the *Swift* sample.

2.2. Statistical metrics

We considered the following four metrics, which were also used by SS96:

1. the average peak-aligned post-peak time profile (Mitrofanov 1996), in the time range 0–150 s *after* the brightest peak. It is evaluated by averaging the normalised count rate of all the LCs in the sample, i.e. $\langle F/F_p \rangle$, F_p being the peak count rate. Further details are given in Stern (1996);
2. the average peak-aligned third moment of post-peak time profiles $\langle (F/F_p)^3 \rangle$, evaluated analogously to the first moment;
3. the average auto-correlation function (ACF). For both data samples the ACF is corrected for the counting statistics noise as in Link et al. (1993) and is computed in the 0–150 s interval;
4. the $T_{20\%}$ distribution, with $T_{20\%}$ used as a proxy of the duration.

As in SS96, (1)–(4) are used as metrics to evaluate the degree of similarity between the real and the simulated LCs.

3. Methods

3.1. Light curve simulations

The stochastic process conceived by SS96 belongs to the class of so-called 'branching' processes, which describe the development of a population whose members reproduce according to some random process (Harris 1963). We outline its key features below, and refer the reader to SS96 for more details.

The SS96 model is based on the assumptions that (i) GRB LCs can be viewed as distinct random realisations of a common stochastic process, within narrow parameter ranges; (ii) the stochastic process should be scale invariant in time, and (iii) it operates close to a critical state. With this model, each LC consists of a series of spontaneous primary (or *parent*) pulses, each of which can give rise to secondary (or *child*) pulses, which can then further generate pulses until the process reaches subcritical conditions and stops. Each pulse, which acts as a building block, is described by a Gaussian rise followed by a simple exponential decay:

$$f(t) = \begin{cases} A \exp\left\{-(t-t_p)^2/\tau_r^2\right\}, & \text{for } t < t_p \\ A \exp\left\{-(t-t_p)/\tau\right\}, & \text{for } t > t_p \end{cases} \quad , \tag{1}$$

where τ is roughly the pulse width, t_p is the peak time, A is the amplitude, and we assume $\tau_r = \tau/2$ (Norris et al. 1996). Differently from SS96, we do not sample A from a uniform distribution $\mathcal{U}[0,1]$, rather, for each GRB we sample the value $A_{\max}$ from the distribution of the peak count rates of the real observed LCs, and then the amplitude of each pulse composing that LC is sampled from $\mathcal{U}[0, A_{\max}]$.

The model is described by seven parameters:

- μ_0 rules the number μ_s of spontaneous initial pulses per GRB, which is sampled from a Poisson distribution with μ_0 as expected value:

$$p(\mu_s|\mu_0) = \frac{\mu_0^{\mu_s} \exp(-\mu_0)}{\mu_s!} \quad . \tag{2}$$

- μ rules the number of child pulses μ_c generated by each parent pulse, which is sampled from a Poisson distribution with μ as expected value:

$$p(\mu_c|\mu) = \frac{\mu^{\mu_c} \exp(-\mu)}{\mu_c!} \quad . \tag{3}$$

- α rules the delay Δt between a child and its parent. This delay is exponentially distributed, with e-folding time given by $(\alpha\tau)$, where τ is the time constant of the child pulse:

$$p(\Delta t) = (\alpha\tau)^{-1} \exp(-\Delta t/\alpha\tau) \quad . \tag{4}$$

  Moreover, the spontaneous μ_s primary pulses are all assumed to be delayed with respect to a common invisible trigger event; the probability distribution of such delay t is exponentially distributed:

$$p(t) = (\alpha\tau_0)^{-1} \exp(-t/\alpha\tau_0) \quad , \tag{5}$$

  τ_0 being the time constant of the primary pulse.
- $\tau_{\min}$ and $\tau_{\max}$ define the boundaries for the constant τ_0 of the primary spontaneous pulses and whose probability density function is $p(\tau_0) \propto 1/\tau_0$, equivalent to a uniform distribution of $\log \tau_0$:

$$p(\log \tau_0) = [\log \tau_{\max} - \log \tau_{\min}]^{-1} \quad , \tag{6}$$

  where $\tau_{\min}$ has to be shorter than the time resolution of the instrument. Varying $\tau_{\max}$ is equivalent to rescaling all average avalanche properties in time.
- δ_1 and δ_2 define the boundaries, $[\delta_1, \delta_2]$, of a uniform distribution assumed for the logarithm of the ratio between τ of the child and τ_p of its parent:

$$p[\log(\tau/\tau_p)] = |\delta_2 - \delta_1|^{-1} \quad , \tag{7}$$

  with $\delta_1 < 0$, $\delta_2 \geq 0$, and $|\delta_1| > |\delta_2|$.

Each of the μ_s spontaneous initial pulses gives rise to a pulse avalanche, acting as a parent, spawning another set of child pulses, in a recurrent way. Finally, it is the superposition of all the parent and child pulses generated during the avalanche that shapes the LC of an individual GRB.

The stochastic pulse avalanche model was used to simulate both BATSE and *Swift*/BAT LCs. The statistical noise depends on the total counts in each time bin, which requires the knowledge of the typical background count rate for a given instrument. For BATSE, which consisted of NaI(Tl) scintillators, we assumed a constant background rate of 2.9 cnt $s^{-1}cm^{-2}$, which corresponds to the median of the distribution of the measured error rates. Each final simulated LC was the result of a Poisson realisation, assuming for each time bin the total counts (that is, noise-free simulated profile plus background) as expected value. Lastly, the background was removed.

Swift/BAT is a coded mask coupled with a CZT detection array. Its background-subtracted LCs are the result of the deconvolution of the detection with the pattern of the mask, so the rate in each time bin can be modelled as a Gaussian variable. To simulate BAT LCs, the rate of each time bin was sampled from a Gaussian distribution centred on the LC (noise-free) model obtained with the pulse avalanche model, and with standard deviation randomly sampled from the errors measured in the real *Swift*/BAT LCs.

All the simulations were carried out using an open-source Python[4] implementation[5] by one of the authors.

[4] https://www.python.org/
[5] https://github.com/anastasia-tsvetkova/lc_pulse_avalanche

3.2. Genetic algorithm

SS96 proposed a set of values for the seven model parameters as the result of an educated guess. The optimisation of these parameters, however, is an ideal task for nowadays routinely used ML techniques.

GAs are a specific type of algorithms in the larger family of the so-called evolutionary algorithms (Russell & Norvig 2021; Rojas 1996; Aggarwal 2021; Hurbans 2020), where a Darwinian evolution process is simulated to find the parameters that maximise a function.

In GAs, each solution to an optimisation problem can be seen as an *individual*, with the "fitness" of that individual being determined by the objective function value of the corresponding solution. These solutions are points in the domain of the function to be optimised. In our work, each individual is represented by a genome made of seven genes, which are the parameters of the SS96 model described in Section 3.1.

At each generation, a new set of individuals is created. Over time, the points belonging to the new generations gradually converge towards local maxima of the fitness function. In order to improve over successive generations the overall fitness of the population, GAs incorporate three fundamental processes: selection, crossover, and mutation.

The typical life cycle of a GA, made up of a succession of the so-called *generations*, includes the following steps:

1. Population initialisation: Generating randomly a population of potential solutions;
2. Evaluating fitness: Assessing the quality of each individual by employing a fitness function that assigns scores to evaluate their fitness;
3. Parent selection: Choosing pairs of parents for reproduction based on their fitness score;
4. Offspring creation: Producing offspring by combining genetic information from parents, and introducing random mutations;
5. Generation advancement: Selecting individuals and offspring from the population to progress to the next generation.

GAs are particularly useful in situations where there is no available information about the function's gradient at the evaluated points. Indeed, GA can effectively handle functions that are not continuous or differentiable (Rojas 1996).

3.3. Parameter optimisation

The GA has been implemented using `PyGAD`[6], an open-source Python library containing a collection of several ML algorithms (Gad 2023).

We constrain the seven parameters of the model within the intervals shown in Table 1.

The GA evolves through a sequence of generations consisting of a population with $N_{\rm pop} = 2000$ individual sets of seven parameters. Each set of parameters, hereafter referred to as an individual, is then used to generate $N_{\rm grb} = 2000$ LCs. The very same three constraints, mentioned in Section 2.1, and used for the selection of BATSE and *Swift*/BAT dataset, are applied also on the simulated GRB LCs, the generated ones not satisfying such constraints being discarded. For each of the $N_{\rm pop}$ individuals, we evaluate the same four metrics defined in SS96 over the corresponding $N_{\rm grb}$ LCs (cfr. Section 2.2), and compare them with the values obtained from the real datasets, by computing the $L2$ loss between these four observables. The final loss associated with a given individual is simply defined as the average of these four quantities, the fitness score being the inverse of this value.

Table 1: Region of exploration during the GA optimisation of the seven parameters of the SS96 stochastic model.

Parameter	Lower bound	Upper bound
μ	0.80	1.7
μ_0	0.80	1.7
α	1	15
δ_1	−1.5	−0.30
δ_2	0	0.30
$\tau_{\rm min}$	0.01 s	`bin_time` s
$\tau_{\rm max}$	1 s	60 s

Individuals are then ranked based on their loss. The next generation of individuals is obtained by mixing the genes (i.e. the values of the seven parameters) of the fittest individuals in the current generation. No individuals are instead automatically kept in the next generation, that is, we set to zero the so-called "elitism"[7]. The offspring is obtained by randomly sampling two individuals among the top 15% in the current generation and assigning to each gene the value of the seven parameters from one of the two parents, with equal probability.

Finally, we include the possibility for genetic random mutations to occur. During the mating step, each one of the seven parameters has a 4% probability of undergoing mutation, meaning that the value of the parameters is not inherited from one of the two parents, but instead, it is randomly sampled from the exploration range of the parameter (Table 1).

The optimisation process is stopped when convergence of the loss, and thus of the value of the seven parameters, is reached.

4. Results

In Table 2 we compare the values of the seven model parameters suggested in SS96 with the results of our GA optimisation on the BATSE and *Swift* training datasets. The final optimised values of the seven parameters are obtained as the median value in the whole population of the last GA generation. We also list the achieved values of the loss function evaluated on the training set (both in terms of best parameter configuration and by averaging on the last population) as well as on the test set (i.e. estimated by using 5000 newly simulated GRB LCs). In the bottom, we resolve the individual contribution of each component to the test loss.

Figure 1 displays the comparison of the four observables, described in Section 2.2, between the real BATSE curves and simulated ones (test set). In particular, the panels show the average profiles obtained from the 585 useful BATSE events (blue), the ones estimated from 5000 simulated GRBs with optimised parameters (red), and the ones estimated from 5000 LCs simulated using the parameter values guessed by SS96 (green). Figure 2 shows the analogous comparison between the simulated and the real *Swift*/BAT curves.

We find an excellent agreement for three out of the four metrics computed from real and simulated BATSE LCs, in particular for the average post-peak time profile, its third moment, and the

[6] https://github.com/ahmedfgad/GeneticAlgorithmPython

[7] Due to the stochastic nature of the SS96 algorithm, the same set of parameters will never produce a set of LCs with the same loss; therefore keeping a set of individuals in the next generation is not helping, since in reality, given seven fixed parameters, there are fluctuations in the value of the corresponding loss.

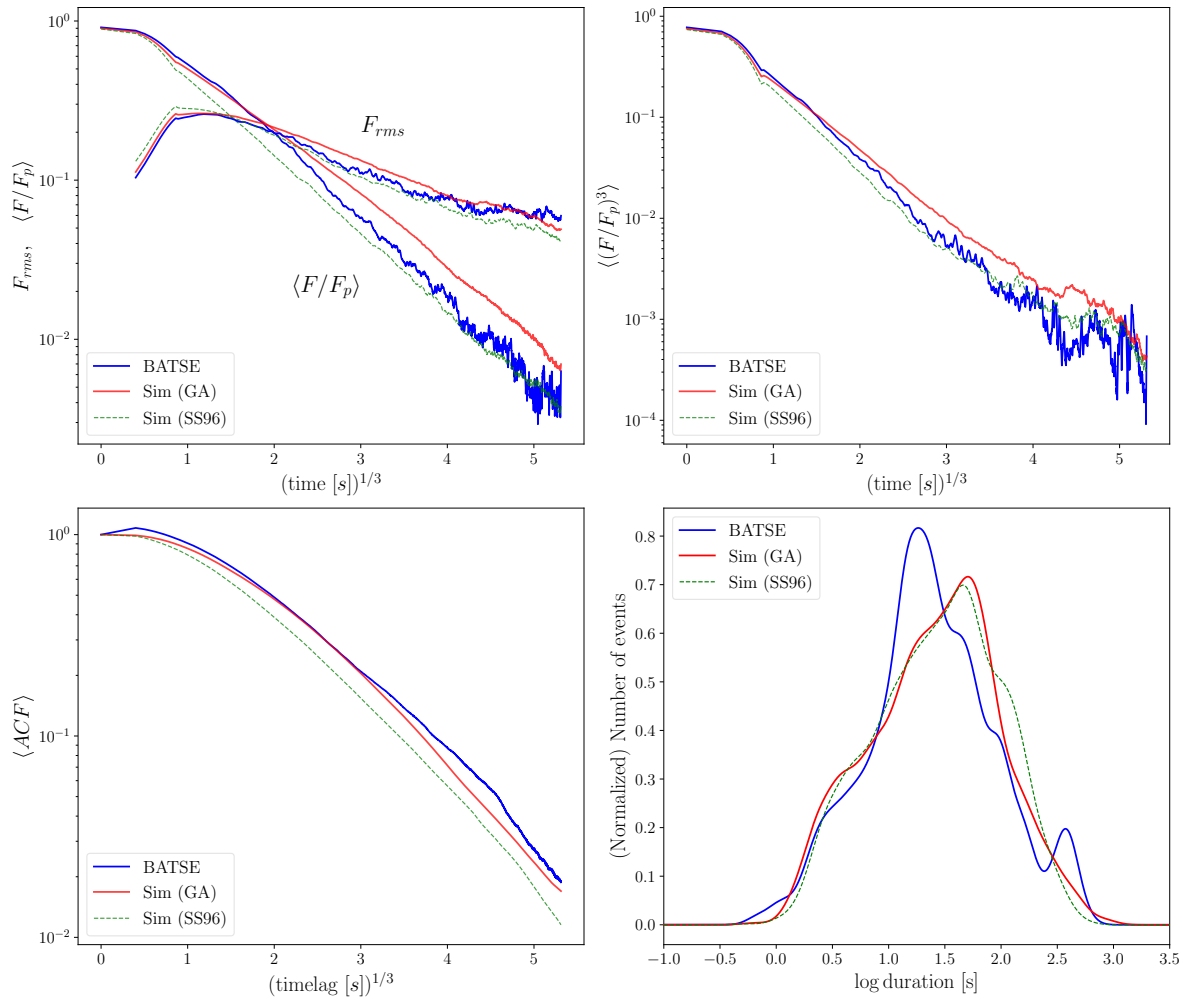

Fig. 1: Average distributions of real (blue), simulated GA-optimised (red), and simulated SS96 (green) BATSE GRB profiles, estimated on the test set (see Table 2). *Top left*: average peak-aligned post-peak normalised time profile, together with the r.m.s. deviation of the individual peak-aligned time profiles, $F_{\rm rms} \equiv \left[\langle (F/F_p)^2 \rangle - \langle F/F_p \rangle^2\right]^{1/2}$. *Top right*: average peak-aligned third moment test. *Bottom left*: Average ACF of the GRBs. *Bottom right*: distribution of duration, measured at a level of 20% of the peak amplitude ($T_{20\%}$). In *top left* and *top right* panels, both real and simulated averaged curves were smoothed with a Savitzky-Golay filter to reduce the effect of Poisson noise. In *bottom right* panel, a Gaussian kernel convolution has been applied to both real and simulated distributions.

average auto-correlation, whose *L2* loss values are smaller than the corresponding ones estimated with SS96 non-optimised parameters, as can be seen from the bottom part of Table 2. For instance, the average ACF metric shows a relative improvement of $\sim 74\%$ after the optimisation. The $T_{20\%}$ distribution holds the largest contribution to the loss; yet, it slightly improves the SS96 performance ($\sim 8\%$ relative improvement). Overall, compared with SS96, our GA-optimised results on BATSE data better reproduce the observed distributions.

As can be inferred from Table 2, and graphically from Figure 2, according to the loss function the avalanche model appears to work even better in the case of *Swift* data: the results on the average ACF and third moment of peak-aligned profiles are comparably good, whereas the average peak-aligned profile and duration distributions are significantly improved with respect to the BATSE case, with a relative loss decrease of $\sim 43\%$ and $\sim 58\%$, respectively.

Notably, the two sets of best-fitting parameters obtained with BATSE and with *Swift*/BAT are very similar and, surprisingly, overall not too different from the one guessed by SS96. In Section 5 we discuss the relevance of this result in more detail.

The parameters for which our optimal values for both sets are somewhat different from those of SS96 are (δ_1, δ_2), $\tau_{\rm max}$, and α. The former pair defines the dynamic range of the child-to-parent pulse duration ratio: our values turn into broader dynamical ranges than SS96, and, at variance with those authors, they admit the possibility of children lasting longer than parents, being $\delta_2 > 0$. While SS96 assumed $\tau_{\rm max} = 26$ s as the maximum value for the duration of parent pulses, our optimised solution favours the possibility of longer parent pulses: 40.2 s for BATSE and 56.8 s for *Swift*/BAT. Finally, our best-fit values for α, which rules the time delay between parent and child, lean towards slightly shorter intervals than SS96.

As in SS96, Figure 3 presents the comparison of four real BATSE time profiles with four simulated LCs of similar morphology and complexity, sampled from the test set, generated using the best-fitting set of BATSE model parameters given above. This qualitative plot shows the ability of the SS96 stochastic model to

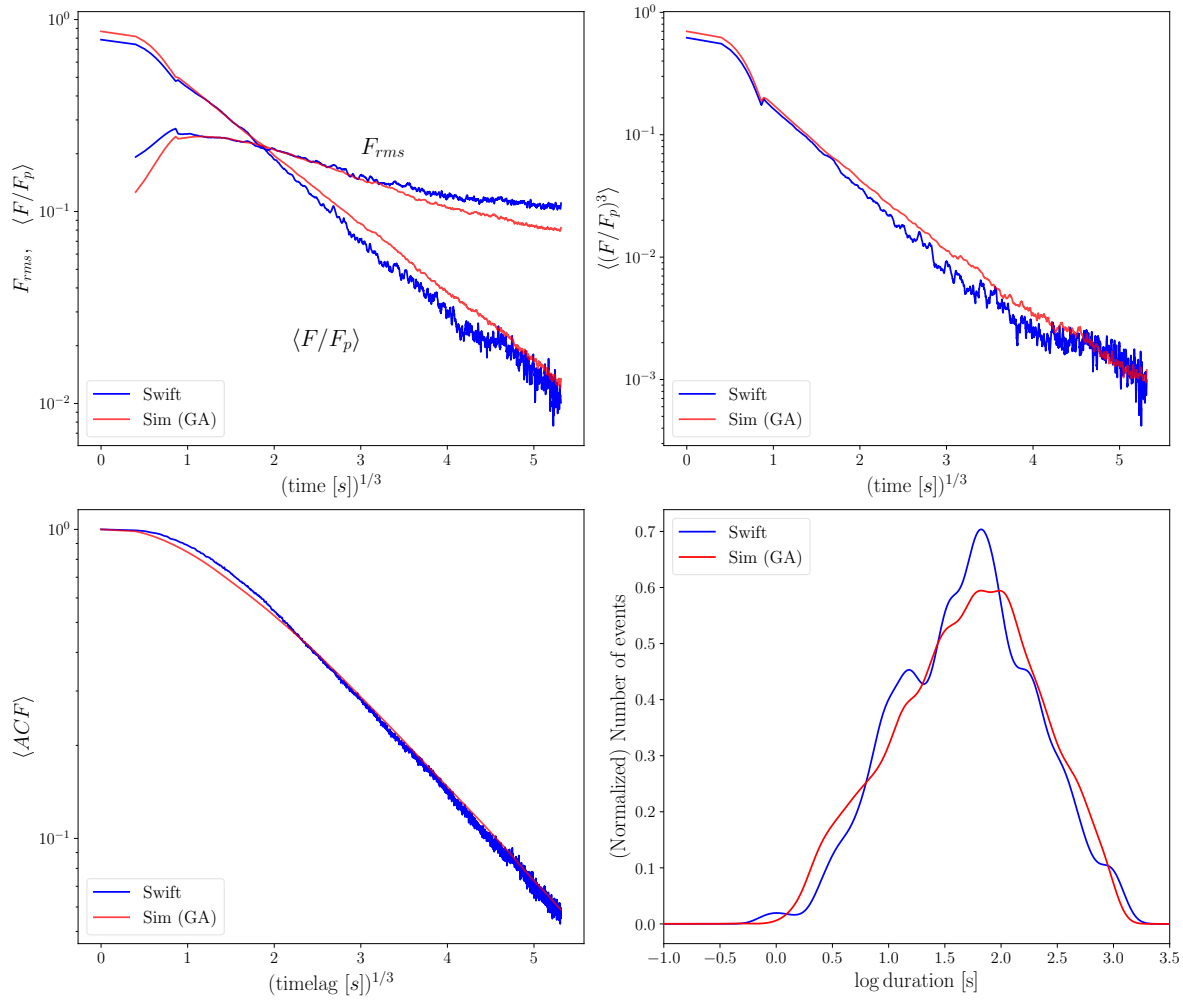

Fig. 2: Comparison between the real *Swift*/BAT dataset and the corresponding simulated dataset on the same four metrics defined for the BATSE dataset, analogously to Figure 1.

reproduce the different morphological classes of LCs discussed in the literature from the earliest observations (Fishman & Meegan 1995).

5. Discussion and conclusions

For the first time in the GRB literature, here we developed and implemented an ML technique to optimise the parameters of a stochastic model capable of generating ex-novo realistic GRB LCs. Our work confirmed the soundness of the insight by SS96: a simple toy model like the stochastic pulse avalanche one is able to generate populations of LCs, whose average behaviour closely resembles that of the real populations of BATSE and *Swift*/BAT long GRBs. With the implementation of GA, we found the two best fit sets of the seven parameters of the model that best reproduce the average behaviours of the two datasets, thus (i) progressing from the educated-guessed values of the original paper to a real fit of the model on BATSE data, and (ii) applying it for the first time to an independent catalogue of GRB LCs like *Swift*/BAT, whose data differ from the BATSE one in many aspects, as detailed below.

In light of our GA-optimised results on BATSE data, the educated guess by SS96 turns out to be surprisingly good. In particular, the finding that μ, that is the average number of child-pulses generated by each parent-pulse, must be close to unity (our $1.10^{+0.03}_{-0.02}$ vs. 1.20 of SS96) confirms the insightful Ansatz by SS96 that the model must operate very close to a critical regime ($\mu = 1$), to account for the observed variety of GRB profiles. Interestingly, the same clue is also obtained in the GA-optimised parameters of the *Swift*/BAT sample. This result is far from obvious for three main reasons: (i) the passband of the two experiments is significantly different, with *Swift*/BAT profiles being softer and, as such, less spiky (e.g., Fenimore et al. 1995); (ii) the average S/N of the two sets is also remarkably different, with a minimum value of 70 for BATSE, to be compared with the poorer lower threshold of 15 for *Swift*/BAT (see Section 2); (iii) the GRB populations seen by the two experiments are likely different: thanks to its larger effective area at low energies, longer trigger accumulation times and much more complex trigger algorithms, *Swift*/BAT detects more high-redshift GRBs (Band 2006; Lien et al. 2014; Wanderman & Piran 2010). Therefore, our results provide additional evidence for a nearly critical regime in which GRB engines would work, in agreement with other independent investigations (Maccary et al. 2024; Guidorzi et al. 2024).

In addition to providing new clues on the dynamical behaviour of LGRB inner engines or, more generally, on the way some kind of energy is dissipated into gamma-rays, this model offers the practical possibility of simulating realistic GRB profiles with future experiments, such as HERMES (Fiore et al. 2020) and

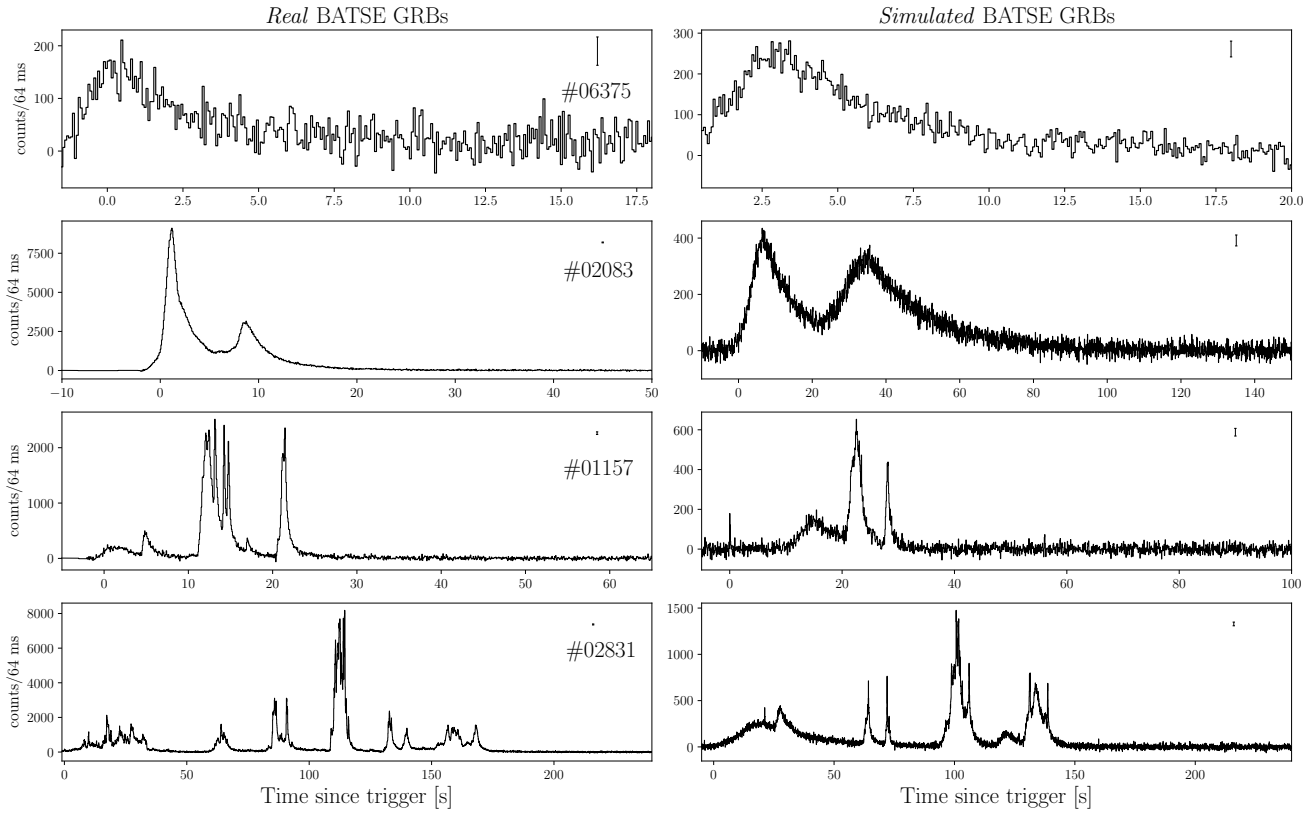

Fig. 3: Four examples of as many classes of GRB LCs from the BATSE real sample (*left*) along with their trigger number, and the corresponding simulated one (*right*). Following the same qualitative classification adopted by SS96, from top to bottom the four classes are "single pulse", "blending of some pulses", "moderately structured", and "highly erratic". On the top right of each subplot is shown the average error on the counts of the corresponding LC.

possibly the X/Gamma-ray Imaging Spectrometer (XGIS; Amati et al. 2022) aboard ESA/M7 candidate THESEUS (Amati et al. 2021) currently selected for a phase A study. The task of simulating realistic GRB time profiles, as they will be seen by forthcoming detectors, is far from obvious: the alternative option of renormalising real LCs observed with different instruments is inevitably hampered by the presence of counting statistics (Poisson) noise, which cannot be merely rescaled without altering its nature. A filtering procedure would be then required, which in turn assumes that the uncorrelated Poisson noise can be disentangled from the genuine (unknown) variance of GRBs, which also requires substantial effort.

Summing up, the present work showcases the potential of a simple toy model like the avalanche one conceived by SS96, once it is properly bolstered with ML techniques. Moreover, it paves the way to further optimisation of the model in different directions: (i) by adding further metrics, such as the distributions of the following observables: GRB S/N, duration of observed pulses, or the number of peaks per GRB (Guidorzi et al. 2024); (ii) by studying in more detail the dependence of the model parameters on the energy channels; (iii) by carrying out the same study in the comoving frame of a sample of GRBs with known redshift, assuming the luminosity and released energy distributions of individual pulses (Maccary et al. 2024). Eventually, these efforts should end up with a reliable and accessible machine for simulating credible LGRB profiles with any experiment. In parallel, the final outcome would be a detailed characterisation of the dynamics that rules long GRB prompt emission, possibly disclosing the nature of long GRB engines.

The source code of our algorithm, alongside all the scripts used to perform the data analysis and produce the plots, will be publicly released on GitHub[8] upon publication.

Acknowledgements. LB is indebted to the communities behind the multiple free, libre, and open-source software packages on which we all depend. AT acknowledges financial support from ASI-INAF Accordo Attuativo HERMES Pathfinder operazioni n. 2022-25-HH.0 and the basic funding program of the Ioffe Institute FFUG-2024-0002.
CG conceived the research based on the original code developed by AT according to the SS96, LB, GA, and CG developed the methodology, LB, LF and CG performed all the numerical work, including software development, investigation, and validation. All authors contributed to the discussion of the results, the editing and revision of the paper.
This work uses the following software packages: `Python` (Van Rossum & Drake 2009), `PyGAD` (Gad 2023), `NumPy` (van der Walt et al. 2011; Harris et al. 2020), `SciPy` (Virtanen et al. 2020) `matplotlib` (Hunter 2007), `seaborn` (Waskom 2021), `MEPSA` (Guidorzi 2015), `gnuplot` (Williams et al. 2023), `bash` (GNU 2007).

References

Aggarwal, C. C. 2021, Artificial Intelligence: A Textbook (Springer)
Ahumada, T., Singer, L. P., Anand, S., et al. 2021, Nature Astronomy, 5, 917
Amati, L., Labanti, C., Mereghetti, S., et al. 2022, in Society of Photo-Optical Instrumentation Engineers (SPIE) Conference Series, Vol. 12181, Space Telescopes and Instrumentation 2022: Ultraviolet to Gamma Ray, ed. J.-W. A. den Herder, S. Nikzad, & K. Nakazawa, 1218126
Amati, L., O'Brien, P. T., Götz, D., et al. 2021, Experimental Astronomy, 52, 183
Band, D. L. 2006, ApJ, 644, 378
Barthelmy, S. D., Barbier, L. M., Cummings, J. R., et al. 2005, Space Sci. Rev., 120, 143

[8] https://github.com/LBasz/geneticgrbs

Table 2: Results of the GA optimisation on the BATSE and *Swift* datasets.

Parameter	SS96	BATSE	*Swift*/BAT
μ	1.20	$1.10^{+0.03}_{-0.02}$	$1.34^{+0.03}_{-0.02}$
μ_0	1.00	$0.91^{+0.06}_{-0.07}$	$1.16^{+0.18}_{-0.10}$
α	4.00	$2.57^{+0.07}_{-0.52}$	$2.53^{+0.25}_{-0.01}$
δ_1	−0.50	$-1.28^{+0.16}_{-0.05}$	$-0.75^{+0.11}_{-0.29}$
δ_2	0	$0.28^{+0.01}_{-0.03}$	$0.27^{+0.01}_{-0.02}$
$\tau_{\rm min}$	0.02 s	$0.02^{+0.02}_{-0.01}$ s	$0.03^{+0.02}_{-0.02}$ s
$\tau_{\rm max}$	26.0 s	$40.2^{+0.9}_{-1.2}$ s	$56.8^{+0.4}_{-1.3}$ s
Loss (*Train* best)	–	0.72	0.38
Loss (*Train* avg.)	–	0.98	0.66
Loss (*Test*)	1.47	0.88	0.56
Loss (*Test*: $\langle F/F_p \rangle$)	1.01	0.67	0.46
Loss (*Test*: $\langle (F/F_p)^3 \rangle$)	0.40	0.20	0.20
Loss (*Test*: $\langle$ACF$\rangle$)	2.24	0.64	0.49
Loss (*Test*: $T_{20\%}$)	2.22	2.04	1.08

Notes. Col. 2 presents the parameters given by SS96 (for the BATSE dataset), while Col. 3 and Col. 4 show the optimised ones obtained after 30 generations of the GA for BATSE and *Swift*/BAT, respectively. From the distribution of the seven parameters in the last generation we estimated their best-fitting values as the median, and their corresponding errors as the 16-th and 84-th percentiles. "Train best" is the loss of the best generation, while "Train avg." is the average loss in the last generation. The test set is a newly produced set of 5000 simulated LCs; the last four rows show all the single contributions to the "Test" loss.

Becerra, L., Ellinger, C. L., Fryer, C. L., Rueda, J. A., & Ruffini, R. 2019, ApJ, 871, 14
Beloborodov, A. M., Stern, B. E., & Svensson, R. 1998, ApJ, 508, L25
Camisasca, A. E., Guidorzi, C., Amati, L., et al. 2023, A&A, 671, A112
Costa, E., Frontera, F., Heise, J., et al. 1997, Nature, 387, 783
Dichiara, S., Guidorzi, C., Amati, L., & Frontera, F. 2013, MNRAS, 431, 3608
Eichler, D., Livio, M., Piran, T., & Schramm, D. N. 1989, Nature, 340, 126
Feigelson, E. D., de Souza, R. S., Ishida, E. E. O., & Jogesh Babu, G. 2021, Annual Review of Statistics and Its Application, 8, 493
Fenimore, E. E., in 't Zand, J. J. M., Norris, J. P., Bonnell, J. T., & Nemiroff, R. J. 1995, ApJ, 448, L101
Fiore, F., Burderi, L., Lavagna, M., et al. 2020, in Society of Photo-Optical Instrumentation Engineers (SPIE) Conference Series, Vol. 11444, Space Telescopes and Instrumentation 2020: Ultraviolet to Gamma Ray, ed. J.-W. A. den Herder, S. Nikzad, & K. Nakazawa, 114441R
Fishman, G. J. & Meegan, C. A. 1995, ARA&A, 33, 415
Gad, A. F. 2023, Multimedia Tools and Applications, 1
Gehrels, N., Chincarini, G., Giommi, P., et al. 2004, ApJ, 611, 1005
Gehrels, N., Norris, J. P., Barthelmy, S. D., et al. 2006, Nature, 444, 1044
Geng, J.-J., Zhang, B., & Kuiper, R. 2016, ApJ, 833, 116
GNU, P. 2007, Free Software Foundation. Bash (3.2. 48)[Unix shell program]
Gompertz, B. P., Ravasio, M. E., Nicholl, M., et al. 2023, Nature Astronomy, 7, 67
Gottlieb, O., Bromberg, O., Levinson, A., & Nakar, E. 2021a, MNRAS, 504, 3947
Gottlieb, O., Bromberg, O., Singh, C. B., & Nakar, E. 2020a, MNRAS, 498, 3320
Gottlieb, O., Levinson, A., & Nakar, E. 2020b, MNRAS, 495, 570
Gottlieb, O., Nakar, E., & Bromberg, O. 2021b, MNRAS, 500, 3511
Greiner, J., Hugentobler, U., Burgess, J. M., et al. 2022, A&A, 664, A131
Guidorzi, C. 2015, Astronomy and computing, 10, 54
Guidorzi, C., Dichiara, S., & Amati, L. 2016, A&A, 589, A98
Guidorzi, C., Dichiara, S., Frontera, F., et al. 2015, ApJ, 801, 57
Guidorzi, C., Margutti, R., Amati, L., et al. 2012, MNRAS, 422, 1785
Guidorzi, C., Sartori, M., Maccary, R., et al. 2024, A&A, in press, arXiv:2402.17282
Harris, C. R., Millman, K. J., van der Walt, S. J., et al. 2020, Nature, 585, 357–362
Harris, T. E. 1963, The theory of branching processes, Die Grundlehren der Mathematischen Wissenschaften, Bd. 119 (Berlin: Springer-Verlag), xiv+230
Hunter, J. D. 2007, Computing in Science & Engineering, 9, 90
Hurbans, R. 2020, Grokking Artificial Intelligence Algorithms (Manning)
Kumar, P. & Zhang, B. 2015, Phys. Rep., 561, 1
Levan, A. J., Gompertz, B. P., Salafia, O. S., et al. 2024, Nature, 626, 737
Levan, A. J., Malesani, D. B., Gompertz, B. P., et al. 2023, Nature Astronomy, 7, 976
Li, X.-J. & Yang, Y.-P. 2023, ApJ, 955, L34
Lien, A., Sakamoto, T., Gehrels, N., et al. 2014, ApJ, 783, 24
Link, B., Epstein, R. I., & Priedhorsky, W. C. 1993, ApJ, 408, L81
Lyu, F., Li, Y.-P., Hou, S.-J., et al. 2020, Frontiers of Physics, 16, 14501
Maccary, R., Guidorzi, C., Amati, L., et al. 2024, ApJ, in press, arXiv:2401.14063
MacFadyen, A. I. & Woosley, S. E. 1999, ApJ, 524, 262
Mitrofanov, I. G. 1996, Mem. Soc. Astron. Italiana, 67, 417
Morsony, B. J., Lazzati, D., & Begelman, M. C. 2010, ApJ, 723, 267
Nakar, E. & Piran, T. 2002, MNRAS, 331, 40
Narayan, R., Paczynski, B., & Piran, T. 1992, ApJ, 395, L83
Norris, J. P. & Bonnell, J. T. 2006, ApJ, 643, 266
Norris, J. P., Nemiroff, R. J., Bonnell, J. T., et al. 1996, ApJ, 459, 393
Paciesas, W. S., Meegan, C. A., Pendleton, G. N., et al. 1999, ApJS, 122, 465
Paczynski, B. 1991, Acta Astron., 41, 257
Paczyński, B. 1998, ApJ, 494, L45
Quilligan, F., McBreen, B., Hanlon, L., et al. 2002, A&A, 385, 377
Ramirez-Ruiz, E., Merloni, A., & Rees, M. J. 2001, MNRAS, 324, 1147
Rastinejad, J. C., Gompertz, B. P., Levan, A. J., et al. 2022, Nature, 612, 223
Rojas, R. 1996, Neural Networks: A Systematic Introduction (Springer Nature)
Rossi, A., Rothberg, B., Palazzi, E., et al. 2022, ApJ, 932, 1
Rueda, J. A. & Ruffini, R. 2012, ApJ, 758, L7
Russell, S. J. & Norvig, P. 2021, Artificial Intelligence: a modern approach, 4th edn. (Pearson)
Sanna, A., Burderi, L., Di Salvo, T., et al. 2020, in Society of Photo-Optical Instrumentation Engineers (SPIE) Conference Series, Vol. 11444, Space Telescopes and Instrumentation 2020: Ultraviolet to Gamma Ray, ed. J.-W. A. den Herder, S. Nikzad, & K. Nakazawa, 114444X
Savitzky, A. & Golay, M. J. E. 1964, Analytical Chemistry, 36, 1627
Stern, B. E. 1996, ApJ, 464, L111
Stern, B. E. & Svensson, R. 1996, ApJ, 469, L109
Troja, E., Fryer, C. L., O'Connor, B., et al. 2022, Nature, 612, 228
van der Walt, S., Colbert, S. C., & Varoquaux, G. 2011, Computing in Science Engineering, 13, 22
Van Rossum, G. & Drake, F. L. 2009, Python 3 Reference Manual (Scotts Valley, CA: CreateSpace)
Vargas, F., De Colle, F., Brethauer, D., Margutti, R., & Bernal, C. G. 2022, The Astrophysical Journal, 930, 150
Virtanen, P., Gommers, R., Oliphant, T. E., et al. 2020, Nature Methods, 17, 261
Wanderman, D. & Piran, T. 2010, MNRAS, 406, 1944
Wang, F. Y. & Dai, Z. G. 2013, Nature Physics, 9, 465
Waskom, M. L. 2021, Journal of Open Source Software, 6, 3021
Wei, J.-J. 2023, Physical Review Research, 5, 013019
Williams, T., Kelley, C., & many others. 2023, Gnuplot 6.0: an interactive plotting program
Woosley, S. E. 1993, ApJ, 405, 273
Yang, J., Ai, S., Zhang, B. B., et al. 2022, Nature, 612, 232
Yi, S.-X., Lei, W.-H., Zhang, B., et al. 2017, Journal of High Energy Astrophysics, 13, 1
Zhang, B. 2018, The Physics of Gamma-Ray Bursts
Zhang, B. & Yan, H. 2011, ApJ, 726, 90
Zhang, B. B., Liu, Z. K., Peng, Z. K., et al. 2021, Nature Astronomy, 5, 911

Università degli Studi di Ferrara

Sezioni

Dottorati di ricerca

Il tuo indirizzo e-mail

frrlsi@unife.it

Oggetto:

Dichiarazione di conformità della tesi di Dottorato

Io sottoscritto Dott. (Cognome e Nome)

Ferro Lisa

Nato a:

Rovigo

Provincia:

RO

Il giorno:

16/12/1995

Avendo frequentato il Dottorato di Ricerca in:

Fisica

Ciclo di Dottorato

36

Titolo della tesi:

Development of new technologies and methods for next-generation gamma-ray telescopes

Titolo della tesi (traduzione):

Sviluppo di nuove tecnologie e metodi per telescopi gamma di nuova generazione

Tutore: Prof. (Cognome e Nome)

Piero Rosati

Settore Scientifico Disciplinare (S.S.D.)

FIS/05

Parole chiave della tesi (max 10):

focusing optics, X-ray astrophysics, gamma-ray, polarimetry, astrophysics

Consapevole, dichiara

CONSAPEVOLE: (1) del fatto che in caso di dichiarazioni mendaci, oltre alle sanzioni previste dal codice penale e dalle Leggi speciali per l'ipotesi di falsità in atti ed uso di atti falsi, decade fin dall'inizio e senza necessità di alcuna formalità dai benefici conseguenti al provvedimento emanato sulla base di tali dichiarazioni; (2) dell'obbligo per l'Università di provvedere al deposito di legge delle tesi di dottorato al fine di assicurarne la conservazione e la consultabilità da parte di terzi; (3) della procedura adottata dall'Università di Ferrara ove si richiede che la tesi sia consegnata dal dottorando in 1 originale cartaceo e 1 in formato PDF/A caricata sulla procedura informatica Esse3 secondo le istruzioni pubblicate sul sito: http://www.unife.it/studenti/dottorato alla voce ESAME FINALE – disposizioni e modulistica; (4) del fatto che l'Università, sulla base dei dati forniti, archivierà e renderà consultabile in rete il testo completo della tesi di dottorato di cui alla presente dichiarazione attraverso la pubblicazione ad accesso aperto nell'Archivio Istituzionale dei Prodotti della Ricerca IRIS-UNIFE (www.iris.unife.it) oltre che attraverso i Cataloghi delle Biblioteche Nazionali Centrali di Roma e Firenze; DICHIARO SOTTO LA MIA RESPONSABILITA': (1) che la copia della tesi depositata presso l'Università di Ferrara in formato cartaceo è del tutto identica a quella caricata in formato PDF/A sulla procedura informatica Esse3, a quelle da inviare ai Commissari di esame finale e alla copia che produrrò in seduta d'esame finale. Di conseguenza va esclusa qualsiasi responsabilità dell'Ateneo stesso per quanto riguarda eventuali errori, imprecisioni o omissioni nei contenuti della tesi; (2) di prendere atto che la tesi in formato cartaceo è l'unica alla quale farà riferimento l'Università per rilasciare, a mia richiesta, la dichiarazione di conformità di eventuali copie; (3) che il contenuto e l'organizzazione della tesi è opera originale da me realizzata e non compromette in alcun modo i diritti di terzi, ivi compresi quelli relativi alla sicurezza dei dati personali; che pertanto l'Università è in ogni caso esente da responsabilità di qualsivoglia natura civile, amministrativa o penale e sarà da me tenuta indenne da qualsiasi richiesta o rivendicazione da parte di terzi; (4) che la tesi di dottorato non è il risultato di attività rientranti nella normativa sulla proprietà industriale, non è stata prodotta nell'ambito di progetti finanziati da soggetti pubblici o privati con vincoli alla divulgazione dei risultati, non è oggetto di eventuali registrazioni di tipo brevettale o di tutela. PER ACCETTAZIONE DI QUANTO SOPRA RIPORTATO

Firma del dottorando

Ferrara, li 16/05/2024 (data) Firma del Dottorando Lisa Ferro

Firma del Tutore

Visto: Il Tutore Si approva Firma del Tutore Piero Rosati